京都大学化学研究所
国際共同利用・共同研究拠点

令和３年度
成果報告書

化学関連分野の深化・連携を基軸とする
先端・学際グローバル研究拠点

京都大学化学研究所
国際共同利用・共同研究拠点

化学関連分野の深化・連携を基軸とする
先端・学際グローバル研究拠点

令和３年度
成果報告書

まえがき

京都大学化学研究所は、平成２２年度から「化学関連分野の深化・連携を基軸とする先端・学際研究拠点」（平成２８年度から第二期）として国内外の共同利用・共同研究を推し進め、それを新たな糧としてより多様でグローバルな化学研究の展開と若手研究者の育成・輩出を図って参りました。特に本拠点では、化学関連コミュニティの研究者の皆様からの要請を踏まえながら、化学研究所の研究分野の広がりと深さに加えて、これまでの様々な連携実績を活かし、国内外の研究機関の相互協力を担保するハブ環境も提供しています。先端・学際的分野深耕にあたっては、関連コミュニティの研究者の皆様と化学研究所の教員が推進する分野選択型、課題提案型、施設・機器利用型、連携・融合促進型等の多彩な共同研究と、拠点として主催・共催する各種国際会議、シンポジウム、研究会等を通じて、多様性と先進性を担保し、さらに、国際的視点に基づいて次代の化学関連分野を担う若手研究者の育成にも注力しています。また、拠点運営では、所外、学外の関連分野有識者と化学研究所の教員を委員とする共同研究委員会および運営評議会を核として、共同研究課題の公募・採択などを戦略的に遂行しております。

このようなグローバルな拠点活動が評価され、化学研究所は、平成３０年１１月１３日文部科学大臣から国際共同利用・共同研究拠点に認定され、「化学関連分野の深化・連携を基軸とする先端・学際グローバル研究拠点」として活動を強化しています。国際拠点活動の四年目（最終年度）にあたる令和３年度には、化学研究所教員が一丸となって、１９９件の応募の中から採択された１３３件の共同研究を遂行しました。そのうち、グローバルな化学研究の展開と人材育成のため、採択数の４４％に当たる５９件（若手国際枠７件を含む）の国際共同研究を遂行しました。しかし、令和２年度から続く世界的な新型コロナウイルス感染症拡大のため、国際・国内共同研究の実施にあたり対面交流が制限される状況が未だ続いております。これを補完する拠点活動支援として、本拠点ではリモート実験環境整備やハイブリッド会議システム導入など、研究・教育環境整備に引き続き取り組んで参りました。今後とも、国際的ハブ機能を活用し、国際共同利用・共同研究の一層の促進、国際学術ネットワークの充実、国際的・先進的視野をもつ若手研究者の育成に取り組むことで、化学を中心とする研究分野の深化と境界学術分野の新規開拓を一層推進して参ります。令和４年度からは第二期の国際共同利用・共同研究拠点活動が始まります。皆様にはさらなるご支援・ご協力のほどよろしくお願い申し上げます。

本報告書は、令和３年度の本拠点における研究成果をとりまとめたものです。本報告書をご一読頂き、今後の本拠点の目指すべき方向や活動の推進方法などに関する忌憚のないご意見・ご提案などをお聞かせ下されば幸甚に存じます。

化学研究所
所長 辻井 敬亘

令和3年度 共同利用・共同研究報告書 目次

1. 共同研究成果報告

分野選択型共同研究

ビーム科学分野

2021-1 アスペクト比の制御された金ナノらせんの合成および光学特性評価
大阪産業技術研究所 中川 充 1

2021-2 蓄積リングのための位置感度型アクティブ標的の開発
理化学研究所 山口 由高 2

2021-3 Crystal Structure Analysis of GraE from Root-Nodule-Forming Bacterium
Kansai University Tadao Oikawa 3

2021-4 プリパルス付与による高変換TNSAイオン加速機構実証
大阪大学レーザー科学研究所 砂原 淳 4

2021-5 電子線を用いた超高線量率放射線がん治療（FLASH）の作用機序の解明
量子科学技術研究開発機構 小平 聡 5

2021-6 ナノ構造を持つ ISOL 用標的の開発
理化学研究所 大西 哲哉 6

2021-7※ Electronic Structure of Biomimetic [Mo_3S_4Fe] Clusters and its Relation to the catalytic N_2-Reduction: A Computational Study
Hokkaido University W. M. C. Sameera 7

元素科学分野

2021-8※ Development and device evaluation of new D-π-A emitters based on fluorinated triarylborone acceptors
Julius-Maximilians-Universität Würzburg Todd B. Marder 8

2021-9※ Gas sensing properties research of metal oxides
Chinese Academy of Sciences Haichuan Guo 9

2021-10※ Design and Tailoring Advanced Functional Materials: Symmetry Operation and High Pressure Synthesis
National Taiwan University Wei-tin Chen 10

2020-11※ Investigating iron nitrides prepared by new high-pressure synthesis with Mössbauer spectroscopy
University of Edinburgh Simon D. Kloß 11

2021-12※ Small molecule activation using anionic crypto-FLPs
University of Bonn Rainer Streubel 12

2021-13※ Development of Unsymmetrical π-Electron Systems of Heavier Main Group Elements and Elucidation of Their Property
Tohoku University Takeaki Iwamoto 13

2021-14※ C—H Borylation and Silylation under visible-light enabled Fe-catalysis
Visva-Bharati University Alakananda Hajra 14

2021-15※ Development of Iron-based Electrocatalysts for Electrocatalytic Conversion of Biomass into Value Added Chemicals
Indian Institute of Technology Indore Apurba K. Das 15

2020-16※ Iron-Catalyzed Asymmetric Carbozincation and Ring-Opening Reactions of Oxabicyclic Alkenes
Indian Institute of Engineering Science and Technology Laksmikanta Adak 16

2021-17 Synthesis of ferrocenyl-phosphines and their application in the preparation of Fe clusters
Tokushima University Masamichi Ogasawara 17

※ 国際共同利用・共同研究

2021-18 極低温強磁場対応THz-STMの開発
東海大学　立崎 武弘 18
2021-19 微弱な分子振動モードと結合させた極薄膜半導体における励起子発光の変調
大阪府立大学　桐谷 乃輔 19
2021-20 高強度テラヘルツパルスを駆使したマルチフェロイック物質における
マグノン・フォノン励起
東京工業大学　佐藤 琢哉 20
2021-21 高圧合成法を利用したエネルギー材料の開発
横浜国立大学　藪内 直明 21
2021-22 Study on the physical mechanism on novel-ternary nanoparticle formation
Meio University Yasutomi Tatetsu 22
2021-23 Development of collaborative reaction fields based on dinuclearization of
mononuclear complexes
Yokohama National University Yoshitaka Yamaguchi 23
2021-24 磁性微粒子を用いたウルシオール塗膜の機能発現
京都市産業技術研究所　橘 洋一 24
2021-25 Creation of Effective Oxidation Scavenger for Efficient Perovskite-based
Solar Cells
University of Tsukuba Takahiro Sasamori 25
2021-26 Development of heteroacenes with excellent photophysical and
electrochemical properties
Okayama University Koichi Mitsudo 26
バイオ情報学分野
2021-27※ Integrating Omics Data and Module-based Network with Deep Learning to
Develop Cancer Type Predictive Models
National Yang Ming Chiao Tung University Jinn-Moon Yang 27
2021-28※ Developing Data-driven Deep Learning Approaches for Accurate
Identification of Protease Specific Substrate Targets and Cleavage Sites
Monash University Jiangning Song 28
2021-29※ Unveiling the genomic contents of ecologically important marine giant viruses
CNRS Tom O. Delmont 29
2021-30※ Revealing associations between giant viruses and eukaryotes in the global
ocean through community networks inference and mining
CNRS Samuel Chaffron 30
2021-31※ A Study on Statistical Machine Learning for Efficient Graph Structured Data
Analysis
Nagoya Institute of Technology Masayuki Karasuyama 31
2021-32 Control and Analysis of Complex Networks via Probabilistic Minimum
Dominating Sets
Toho University Jose C. Nacher 32
2021-33 Comprehensive analysis of viral succession during the transition of multiple
types of algal blooms
Fukui Prefectural University Keizo Nagasaki 33
2021-34 Development of the method for the detection of coronavirus diversity
Osaka University Tokiko Watanabe 34
2021-35 効果的な分子ネットワーク解析方法の開発と医学・農学への応用
帯広畜産大学　茅野 光範 35

※ 国際共同利用・共同研究

物質合成分野
2021-36※ Synthesis of inorganic molecules for elucidation of biosynthetic pathways of iron-sulfur clusters
University of California, Irvine Markus W. Ribbe 36
2021-37※ Development of new blue TADF emitters with horizontal molecular orientations
University of St Andrews Eli Zysman-Colman 37
2021-38※ Exploration of Cycloaddition Properties of Guanidine Functionalized Isobenzofurans
Rudjer Boskovic Institute Davor Margetic 38
2021-39※ Development of hole transport materials for tin-perovskite and device characterization
Osaka University Akinori Saeki 39
2021-40 自己集合性含ホウ素化合物の合成、集合過程解明ならびに機能開拓
鈴鹿医療科学大学 若林 成知 40
2021-41 ジベンゾフェナジンを電子アクセプターとするスルースペース電荷移動型熱活性化遅延蛍光材料の創製
大阪大学 武田 洋平 41
2021-42 Chiral Silica with preferred-handed helical structure via chiral transfer
Osaka Institute of Technology Tomoyasu Hirai 42
2021-43 高効率光電変換を志向した非対称型有機半導体分子の開発
大阪大学 鈴木 充朗 43
2021-44 ソルバトクロミズムを示さないπ共役双性イオンの合成と物性
大阪大学 清水 章弘 44
2021-45 Host-Guest Complexation of Cyclohexa-2,7-anthrylene Ethynylene Derivatives with [n]CPP
Shizuoka University Kenji Kobayashi 45
2021-46 超分岐構造高分子の滑剤作用の解明と最適化
東北大学 髙橋 裕 46
現象解析分野
2021-47※ Trace metal elemental and isotopic composition in the North Pacific Ocean: sources and internal cycling (2)
Academia Sinica Tung-Yuan Ho 47
2021-48※ Resolving the structure-dynamics-property relationship in polymer nanocomposites under uniaxial stretching
Stony Brook University Tadanori Koga 48
2021-49※ Development of simulation scheme for wall-slip of polymers
Università degli Studi di Napoli “Federico II” Giovanni Ianniruberto 49
2021-50※ High Frequency Response of Polymeric Liquids: Rheology and Dielectric Relaxation
Yamagata University Sathish K. Sukumaran 50
2021-51※ Molecular understanding on the structures and dynamics of end-modified polymers
Suranaree University of Technology Visit Vao-soongnern 51
2021-52 光エネルギー変換に対する振電効果：固体NMRと時間分解EPRの連携による解明
神戸大学 小堀 康博 52
2021-53 Effect of microplastics on distribution of trace heavy metals in seawater
Kindai University Yuzuru Nakaguchi 53
2021-54 イオン液体含有高分子膜を用いた金属イオンの液膜輸送に関する研究
京都教育大学 向井 浩 54

※ 国際共同利用・共同研究

2021-55 硫黄系高分子薄膜材料における硫黄元素が構成するナノ構造の空間不均一性評価
関西学院大学 藤原 明比古 55
2021-56 Structure analysis of polymer materials having sulfur atoms in a wet state by resonant small-angle scattering methods
Nagoya Institute of Technology Katsuhiro Yamamoto 56
2021-57 プラズモニック合金ナノ粒子を設計するための理論的指針の構築
北海道大学 飯田 健二 57
2021-58 部分フッ素化両親媒性分子の膜物性・構造に対するR_f鎖長依存性の解析
群馬大学 園山 正史 58
2021-59 A spectroscopic analysis on bio-degradation processes of polymer thin film surfaces
Kyoto Institute of Technology Takashi Aoki 59
2021-60 Identification of an active gibberellin compound in the basal land plant Marchantia polymorpha
Kyoto University Takayuki Kohchi 60
2021-61 Glass Transition and Molecular Dynamics of Guest Low Mass Molecules in the Clathrate of Polymer Crystals
Osaka University Osamu Urakawa 61

課題提案型共同研究

2021-62※ Nonlinear Rheological Behavior of Telechelic Ionomer with Distribution of Ionic Stickers at the Ends
Chinese Academy of Sciences Zhijie Zhang 62
2021-63※ Role of PX-PH-type phospholipase Ds in plant intracellular membrane traffic
MRC Laboratory of Molecular Biology Yohei Ohashi 63
2021-64※ Role of phosphoinositide signaling in pollen development
Peking University Sheng Zhong 64
2021-65※ Self-Assembling Adjuvant-Built-In Vaccines for Cancer Immune Therapy
Tsinghua University Yan-Mei Li 65
2021-66※ Site-selective protein acetylation by a small molecule
Fudan University Lu Zhou 66
2021-67※ Orbitronics with new material systems
University of Ulsan Sanghoon Kim 67
2021-68※ Study of characteristics of spin wave in magnetic insulator
KAIST Kab-Jin Kim 68
2021-69※ Application of ferrimagnets for spintronics devices
Far Eastern Federal University Alexander Samardak 69
2021-70※ Highly efficient red thermally activated delayed fluorescence emitters with sterically hindered donor skeleton
Kyung Hee University Jang Hyuk Kwon 70
2021-71※ Developments of highly efficient and high color purity organic electroluminescent devices based on thermally activated delayed fluorescent materials exhibiting ultrafast reverse intersystem crossing
Tsinghua University Lian Duan 71
2021-72※ Structural and functional analysis of the surface polysaccharides of outer membrane vesicles released by bacteria
University of Naples Federico II Maria Michela Corsaro 72
2021-73※ Construction of heterologous protein secretion system at low temperatures by using cold-adapted microorganisms
Southwest University Xianzhu Dai 73

※ 国際共同利用・共同研究

2021-74※ Optimizing sampling devices and procedures to quantify sources of metals and microplastics in Metro Manila, Philippines' water resources
Polytechnic University of the Philippines Abigail P. Cid-Andres 74
2021-75※ Fabrication of Nanotopographical Polymer Surfaces for Bactericidal Properties-III
Stony Brook University Maya Endoh 75
2021-76※ Synthesis of Polyether Nanocomposite Solid Polymer Electrolytes for Lithium Ion Batteries
Michigan State University Robert C. Ferrier, Jr. 76
2021-77※ Verification and development of dynamic stiction theory
Yokohama National University Ken Nakano 77
2021-78※ Development of semiconductor quantum dot solid films and their charge carrier dynamics
RMIT University Yasuhiro Tachibana 78
2021-79※ Interdisciplinary Approach to Nanostructured Materials for Applications
Université de Strasbourg Jean-Pierre Bucher 79
2021-80※ Novel strategy for intracellular delivery of nanomedicines
Institute for Bioengineering of Catalonia Sílvia Pujals 80
2021-81※ Structural and functional analysis of curvature-inducing peptides and application
Karlsruhe Institute of Technology Anne S. Ulrich 81
2021-82※ Research toward stable NV centers at shallow region and spin dynamics in diamond
Leibniz institute for surface engineering Gopalakrishnan Balasubramanian 82
2021-83※ Research of quantum controls in multi-qubit diamond quantum processors and quantum sensors
Australian National University Marcus W. Doherty 83
2021-84※ Molecular mechanisms for the inactivation of a growth hormone in rice
Chinese Academy of Sciences Zuhua He 84
2021-85※ Analysis of novel transporters for strigolactones or their biosynthetic intermediates
University of California San Diego Yunde Zhao 85
2021-86※ 1,3-Dipolar Cycloaddition Reactions of Cycloparaphenylenes with Azomethine Ylide
Nanyang Technological University Shingo Ito 86
2021-87※ Dendritic Amphiphilic Block Copolymers as Additive for Polyvinylidenedifluoride Based Membranes
University of Montpellier Mona Semsarilar 87
2021-88※ Search for four-wave-mixing in the vacuum
- Unveiling dark components in the Universe –
Graduate School of Advanced Science and Engineering Kensuke Homma 88
2021-89※ Development of Perovskite and Perovskite-like Emitters and Their Applications
National Tsing Hua University Hao-Wu Lin 89
2021-90 モデルポリアルキルスチレン類を用いた分子構造と粘弾性パラメータの相関解析
名古屋大学 高野 敦志 90
2021-91 Study on the Regulatory Network of Plant Epidermal Cell Differentiation
Hiroshima University Rumi Tominaga 91
2021-92 免疫賦活化するナノ集合体
大阪大学 山崎 晶 92

※ 国際共同利用・共同研究

2021-93 自己集合性分子による心筋細胞移植の効率化
信州大学 柴 祐司 93
2021-94 共役系ポリマーの開発と非フラーレン型太陽電池の高効率化
広島大学 尾坂 格 94
2021-95 Demonstration of topological phase control in chalcogenide superlattice
AIST Misako Morota 95
2021-96 Study of spin dynamics in garnet nanocrystal thin films prepared by co-precipitation method
Gifu University Keisuke Yamada 96
2021-97 Study on electronic and magnetic behavior of perpendicularly magnetized cobalt ferrite films
Nagoya Institute of Technology Masaaki Tanaka 97
2021-98 Electronic and spintronic properties of multilayer system including $NiCo_2O_4$ and Fe_3O_4
Hokkaido University Taro Nagahama 98
2021-99 ナノ秒オーダーの逆項間交差を示す熱活性化遅延蛍光材料の開発
大阪大学 相澤 直矢 99
2021-100 時間分解分光計測による熱活性化遅延蛍光における逆項間交差の機構解明
豊田工業大学 山方 啓 100
2021-101 Functional characterization of extracellular vesicles produced by intestinal bacteria and development of their applications
Kansai University Shino Yamasaki 101
2021-102 Analysis of membrane lipid-dependent fermentation stress response in acetic acid bacteria
Ritsumeikan University Yosuke Toyotake 102
2021-103 擬秩序ガラスの熱伝導
弘前大学 増野 敦信 103
2020-104 異常高原子価イオンを含む機能性酸化物合成とその構造物性研究
高エネルギー加速器研究機構 齊藤 高志 104
2021-105 界面活性剤を抽出剤として利用した固相抽出によるEu分離法の開発
大阪府立大学工業高等専門学校 倉橋 健介 105
2021-106 Fine synthesis of polymer brush on nano-platelet for functional photonic LC
Osaka University Yoshiaki Uchida 106
2021-107 高分子ブラシ層内の水の構造および凍結挙動の解析
富山大学 源明 誠 107
2021-108 Study on water freezing with lignocellulose nanofibers and their surface modification toward functional materials
National Institute of Advanced Industrial Science and Technology Keita Sakakibara 108
2021-109 Giant Magnetic Resistance on Single-Electron Transistor
Tokyo Institute of Technology Yutaka Majima 109
2021-110 再生可能資源・木質バイオマスの先端化学材料への効率的変換法の開
奈良県立医科大学 秦野 修 110
2021-111 新規細胞内取込誘導タンパク質の同定
名古屋大学 桑田 啓子 111
2021-112 マクロピノサイトーシスによる細胞内取込様式
慶應義塾大学 前川 大志 112
2021-113 原子レベル平坦表面ダイヤモンドを用いた量情報科学研究
金沢大学 徳田 規夫 113

※ 国際共同利用・共同研究

2021-114 量子センサの高感度化に向けたダイヤモンド合成と量子技術開発研究
産業技術総合研究所 牧野 俊晴 114
2021-115 Functional analysis of non-canonical strigolactones as plant hormones and root-derived signals
Meiji University Yoshiya Seto 115
2021-116 光励起に伴うシクロパラフェニレン酸化体の芳香族性・反芳香族性のスイッチング
大阪大学 藤塚 守 116
2021-117 高強度レーザーと構造性媒質の相互作用による高エネルギー密度プラズマの生成・保持に関する実験研究
京都大学 岸本 泰明 117
2021-118 Coupling of concentration fluctuation and orientation fluctuation in mixture of nematic liquid crystal and solvent
Japan Women's University Ryoko Shimada 118
連携・融合促進型共同研究
2021-119※ Determine the three-dimensional structure of ^{13}C labeled α-synuclein(61-95) in the Langmuir-Blodgett film and supported phospholipids bilayers by p-MAIRS FT-IR
Middle Tennessee State University Chengshan Wang 119
2021-120※ Modulation of in-cell protein-protein interactions using mid-sized peptides
Tokyo University of Phermacy and Life Sciences Yoshio Hayashi 121
2021-121※ Instead of the 16th International Workshop for East Asian Young Rheologists
Osaka University Tadashi Inoue 123
施設・機器利用型共同研究
2021-122※ Micro- and Nano-structural characterization by advanced transmission electron microscopy of novel functional materials for battery development
Chiang Mai University Torranin Chairuangsri 126
2021-123※ Tackling the Electronic Instability of Charge-Density Waves by Electron Energy-Loss Spectroscopy
National Taiwan University Ming-Wen Chu 127
2021-124※ High-pressure synthesis of potential multiferroic oxides
University of Edinburgh Kunlang Ji 128
2021-125※ Synthesis and Characterization of Novel Group 16 Element Compouds
Rikkyo University Mao Minoura 129
2021-126 固体NMRを駆使した有機結晶および有機薄膜の分析
大阪大学 家 裕隆 130
2021-127 核融合プラズマ対向材料中の水素・ヘリウム挙動の高精度測定
島根大学 宮本 光貴 131
2021-128 希土類共ドープナノ粒子の寿命制御
九州大学 斉藤 光 132
2021-129 単結晶X線構造解析を用いた、含フッ素共役分子の結晶構造におけるフルオラス相互作用の解明
茨城大学 吾郷 友宏 133
2021-130 Synthesis and Structural Characterization of Halostannylenes
Kindai University Tsukasa Matsuo 134
2021-131 Theoretical design of planar silicene nanoribbons and search for new operating principles
Tohoku University Masae Takahashi 135

※ 国際共同利用・共同研究

2021-132　Synthesis and structures of cationic aromatics bearing thiopyrylium units
Fukuoka University　Noriyoshi Nagahora　136
2021-133　FT−ICR−MSを用いた湖沼及び土壌環境中溶存有機物の化学特性および起源解析
京都工芸繊維大学　布施 泰朗　137

※ 国際共同利用・共同研究

２．国際学会、シンポジウム・研究報告会

国際会議

・6th International TADF Workshop 139

・10th Aquatic Virus Workshop (AVW10) 140

シンポジウム・研究会

・第 5 回 MAIRS ワークショップ 145

・第 42 回生体膜と薬物の相互作用シンポジウム 147

３．成果発表論文 149

（令和 4 年 2 月までに刊行された論文で、平成 22ー令和 2 年度の成果報告書に掲載されていないもの）

紙数の都合により、*を付けた論文のみについて、別刷りを本報告書に記載する。

1)* Ultra-high dynamic range quantum measurement retaining its sensitivity, *Nat. Commun.*, 12, 306 (2021).

2)* Mixed lead-tin perovskite films with >7 μs charge carrier lifetimes realized by maltol post-treatment, *Chem. Sci.*, 12, 13513–13519 (2021).

3) Discovery of Self-Assembling Small Molecules as Vaccine Adjuvants, *Angew. Chem. Int. Ed.*, 60, 961–969 (2021).

4) Fused-Nonacyclic Multi-Resonance Delayed Fluorescence Emitter Based on Ladder-Thiaborin Exhibiting Narrowband Sky-Blue Emission with Accelerated Reverse Intersystem Crossing, *Angew. Chem. Int. Ed.*, 60, 20280–20285 (2021).

5) Synthesis of Carbazole-Fused Azaborines via a Pd-Catalyzed C-H Activation-Cyclization Reaction, *Bull. Chem. Soc. Jpn.*, 94, 21–23 (2021).

6) Amino-Functionalized Cage-Opened C_{60} Derivatives, *Org. Lett.*, 23, 9586–9590 (2021).

7) Reductive Decarbonylation of a Cage-Opened C_{60} Derivative, *Org. Lett.*, 23, 9495–9499 (2021).

8) Synthesis and Oligomerization of $CpM(CO)_2$, *ACS Omega*, 6, 34137–34141 (2021).

9) Water-Mediated Thermal Rearrangement of a Cage-Opened C_{60} Derivative, *ChemPlusChem*, 86, 1559–1562 (2021).

10) Cage-Expansion of Fullerenes, *J. Am. Chem. Soc.*, 143, 12450–12454 (2021).

11) Pressure-induced annulative orifice closure of a cage-opened C_{60} derivative, *Chem. Commun.*, 57, 5322–5325 (2021).

12) Precise Fixation of an NO Molecule inside Carbon Nanopores: A Long-Range Electron–Nuclear Interaction, *Angew. Chem. Int. Ed.*, 60, 2866–2870 (2021).

13) Morphology-Dependent Coherent Acoustic Phonon Vibrations and Phonon Beat of Au Nanopolyhedrons, *ACS Omega*, 6, 5485–5489 (2021).

14) Determinants of crystal structure transformation of ionic nanocrystals in cation exchange reactions, *Science*, 373, 332–337 (2021).

15) Gold Nanocluster Functionalized with Peptide Dendron Thiolates: Acceleration of the Photocatalytic Oxidation of an Amino Alcohol in a Supramolecular Reaction Field, *ACS Catal.*, 11, 13180–13187 (2021).

16) Near-Zero Azimuthal Anchoring of Liquid Crystals Assisted by Viscoelastic Bottlebrush Polymers, *ACS Appl. Polym. Mater.*, 3, 2618–2625 (2021).

17) SOMO-HOMO Conversion in Triplet Carbenes, *Org. Lett.*, 23, 4955–4959 (2021).

18) Evidence for Polarity-and Viscosity-Controlled Pathways in the Termination Reaction in the Radical Polymerization of Acrylonitrile, *Macromolecules*, 54, 4497–4506 (2021).

19) 1,3-Diradicals Embedded in Curved Paraphenylene Units: Singlet versus Triplet State and In-Plane Aromaticity, *J. Am. Chem. Soc.*, 143, 7426–7439 (2021).

20) Shallow NV centers augmented by exploiting n-type diamond, *Carbon*, 178, 294–300 (2021).

21) Low current driven vertical domain wall motion memory with an artificial ferromagnet, *J. Mag. Soc. Jpn.*, 45, 6–11 (2021).

22) High thermal stability and low driven current achieved by vertical domain wall motion memory with artificial ferromagnet, *Appl. Phys. Exp.*, 14, 023001 (2021).

23) Spin wave resonance in perpendicularly magnetized synthetic antiferromagnets, *J. Mag. Soc. Jpn.*, 45, 25–29 (2021).

24) Investigation of the upper critical field in artificially engineered Nb/V/Ta superlattices, *J. J. Appl. Phys.*, 60, 060902 (2021).

25) Estimation of Angular Momentum Compensation Temperature in GdFe Film by mMagnetic Compton Scattering*, J. Mag. Soc. Jpn.*, 45, 1–5 (2021).

26) Field-driven domain wall creep motion in ferrimagnetic Tb/CoFeB/MgO microwires, *J. J. Appl. Phys.*, 60, 020902 (2021).

27) Change of longitudinal spin Seebeck voltage with annealing in $Y_3Fe_5O_{12}$ films formed by densely packed nanocrystals, *J. Magn. Magn. Mater.,* 535, 168093 (2021).

28) Interfacial Dzyaloshinskii-Moriya interaction and dampinglike spin-orbit torque in [Co/Gd/Pt]N magnetic multilayers, *Phys. Rev. B*, 103, 104409 (2021).

29) Observation of nonreciprocal superconducting critical field, *Appl. Phys. Exp.*, 14, 073003 (2021).

30) Positive correlation between interlayer exchange coupling and the driving current of domain wall motion in a synthetic antiferromagnet, *Appl. Phys. Lett.,* 119, 032407 (2021).

31) Control of antiferromagnetic resonance and the Morin temperature in cation doped α-$Fe_{2-x}M_xO_3$ (M = Al, Ru, Rh, and In), *Appl. Phys. Lett.*, 119, 032408 (2021).

32) Dzyaloshinskii–Moriya interaction in noncentrosymmetric superlattices, *npj Comput. Mater.*, 7, 129 (2021).

33) Inhomogeneous magnetic properties characterized by simultaneous electrical and optical detection of spin-torque ferromagnetic resonance, *Appl. Phys. Lett.*, 119, 192409 (2021).

34) Influence of the Dabcyl group on the cellular uptake of cationic peptides: short oligoarginines as efficient cell-penetrating peptides, *Amino Acids*, 53, 1033–1049 (2021).

35) Synthesis and structural confirmation of calibagenin and saxosterol, *Tetrahedron*, 91, 132194 (2021).

36) Arabidopsis PLDζ1 and PLDζ2 localize to post-Golgi membrane compartments in a partially overlapping manner, *Plant Mol. Biol.*, 108, 31–49 (2021).

37) Discovery of a Vitamin D Receptor-Silent Vitamin D Derivative That Impairs Sterol Regulatory Element-Binding Protein in Vivo, *J. Med. Chem.*, 64, 5689–5709 (2021).

38) Multichromophore Molecular Design for Thermally Activated Delayed-Fluorescence Emitters with Near-Unity Photoluminescence Quantum Yields, *J. Org. Chem.*, 86, 11531–11544 (2021).

39) Effect of a twin-emitter design strategy on a previously reported thermally activated delayed fluorescence organic light-emitting diode, *Beilstein J. Org. Chem.*, 17, 2894–2905 (2021).

40) Acceleration of Reverse Intersystem Crossing using Different Types of Charge Transfer States, *Chem. - An Asian J.*, 16, 1073–1076 (2021).

41) Formation of trans-Poly(thienylenevinylene) Thin Films by Solid-State Thermal Isomerization, *Chem. Mater.*, 33, 5631–5638 (2021).

42) Progress in recycling organic-inorganic perovskite solar cells for eco-friendly fabrication, *J. Mater. Chem. A*, 9, 2612–2627 (2021).

43) Near-Ultraviolet Transparent Organic Hole-Transporting Materials Containing Partially Oxygen-Bridged Triphenylamine Skeletons for Efficient Perovskite Solar Cells, *ACS Appl. Energy Mater.*, 4, 1484–1495 (2021).

44) Starburst Carbazole Derivatives as Efficient Hole Transporting Materials for Perovskite Solar Cells, *Solar RRL*, 6, 2100877 (2021).

45) Deuterium and helium desorption behavior and microstructure evolution in beryllium during annealing, *J. Nucl. Mater.*, 544, 152686 (2021).

46) Facile Synthesis Sandwich-Structured Fe/NrGo Nanocomposite as Anodes for High-Performance Lithium-Ion Batteries, *Crystals*, 11, 1582 (2021).

47) Synthesis of a Mechanically Planar Chiral and Axially Chiral [2]Rotaxane, *Org. Lett.*, 23, 8678–8682 (2021).

48) Iron-catalysed enantioselective carbometalation of azabicycloalkenes, *Chem. Commun.*, 57, 6975–6978 (2021).

49) Iron-catalyzed cross-coupling reactions tuned by bulky ortho-phenylene bisphosphine ligands, *Bull. Chem. Soc. Jpn.*, 94, 1125–1141 (2021).

50) Substitutional tuning of electronic phase separation in $CaFe_3O_5$, *Phys. Rev. Mater.*, 5, 024406 (2021).

51) Colossal Barocaloric Effect by Large Latent Heat Produced by First-Order Intersite-Charge-Transfer Transition, *Adv. Funct. Mater.*, 31, 2009476 (2021).

52) Integrated sensing array of the perovskite-type $LnFeO_3$ (Ln=La, Pr, Nd, Sm) to discriminate detection of volatile sulfur compounds, *J. Hazard. Mater.*, 413, 125380 (2021).

53) Tuning magnetic anisotropy by continuous composition-gradients in a transition metal oxide, *J. Appl. Phys.*, 129, 183902 (2021).

54) 3D to 2D Magnetic Ordering of Fe^{3+} Oxides Induced by Their Layered Perovskite Structure, *Inorg. Chem.*, 60, 8027–8034 (2021).

55) Giant multiple caloric effects in charge transition ferrimagnet, *Sci. Rep.*,11, 12682 (2021).

56) Spin reorientation in tetragonally distorted spinel oxide epitaxial films, *Phys. Rev. B*, 104, 014422 (2021).

57) Ultrafast demagnetization in $NiCo_2O_4$ thin films probed by time-resolved microscopy, *Appl. Phys. Lett.*, 119, 102404 (2021).

58) Scaling of the anomalous Hall effect in perpendicularly magnetized epitaxial films of the ferrimagnet, *Phys. Rev. B*, 104, 134407 (2021).

59) Slow oxidation of magnetite nanoparticles elucidates the limits of the Verwey transition, *Nat. Commun.*, 12, 6356 (2021).

60) Multi-*k* spin ordering in $CaFe_3Ti_4O_{12}$ stabilized by spin-orbit coupling and further-neighbor exchange, *Phys. Rev. Research*, 3, 043208 (2021).

61) Oxygen Release and Incorporation Behaviors Influenced by A-Site Cation Order/Disorder in $LaCa_2Fe_3O_9$ with Unusually High Valence $Fe^{3.67+}$, *Chem. Mater.*, 34, 345–350 (2022).

62) Donor-Acceptor Polymers Containing 4,8-Dithienylbenzo[1,2-b:4,5-b']dithiophene via Highly Selective Direct Arylation Polymerization, *ACS Appl. Polym. Mater.*, 3, 830–836 (2021).

63) Tracing the incorporation of the "ninth sulfur" into the nitrogenase cofactor precursor with selenite and tellurite, *Nat. Chem.*, 13, 1228–1234 (2021).

64) High-order harmonic generation in graphene: Nonlinear coupling of intraband and interband transitions, *Phys. Rev. B*, 103, L041408 (2021).

65) Spectral characterization of the Rashba spin-split band in a lead halide perovskite single crystal by photocurrent heterodyne interference spectroscopy, *Phys. Rev. B*, 103, L081201 (2021).

66) On the progress of ultrafast time-resolved THz scanning tunneling microscopy, *APL Mater.*, 9, 060903 (2021).

67) Determination of localized surface phonons in nanocrystalline silicon by inelastic neutron scattering spectroscopy and its application to deuterium isotope enrichment, *Phys. Rev. Mater.*, 5, 066003 (2021).

68) Eukaryotic virus composition can predict the efficiency of carbon export in the global ocean, *iScience*, 24, 102002 (2021).

69) Quantitative Assessment of Nucleocytoplasmic Large DNA Virus and Host Interactions Predicted by Co-Occurrence Analyses, *mSphere*, 6, e01298-20 (2021).

70) Draft genome sequence of medusavirus stheno, isolated from the tatakai river of Uji, Japan, *Microbiol. Resour. Announc.*, 10, e01323-20 (2021).

71) Discovery of Viral Myosin Genes With Complex Evolutionary History Within Plankton, *Front. Microbiol.*, 12, 683294 (2021).

72) RNA sequencing of medusavirus suggests remodeling of the host nuclear environment at an early infection stage, *Microbiol. Spectr.*, 9, e0006421 (2021).

73) Year-round dynamics of amplicon sequence variant communities differ among eukaryotes, Mimiviridae, and prokaryotes in a coastal ecosystem, *FEMS Microbio. Ecol.*, 97, fiab167 (2021).

74) ReCGBM: a gradient boosting-based method for predicting human dicer cleavage sites, *BMC Bioinformatics*, 22, 63 (2021).

75) Weighted minimum feedback vertex sets and implementation in human cancer genes detection, *BMC Bioinformatics*, 22, 143 (2021).

76) Uncovering and classifying the role of driven nodes in control of complex networks, *Sci. Rep.*, 11, 9627 (2021).

77) ILearnPlus: A comprehensive and automated machine-learning platform for nucleic acid and protein sequence analysis, prediction and visualization, *Nucleic Acids Res.*, 49, e60 (2021).

78) DeepVF: A deep learning-based hybrid framework for identifying virulence factors using the stacking strategy, *Brief. Bioinform.*, 22, bbaa125 (2021).

79) DeepBL: A deep learning-based approach for in silico discovery of beta-lactamases, *Brief. Bioinform.*, 22, bbaa301 (2021).

80) Computational identification of eukaryotic promoters based on cascaded deep capsule neural networks, *Brief. Bioinform.*, 22, bbaa299 (2021).

81) Probabilistic critical controllability analysis of protein interaction networks integrating normal brain ageing gene expression profiles, *Int. J. Mol. Sci.*, 22, 9891 (2021).

82) Anthem: A user customised tool for fast and accurate prediction of binding between peptides and HLA class I molecules, *Brief. Bioinform.*, 22, bbaa415 (2021).

４．参考資料

4-1.令和３年度公募要領 165
4-2.令和３年度採択課題一覧 169

1. 共同研究成果報告

アスペクト比の制御された金ナノらせんの合成および光学特性評価

中川充　大阪産業技術研究所

【目的】貴金属ナノ構造体はサイズや形状に依存した特異な光学特性を示すことから盛んに研究されている。しかしながら、複雑なナノ構造の作製は容易ではなく、多くの課題が残されている。そこで、先行研究により見出した、分子集合体を鋳型とするらせん状金ナノワイヤーの合成法を発展させることで、簡便かつ多様なナノ構造を作製可能な手法を確立する。さらに、得られた種々のナノワイヤーの光学特性を比較することで、ナノ構造と機能の関係について検討する。

【方法】分子集合体の存在下で塩化金(III)酸を L-アスコルビン酸を用いて還元し、らせん状金ナノワイヤーを合成した。次に、超音波処理およびグロース処理により長さと直径の異なるナノワイヤーを調製した。合成した各ナノワイヤーの分散液について、紫外-可視-近赤外（UV-vis-NIR）吸収および円偏光二色性（CD）スペクトルを測定した。さらに、種々の直径および長さを有するナノワイヤーについて、走査型透過電子顕微鏡によるエネルギー損失スペクトル（STEM-EELS）測定を行った。

【結果と考察】らせん状金ナノワイヤーの NIR 領域の吸収スペクトルは直径の増大および長さの減少によりブルーシフトした。EELS 測定（Fig. 1）の結果から、光吸収スペクトルの変化はナノワイヤーのアスペクト比の減少による長軸モードの表面プラズモン共鳴の周波数変化に対応することがわかった。ワイヤー径の変化による UV-vis 領域の吸収スペクトルの変化はわずかであったにもかかわらず、同領域の CD スペクトルは大きく変化し、一部反転、増大した。以上の結果から、らせん状金ナノワイヤーの光吸収および円偏光特性はアスペクト比とワイヤー径などのワイヤーの形状を制御することで、別々に調節できる可能性が示唆された。

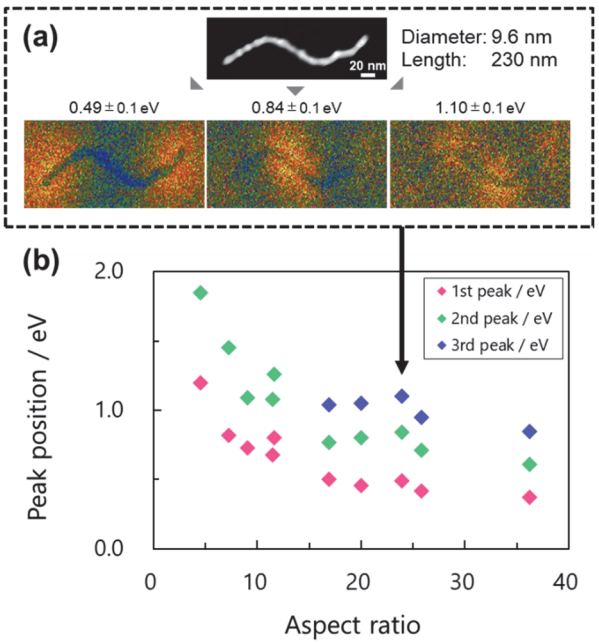


Figure .1 (a) A STEM image and EELS maps of a single gold nanowire. (b) Plots of EELS peak positions vs. aspect ratio of gold nanowires.

【成果報告】M. Nakagawa, R. Kakehashi, N. Tokai, H. Kurata, T. Kawai, Tuning the Structure and Chiroptical Properties of Helical Gold Nanowires Synthesized Using Supramolecular Templates, , 2021 International Chemical Congress of Pacific Basin Societies (Virtual congress), 18/Dec/2021, 3413516.

蓄積リングのための位置感度型アクティブ標的の開発

山口由高　理化学研究所

【目的と研究方法】

本研究の目的は、蓄積リングを用いたビームリサイクル技術を確立する上で必要な要素の一つである、位置感度型アクティブ標的を開発することである。内部標的を備えた蓄積リングで稀少なRIビームを周回させ、標的を通り抜けても再び標的に入射、核反応が起きるまで回し続ける、これがビームリサイクル技術の特徴である。従来の大強度RIビームを標的に１回入射して核反応研究を行う手法に比べ圧倒的に高効率である。しかしながら、内部標的の通過を繰り返す度にRIビームはエネルギーを失い、さらにエネルギー分散や角度分散が生じて、たちまち蓄積リングのアクセプタンスから外れ周回できなくなってしまう。それらを補償する装置が特別に必要だが、まず補償装置にRIビーム情報をフィードバックする必要がある。本研究では、核反応のための内部標的を、周回する個々のRIビームの情報源として利用するアクティブ標的のプロトタイプを製作し、その特性を調べた。

【研究内容、結果、今後の課題】

薄膜標的をビームが通過する際に放出する二次電子を、周回するRIビームの邪魔にならないように検出器まで輸送し、標的通過の時刻と位置を特定する信号を取り出す仕組みである。RIビーム進行方向に飛び出した二次電子は静磁場と静電場の中で、加速・偏向され検出器(MCP)まで輸送され、標的上の像がMCP上に転写される。MCPではアノード信号と、ディレーラインによる読み出しをすることで時刻と位置の情報が取得される。

図1（左写真）は本研究で試作したアクティブ標的である。特性試験のために、RIビームに代わり^{241}Amからのα線を使用した。標的にはAl蒸着マイラーフィルム（厚さ15μm）を用いた。位置情報の分解能、転写画像の歪みを測定するため、標的には格子状の点に小さな穴を開けたマスクを用いた。図１の右図はそのマスク画像がMCP上に映された像を示している。詳細解析とパラメータ最適化など調整は今後引き続き行うが、当初の目標であった標的からビームの時刻と位置情報を取り出すことは可能であることが実証された。

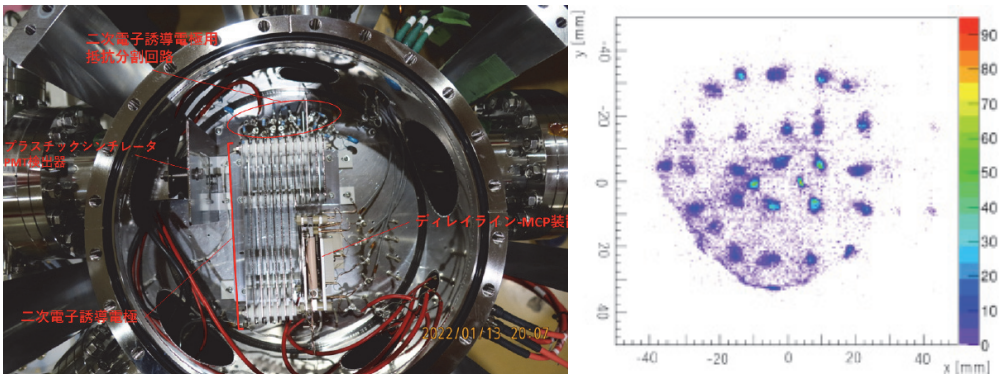


図 1. 試作したアクティブ標的

Crystal Structure Analysis of GraE from Root-Nodule-Forming Bacterium

Tadao Oikawa　Kansai University

Rhizobium is a genus of tubercle-forming bacteria. It grows in symbiosis with the root of a plant to fix nitrogen from the air. In the course of a screening experiment, *Rhizobium* sp. strain MTP-10005 was isolated from natural river water. Enzymological and genetic studies showed that the translational products of the gene cluster *graRDAFCBEK* in the bacterium (GraR, GraD, GraA, GraF, GraC, GraB, GraE, and GraK, respectively) were probably involved in the degradation pathway of γ-resorcylate. To reveal the structure and function of all these proteins, I have collaborated with Dr. Tomomi Fujii and Prof. Emeritus Dr. Yasuo Hata, Institute for Chemical Research, Kyoto University, and have performed already X-ray structural studies of GraA, GraC, and GraD. In this study, we focused on GraE, whose function and role in the degradation pathway of γ-resorcylate are currently unknown. The X-ray crystal structure of GraE is expected to reveal its function and role *in vivo*.

N-terminal His-tagged GraE was overexpressed in *Escherichia coli* BL21 (DE3), purified, and used for crystallization. Thin plate-shaped crystals were obtained using a crystallization solution consisting of 3 M NaCl and 0.1 M citric acid buffer pH 3.5. Diffraction experiments were performed on beamline BL-5A, Photon Factory, KEK, Japan. The crystal was mounted with a cryoloop and cooled with a cold stream of nitrogen. Diffraction data were collected up to 1.8 Å resolution. The crystal belonged to space group $P2_1$, with unit-cell parameters of a = 34.31 Å, b = 80.90 Å, c = 43.38 Å, and β = 107.36°. The structure was determined using the molecular replacement method, while the starting model was prepared with homology modeling. The orientation of the model was determined by calculating rotation functions. The translational position of the rotated model was found via *R*-factor search accompanied by simulated annealing refinement. The solution model was subjected to automated model-building followed by iterative model-building and refinement. The structure was refined to *R*-factor and R_{free} of 16.6 and 20.2 %, respectively.

In the present crystal, one homodimer GraE molecule exists in an asymmetric unit and each subunit binds chloride ions. The polypeptide chain of the protein has 112 amino acid residues. The subunit structure consists of three α-helices and five β-strands, and it roughly resembles a bacterial-type ferredoxin fold. The dimer interface is formed by packing the four-stranded β-sheets from the two subunits against each other. The putative active site is located in the cleft made of an α-helix α1 and two β-strands β2 and β3 from one subunit and *C*-terminal loop from the other subunit. The chloride ion in the putative active site binds to the side chains of arginine and tyrosine residues. The conserved histidine residue is positioned in the putative active site. These residues may be involved in substrate binding or catalysis.

プリパルス付与による高変換 TNSA イオン加速機構実証

砂原淳　大阪大学

我々は Target Sheath Normal Acceleration(TNSA)イオン加速機構で得られる MeV 以上の高エネルギーイオンを利用し,高輝度(点光源)、短パルス(数 10 ナノ秒以下)で比較的コンパクト（規模に比較して高フラックス）なレーザー駆動中性子源の実現を目指している.これを高時間分解中性子検出器と組み合わせることにより,共鳴散乱イメージングなど,レーザー加速中性子源の特徴を生かした研究展開が期待できる.

これまでの研究で、高強度フェムト秒レーザーに先行してプレパルスを適切なタイミングでターゲット照射することにより,加速イオンのエネルギー,粒子数共に著しく増大できる可能性が理論的に見出されており,京都大学化学研究所（受け入れ若杉教授）のレーザー施設を用いて実験配置で実証実験を行なった. 図 1 に示すように 10μm 厚ポリエチレン（CH）ターゲット上のアルミニウム 1000Åのコーティング有無、及びプリパルスレベルを五段階に強度変化(条件 1→条件 5)させた条件で TNSA イオン加速を行い、CR39 を用いて発生するプロトンのエネルギー分解計測を行なった。実験結果はアルミコートの有無で加速されたプロトンエネルギースペクトル（図 2）が大きく変化した.アルミコート無し（図 2 下）では(条件 3)のプリパルス(PP)レベルを超えると TNSA イオン加速が抑制されるのに対し,(図 2 上)に示したアルミコートを施したターゲットではプロトンの数、最大エネルギー共にプリパルスの増大に伴って単調に増大している. このことは透明ターゲット TNSA 加速におけるプリパルスのシャインスルー制御の重要性を示している.**本実験により、プリプラズマを付与による高効率 TNSA イオン加速（加速プロトン数、最大エネルギーの増大）の実験的な実証データが得られた**.プリパルスによる誘電体の電離過程、プラズマ化、レーザーとターゲットの相互作用の観点から目下データ解析中である.

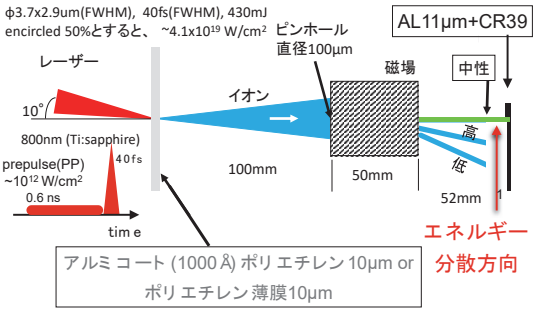


図 1 実験配置

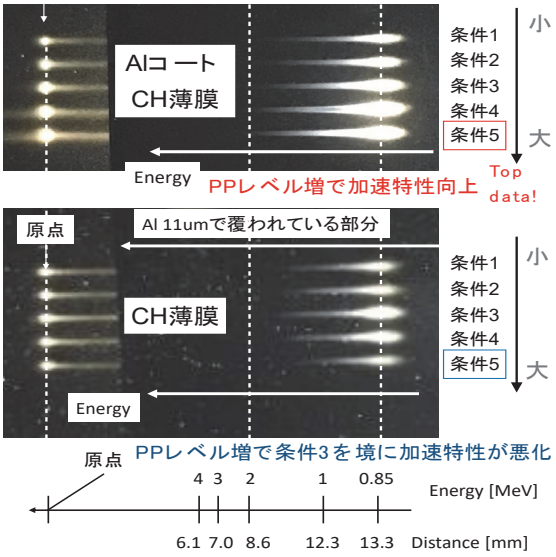


図 2 測定されたプロトンの energy spectrum

電子線を用いた超高線量率放射線がん治療（FLASH）の作用機序の解明の試み

小平聡　量子科学技術研究開発機構

通常の放射線治療で用いる照射線量率（0.03 Gy/s 程度）に比べて 1000 倍以上の極端に高い線量率（>40 Gy/s）で照射する超高線量率放射線がん治療（FLASH）では、腫瘍への治療効果を維持しつつ、周囲の正常組織への副作用の低減が期待される新しい治療照射法である。FLASH 照射効果は細胞や動物を用いた生物実験によって確認されており、放射線が生体中（水）で生成する放射線分解生成物同士の再結合や反応過程における溶存酸素量低下と考えられている、実験的なエビデンスは得られていない。本研究では照射線量率に対する水の放射線分解生成物の収率依存性の実測による作用機序の解明を目的としている。最終的には、治療計画時の臨床効果を推定するシミュレーションコードへの実装を通じ、我が国における FLASH 治療の進展に貢献したいと考えている。

これまで、水中に生成したヒドロキシルラジカル（OH ラジカル）と反応し蛍光を呈する 3-クマリン酸-カルボン酸（C3CA）水溶液系を用いて、30-60 MeV の陽子線と 130 MeV/u の炭素線の高線量率照射による溶存酸素量低下やラジカル再結合が示唆されるデータが得られてきている。これは OH ラジカル収率の変化ではなく、C3CA が OH ラジカルを捕捉して生成する蛍光性の 7-ヒドロキシ-クマリン-3-カルボン酸（7OH-C3CA）の収率が周囲の酸素量に依存することを利用している。本研究課題では、京大化研において開発・整備が進められている電子線加速器を用いて、数 10MeV の電子線の高線量率照射による放射線分解生成物の収率測定に向けた準備を進めている。

2022 年 3 月 9 日から 11 日かけて電子線加速器における照射実験系の確立と放射線分解生成物の測定試験を予定しており、本報告書では実験データを示すことはできないが、準備状況について報告する。京大化研の加速器で得られる電子線を用いて放射線化学収率を定量測定するためには、①電子線の吸収線量測定、②照射線量の制御、③照射野平坦度測定が必要である。①吸収線量測定には、放射線治療の品質評価標準であるアドバンストマーカス電離箱（PTW・型式 34045）を用い、その出力電荷は電位計（ケースレー・型式 6517B）により計数する。この電離箱と電位計の組み合わせに対する線量校正をコバルト 60 線源を用いて実施した（日本医学物理学会・標準測定法 01 に準拠）。照射線量のビームモニターとして、大口径（有効直径 170mm）の大気開放型並行平板電離箱（応用技研・型式 AE-175）を用い、出力電荷をデジタルカレントインテグレータ（ORTEC・Model439）によりモニターカウントとして計数する。照射試料位置でのマーカス電離箱の水吸収線量値を用いてビームモニターカウント値を校正し、照射線量を制御する予定である。照射野の平坦度測定は試料への均一照射に重要であり、直径 30mm 程度内の照射線量が±5%以内が望ましい。照射野形成の確認は ZnS 蛍光板、定量測定にはラジオクロミックフィルム（Ashland・型式 EBT3）を用いる予定である。2022 年 3 月の実験では、まず電子線の照射野形成と線量測定・ビームモニターの動作・運用確認を行う。その後、C3CA 水溶液を用いた 7OH-C3CA 収率の測定試験を行う予定である。

ナノ構造を持つ ISOL 用標的の開発

大西哲哉　理化学研究所

［目的］不安定核生成法の一つである ISOL 法では、標的に高速の粒子を照射し、標的内で生成した不安定核を、標的を高温(～2000℃)にすることで取り出している。そのため、高温でも蒸気圧が低くかつ融点も高い、炭化物が標的として用いられることが多い。しかし、これまでの研究によって、炭化物標的の寿命が約一週間程度であることが分かっている。これは、高温環境下では炭化物の焼結が進むため、標的内部の隙間が小さくなり、不安定核が出てこなくなるためである。解決策として、近年カーボンナノチューブを用いた炭化物標的が提案されるが、ナノ構造を持つが故に燃焼しやすく、取り扱いには専用の設備が必要である。本研究の目的は、カーボンナノチューブやグラフェン等のナノ構造をもつ新たな炭化物を用いて、取り扱いやすい ISOL 用標的を開発することである。

［実験手法］対象とする元素の化合物(酸化物など)を炭素材料と混合し、高圧をかけ、厚さ 1 mm、直径 20 mm 程度の円板標的を作成する。作成した標的は真空チェンバー内で高温に加熱し、炭化物へと変換する。作成した炭化物標的は、電子顕微鏡を用いて、そのナノ構造を調べる。その後、電子ビームもしくは陽子ビームを照射し、不安定核生成量の変化から標的寿命や生成効率などを調べる。

本年度は、グラフェンを用いた円板標的の取り扱い方法に関する開発及び環境整備を行った。昨年度の結果から、炭化物の燃焼速度が予想していたよりも非常に速いことが判明した。そこで安全性を考慮し、標的取り扱い法や作業環境の整備を先に行うこととした。炭化作業及びイオン源でのテストのしやすさを考慮し、作業場所としては理化学研究所仁科加速器科学研究センター E21 実験室内 RTM 前室のフードとした。

［結果］作業環境の整備として、RTM 前室フード周りの環境整備しつつ、フード内に真空引き対応のガス置換型グローブボックスを導入した。大きさとしてフード内に収まり、かつ、標的関係の作業ができるものを選んだ。(写真 1a) 参照。) 置換ガスには窒素ガスを用いている。作業時には、標的入り小型真空容器と必要な道具をあらかじめグローブボックス内に入れ、真空引きによるガス置換を行う。その際、十分に酸素濃度を下げる必要があるため、ガス置換を三回行うことで、酸素濃度が 10^{-4} %以下になることを担保した。炭化標的を用いた作業、具体的には標的槽の載せ替え、を行いながら、グローブボックスを使用したときの作業手順の確認及びマニュアル作りを行った。作業の様子は写真 1b) を参照のこと。

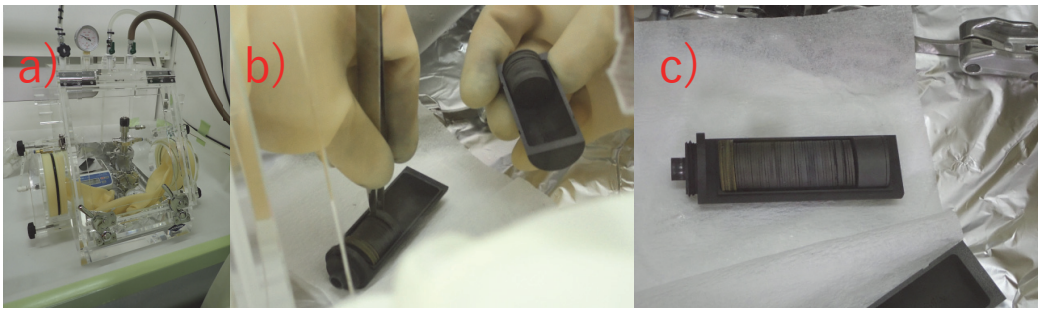


写真 1: a) フード内グローブボックスの様子。 b) グローブボックス内での標的作業。標的槽間での移し替え作業を示している。c) リモートハンドリング用標的槽に載せられた炭化ウラン標的。標的円板が 43 枚載せられている。

現在は、炭化標的を昨年度制作したリモートハンドリング用標的槽に移し替え(写真 1c)参照)、イオン源にセットし実際に電子ビームによる照射実験(不安定核生成実験)を準備している。

［考察］今年度の整備の結果、炭化標的を安全に取り扱う環境が整備された。来年度は照射後の放射化した標的の取り扱いについて、手順を検討しつつマニュアル作り及び環境整備を行う予定である。その後、炭化標的の製作を条件を変えて製作を行っていく予定である。

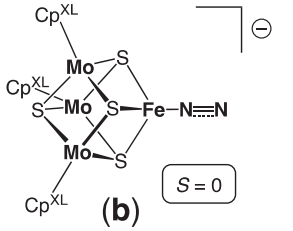
［成果報告］特になし。

Electronic Structure of Biomimetic [Mo_3S_4Fe] Clusters and its Relation to the catalytic N_2-Reduction: A Computational Study

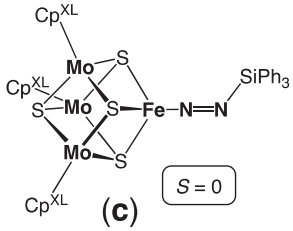
W. M. C. Sameera　Hokkaido University

The development of transition metal clusters is one of the main themes of inorganic chemistry. Quantitative details of the electronic structure of the transition metal complexes and clusters and their relations to catalytic activity cannot be rationalized from the experimental results alone. Density functional theory (DFT) can provide quantitative insights into the electronic structure and function relationships.

Objectives: Determine the electronic structure of the N_2-bound [Mo_3S_4Fe] clusters; [{$Cp^*_3Mo_3S_4Fe$}$_2$(μ-N_2)]$^{2-}$ (**a**), [$Cp^{XL}_3Mo_3S_4Fe(N_2)$]$^-$ (Cp^R = Cp^{XL} (**b**), and ([$Cp^{XL}_3Mo_3S_4Fe(N_2SiPh_3)$] (**c**).



Computational methods: Geometries of the possible spin states of **a**, **b**, and **c** transition metal clusters were optimized using DFT and standard basis sets.



Results and discussion: According to DFT calculations, the ground state of **a**, **b**, and **c** transition metal clusters is S = 0. Structural parameters of the optimized ground state structures are in agreement with the X-ray structures and spectroscopic properties. Electronic structure analysis indicated that the oxidation state of Fe in all three systems is Fe(II) but slightly reduced.

Publications: Two joint publications were made from this project in this FY.

(a) W. M. C. Sameera, Y. Takeda, Y. Ohki, "Transition metal catalyzed cross-coupling and nitrogen reduction reactions: lessons from computational studies", *Advances in Organometallic Chemistry*, 78, **2022**.

(b) Y. Ohki, K. Munakata, R. Hara, M. Kachi, K. Uchida, M. Tada, R. E. Cramer, W. M. C. Sameera, T. Takayama, Y. Sakai, S. Kuriyama, Y. Nishibayashi, K. Tanifuji, "Nitrogen reduction by the Fe sites of synthetic [Mo_3S_4Fe] cubes", 12 May 2021, PREPRINT (Version 1) available at Research Square https://doi.org/10.21203/rs.3.rs-477541/v1

Development and device evaluation of new D-π-A emitters based on fluorinated triarylborone acceptors

Todd B. Marder　Julius-Maximilians-Universität Würzburg

Thermally activated delayed fluorescence (TADF) emitters are a promising avenue for the development of organic light-emitting diodes (OLEDs) for flat displays and solid-state lighting applications, as they show improved efficiency. Planar 3-coordinate boron can be used as an acceptor moiety due to the vacant p_z orbital perpendicular to its plane. Triarylboranes have been employed for a number of applications such as linear and nonlinear optics, sensors, and OLEDs. One of the most successful examples of the use of triarylboron acceptors is their application to TADF emitters. In applications, electronic or steric protection of boron atom is necessary to reduce reactivity of the boron center toward nucleophiles. We and others have recently reported methodologies to enhance the accepting properties as well as the stability of boron by the introduction of *ortho*-trifluoromethylaryl moieties. Recently, we computationally designed a series of D-π-A TADF emitters with fluorinated triarylboron acceptors. The synthesized emitters showed blue to red emission with relatively short delayed fluorescence lifetimes, implying efficient reverse intersystem crossing (RISC) from the triplet to singlet excited states (A. K. Narsaria *et al., Adv. Funct. Mater.* **2020**, *30*, 2002064). These studies demonstrate the effectiveness of our design strategy for triarylboron-based TADF emitters based on accurate theoretical descriptions of the local and charge-transfer states. However, their TADF performance in host materials and device efficiencies have not yet been characterized. Thus, a series of selected D-π-A TADF emitters (the emission wavelengths in 1% PMMA were 477, 568, and 598 nm) with fluorinated triarylboron acceptors were synthesized in sufficient quantities (227 – 700 mg) by the Würzburg group which were sent to the Kaji group in Kyoto who subsequently constructed OLED devices from these compounds and examined their properties.

This past year, due to COVID-19 related difficulties, and the inability to travel to Kyoto, our group and the Kaji group have independently advanced the project: our group having carried out the chemical synthesis of the chromophores and the Kaji group carrying out the photophysical measurements, device fabrication and testing (Figure 1). We found that our designed molecules exhibited efficient RISC with the rate constant exceeding 10^6 s^{-1}. This has also led to suggested design features for new compounds which we plan to prepare and evaluate in the coming year. We anticipate that a breakthrough in OLED performance can be achieved by continuing our collaborative work, and this is highly desired in both the academic and industrial communities.

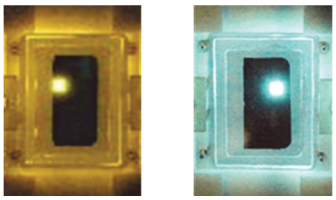


Figure 1. Fabricated OLEDs by Kaji group using our designed materials.

Gas sensing properties research of metal oxides

Haichuan Guo　Chinese Academy of Sciences

Introduction

The perovskite-type oxides are widely used to detect organic gases because of high sensitivity and excellent stability, which demonstrates excellent application potential in the field of gas sensors. Doping of perovskite oxide usually change the crystal structure as well as the electronic structure, thereby effecting the gas sensing properties. Herein, we succeeded in doping Lu on *B*-site of perovskite oxide $LaFeO_3$, and significantly improve the gas sensing performance for ethanol.

Experiments and results

$LaFe_{1-x}Lu_xO_3$ (x = 0, 0.1) were synthesized by the citrate sol-gel method using metal nitrates. As-prepared oxide powders were dispersed in deionized water and drop-coated on alumina ceramic substrates with comb-type Au electrodes. The ceramic chips were calcined at 300ºC for 1 h to strengthen the stability and repeatability. Gas sensing properties were measured using an intelligent gas sensing analysis system by the static volumetric method. The response value is the ratio of resistance of sample measured in 100 ppm organic gas to that measured in air.

As the XRD patterns shown in Fig.1, all the peaks shift to low angles slightly after the partial substitution of smaller Fe^{3+} (radius: 0.65 Å) on *B*-site by larger Lu^{3+} (0.86 Å). Although the response for acetone nearly keep constant after doping, the improvement of the gas sensing performance for ethanol is obvious (Fig.2). The response increase from 56.2 for $LaFeO_3$ to 756.0 for $LaFe_{0.9}Lu_{0.1}O_3$. The lattice expansion should not the only reason of the dramatic change. The local lattice distortion and the change of band structure causing by d^0 Lu^{3+} doping can also be considered.

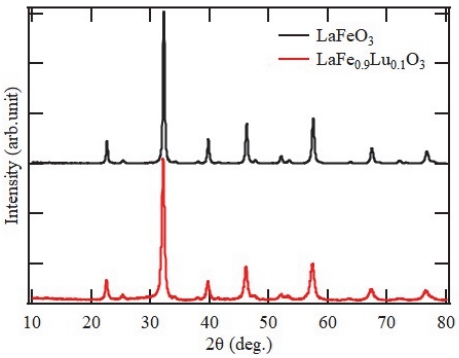


Fig.1 XRD patterns of $LaFe_{1-x}Lu_xO_3$

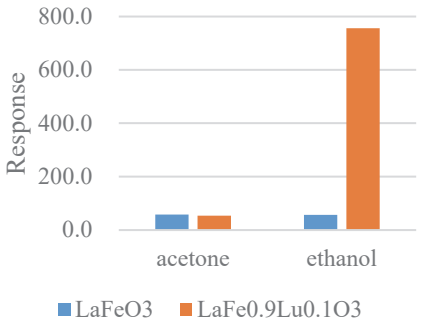


Fig.2 Gas sensing performance for organic gases

Design and Tailoring Advanced Functional Materials: Symmetry Operation and High Pressure Synthesis

Wei-tin Chen　National Taiwan University

[Introduction] In modern condensed matter sciences, the exploration of novel functionalities and exotic physical phenomena is motivated by fundamental scientific understanding and potential technology applications. High pressure synthesis techniques are one of most important and effect methods to prepare such novel materials. With previously supported project, we have successfully demonstrated the effectiveness and powerfulness of high-pressure synthesis, and this project proposes to continue the utilization of such unique techniques for novel materials exploration. It is targeted to design and investigate, for instance, ferroelectric, magnetic or multiferroic compounds, which usually contains unusual high valence state or showing exotic structural/charge/orbital/spin phase transitions. With the 6-8 two-stage Kawai-type 111 geometry and cubic anvil DIA-type high-pressure apparatus equipped at Advanced Solid State Chemistry Laboratory (Shimakawa lab), extreme pressure and temperature synthesis conditions were realized for novel materials synthesis, and further high resolution synchrotron x-ray diffraction experiments were conducted at Taiwan with joint research beamtime.

[Results and discussion] The joint research remains difficult with the situation of pandemic in year 2021. Nevertheless, high pressure experiments were conducted Prof. Shimakawa lab, and high resolution SXRD data were collected at Taiwan Photon Source, NSRRC. For example, the colossal barocaloric effect by large latent heat produced by first order intersite charge transfer transition in $NdCu_3Fe_4O_{12}$ quadruple perovskite, showing potential application in efficient refrigeration. [1] A series of AMn_7O_{12} quadruple perovskite solid solutions were designed to investigate the long-standing conundrum of colossal magnetoresistance in manganite perovskites. With high resolution SXRD and NPD with detailed symmetry operation analysis, alternating ordered-insulating and disordered-conducting electron stripes arrangement forms a new state of matter (Fig. 1). [2] Magnetic structure and spin reorientation behavior was observed and studied in B-site disordered $PrFe_{0.5}Cr_{0.5}O_3$ perovskite, [3] further investigation on praseodymium-containing perovskites are ongoing. We are continuing further exploration of novel functional oxide materials with exotic physical behaviors.

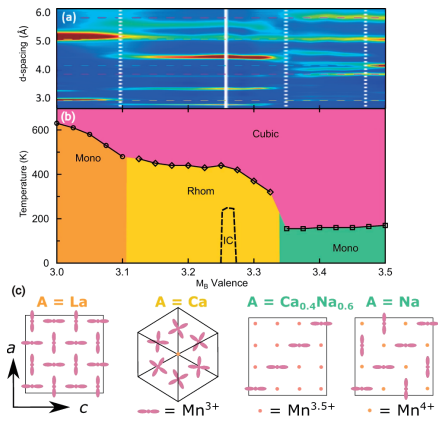


Fig. 1 Compositional phase diagram and orbital orderings of AMn_7O_{12} quadruple perovskites.

[References]

1. Y. Kosugi *et. al.*, *Adv. Funct. Mater.*, **31**, 2009476 (2021)
2. W.-T. Chen *et. al.*, *Nat. Commun.*, **12**, 6319 (2021)
3. C.-W. Wang *et. al.*, *JMMM*, **538**, 168273 (2021)

Investigating iron nitrides prepared by new high-pressure synthesis with Mössbauer spectroscopy

Simon D. Kloß　University of Edinburgh

Transition metal nitrides are an important class of materials with applications as abrasives, semiconductors, superconductors, Li-ion conductors, and thermoelectrics. However, nitrogen-rich transition metal nitrides in high oxidation states were notoriously difficult to prepare owing to the chemical inertness of N_2 and the positive electron affinity of nitrogen leading to elimination of N_2 at elevated temperatures. The research group in Edinburgh found a versatile synthesis route using azide-mediated oxidation under pressure that is used to prepare the highly oxidised ternary nitride Ca_4FeN_4 containing Fe^{4+} ions. In the joint research program we investigated new multinary iron nitrides with unprecedented physical and chemical properties. A key step in the investigation of these compounds is the assignment of the iron oxidation state with ^{57}Fe Mössbauer spectroscopy, which is often non-trivial owing to complicated structures.

We found that this nitridometallate features trigonal planar $[FeN_3]^{5-}$ anions with low-spin Fe^{4+} and antiferromagnetic ordering below a Neel temperature of 25 K, which are characterised by neutron diffraction, ^{57}Fe-Mössbauer and magnetisation measurements. Azide-mediated high-pressure synthesis opens a way to the discovery of highly oxidised nitrides.

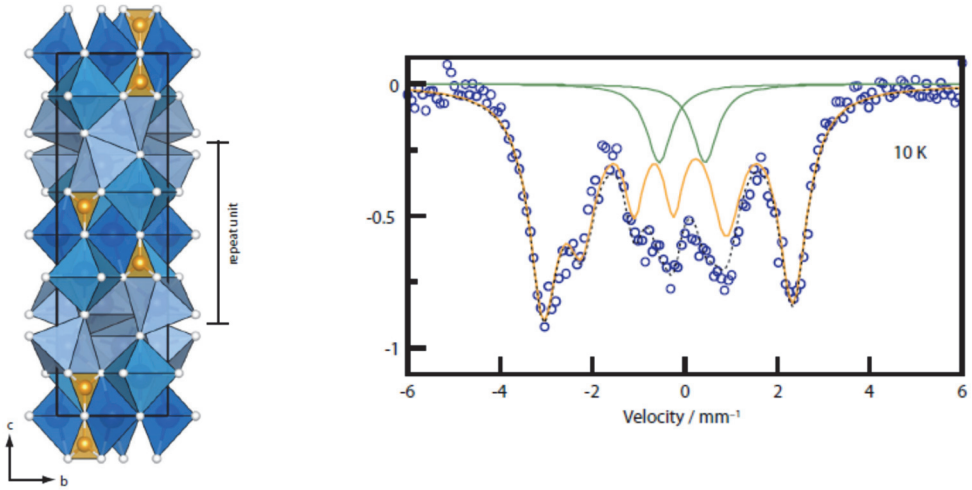


Fig. Crystal structure (right) and ^{57}Fe Mössbauer spectra at 10 K (left) of Ca_4FeN_4.

References

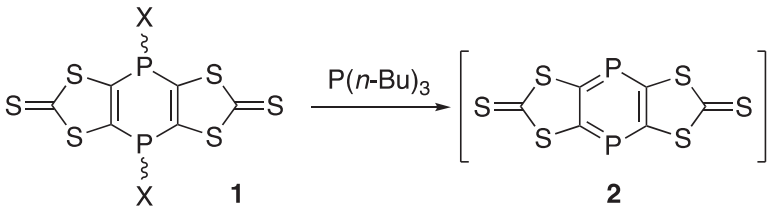
1. S. D. Kloß, A. Haffner, P. Manuel, M. Goto, Y. Shimakawa, & J. P. Attfield, Preparation of iron(IV) nitridoferrate Ca_4FeN_4 through azide-mediated oxidation under high-pressure, *Nature Communications*, **2021**, 12, 571.

Small molecule activation using anionic crypto-FLPs

Rainer Streubel University of Bonn

Metal-free small molecule activation has become an increasingly important and active field in main group element chemistry and the catalytic applications in organic synthesis have been established. The systems used were initially called “frustrated Lewis pairs” (FLPs) as introduced by Stephan in 2006, and they usually combine group 13/15 elements in mono- or bimolecular systems having spacers which allow only for rather weak (or no) attractive interactions. Based on this concept, we have already reported the FLP-type reactivity, *that is*, small molecule activation, of phosphorus complexes, *e.g.*, azaphosphiridine (P/N/C three-membered ring) complex and P–O–B complex with an anionic phosphorus center.

Related to this chemistry, we are investigating the synthesis and reactivity of various phosphorus compounds. We have recently summarized a series of research results on oxaphosphirane (P/O/C three-membered ring) complexes in a review.[1] We also succeeded in the synthesis of phosphorus-containing tricyclic compounds **1** with a high level of sulfur atoms, which can be applied to novel TTFs.[2] The reduction of **1** with P(*n*-Bu)$_3$ afforded a mixture containing unprecedented aromatic tricyclic compound **2**.



Through discussions with us, Prof. Tokitoh and his colleagues discovered that P–Al single bond compound **3**, of which bond between Lewis base and acid is normally inactive, can undergo addition reactions with alkynes and alkyne,[3] and reported that their addition products **4** also function as FLPs. It can be regarded as a masked FLP, showing that the potential of FLPs can be further expanded by utilizing high-period elements.



1) R. Streubel *et al*. *Coord. Chem. Rev.*, **2021**, 437, 213818. doi: 10.1016/j.ccr.2021.213818.
2) R. Streubel *et al*. *Inorg. Chem.*, **2021**, 60, 13029. doi: 10.1021/acs.inorgchem.1c01463.
3) N. Tokitoh *et al*. *Chem. Eur. J.*, **2021**, 27, 11273. doi: 10.1002/chem.202101649.

Development of Unsymmetrical π-Electron Systems of Heavier Main Group Elements and Elucidation of Their Property

Takeaki Iwamoto　Tohoku University

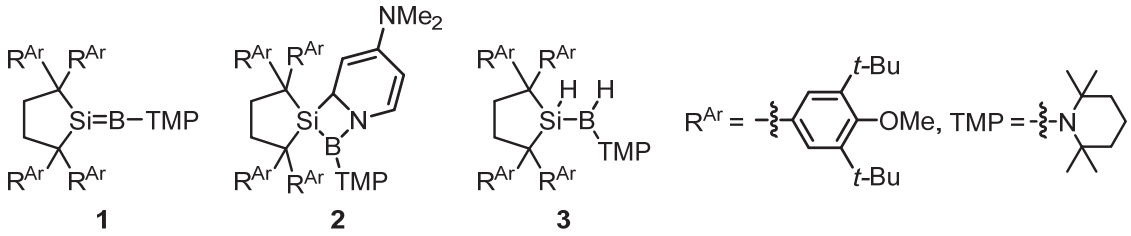
Objectives: π-Electron systems containing multiple bonds of heavier main group elements have been studied as prospects for advanced materials and reagents for small molecule activation. We aimed at developing unsymmetrical π-electron systems containing a double bond between group-14 and group-13 elements, which remain scarce compared to other heavier π-electron systems.

Experimental Methods: Dialkylborasilene **1** (Chart 1) was synthesized by the lithium-naphthalenide reduction of the corresponding (chlorosilyl)chloroborane obtained from an isolable dialkylsilylene with TMP-substituted dichloroborane (TMP = 2,2,6,6-tetramethylpiperidyl).

Outcomes: Novel dialkylborasilene **1** was isolated as red crystals in 74% yield. Preliminary X-ray single crystal diffraction (XRD) analysis revealed that in the solid state **1** adopts a non-planar structure with the sum of the angles around the three-coordinate silicon atom of 327°. Borasilene **1** reacted with 4-(dimethylamino)pyridine (DMAP) to provide a formal dearomative [2+2]-cycloadduct **2** as yellow crystals. It should be noted that **1** reacted with H_2 at ambient pressure at room temperature to provide (hydridosilyl)hydroborane **3** as a major product, and it suggests borasilene **1** can activate other small molecules.

Analysis: Borasilene **1** and its DMAP adduct **2** were fully characterized by a combination of NMR spectroscopy, elemental analysis, and XRD analysis.

Chart 1.



This project was done in collaboration with Professors Norihiro Tokitoh (ICR Partner Researcher) and Shigeyoshi Inoue (International Collaborating Researcher, Technical University of München, Germany).

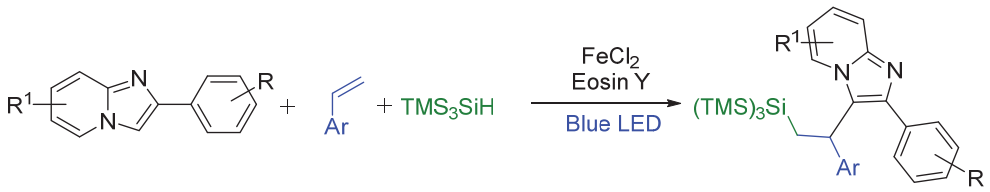
Publications: S. Abe, T. Iwamoto, “Synthesis and Property of Silicon-Boron Doubly-Bonded Compounds Containing an Unsaturated Silicon Atom Substituted by Two Alkyl Groups or (Alkyl)(Amino) Groups”, the 102nd annual meeting of the Chemical Society of Japan, March 25, 2022.

C–H Borylation and Silylation under visible-light enabled Fe-catalysis

Alakananda Hajra　Visva-Bharati University

Objective: Fe-catalyzed sp2-C–H borylation and silylation of alkenes and imidazo[1,2-*a*]pyridines under visible light mediated photoredox catalysis

Visible-light photocatalysis has become an impressive tool in organic synthesis. In this realm, the merger of transition metal catalysis and visible light photoredox catalysis offers an exciting opportunity to perform the organic transformations in mild conditions. Organosilicon compounds are one of the vital synthetic building blocks in the field of organic chemistry and they have widespread applications in material science, polymer science and agrochemistry. Notably, the silicon analogues of biologically active molecules and organosilicon compounds exhibit exceptional physicochemical properties, allowing them to be extensively used in medicinal chemistry. Imidazopyridine, an important class of nitrogen containing heterocycles, shows a wide range of biological activities. Presently we are studying a three-component carbosilylation of alkenes with imidazoheterocycles and silanes by merging visible light photocatalysis and iron(II) catalysis .



Presently we are focusing on the precise role of $FeCl_3$ and visible light, and late stage modification of the compound.

Development of Iron-based Electrocatalysts for Electrocatalytic Conversion of Biomass into Value Added Chemicals

Apurba K. Das　Indian Institute of Technology Indore

Molecular hydrogen (H_2) has attracted attention as one of the favourable alternative green energy carriers for diminishing fossil fuels in view of its highly pure products, high gravimetric energy density and environment friendliness. The hydrogen evolution reaction (HER) is an effective way to produce hydrogen from water.

Objectives: The main aims of this project proposal are:

(a) Design and develop peptide-anchored electrocatalyst

(b) Experimental validation of electrocatalytic biomass conversion to value added chemicals

(c) To study the mechanistic insights for electrocatalytic biomass conversion

Experimental Methods: The platinum nanoparticles (Pt NPs) have been generated in situ within the cross-linked nanofibrillar network of the hydrogel matrix of the peptide bolaamphiphile. The Pt6@hydrogel shows efficient catalytic activity for the electrochemical hydrogen evolution reaction (HER) in 0.5 M H_2SO_4 solution.

Experimental Results: In this study, Pt NPs have been synthesized *in situ* in the 3D cross-linked network of the peptide bolaamphiphile hydrogel. The ultrafine Pt NPs stabilized over a cross-linked nanofibrillar network of the peptide bolaamphiphile have been utilized as an electrocatalyst for the HER. The hybrid interface of Pt6@hydrogel/CP displayed excellent catalytic activity toward the electrochemical HER in 0.5 M H_2SO_4 solution. The Pt@hydrogel showed an overpotential of 45 mV at −10 mA cm^{-2} with a Tafel slope of 52 mV dec^{-1}. The Pt6@hydrogel/CP exhibited outstanding stability for 20 h of reaction time.

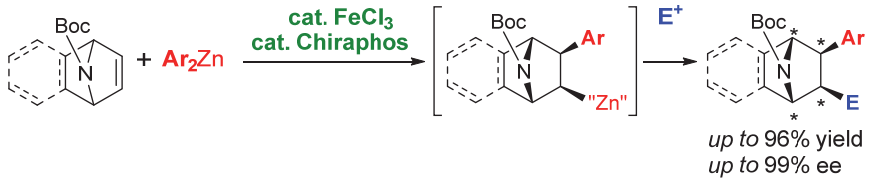
Discussion: The electrocatalytic performance of the catalyst depends upon its composition and surface structure. The amino acid functionalized peptide nanomaterials offer a novel approach to modulate electrocatalytic HER activity. Peptides have the ability to modify catalytic activity by controlling surface exposure to the solution. Nanoparticles in the 3D matrix of peptides could vary surface exposure by varying the degree of peptide binding to the catalyst surface. The self-assembled peptides can also increase proton transfer kinetics to enhance the kinetics of the HER process. The presence of phenylalanine and tyrosine improves the HER by tuning the surface composition and proton conductivity during the electrocatalytic HER process.

Publications: D. K. K. Kori, A. K. Das, A platinum nanoparticle embedded self-assembled peptide bola amphiphile hydrogel as an efficient electrocatalyst for the hydrogen evolution reaction, Chemistry In-house Symposium (CHEM-2022), Indian Institute of Technology Indore, March 11, 2022.

Iron-Catalyzed Asymmetric Carbozincation and Ring-Opening Reactions of Oxabicyclic Alkenes

Laksmikanta Adak　Indian Institute of Engineering Science and Technology

The transition-metal-catalyzed carbometalation of alkenes has attracted considerable interest among synthetic organic chemists, as it offers a useful pathway for the efficient and selective construction of carbon-carbon bonds. Because of the importance of asymmetric reaction for the synthesis of pharmaceuticals and natural products, significant efforts have been made to develop catalytic enantioselective carbometalation reactions of olefins. Palladium, rhodium, copper, and iridium-catalyzed asymmetric transformations of oxa- and azabicyclic alkenes have been extensively studied, where enantioposition-selective addition of oxygen, nitrogen, and carbon nucleophiles brings about subsequent ring-opening reactions provide access to enantioenriched compounds bearing multiple stereocenters. Only one example was found for the catalytic asymmetric addition of terminal alkynes to oxabenzonorbornadienes without the ring opening, which was achieved by use of a chiral phosphine-cobalt catalyst system. Although the use of iron catalysts in organic synthesis are attracting increased attention due to its economic and ecological points, but there application in enantioselective carbometalation has been limited to only highly strained cyclopropene derivatives. In this study, we have developed an iron-catalyzed enantioselective carbometallation: The screening of reaction conditions for iron-catalyzed enantioselective carbozincation of azabicyclic alkene with arylzinc reagent were performed. Various chiral ligands and metal salts were used for the screening and optimization of reaction condition. As shown below, it was found that the catalytic combination of $FeCl_3$ and (*S,S*)-Chiraphos provided the best result for the enantioselective carbometalation reaction.



Publications:

(1) “Iron-catalysed enantioselective carbometalation of azabicycloalkenes” Adak, L.; Jin, M.; Saito, S.; Kawabata, T.; Itoh, T.; Ito, S.; Sharma, A. K.; Gower, N. J.; Cogswell, P.; Geldsetzer, J.; Takaya, H.; Isozaki, K.; Nakamura, M. *Chem. Commun.* **2021,** *57,* 6975–6978.

Synthesis of ferrocenyl-phosphines and their application in the preparation of Fe clusters

Masamichi Ogasawara Tokushima University

Phosphaferrocenes are by far the most investigated among the various heterometallocenes reported to date. Since the phosphorus atom in a phosphaferrocene retains a lone pair on it, phosphaferrocenes have been used as *P*-donor ligands for transition metals. In the joint research project of this fiscal year, our research team collaborated with the Ohki group of ICR, Kyoto University, to establish a versatile method to prepare monophosphaferrocenes. This work was published in a scientific journal this year.[1]

A previously reported protocol for preparing monophosphaferrocenes requires two equivalents of [(mesitylene)FeCp][PF_6] (**A**), which reacts with a mixture of phospholide anions and phenyllithium generated by the reductive cleavage of the exocyclic P-C bond in *P*-phenylphospholes with metallic lithium (Figure 1). In this study, we attained a 50% reduction of required **A** by the use of inexpensive aluminium chloride as a phenyllithium scavenger and Et_3N for trapping Lewis acidic triphenylalminium byproduct (Figure 2). The reaction between a phospholide and complex **A** was proposed to proceed via the initial nucleophilic attack of the negatively charged phosphorus atom to the iron(II) center in **A**.

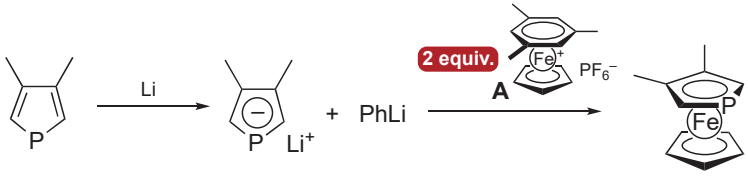


Figure 1. A known protocol reported by Roberts & Wells (1986).

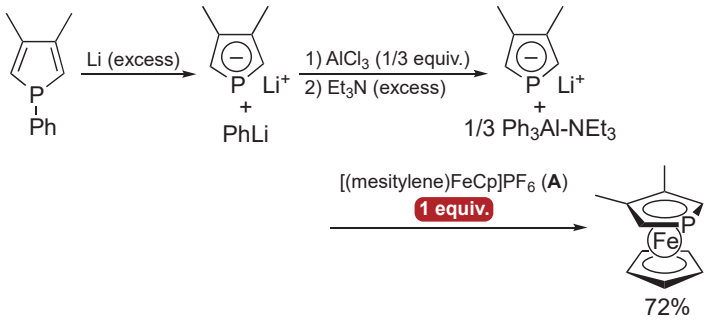


Figure 2. A modified and versatile method to prepare mono-phosphaferrocenes. An example to furnish 3,4-dimethylphosphaferrocene is shown.

Our next plan is to apply monophosphaferrocenes as supporting ligands for Fe-based metal-cluster complexes.

Publication from this joint project:

[1] Kakeru Masaoka, Manami Ohkubo, Haruka Taue, Masayuki Wakioka, Yasuhiro Ohki, and Masamichi Ogasawara, “Synthesis of Monophosphaferrocenes Revisited”, *ChemistrySelect* **2022**, *7*, e202104472. doi: 10.1002/slct.202104472.

極低温強磁場対応 THz-STM の開発

立崎武弘　東海大学

現代物性物理学における最先端の関心である非平衡量子系の動的挙動を実験的に解き明かすため、ピコ秒時間分解能とナノメートル空間分解能、1 meV エネルギー高分解能を達成する計測技術の確立を目指している。この技術はテラヘルツ（THz）パルスをトンネルバイアスに利用したピコ秒の時間分解能を有する走査トンネル顕微鏡（STM）でによって実現される。本研究では化学研究所　金光研究室において、THz-STM に関わる以下 4 点の開発を行い、低温強磁場 THz-STM として必要な機能を備えた原子像の観察が可能な装置を確立できた。

［1］高安定駆動機構を備えた極低温対応 STM ヘッドを改良し、冷凍機外からレーザービームを導入して探針先端を光学観察可能な STM ヘッドを開発した。本光学系を利用することで、試料表面における 100 μm スケールの微細構造と探針先端を外部より観察可能となった［図 1(a)］。

［2］超電導マグネット内に設置した STM ヘッドへ探針と試料を搬送する機構と、真空内で試料を劈開してクリーンで平坦な試料表面を得るための機構を備えた真空チャンバを構築した［図 1(b)］。また、超電導マグネットは 10 T 磁場が印加可能であることを確認し、強磁場 STM 計測が可能な装置を構築できた。

［3］液体ヘリウム貯め込み式冷凍機内に設置した STM を制御するエレクトロニクスを最適化し、ノイズフロア≲10 fA の低ノイズ測定系を構築した［図 1(c)］。電源起因のノイズが 60 Hz と 300 Hz で 10 fA を越えているが、このノイズレベルであれば安定して原子像を得られる。

［4］高配向性熱分解グラファイト（HOPG）表面を、白金イリジウム（PtIr）探針で計測した結果、HOPG 表面原子を計測できることを確認できた。

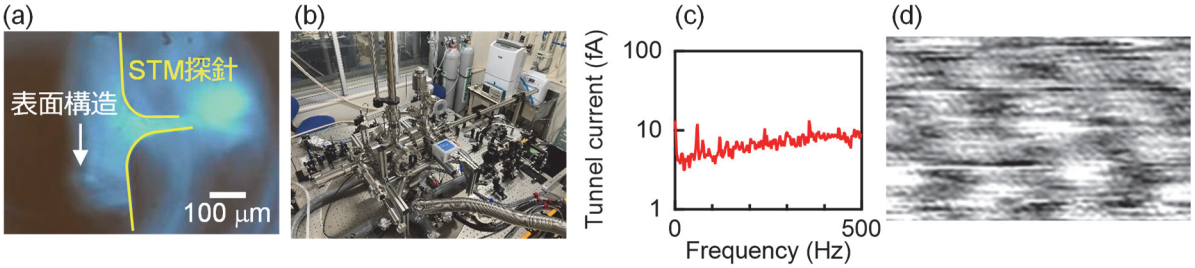


図 1　成果　(a) 顕微望遠鏡によって観察した試料表面と探針先端の光学像 (b) 構築した真空チャンバと試料搬送機構、試料表面処理機構の外観　(c) 開発した装置の電気ノイズスペクトル　(d) HOPG 表面観察像

■成果：論文発表

[1] T. Tachizaki, Kan Hayashi, Yoshihiko Kanemitsu, and Hideki Hirori, APL Materials **9**, 060903 (2021).

微弱な分子振動モードと結合させた極薄膜半導体における励起子発光の変調

桐谷乃輔　大阪府立大学

本研究は、帯電環境におけるデバイ長程度の厚みしか持たない二次元半導体に対して、隣接し電子相互作用をした分子の振動モードを変調させることで、結合・連動した二次元半導体の電子状態の変調を巨視的に起こすことを目的に研究を進めている。微弱な振動モードから、半導体の電子状態を変調するという新たな物質操作法の開拓に繋がると期待している。当初、分子振動モードと分子の電子状態に強い相関関係を持つ酸化還元活性分子に対して、検討を進めた。振動モードを制御するため光共振器と分子種の結合を試みた。種々の分子溶液の濃度を調整して、結合を試みたが非常に高い濃度の分子溶液環境が必要となることが判明した。さらに検証を進めるためには、分子/二次元半導体界面を効果的に検証するための低濃度化が必要となるものと考えている。あわせて検証を進めた他の分子種として、強いプロトン供給能を有する超酸分子と二次元半導体界面について研究を行なった。超酸分子種においては、分子接合によりフォトルミネッセンス光を数百倍に定量的に上昇させることが可能であるが、そのメカニズムを検証した。分子種の二次元半導体表面への接合が鍵となることを明らかとした。このことは、分子種の状態（振動モードなど）に二次元半導体の巨視的な光学物性が強く変調を受けることを意味している。今後、分子内振動モードに強制的な変調を加えることができれば、特定の相互作用や酸化状態を誘起し、界面で相互作用をした二次元半導体の光学特性が連動して変動・振動するなど、極微弱な分子振動の情報を巨視的な観測量（半導体の状態変化）として表出できると期待している。

学会発表：

1. T. Nakahara et al., ″Organic-Polymer Coated Superacid-Treated Tungsten Disulfide with Air-Stable Strong Photoluminescence″, 2021 MRS Fall Meeting & Exhibit (virtual conference), 2021, 11, 6 (Oral).
2. 中原隆宏, 吉村武, 藤村紀文, 桐谷乃輔, パラフィン被覆による WS2 発光強度向上のメカニズムの考察, 第 82 回応用物理学会秋季学術講演会, 2021 年 9 月.

2021-20

高強度テラヘルツパルスを駆使したマルチフェロイック物質におけるマグノン・フォノン励起

佐藤琢哉　東京工業大学

【目的】

強誘電性と（反）強磁性を併せ持つマルチフェロイック物質は次世代の機能的スピントロニクス材料として注目されている。マルチフェロイック特性を室温で示す唯一の物質であり、電場による磁性制御、磁場による電気分極制御が実現されている。過去にラマン散乱や赤外吸収によってフォノンやマグノンがテラヘルツ帯に存在することが報告されている。申請者は、これまで近赤外フェムト秒光パルスを用いて、NiO、CoO、$YMnO_3$、ガーネット、$BiFeO_3$等のフォノン、マグノンをコヒーレントに励起し、その時空間ダイナミクスを観測する研究を行ってきた。また、そのメカニズムを光パルスの電場成分によるインパルシブ誘導ラマン散乱に基づいて解明してきた。本研究では、高強度テラヘルツ励起によって、非線形なマグノン励起を伴う物性制御の確立を目指して実験装置の開発を行った。

【実験方法】

マグノンを強力なテラヘルツ磁場で励起するために、フェムト秒パルスレーザーの$LiNbO_3$結晶中での光整流効果を用いた高強度なテラヘルツパルス発生の光学系の構築を共同研究者（廣理、金光）と協力して行った。さらに、発生させた高強度テラヘルツ磁場により磁性体の磁化変化を測定するための光ファラデー回転およびカー回転測定のための光学実験系を構築した。

【実験結果】

フェムト秒パルスレーザーによって発生させたテラヘルツパルスの最大電場強度は1 MV/cmを超えており、極めて大きな磁化変化を誘起することが期待できる。実際に、反強磁性体試料中（$HoFeO_3$）のテラヘルツ帯にあるマグノンを励起し観測することに成功した。とくに、励起磁場強度とともにマグノンのピーク周波数が大きくレッドシフトしており、大振幅のマグノン励起を実現したことを確かめることができた。

【考察】

観測された反強磁性体におけるマグノン振動を理論的に説明するためにランダウ・リフシッツ・ギルバート方程式による解析を行った。低強度の励起磁場領域ではこの理論モデルによっておおよそ再現された。一方で、高強度な励起磁場領域では、周波数変化や時間波形の非対称性など理論モデルでは再現できない現象があることが分かった。これまでに、このような極端に非線形なマグノン振動を観測した例はなく、非線形振動領域での新たな理論モデルの構築を促す結果を得ることに成功したといえる。

高圧合成法を利用したエネルギー材料の開発

藪内直明　横浜国立大学

蓄電固体材料は、構造中の遷移金属イオンが酸化・還元しその電荷補償の結果、構造中のイオン濃度を任意に変化させることができるため、エネルギー材料として研究・開発が行われている。これまで、固体中に高次元のイオンの拡散経路を有し、固体界面（粒界）濃度が低い物質が、優れたイオン輸送特性を示す材料であると考えられてきた。一方、最近では、これまでの常識では考えられないような材料、例えば固体中の界面の濃度を極端に増加させた材料においても、優れた蓄電固体特性が見出されている。界面構造やその特性は固体の持つ結晶構造に強く依存すると考えられる。これまで、従来型の固相反応で合成可能な物質における界面特性は調べられてきたが、従来型の反応では到達できない極限環境下でのみ安定化できる準安定物質において、その界面における特性はほとんど調べられていない。本研究課題では、高圧・高温といった極限条件を用いた条件下で安定化される異常高原子価状態を有するマンガン(Mn^{5+})を含んだペロブスカイト酸化物に着目し、高密度界面を有する蓄電固体材料開発を行った。

Mn^{5+}を含んだペロブスカイト酸化物の安定化を目指して試料合成を行った。図 1 に示すのは、出発原料を KO_2、SrO_2 および MnO として、8GPa で 1000℃の条件下で反応させて得られた文末試料の X 線回折パターンである。参照試料として、ペロブスカイト構造を有する $SrMnO_3$ の X 線回折プロファイルも載せている。出発原料に SrO_2 を含まない場合（青線）では、ペロブスカイト構造に帰属できる回折ピークは観測されなかった。一方で出発原料に SrO_2 を加えて合成した試料(赤線)では、2θ~33°にペロブスカイト構造に帰属できる回折ピーク(▪印)が観測できた。これらの結果は、M5+の形成エネルギーは高いものの、形式価数が 4 から 5 の間の値となる混合原子価状態を持つペロブスカイト酸化物$(K,Sr)MnO_3$ を形成することで、Mn^{5+}を安定化できることを示唆するものである。今後は、出発原料の SrO_2 量を調整し合成条件を探索することで Mn^{5+}を含んだペロブスカイト酸化物の単相化を進め、高密度界面を有する蓄電固体材料開発を推進する。

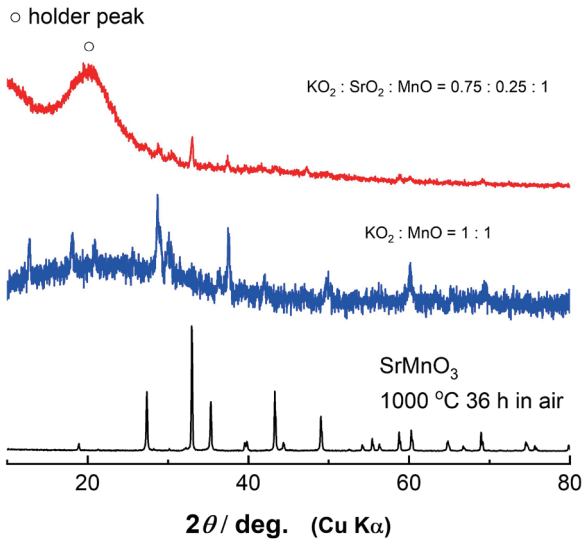


図 1：高圧合成で得られた粉末試料の X 線回折パターン. (赤線)出発原料として KO_2、SrO_2 および MnO を使用した試料. (青線) 出発原料として KO_2 と MnO を使用した試料. (黒線) 参照試料としてペロブスカイト構造を持つ $SrMnO_3$ の回折パターン.

Study on the physical mechanism on novel-ternary nanoparticle formation

Yasutomi Tatetsu　Meio University

There is a growing interest in finding novel materials that are not only thermodynamically stable, but also thermodynamically unstable for applications. Chemical synthesize techniques, which control nano particles precisely, are being developed in order to discover new functional materials. Recently, Teranishi's group at Kyoto University found a new $Z3$-type $Fe(Pd,In)_3$ crystal structure, which was synthesized by introducing a third element of In into $L1_2$-$FePd_3$ [1]. Typically, $L1_2$-$FePd_3$ is the thermodynamically stable phase of binary Fe–Pd systems. In our previous studies we confirmed, by experimental and theoretical analyses, that the most stable site for In in the $Z3$-$Fe(Pd,In)_3$ structure is in the center layer of this structure. The $Z3$-$Fe(Pd,In)_3$ structure can be stably synthesized in a narrow range of In concentrations. Furthermore, the magnetic hysteresis loop of $L1_2$-$(Fe,In)Pd_3$ and $Z3$-$Fe(Pd,In)_3$ shows that the coercivity value of the $Z3$-$Fe(Pd,In)_3$ structure is 15 times higher that of the $L1_2$-$(Fe,In)Pd_3$ structure.

In this report, we performed first-principles non-collinear calculations in order to explain the higher coercivity value in the $Z3$-$Fe(Pd,In)_3$ structure. We used the ab-initio code, OpenMX [2], for calculating the magnetic anisotropy energies of $L1_2$-$(Fe,In)Pd_3$ and $Z3$-$Fe(Pd,In)_3$ structures and compared these energies to find easy axes. In each calculation, the spin directions of each atom in these systems were set from [001] to [100] when $\varphi = 0$ and from [100] to [110] when $\theta = 0$. The model structures for these calculations were set to the same chemical composition ratio of $L1_2$-$(Fe_7,In_1)Pd_{24}$ and $Z3$-$Fe_8(Pd_{20},In_4)$, which were obtained through experiments. We found that the magnetic anisotropy energies show −1.38 μeV/atom for the $L1_2$-$(Fe,In)Pd_3$ structure and −0.213 meV/atom for the $Z3$-$Fe(Pd,In)_3$ structure. The easy axis for $Z3$-$Fe_8(Pd_{20},In_4)$ is the c axis, as shown in the figure. These absolute values and the ratio between these two values are not the same as the experimental values due to some limitation of first-principles calculations. However, the tendency which the $Z3$-$Fe(Pd,In)_3$ structure has higher coercivity values than the $L1_2$-$(Fe,In)Pd_3$ structure is consistent with the experimental measurement. We assume that added In atoms might be one of the reasons to increase the magnetic anisotropy of the $Z3$-$Fe(Pd,In)_3$ structure. Further theoretical studies are needed to explain the mechanism of the coercivity increase in the $Z3$-$Fe(Pd,In)_3$ structure.

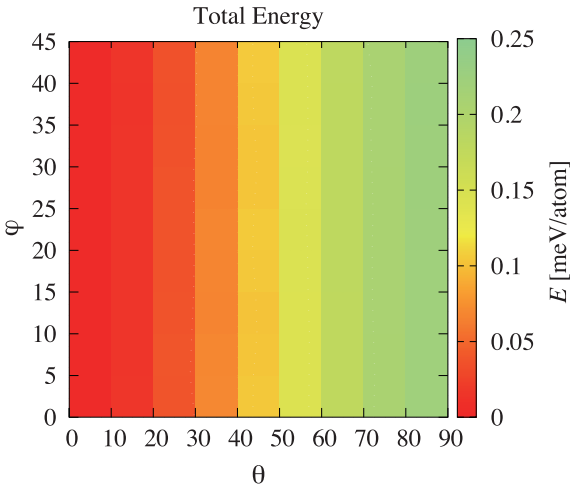


Figure: Total energy analysis for the $Z3$-$Fe(Pd,In)_3$ structure depending on the spin directions.

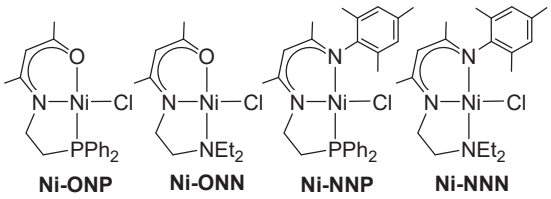
[1] K. Matsumoto, R. Sato, Y. Tatetsu, T. Teranishi, *et al.*, Nature Commun., **13**, 1047 (2022).

[2] http://www.openmx-square.org

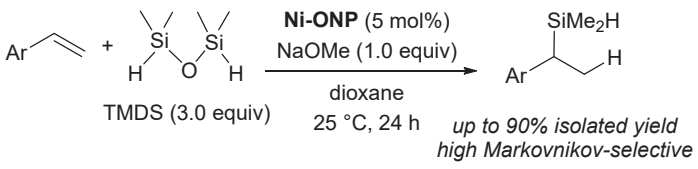
Development of collaborative reaction fields based on dinuclearization of mononuclear complexes

Yoshitaka Yamaguchi　Yokohama National University

A tridentate pincer-type ligand is often used to provide an appropriate steric and electronic environment around the metal center and thus pincer-type complexes have received significant attention. We have already reported the synthesis of a series of pincer-type nickel(II) complexes utilizing a combination of β-aminoketonato or β-diketiminato frameworks with a third donor such as phosphino or amino group. Our study on nickel(II) complexes revealed that the modification of the ligand framework has a significant influence on the catalytic performance such as in the biaryl cross-coupling reaction (*Dalton Trans*. **2018**, *47*, 8003.; *Eur. J. Inorg. Chem*. **2019**, 126.). We have recently demonstrated that (i) **Ni-ONP** serves as a catalyst in the highly Markovnikov-selective hydroboration of vinylarenes with bis(pinacolato)diboron (B_2Pin_2) (*Org. Lett.* **2020**, *22*, 4033.) and that (ii) **Ni-ONN** shows high catalytic activity for the synthesis of alkyl aryl ethers via the cross-coupling of aryl halides with primary and secondary aliphatic alcohols in the presence of B_2Pin_2 and KO^{t}Bu (*Adv. Synth. Catal.* **2021**, *363*, 1625.). We have continuously focused our attention on catalytic transformations promoted by well-defined these nickel(II) complexes.



The hydrosilylation of alkenes is one of the most important processes to produce organosilicon compounds. Platinum-catalyzed alkene hydrosilylation is industrially the most frequently conducted catalytic processes. However, recently, the economic and environmental concerns associated with precious metal catalysts have led to considerable interest in replacing them with catalysts based on earth-abundant first-row late-transition metals. We were interested in developing the hydrosilylation reaction of vinylarenes using our nickel(II) complexes as catalysts. We found that **Ni-ONP** shows high catalytic activity for the hydrosilylation of styrene derivatives with 1,1,3,3-tetramethyldisiloxane (TMDS), which acts as a highly efficient surrogate for Me_2SiH_2, in the presence of NaOMe as a base. These reactions proceeded in a regioselective manner under mild conditions and afforded the corresponding Markovnikov products in high yield [1].



[1] Hashimoto, T.; Shiota, K.; Ishimaru, T.; Yamaguchi Y. “Hydrosilylation of Alkenes Using a Hydrosiloxane as a Surrogate for Me_2SiH_2 and Catalyzed by a Nickel-Pincer Complex”, *Eur. J. Org. Chem.* **2021**, 5449.

磁性微粒子を用いたウルシオール塗膜の機能発現

橘洋一　京都市産業技術研究所

【目的】

近年，電子機器の精密化・高性能化が進み，電子機器の誤作動，混信，健康被害といった電磁波による障害を回避するため，これまで以上に電磁波遮蔽の技術が求められている。電磁波遮蔽材料は，電気絶縁性を持ったバインダーと電磁波を吸収する添加剤を組合せて作製される。天然樹脂である漆は，電気絶縁性があり，環境に優しい電磁波遮蔽材料のバインダーとして期待が持たれる。そこで，電磁波吸収の添加剤として，磁性を持った鉄フェライトを混合した漆塗膜を作製し，電磁波遮蔽の性能について検討を行った。

【実験】

初めに天然の漆に対し，粒径が 40 μm より小さい鉄フェライト（以下，F40 と記す），40 μm 以上かつ 75 μm より小さい鉄フェライト（以下, F75），比較対象として磁性を持たないベンガラ（以下，B）を所定の割合（0, 1, 5, 10, 25 wt%）で混合し，フーバーマーラーにて 1 分間撹拌することで添加物を混合した漆を得た。さらに，得られた漆を 20 ºC/60%の条件下で乾燥させ，漆塗膜を形成させた。塗膜の膜厚は，濡れ膜厚で 50 μm とした。同時に，乾燥時間の測定を行い，得られた漆塗膜を電磁波測定器 RT-100（ERICKHILL 社製）により電磁波遮蔽性の評価を行った。

【結果】

初めに，乾燥時間の測定を行った（図 1）。鉄フェライトを添加した塗膜では，乾燥時間が短縮する傾向が見られた。これは，フェライト中に含まれる鉄イオンが漆と反応しているためと予想される。続いて，電磁波遮蔽性の評価として，簡易的に電界強度にて評価を行った。今回の測定では，電界強度が 30 V/m 以下の塗膜において，電磁波遮蔽性を有する。その結果，粒径の細かな鉄フェライト F40 を 25 wt% 添加した漆塗膜において，10 V/m という高い電磁波遮蔽性が確認された。

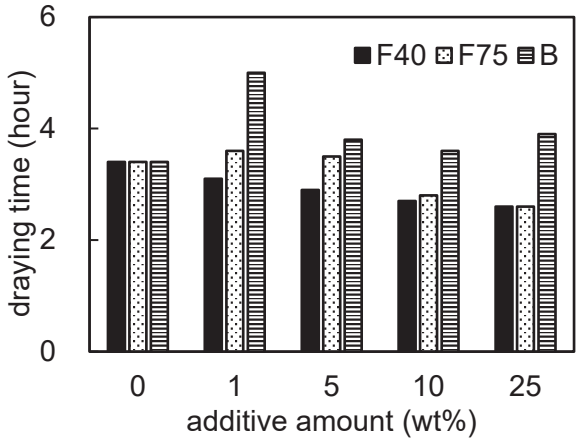


図 1. 作製した漆塗膜の乾燥時間

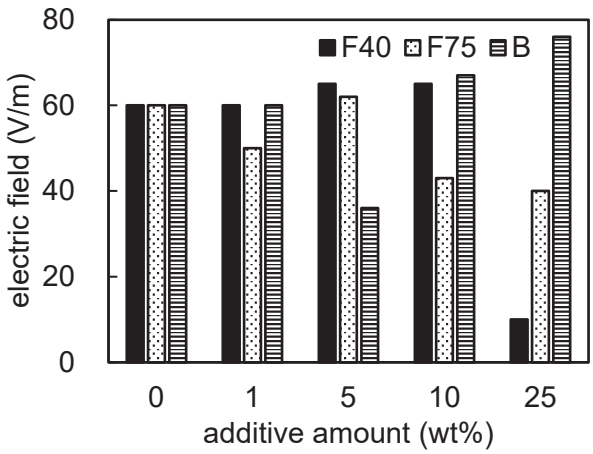


図 2. 作製した漆塗膜の電磁波遮蔽性

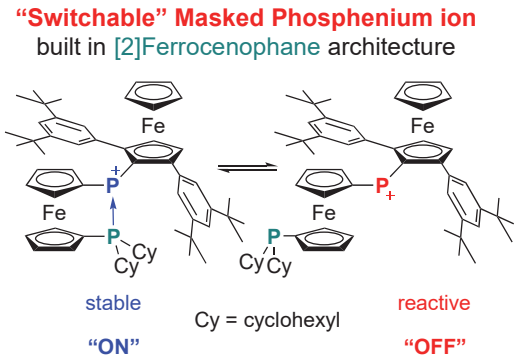
Creation of Effective Oxidation Scavenger for Efficient Perovskite-based Solar Cells

Takahiro Sasamori University of Tsukuba

The goal of our collaborative research with Prof. Dr. Atsushi Wakamiya (ICR, Kyoto University) is development of an organic oxidation scavenger for the creation of efficient lead-free perovskite-based solar cells, and pioneering research achievements on the basis of the fusion of elemental science and functional physical chemistry. Challenges for lead-free efficient perovskite-based solar cells such as Sn(II)-based ones compared with their Pb counterparts predominantly include the facile oxidation of divalent Sn(II) into Sn(IV) which leads to the increased nonradiative charge recombination in the perovskite films. Thus, we have focused our research targets on the creation of low-coordinated main group element species as effective oxidation scavengers, which exhibit redox-active property and considerable solubility in organic solvents.

Organic phosphenium ions ($R_2P:^+$) are attractive intrinsically extremely reactive species, which would exhibit possible ability of working as effecting oxidation scavengers. Isolable stable phosphenium ions remain scarce, and in most hitherto reported examples, the phosphenium center is stabilized by electron-donating substituents (e.g., heteroatoms such as nitrogen), which results in electronic perturbation. We have been interested in the chemistry of redox-active phosphenium ions with carbon-based substituents such as ferrocenyl groups. Furthermore, we have designed a ferrocene-based phosphenium ion with "reversible" intramolecular donor coordination, $[Fc^*Fc^PP]^+$, Fc* = 2,5-(3,5-*t*Bu$_2$-C$_6$H$_3$)$_2$-1-ferrocenyl, Fc^P = 1'-dicyclohexylphosphino-1-ferrocenyl). The Fc^P group ascribes both stability and reactivity for the phosphenium ion center with its "switchable" donor coordination caused by the rotation of the cyclopentadienyl moiety Accordingly, the well-designed phosphino-phosphonium ion incorporated within [2]ferrocenophane framework was synthesized as an air-stable phosphenium ion as a potential "bottleable" oxidation scavengers.

We are grateful to Prof. Wakamiya (ICR, Kyoto Univ.), Prof. Yoshida (Nagoya Univ.) and Prof. Tsuchiya (Kitasato Univ.) for their support on the research, and fruitful discussions.

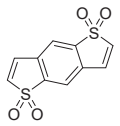


1. Nakamura, T.; Yakumaru, S.; Truong, M. A.; Kim, K.; Liu, J.; Hu, S.; Otsuka, K.; Hashimoto, R.; Murdey, R.; Sasamori, T.; Kim, H. D.; Ohkita, H.; Handa, T.; Kanemitsu, Y.; Wakamiya, A. *Nature Communications* **2020**, *11*, 3008.
2. Zhang, T.; Lee, V. Y.; Morisako, S.; Aoyagi, S.; Sasamori, T. *Eur. J. Inorg. Chem.* **2021**, *2021*, 3988-3991.

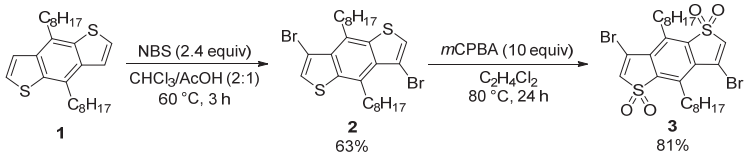
Development of heteroacenes with excellent photophysical and electrochemical properties

Koichi Mitsudo Okayama University

Thienoacenes, which are acene molecules incorporating thiophene rings, are known to exhibit excellent semiconductor properties and are used as active materials in organic field-effect transistors (OFETs) and organic photovoltaic cells (OPVs). Therefore, this field has been studied intensively, and various thienoacenes have been synthesized to validate their physical properties. Meanwhile, thiophene ring is an electron-rich donor aromatic ring, whereas thiophene-dioxide, which is obtained by oxidizing the thiophene ring, loses its aromaticity and behaves as an electron-deficient acceptor molecule. In recent years, some π-conjugated molecules incorporating thiophene-dioxide have been reported to have unique luminescent properties, and have begun to attract attention. However, there have been few reports on the synthesis of thienoacene derivatives containing multiple thiophene-dioxides, even though they are expected to have interesting properties, and little is known about their physical properties. In this study, we focused on synthesis of thienoacenes which have benzo[1,2-*b*:4,5-*b*′]dithiophene 1,1,5,5-tetraoxide (BDT-teraoxides) as a key skeleton.

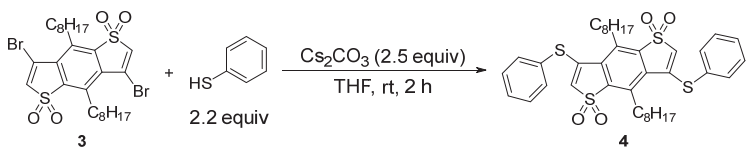

BDT tetraoxides

Even though BDT is one of the most common skeletons in thienoacenes, there have been few reports on the synthesis of their oxides. We therefore set out to develop a synthetic method for the BDT tetraoxides. Treatment of 4,8-dioctylbenzo[1,2-*b*:4,5-*b*′]dithiophene (**1**) with NBS took place bromination to afford dibromominated BDT **2** regioselectively. Thus obtained **2** could be oxidized with mCPBA to afford dibromoinated BDT tetraoxides **3**.



1 → **2** 63% → **3** 81%

We applied thus-obtained dibrominated BDT tetraoxides **3** to addition–elimination reactions and found that the desired substitution reaction proceeded smoothly. For instance, the reaction with benzenethiol gave BDT tetraoxides **4** quantitatively which has two phenylsulfanyl units. The studies on photophysical properties of the substituted BDT tetraoxides and further transformation of them are ongoing in our group.



3 → **4** quant

Integrating Omics Data and Module-based Network with Deep Learning to Develop Cancer Type Predictive Models

Jinn-Moon Yang National Yang Ming Chiao Tung University

Objective. Prediction and classification of cancer subtypes have been a major topic both in biomedicine and bioinformatics. For that purpose, various machine learning methods have been developed to better analyze mRNA expression data and improve the classification accuracy. However, most of current studies focus on specific cancer types, and thus it is needed to explore mechanisms across multiple cancer types. To address these issues, we have been collaborating with Professor Akutsu in ICR. In this proposal, we will continue our collaboration to extend our previous approach to include other kinds of omics data, such as PPI and metabolic networks as well as PPI modules. We will also study deep learning-based methods for identifying interaction sites of protein kinase inhibitors because protein kinases play important roles in various diseases including cancers.

Results. In this year, we focused on identification of interaction sites of protein kinase inhibitors. We developed the Prediction of Interaction Sites of Protein Kinase Inhibitors (PISPKI) model [1], which is a graph convolutional neural network (GCN) to predict the interaction sites of protein kinase inhibitors. The core of the PISPKI model is the WL Box, which was newly designed based on the well-known Weisfeiler-Lehman algorithm. The most important feature of the WL Box is that it assembles multiple switch weights to effectively compute graph features. The PISPKI model was evaluated by testing with shuffled datasets using 11 kinase classes. The resulting accuracy varied from 83 to 86%, demonstrating superior performance compared to two baseline models. Furthermore, the importance of each component was analyzed via the ablation study, and the result suggests that the WL Box module is critical.

Publication

[1] F. Wang, Y-T. Chen, J-M. Yang, T. Akutsu: A novel graph convolutional neural network for predicting interaction sites on protein kinase inhibitors, Scientific Reports, vol. 12, Paper ID. 229, 2022.

Developing Data-driven Deep Learning Approaches for Accurate Identification of Protease Specific Substrate Targets and Cleavage Sites

Jiangning Song　Monash University

Objective. It is important to understand the mechanisms of regulation of proteolysis by proteases for elucidation of cellular processes. For that purpose, it is highly desirable to develop high-throughput, cost-effective computational methods that can be used to accurately identify the target substrates for a specific protease. I have been working on this important problem with Prof. Akutsu at ICR. In this project, building upon our successful collaborations, we continue and extend our development of next-generation bioinformatics methods for improved prediction of protease-specific target substrates and their cleavage sites. We will also study other related bioinformatics problems in sequence analysis and structural informatics.

Results. As a result of this project, we have developed several bioinformatic methods/tools for analysis of protein and nucleotide sequence data, which include, *iLeanPlus*: a general purpose tool for analyzing protein and nucleic acid sequence [1], *DeepVF*: a deep learning-based tool for identifying virulence factors from protein sequences in bacterial pathogens [2], and *Anthem*: a bioinformatic tool for prediction of binding between peptides and HLA class I molecules [3].

Publications

[1] Z. Chen, P. Zhao, C. Li, F. Li, D. Xiang, Y. Z. Chen, T. Akutsu, R. J. Daly RJ, G. I. Webb, Q. Zhao, L. Kurgan, J. Song. iLearnPlus: a comprehensive and automated machine-learning platform for nucleic acid and protein sequence analysis, prediction and visualization. ***Nucleic Acids Research***, vol. 49, Paper ID. e60, 2021 (17 citations).

[2] R. Xie, J. Li, J. Wang, W. Dai, A. Leier, T. T. Marquez-Lago, T. Akutsu, T. Lithgow, J. Song, Y. Zhang. DeepVF: a deep learning-based hybrid framework for identifying virulence factors using the stacking strategy. ***Briefings in Bioinformatics***, vol. 22, Paper ID. bbaa125, 2021 (10 citations).

[3] S. Mei, F. Li, D. Xiang, R. Ayala, P. Faridi, G. I. Webb, P. T. Illing, J. Rossjohn, T. Akutsu, N. P. Croft, A. N. Purcell, J. Song. Anthem: a user customised tool for fast and accurate prediction of binding between peptides and HLA class I molecules. ***Briefings in Bioinformatics***, vol. 22, Paper ID. bbaa415, 2021 (4 citations).

Unveiling the genomic contents of ecologically important marine giant viruses

Tom O. Delmont CNRS

Large double-stranded DNA viruses of phylum *Nucleocytoviricota* are a group of eukaryotic viruses that are highly diverse and abundant in marine environments. This group of viruses has complex genomes with sizes of up to 2 Mb that are even larger than small cellular organisms. However, the discovery of giant viruses has mainly been driven by the co-cultivation with amoebae or algal hosts. Consequently, the number of viruses and functions are primarily underestimated compared to the metagenomics-driven viral signals detected in the ocean. Thus, in this study, we (Tom O. Delmont et al.) investigated metagenomic data set from the sunlit ocean, built comprehensive marine giant virus genomes, and analyzed their genetic repertoires.

We first developed a phylogeny-guided framework to generate the giant virus genome database using a single hallmark gene, a subunit of DNA-dependent RNA polymerase, as a compass [1]. In total, 697 *Nucleocytoviricota* genomes were reconstructed. Along with the genomes from previous marine metagenomic surveys and isolated references, a total of 1817 non-redundant genomes were included in the final database. We then performed a phylogenetic analysis and surprisingly found two monophyletic deep-branching clades, *Proculviricetes* and *Mirusviricetes*. *Mirusviricetes* lacks several hallmark genes critical to particle morphogenesis but are enriched with some unique functions. A comparative functional analysis provided a result consistent with the monophyly of *Mirusviricetes*. In addition, we discovered myosin homologs in the database and revealed that these viral myosins formed a monophyletic group and had multiple origins [2].

The diversity of giant viral lineages draws attention to discovering new viral genomes. However, previous works might have overlooked putative lineages diverging from the traditional core gene-based definition of *Nucleocytoviricota*. Our phylogeny-guided framework has shown the efficiency in characterizing previously unknown lineages. The discovery of two conspicuously new lineages, *Proculviricetes* and *Mirusviricetes*, reminds us that we have not grasped the full diversity of giant viruses. *Mirusviricetes* is a major, functionally divergent class that implies a probability of an enigmatic viral lifestyle. Finally, the environmental genomic database for *Nucleocytoviricota* will contribute to future endeavors exploring the ecology and evolution of giant viruses.

Publication:

[1] **GaiaM.**, **Meng L.**, Pelletier E., Forterre P., Vanni C., Fernendez-Guerra A., Jaillon O., Wincker P., **Ogata H.**, **Delmont T.O**. Discovery of a class of giant virus relatives displaying unusual functional traits and prevalent within plankton: the Mirusviricetes. bioRxiv doi.org/10.1101/2021.12.27.474232 (2021).

[2] Kijima S., **Delmont T.O.**, Miyazaki U., **Gaia M.**, Endo H., **Ogata H.** Discovery of viral myosin genes with complex evolutionary history within plankton. Front. Microbiol. 12, 683294 doi: 10.3389/fmicb.2021.683294 (2021).

Revealing associations between giant viruses and eukaryotes in the global ocean through community networks inference and mining

Samuel Chaffron　CNRS

Large double-stranded DNA viruses are a monophyletic group of eukaryotic viruses, corresponding to the phylum *Nucleocytoviricota*, which is highly diverse and abundant in marine environments. Giant viruses have a broad range of eukaryotic hosts, from unicellular eukaryotes to animals. However, the number of viruses isolated in the laboratory represents a small fraction of viral signals detected in the ocean. The interactions between giant viruses and eukaryotes and factors driving these interactions remain poorly known. In this study, taking advantage of the recent large-scale marine metagenomics census, we used *in silico* approaches to investigate the global biogeography of marine giant viruses and their associations with eukaryotes.

First, using recently published environmental genomic databases for *Nucleocytoviricota* and eukaryotes, we built co-occurrence networks of metagenome-assembled genomes (MAGs). We then used a phylogeny-informed filtering method, Taxon Interaction Mapper (TIM), to refine these associations by integrating co-evolution information and improve the prediction of virus-host pairs. To further validate these predictions, we conducted a series of genome-based analyses, such as pairwise gene alignment and Giant Endogenous Viral Elements (GEVEs) detection, using eukaryotic MAGs and reference genomes.

We observed a total of 2,083 virus-eukaryote associations in the network, involving 787 viral MAGs that are widespread in the *Nucleocytoviricota* phylogenic tree. After TIM enrichment, we found two documented virus-host pairs, *Prasinovirus* and Mamiellophyceae, and *Coccolithovirus* and Haptophyta. Three other predicted hosts, *Thalassiosirales*, *Isochrysidales*, and *Chaetocerotales*, showed a large number of signals of giant viruses and virophages (parasites of giant viruses) insertions. Additionally, we leveraged a published *Chaetoceros muellerii* genome and found that the GEVE in *C. muellerii* and the giant virus clade, which were predicted to infect with *Chaetocerotales*, are congruent in the phylogenetic tree. Moreover, we demonstrated that the virus-host network was highly structured along the latitudinal gradient of temperature from the equator to the poles.

Focusing on the associations between giant viruses and eukaryotes in the global ocean, this project has demonstrated that network-based approaches are efficient hypothesis generators in giant virus-host prediction [1]. Genome-resolved networks provide genomic information improving the interpretability of host predictions. Using the new marine *Nucleocytoviricota* genome database, we could confirm that these associations between giant viruses and eukaryotes are prevalent in the global ocean and influenced by the environment, such as temperature. Overall, this project has thus significantly contributed to further our understanding of the complex relationships between giant viruses and eukaryotes.

[1] **Meng L**, **Endo H**, Blanc-Mathieu R, **Chaffron S**, Hernández-Velázquez R, Kaneko H, **Ogata H**. 2021. Quantitative assessment of NCLDV–host interactions predicted by co-occurrence analyses. mSphere, 6, e01298-20 (2021)

A Study on Statistical Machine Learning for Efficient Graph Structured Data Analysis

Masayuki Karasuyama　Nagoya Institute of Technology

For a variety of scientific fields such as biology, chemistry, and materials science, effective methodologies for analyzing their complicated data are strongly demanded. In particular, the graph-based data representation enables us to handle a variety of data types that is represented by interactions among multiple component objects. For example, a chemical compound is often represented as a graph in which an atom is a graph-vertex and a chemical bond is a graph-edge. Although graph is a versatile tool for data representations, analyzing its statistical property is usually difficult because of its combinatorial nature. In this study, we consider developing statistical machine learning methods for efficiently analyzing graph structured data by combining several techniques from data-mining, machine learning, and numerical optimization. For this inter-disciplinary topic, we have worked with the researchers including prof. Mamitsuka in the bio-knowledge engineering research laboratory of ICR.

We mainly focus on a task that statistically predicts a property associated with a given graph. For instance, predicting toxicity of a compound is a well-known example in this type of problems. We constructed an algorithm that identifies sub-structures of the graph strongly contributing to the target property [1], which can provide insights about the underlying correlation structure. Although a naïve approach to this problem causes prohibitive amount of computations, our proposed method provides an efficient computational procedure by pruning unnecessary sub-structures while maintaining the optimality guarantee. We further extend this method so that it can incorporate different types of the loss functions and inexact (relaxed) matchings of substructures. As another important application of our predictive graph mining framework, we further studied applying the same mining idea to a graph neural networks (GNN) explanation [2]. Recent GNN techniques have been used for a variety of tasks including scientific data analysis, but providing explanations about its behavior is still an open problem. We developed a local explanation approach based on the predictive graph mining surrogate by which a sub-structure based explanation that is difficult to provide by other existing approaches can be obtained.

[1] T. Yoshida, I. Takeuchi, and M. Karasuyama, Distance Metric Learning for Graph Structured Data, *Machine Learning*, vol.110, no.7, 1765-1811, 2021.

[2] H. Asahi, and M. Karasuyama, Local Explanation of Graph Neural Network through Predictive Graph Mining, IEICE technical report, vol.121, no.321, IBISML2021-23, 37-44, 2022 (in Japanese).

Control and Analysis of Complex Networks via Probabilistic Minimum Dominating Sets

Jose C. Nacher Toho University

Objective. We have been studying structural controllability of complex networks and developing theory and methods based on the minimum dominating set (MDS). In particular, we developed a new concept, the probabilistic minimum dominating set (PMDS), by extending the MDS for handling weighted networks. We will develop an efficient method for identifying three classes of nodes (critical/intermittent/redundant nodes) in the PMDS framework and apply it to analysis of brain ageing mechanisms. We will also study the maximum matching (MM)-based model, which is another major approach to analysis of structural controllability of complex networks.

Results. As for the PMDS-model, we developed an efficient integer linear programming (ILP)-based method with pre-processing to identify critical/intermittent/redundant nodes. We compiled the gene expression profiles of four normal brain regions from individuals aged 20–99 years, generated dynamic probabilistic protein networks across their lifespan, and applied the ILP-based method to the networks. The results show that the identified critical proteins were significantly enriched with well-known ageing genes collected from the GenAge database [1]. As for the MM-model, we combined the concept of driven nodes (Pequito et al., IEEE Trans. Automatic Control, 2016) and the concept of critical/intermittent/redundant nodes. We developed an efficient ILP-based method and applied it to analysis of a large number of biological networks. The results indicate that the number of driven nodes is considerably larger than the number of driver nodes, not only in all examined complete plant metabolic networks but also in several key human pathways [2].

Publications

[1] E. Yamaguchi, T. Akutsu, J. C. Nacher: Probabilistic critical controllability analysis of protein interaction networks integrating normal brain ageing gene expression profiles, Int. J. Molecular Sciences, vol. 22, paper ID. 9891, 2021.

[2] Y. Shinzawa, T. Akutsu, J. C. Nacher: Uncovering and classifying the role of driven nodes in control of complex networks, Sci. Rep., vol. 11, ID. 9627, 2021

Comprehensive analysis of viral succession during the transition of multiple types of algal blooms

Keizo Nagasaki　Kochi University

Objectives:

In this study, we investigated the community dynamics of eukaryotes, prokaryotes and a major group of large DNA viruses during 20 months in the Uranouchi Inlet, Kochi prefecture, to better understand community dynamics of free living microbes inhabiting coastal seawater.

Experimental Methods:

Ten liters of seawater were sampled and sequentially pumped through filters with pore sizes of 3μm, 0.8μm, and 0.2μm. The different community compositions of 43 samples were then analyzed with amplicon sequencing of a conserved gene of the respective microbial group.

Experimental Results:

The amplicon sequencing yielded several million, bona fide, cellular and viral reads, which were clustered to amplicon sequence variants (ASVs). Ecological analysis revealed a pronounced seasonality of each microbial group. The ASV communities of eukaryotes, prokaryotes, and a major group of large DNA viruses were compared and we discovered significant differences in their dynamics.

Discussion

Here, we were the first to describe the seasonality of a major group of large DNA viruses. This viral seasonality was strongly linked to the other microbial communities. The comparison of those communities showed that members of the viral community were less persistent and reoccurred less frequently than members of the eukaryotic community. The prokaryotic community showed the longest persistence and highest recurrence of its members after one year. The differences in community dynamics were interpreted as an ability of current communities to influence the formation of future communities, albeit with diminishing influence over time.

Publication

Year-round dynamics of amplicon sequence variant communities differ among eukaryotes, *Imitervirales*, and prokaryotes in a coastal ecosystem.

Florian Prodinger, Hisashi Endo, Yoshihito Takano, Yanze Li, Kento Tominaga, Tatsuhiro Isozaki, Romain Blanc-Mathieu, Yasuhiro Gotoh, Tetsuya Hayashi, Etsunori Taniguchi, Keizo Nagasaki, Takashi Yoshida, and Hiroyuki Ogata.

FEMS Microbiology Ecology, (2022) - *accepted*

Development of the method for the detection of coronavirus diversity

Tokiko Watanabe　Osaka University

Coronaviruses can cause zoonotic diseases and have become a major public health problem. Since bats are one of the natural reservoirs of coronaviruses, surveillance of bat coronaviruses is important for predicting possible future zoonotic diseases. In this study, we aimed to establish an RT-PCR method using degenerate primers designed through bioinformatics analysis to detect coronaviruses comprehensively and with high sensitivity. Using bioinformatics analysis, we designed 39 different degenerate primer pairs to detect conserved coronaviral polymerase genes. The RT-PCR conditions were verified using these primer pairs and control coronaviruses, including SARS-CoV-2. To examine whether this method is applicable to field samples, we attempted to detect the coronaviral genome using RNA extracted from bat organs collected in Sierra Leone. A coronaviral gene was detected in the intestinal tract of one out of 26 bats. Subsequently, we determined the whole genome sequence of this virus by using Next Generation Sequencing. Phylogenetic analysis revealed that this virus was a novel bat alphacoronavirus (Fig. 1). By applying this method to surveillance of bat coronaviruses, proactive measures can be taken against future outbreaks of coronavirus infections.

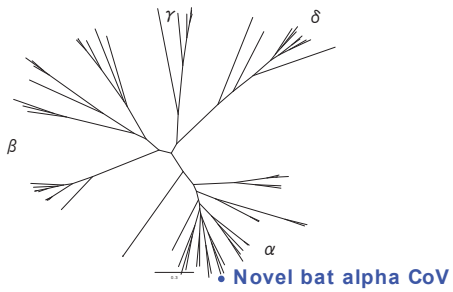


Fig 1. Phylogenetic tree of coronaviruses (whole genome)

<Presentation>

Shichinohe S, Takada K, Hingamp P, Tomita Y, Maemura T, N'jai A, Kawaoka Y, Endo H, Ogata H, Watanabe T. Use of RT-PCR and degenerate primers to comprehensively assess coronavirus genomes, The 68th Annual Meeting of the Japanese Society of Virology, Kobe, Japan, Nov., 2021. (Oral presentation)

効果的な分子ネットワーク解析方法の開発と医学・農学への応用

茅野光範　帯広畜産大学

本研究では、機械学習と統計学を融合させた統計的機械学習の観点から、効果的な分子ネットワーク解析法を提案し、それを用いて医学・農学における問題を解決する。分子レベルとして、ゲノム・遺伝子・代謝に焦点を当て、遺伝子ネットワークや代謝ネットワーク（代謝パスウェイ）の推定や、それらのネットワークへのゲノムの影響、実験条件（健常者と患者等）による違い等を検証するための解析方法を提案する。

我々は、これまで、図 1 に示した分子発現の相関構造の変化を捉える解析手法を提案し、これを改良した提案手法の数値実験による評価、公共の遺伝子発現データ（Gene Expression Omnibus；GEO から入手した延べ約 100 万個の遺伝子群）に提案手法を適用し、生物学的に意義のある遺伝子群が検出出来ることを確認した。また、先行研究で報告されている、相関ネットワークが変化する遺伝子群の具体例を集めた。さらに、これまでの提案手法をさらに発展させ、グラフネットワーク理論、計算機統計学、アルゴリズムやマイニング理論を駆使した機械学習・統計学的な分子ネットワーク解析法の提案へ向けて検討を重ねている。

今年度は、特に、これらの解析法の、医学分野（特に加齢研究）および農学分野（特に農作物）における具体的な生命科学現象への応用を検討し、医学分野として、ヒトと動物の加齢および加齢関連疾患研究、また、農学分野として、農作物のオミックス解析研究を進めている。

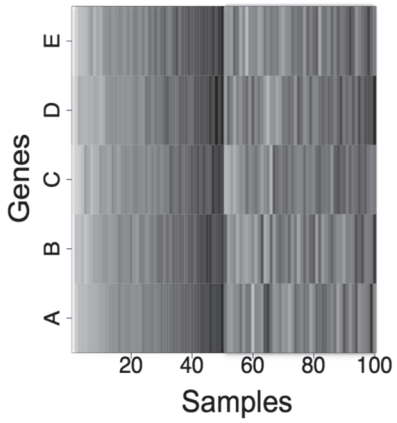


図 1. 2 つの群間（サンプル 1〜50 および 51〜100）で相関構造が変化する 5 つの遺伝子 A, B, C, D, E のヒートマップ表示（濃いほど発現量が高い）。遺伝子 A-E の中から任意の対をとると、サンプル 1 から 50 の群では相関を持つが、サンプル 51-100 の群では相関構造が崩れる［Kayano M., Shiga M. and Mamitsuka H., IEEE/ACM Trans. Comp. Biol. Bioinform., 11(1): 154-167, 2014 より転載］

Synthesis of inorganic molecules for elucidation of biosynthetic pathways of iron-sulfur clusters

Markus W. Ribbe　University of California

Nitrogenase catalyzes the reduction of N_2 to NH_3 at its cofactor site. Designated the M-cluster, the cofactor of Mo-nitrogenase is an [(*R*-homocitrate)$MoFe_7S_9C$] cluster that is synthesized via formation of a [Fe_8S_9C] L-cluster prior to the insertion of Mo and homocitrate. Our previous study has led to the identification of a [Fe_8S_8C] L*-cluster, which is highly similar to the L-cluster in the core structure but lacks the '9^{th} sulfur' in the belt region. However, direct evidence for conversion of the L*-cluster to an L-cluster upon insertion of SO_3^{2-} as the '9^{th} sulfur', as well as the mechanistic details of this reaction, remains elusive. Here we report characterization of the '9^{th} sulfur' insertion using SeO_3^{2-} and TeO_3^{2-} as 'labeled' SO_3^{2-} sources. Biochemical, CW/pulse EPR and XAS/EXAFS studies suggest a crucial role of the '9^{th} sulfur' in cluster transfer during cofactor biosynthesis while revealing the incorporation of SeO_3^{2-} and TeO_3^{2-} as Se^{2-} and Te^{2-}-like species, respectively, in the belt region of the L-cluster. DFT calculations further suggest an insertion mechanism of the '9^{th} sulfur' that involves cluster-facilitated *in situ* reduction of SO_3^{2-} to S^{2-}. These results provide direct evidence for the incorporation of a '9^{th} sulfur' during cofactor biosynthesis and establish an effective means to label the catalytically important belt region for future mechanistic investigations of nitrogenase.

This work was published as a scientific paper in *Nature Chemistry*:

Joint publication from this collaborative work: (team members are underlined)

Kazuki Tanifuji, Andrew J. Jasniewski, David Villarreal, Martin T. Stiebritz, Chi Chung Lee, Jarett Wilcoxen, Yasuhiro Ohki, Ruchira Chatterjee, Isabel Bogacz, Junko Yano, Jan Kern, Britt Hedman, Keith O. Hodgson, R. David Britt, Yilin Hu, Markus W. Ribbe, "Tracing the incorporation of the "ninth sulfur" into the nitrogenase cofactor precursor with selenite and tellurite"

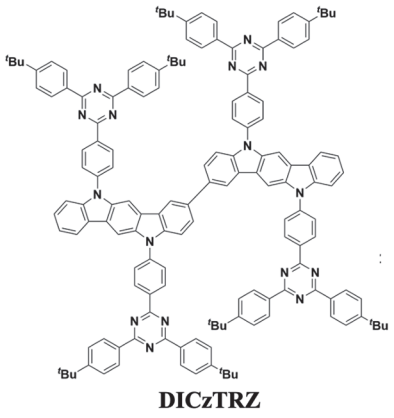
Nature Chem. **2021**, *13*, 1228-1234.　doi: 10.1038/s41557-021-00799-8

Development of new blue TADF emitters with horizontal molecular orientations

Eli Zysman-Colman　University of St Andrews

We have recently reported two collaborative studies between the Zysman-Colman and Kaji labs involving a multichromophore thermally activated delayed fluorescence (TADF) molecular design [1, 2] and their use in solution-processed TADF-OLEDs.

The first project built upon the previously published work on **ICzTRZ**,[3] by developing a dimerized analog **DICzTRZ** (**Figure 1**). The emission maximum ios 488 nm and the photoluminescence quantum efficiency (Φ_{PL}) is 57% in the 20 wt% doped CzSi film, and we observed the presence of both prompt and delayed fluorescence, confirming that **DICzTRZ** shows TADF. Polarization and angle-dependent luminescence spectroscopy were used to measure the orientation factor, *a*, for the solution-processed films of the 20 wt% **DICzTRZ** in CzSi, which yielded an anisotropy factor of 0.53 that disappointingly implies that the emitter presents a strongly vertical orientation, thus leading to blue-green devices with EQE_{max} value of 8.4% with λ_{EL} of 494 nm, corresponding to CIE of (0.22, 0.47).

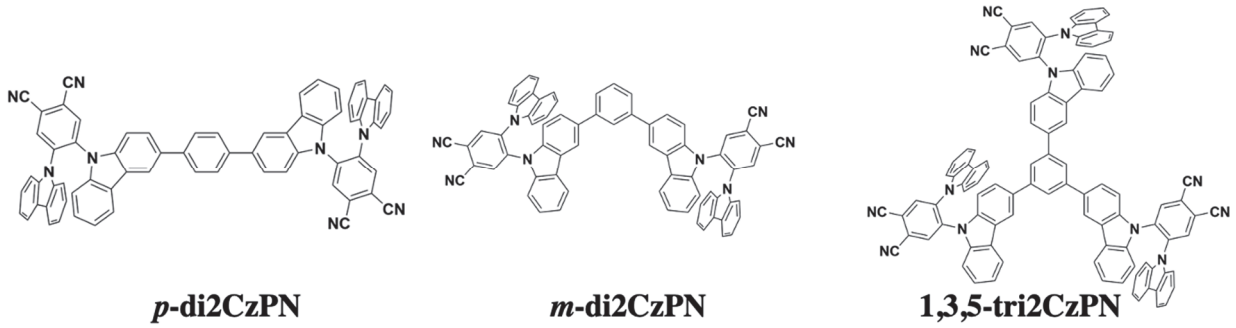


DICzTRZ

Figure 1. Molecular structures of **DICzTRZ**.

The second project disclosed 2 dual and 1 treble core TADF emitters, ***p*-di2CzPN**, ***m*-di2CzPN**, and **1,3,5-tri2CzPN (Figure 2)**. The three emitters exhibited nearly quantitative Φ_{PL} in toluene, of 98%, 96%, and 99%, with an emission maximum of 494 nm, 485 nm, and 483 nm, for ***p*-di2CzPN**, ***m*-di2CzPN**, and **1,3,5-tri2CzPN**, respectively, while those of reference material, **2CzPN** are only 28% and 475 nm, respectively. All materials exhibited TADF. Solution-processed devices for **1,3,5-tri2CzPN** were then fabricated, which showed sky-blue emission at λ_{EL} of 500 nm with CIE of (0.22, 0.44) and EQE_{max} of 7.1%.

Further collaboration between the University of St Andrews and Kyoto University is evidenced in the work from Tsuchiya *et al.*,[4] where we presented exact solution to model the exciton decay kinetics of TADF materials.



***p*-di2CzPN**　　***m*-di2CzPN**　　**1,3,5-tri2CzPN**

Figure 2. Molecular structures of ***p*-di2CzPN**, ***m*-di2CzPN**, and **1,3,5-tri2CzPN**.

References

(1) Crovini, E.; Zhang, Z.; Kusakabe, Y.; Ren, Y.; Wada, Y.; Naqvi, B. A.; Sahay, P.; Matulaitis, T.; Diesing, S.; Samuel, I. D. W.; Brütting, W.; Suzuki, K.; Kaji, H.; Bräse, S.; Zysman-Colman, E. *Beilstein J. Org. Chem.* **2021**, *17*, 2894–2905. doi:10.3762/bjoc.17.197

(2) Chen, D.; Kusakabe, Y.; Ren, Y.; Sun, D.; Rajamalli, P.; Wada, Y.; Suzuki, K.; Kaji, H.; Zysman-Colman, E. *J. Org. Chem.* **2021**, *86* (17), 11531–11544. doi:10.1021/acs.joc.1c01101

(3) Zhang, Z.; Crovini, E.; dos Santos, P. L.; Naqvi, B. A.; Cordes, D. B.; Slawin, A. M. Z.; Sahay, P.; Brütting, W.; Samuel, I. D. W.; Bräse, S.; Zysman-Colman, E. *Adv. Opt. Mater.* **2020**. doi:10.1002/adom.202001354

(4) Tsuchiya, Y.; Diesing, S.; Bencheikh, F.; Wada, Y.; dos Santos, P. L.; Kaji, H.; Zysman-Colman, E.; Samuel, I. D. W.; Adachi, C. *J. Phys. Chem. A* **2021**, *125* (36), 8074–8089. doi:10.1021/acs.jpca.1c04056

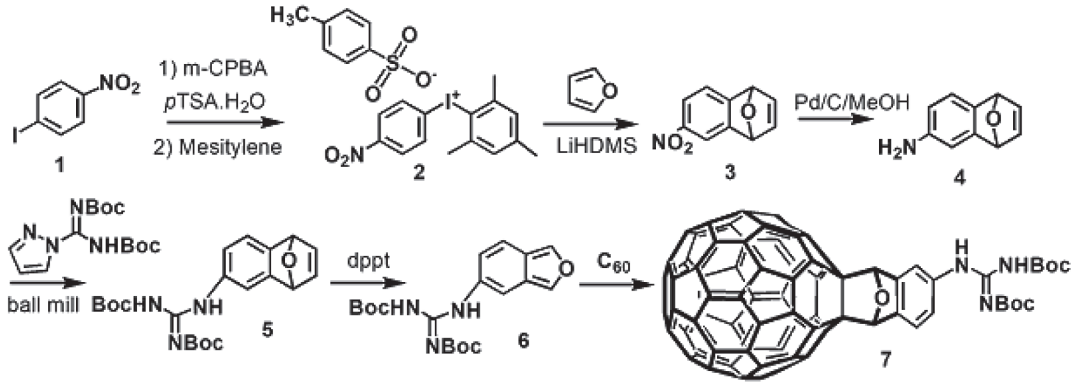
Exploration of Cycloaddition Properties of Guanidine Functionalized Isobenzofurans

Davor Margetic　Rudjer Boskovic Institute

Objectives

Synthesis of novel guanidinium isobenzofuran reagents and investigation of their reactivity for fullerene derivatization with partner ICR researcher Professor Murata Yasujiro.

Experimental results. Several synthetic routes to guanidino isobenzofuras (IBFs) were explored. Synthetically most viable procedure (Scheme 1) includes three-step reaction which afforded amino IBF precursor **4**, which in guanylation reaction carried out in ball mill mechanochemically using *N,N′*-bis-Boc-1-pyrazole-1-carboxamidine provided guanidine **5**. Boc-protected guanidino IBF **6** was prepared *in situ* by the addition of bis(4-pyridyl)-*s*-tetrazine and several experiments were carried out to investigate cycloaddition reactivity of **6**. With *N*-methylmaleimide mixtures of the exo/*endo* cycloadducts were provided, whereas reaction with fullerene C_{60} showed lower reactivity and afforded cycloadduct **7**. Fullerene also readily reacted with nitro-IBF and unsubstituted guanidine-IBF providing functional derivatives of **7**. All new products were spectroscopically fully determined (^{1}H, ^{13}C NMR, and IR).



Scheme 1

Theoretical results. Density functional (DFT) calculations using M062X/6-311+G** and M062X/6-311+G**//M062X/6-31G* models were carried out to predict reactivity of isobenzofuran-guanidine derivatives. Relative Diels-Alder reactivity of IBFs was estimated from the transition state calculations of reactions with two dienophiles (*N*-methylmaleimide and fullerene). Located TS structures correspond to concerted, synchronous [4π+2π] cycloaddition mechanism. Overall, activation energies for cycloadditions with C_{60} are higher than reactions with *N*-methylmaleimide, which is in accordance with experimental observations. Electron donating amino group on IBF lowers the activation energy (E_{act}), whereas guanidine substituents causes the increase of E_{act}.

Planned travel to ICR and lecture was not possible due to COVID-19 pandemic.

Development of hole transport materials for tin-perovskite and device characterization

Akinori Saeki　Osaka University

The outstanding nature of organic-inorganic metal halide perovskites has made these materials most suitable for optoelectronic applications such as perovskite solar cells (PSCs) and light-emitting diodes. The highly efficient perovskite material used in these devices is composed of an ABX_3 type three-dimensional (3D) structure, where A is an organic cation (such as methylammonium, MA; formamidinium, FA), an inorganic cation (such as cesium, Cs), or a mixture of both; B is a lead (Pb) cation; and X is a halogen anion (Cl, Br, I, or a mixture). The power conversion efficiency (PCE) of PSCs almost reaches that of crystalline silicon solar cells, and their applicability in the roll-to-roll solution process and fabrication on a flexible substrate are other notable advantages of PSCs over conventional inorganic solar cells. However, the use of toxic Pb, albeit in small amounts, as well as insufficient long-term stability against environmental conditions (moisture, oxygen, hot/cold) are critical issues for commercialization.

Along these lines, the composition of Ruddlesden-Popper two-dimensional (2D) perovskites described as $R_2A_{n-1}B_nX_{3n+1}$ (n = 1, 2, …, Fig. 1), form an immensely important part of PSC because the insulating layer introduced by R, bulky organic cations such as *n*-but ylammonium cation (BA) and 2-phenyl-ethylammonium cation (PEA), can prevent the intrusion of oxygen and moisture, thus improving the environmental stability compared to traditional 3D perovskites. By sacrificing enhanced stability, 2D perovskites have greater exciton binding energy owing to the formation of quantum wells, resulting in anisotropic charge transport paths. These situations lead to a strict requirement on the orientation and gradient of the 2D/3D component to achieve balanced PCE and improved stability of the PSC.

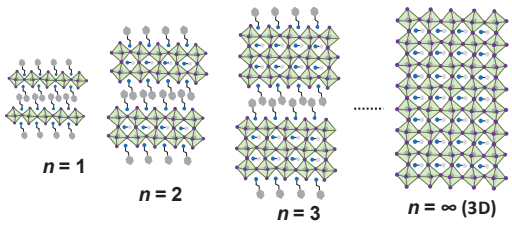


Fig. 1. 2D and 3D perovskite structures.

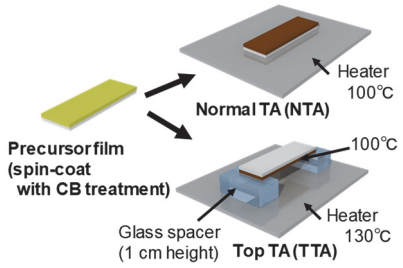


Fig. 2. Schematic of annealing: NTA and TTA.

We report the effect of top thermal annealing (TTA) on the PSC photoconductivity and performance, where TTA is a process that exposes heat from the top side (rather than the bottom (substrate) side in normal annealing) to form the perovskite layer after anti-solvent treatment (Fig. 2). The anisotropic photoconductivity in the in-plane and out-of-plane directions was evaluated, which suggested a vertical gradient of 2D/3D phases with a 3D-rich component on the surface.

[1] R. Shimono, R. Nishikubo, F. Ishiwari, A. Saeki, *J. Photopolym. Sci. Technol.* **2021**, *34*, 263.
[2] S. Hu, M. A. Truong, K. Otsuka, T. Handa, T. Yamada, R. Nishikubo, Y. Iwasaki, A. Saeki, R. Murdey, Y. Kanemitsu, A. Wakamiya, *Chem. Sci.* **2021**, *12*, 13513.

自己集合性含ホウ素化合物の合成、集合過程解明ならびに機能開拓

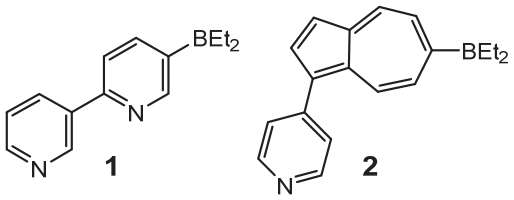
若林成知　鈴鹿医療科学大学

【緒言】

我々はボリルピリジンにおける分子間ホウ素－窒素配位結合に着目し幾つかの自己集合体を構築し、超分子構築におけるユニット分子としての役割を明らかにしてきた。動的平衡過程を有する自己集合性ボリルピリジンには、ゲスト誘起の自己集合という、誘起適合の分子認識の実現が期待される。また非交互系のアズレン骨格を導入したボリルピリジンが集合した超分子には、動的挙動にキラリティーや分子間相互作用によるキラルな高次構造が誘起されるなら、その光学活性を活かした機能性材料への応用が期待される。本研究では化学研究所の大木靖弘教授と共同し、これら新たなボリルピリジン類の設計、合成と基本的性質の検討に取り組んだ。

【結果と考察】

本研究で研究対象としたボリルピリジンは､化合物 **1**, **2** である。**1** の合成は対応する臭素体から *n*-BuLi と Et_2OMe を用いフローマイクロ法により 85%の高収率で達成することができた。



化合物 **1** は各種スペクトル測定、VPO から、環状 3 量体と 4 量体の平衡混合物を生じている。3 量体の比率は溶媒の極性を上げると、42% (重ベンゼン中) から 76% (重アセトン中) に増加した。3 量体の双極子モーメント (3.5D) が 4 量体のそれ (1.3D) に比べ大きいことに起因すると考えられる。**1** のベンゼン溶液とヘキサンとの蒸気拡散平衡法 (7 ℃) により析出した単結晶を X 線結晶構造解析すると、環状 4 量体 $\mathbf{1}_4 \cdot (C_6H_6)_2$ が得られた (**Figure 1**)。ベンゼン 1 分子が CH/π 相互作用により包接され､もう 1 分子のベンゼンは結晶の隙間を埋めている｡**1** の多量体間の平衡は濃度を上げると 4 量体側に片寄ることから、4 量体を主として含む濃厚溶液から 4 量体が優先して結晶化した結果と考えられる。

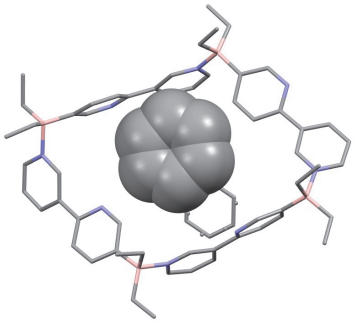


Figure 1. Crystal structure of a cyclic tetramer of compound **1** with a molecule of benzene.

次に、ホウ素原子との配位結合に関わっていないピリジン窒素原子との相互作用を期待し包接実験を行った。メタノール、安息香酸などの添加実験においては、^{1}H NMR スペクトルに全く変化は認められなかった。これらの化合物とホウ素から離れたピリジン窒素の α 位水素との立体反発のためと考えられる。一方、白金錯体やホウ酸との反応では、単量体との錯体が得られ、環状構造を保持したままでの金属イオンの配位は困難であることが示唆された。

【成果報告】若林成知，脇岡正幸，大木靖弘，宅見正浩，永木愛一郎，第 31 回基礎有機化学討論会，2P007，筑波（オンライン），2021.

ジベンゾフェナジンを電子アクセプターとするスルースペース電荷移動型熱活性化遅延蛍光材料の創製

武田洋平　大阪大学

目的：本研究課題では、研究代表者（武田）がこれまでに独自に展開してきた熱活性化遅延蛍光（thermally activated delayed fluorescence: TADF）材料研究（総合論文）：*Chem. Commun.* **2020**, *56*, 8884）を飛躍的に発展・深化させるために、武田の得意とする電子アクセプター合成技術を活用して、共同研究者である梶らが得意とするスルースペース電荷移動（through-space charge transfer: TSCT）型 TADF 材料設計指針ならびに光物性評価技術を融合させ、高効率な新奇 TADF 材料を創製し、有機 EL 発光素子へと応用することを目的とした。

実験方法：研究代表（武田）が独自に開発した含窒素芳香環分子を電子アクセプター（A）として採用し、適切な距離（3.7 Å）を保つことのできるπリンカーを介して、トリアリールアミン骨格を有する電子ドナー(D)と連結した分子を設計し、有機合成化学的手法を用いて合成し、基礎的な光物性を調査した。

実験結果および考察：市販されている化合物から６ステップでドナー及びπリンカーを有するユニットの合成ルートの確立を成功した。さらに、これと電子アクセプターユニットとを、Pd 触媒を用いるカップリング反応により連結させ、目的分子を良好な収率で合成することに成功した。^{1}H NMR スペクトルを測定したところ、D ユニットおよび A ユニットの一部の水素核が単独のユニットよりも高磁場側に観測されたことから、溶液中に置いて D 及び A 平面が対面して重なり配座をとっていることが示唆された。また、様々な極性を持つ有機溶媒中における吸収・発光スペクトルを調査したところ、吸収スペクトルは極性に依存することなく重なりの良いスペクトルを示したのに対して、発光スペクトルにおいては、溶媒極性の増大に伴って顕著に発光波長の長波長化およびスペクトルのブロード化が観測されたことから、本発光は空間を通じた電荷移動により生じた励起状態からの輻射であることがわかった。以上のように、本研究では、新規な TSCT 型分子の合成に成功し、その基礎的な光物性を明らかにした。今後、詳細な時間分解分光測定及び有機 EL 素子による評価を行って行く予定である。

成果報告：特になし。

Chiral Silica with preferred-handed helical structure via chiral transfer

Tomoyasu Hirai　Osaka Institute of Technology

Chiral silica has attracted considerable attention in the various kinds of fields such as catalysis, templating, chiral recognition and so on. These materials are generally prepared by sol-gel transcription using an organic chiral molecule as a template. This process, however, requires tedious reaction steps. To overcome this problem, we focused on stereoregular polymer with polyhedral oligomeric silsesquioxane (POSS) side chain.

We designed and synthesized novel isotactic POSS-containing polymethacrylate (*it*-PMAPOSS) using living anionic polymerization method[1]. To control the secondary structure, *it*-PMAPOSS thus obtained was mixed with (*R*) or (*S*)-binaphthol derivatives (*R* or *S*-BN). Figure 1a shows a vibrational circular dichroism (VCD) spectrum of *it*-PMAPOSS with enantiomeric BNs. Specific split-type and mirror-image VCD signals were observed in *it*-PMAPOSS with enantiomeric BN at 1730 cm^{-1} corresponding to carbonyl stretching in the ester group of PMAPOSS. Though several IR peaks ranging from 1000 to 1250 cm^{-1} overlapped, clear split-type Cotton effects on C-O-C (1050-1250 cm^{-1}) and asymmetric Si-O-Si (1000-1240 cm^{-1}) vibrations could be observed. This result suggests that *it*-PMAPOSS formed preferred-handed helical conformation.

Based on this knowledge, we calcinated the mixture of *it*-PMAPOSS and enantiomeric BNs at 600°C under air atmosphere and the residue thus obtained was evaluated using VCD. Interestingly, the split-type Cotton effect could still be observed on the Si-O-Si vibration region and was more striking than that of the unannealed one, indicating that silica with optical activity could be successfully prepared. Figure 1b shows the transmission electron microscopy (TEM) image of the calcinated sample. A helical structure with the preferred handedness was clearly observed in each calcinated samples. We prepared chiral silica using polymer with well-controlled stereoregularity as a template.

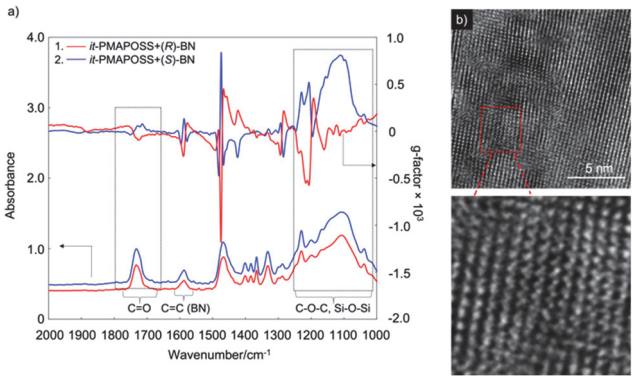


Figure 1 a) VCD spectrum of *it*-PMAPOSS with enantiomeric BNs. b) TEM image of chiral silica prepared from *it*-PMAPOSS with (*R*)-BN.

Achievements:

1. *JACS Au*, **2021**, *1*, 375.
2. *ACC. Mater. Surf. Res*., **2021**, *6*, 132.
3. *J. Polym. Sci.,* **2022**, in press. DOI: 10.1002/pol.20210761

高効率光電変換を志向した非対称型有機半導体分子の開発

鈴木充朗　大阪大学

【研究目的】

有機太陽電池（OPV）材料の分子設計に関し、非対称性を適切に導入することにより電荷キャリアの再結合が低減され、光電変換効率（PCE）の向上につながる可能性が指摘されている。しかし、非対称型 OPV 分子について系統的に評価した報告例は極めて限定的であり、広く適用可能な分子設計指針はいまだ確立されていない。そこで我々は、高効率光電変換を実現するために必要な分子構造要件の明確化を目指し、現在、「非対称性」を鍵とする新規有機半導体分子の設計と評価に取り組んでいる。本研究ではその端緒として、diketopyrrolopyrrole（DPP）のダイマーを中心骨格とする 2 種類のアクセプター分子について比較評価を行った。

【実験と結果】

評価対象とするアクセプター分子 **1** および **2**（Figure 1）は、対応する DPP ダイマーの monoformyl 体および diformyl 体と malononitrile との脱水縮合により合成した。実験的に見積もった HOMO/LUMO 準位は、化合物 **1**、**2** でそれぞれ –5.6/–4.2 eV、–5.8/–4.5 eV となり、いずれも OPV 中でアクセプター材料として機能するために十分低い LUMO 準位をもつことが確認された（Figure 2）。実際に P3HT をドナー材料とするバルクヘテロ接合型 OPV を作製し性能を評価したところ、非対称型分子 **1** を用いた場合の方が対称型分子 **2** を用いた場合に比べて約 1.8 倍高い短絡電流密度（J_{SC}）を示した。一方で、解放電圧（V_{OC}）と曲線因子（FF）は対称型分子 **2** を用いた場合の方が高く、結果として PCE は二つの素子でほぼ等しい値となった。

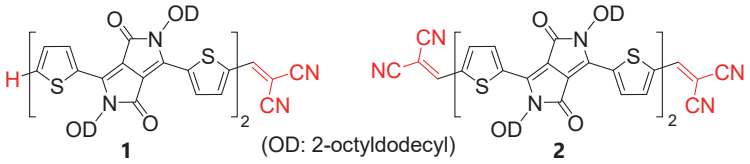


Figure 1. Chemical structures of DPP-based acceptor compounds **1** and **2**.

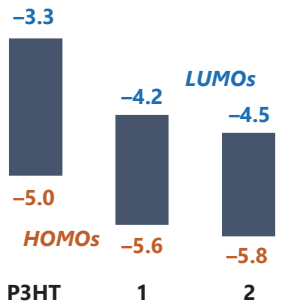


Figure 2. Frontier orbital energy levels.

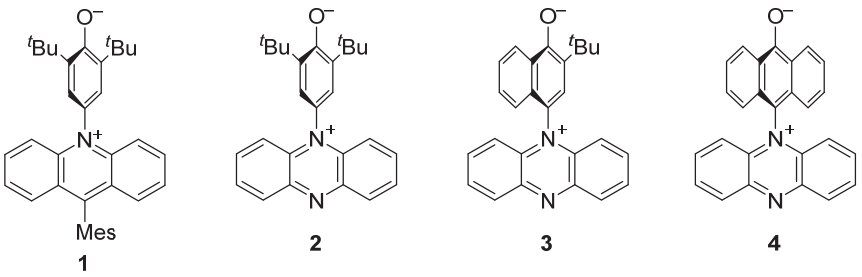
【考察】

化合物 **1** の方が **2** よりも高い J_{SC} を与えたことから、短絡条件では電荷キャリアの生成から取り出しまでのトータル効率において前者のほうが優れると考えられる。しかしながら、V_{OC} や FF は **2** を用いた場合の方が高いことから、分子構造の非対称化がキャリア再結合の抑制につながったとは必ずしも言えない。今後、光電変換プロセスの素過程を切り分けて解析し、非対称化の効果を詳細に評価する予定である。

ソルバトクロミズムを示さないπ共役双性イオンの合成と物性

清水章弘　大阪大学

【目的】HOMO と LUMO のエネルギー差 (ΔE_{HL}) の小さな分子は興味深い光学的・電気化学的特性を示す。我々は高い HOMO 準位をもつ電子ドナー性のアニオンと低い LUMO 準位をもつ電子アクセプター性のカチオンから構成されるπ共役双性イオン **1** と **2** を設計・合成し、比較的小さなπ電子系でありながら、ΔE_{HL} が約 1 eV と非常に小さく、1000 nm 以上に吸収を有することを明らかにしている (*J. Org. Chem.* **2021**, *86*, 770–781.)。興味深いことに、**1** がπ共役双性イオンに特徴的な、大きな負のソルバトクロミズムを示すのに対し、**2** はソルバトクロミズムを示さないことを見出した。本研究では、この原因を明らかにすることを目的として、**3** および **4** を合成し、電子状態と物性を明らかにした。



【結果と考察】**3**, **4** を合成し、X 線結晶構造解析等により同定した。**3** と **4** の電子ドナー性のアニオン部位と電子アクセプター性のカチオン部位の二面角はそれぞれ 57°、68° であり、**2** (53°) より大きいことから、アニオンとカチオンの相互作用が弱いことが示唆された。**3**, **4** はラジカルカチオンへの酸化とラジカルアニオンへの還元に対応する両性の酸化還元特性を示し、酸化電位と還元電位の差から、ΔE_{HL} は **2** (0.87 eV)、**3** (0.69 eV)、**4** (0.54 eV) の順に小さくなることがわかった。これは、二面角が大きくなって相互作用が弱くなることにより、ΔE_{HL} が小さくなるためであると考えられる。

UV-vis-NIR スペクトルを測定したところ、ジクロロメタン中における吸収波長は、**2** (1068 nm)、**3** (1277 nm)、**4** (1637 nm) の順に長くなることがわかった。また、様々な極性の溶媒中 (トルエン、クロロベンゼン、ジクロロメタン、ジメチルスルホキシド) で測定を行ったところ、**2** と同様に、**3** と **4** の吸収波長もほとんど変化しなかった。ソルバトクロミズムを示す **1** の結晶構造における二面角は 69° であり、ほぼ同じ大きさの二面角を有する **4** がソルバトクロミズムを示さないことから、二面角以外の影響が大きいことが実験的に明らかになった。今後、この原因について、量子化学計算等も用いて明らかにする予定である。

Host-Guest Complexation of Cyclohexa-2,7-anthrylene Ethynylene Derivatives with [*n*]CPP

Kenji Kobayashi Shizuoka University

Recently, we have successfully synthesized macrocycle **1a** and found that **1a** exists as a monomeric form and size-specifically encapsulates a cyclic *p*-phenylene 9-member [9]CPP that matches the internal pore size of **1a** (Fig. 1a, b). In this study, we synthesized a macrocycle **2a** in which two of the six acetylene bonds of **1a** at the diagonal position are replaced by butadiyne bonds, and a macrocycle **1b** in which the bulkiness of the side chain is slightly smaller than that of **1a** (Fig. 1a). Here, we report the properties of **2a** and **1b**.

The absorption and emission maxima of **2a** were red-shifted slightly than those of **1a** ($\Delta\lambda_{max}$(abs) = 4 nm, $\Delta\lambda_{max}$(em) = 7 nm), due to π-conjugate expansion of **2a**. In addition, unlike **1a**, **2a** was found to encapsulate [10]CPP in a size-specific manner (Fig. 1c, K_a = 3,170 M^{-1} in $CDCl_3$ at 298 K).

Unlike **1a** and **2a**, which behave as monomers, **1b** was found to self-assemble into a π-stacked dimer (**1b**)$_2$ (Fig. 2). The ^{1}H NMR signals of the π-stacked dimer (**1b**)$_2$ and monomer **1b** did not average, the signals of (**1b**)$_2$ were shifted upfield than those of monomer **1b**, due to its own shielding effect. The self-association constant of (**1b**)$_2$ was estimated to be K_a = 3,560 M^{-1} in $CDCl_3$ at 298 K. The π-stacked dimer (**1b**)$_2$ also encapsulates [9]CPP, and each K_a value of the four equilibrium states at 318 K was calculated (Fig. 2). The K_a of (**1b**)$_2$ was found to increase substantially in the presence of [9]CPP ($K_a(4)/K_a(1) \approx 42.8$), and the [9]CPP inclusion association constant of (**1b**)$_2$ was found to increase substantially more than the K_a of the monomer **1b** ($K_a(3)/K_a(2) \approx 42.7$).

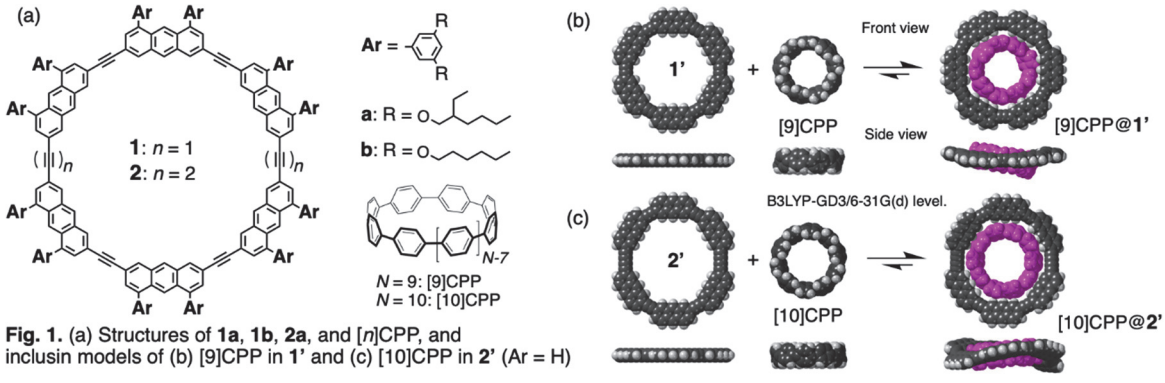


Fig. 1. (a) Structures of **1a**, **1b**, **2a**, and [*n*]CPP, and inclusin models of (b) [9]CPP in **1'** and (c) [10]CPP in **2'** (Ar = H)

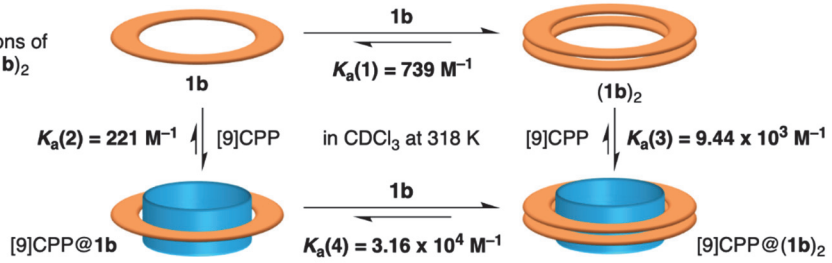


Fig. 2. Schematic representations of formation of π-stacked dimer (**1b**)$_2$ and its inclusion of [9]CPP, and the K_a values of the four equilibrium states

超分岐構造高分子の滑剤作用の解明と最適化

髙橋裕　東北大学

【目的】高分子は潤滑油の添加剤として使用され、その多くは直鎖状構造である。また、直鎖状高分子であるため、潤滑油の粘度を増加させてしまう。共振ずり測定は、高分子ブラシの潤滑性やゲルの表面粘弾性など、高分子材料の特性評価に用いることができる。本研究では潤滑油の基油に PAO401 用いて、潤滑油の添加剤としての超分岐構造高分子の特性を明らかにすることを目的とした。また、分岐構造が潤滑性に及ぼす影響について，直鎖状構造との比較により検討した。

【方法】直鎖状および超分岐構造高分子は制御されたラジカル重合により合成された（共同研究者の登阪准教授の担当）。合成した高分子はPAO401に溶解させた。雲母表面の間に閉じ込められた潤滑油の特性は，共振ずり測定によって評価した（**Fig. 1**）。

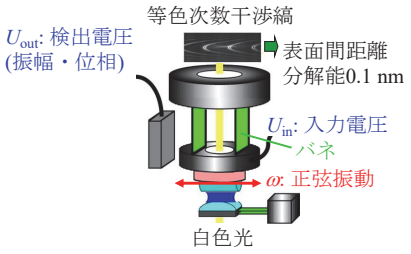


Fig. 1　共振ずり測定装置の模式図。

【結果】合成した高分子の PAO401 への溶解性は、紫外可視分光光度計を用いて評価した。直鎖状および超分岐構造高分子は、室温では PAO401 に溶解しなかったが、40 ℃以上では完全に溶解した。**Fig. 2** は、高分子添加剤を溶解させた潤滑油の様々な荷重（L）における共振ずり測定の結果を示している。空気中で雲母同士が接触している状態（MC、摺動なし）を基準ピークとしたとき、ピーク振幅（U_{out}/U_{in}）は試料の潤滑性を評価するために使用することができる。MC ピークに対する振幅比について、直鎖状高分子と超分岐構造高分子を比較すると、超分岐構造の方が小さい値であった。これは、超分岐構造の方が直鎖状に比べ優れた潤滑性を有していることを示す。さらに、潤滑油の溶液粘度を共振ずり測定に基づいて開発した超微量粘度計で測定をした。超分岐構造高分子の PAO401 溶液の粘度は、直鎖状高分子のそれに比べわずかに低く、PAO401 単独の粘度とほぼ同じであった。これらの共振ずり測定結果は，超分岐構造高分子が直鎖状高分子よりも潤滑性が高く，低粘度であることを明らかにした。

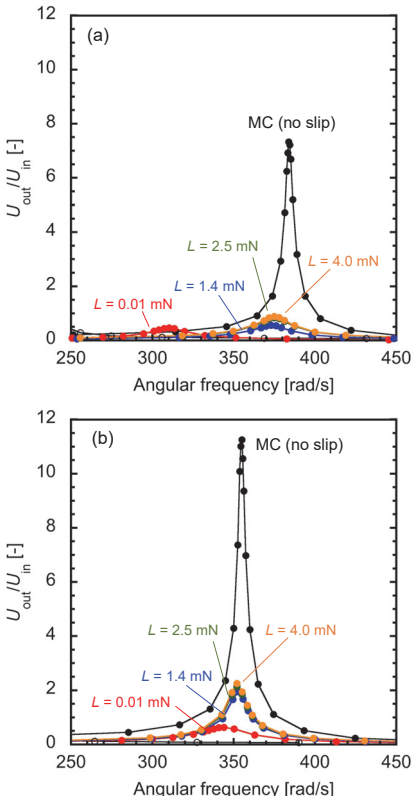


Fig. 2　(a) 超分岐構造および (b) 直鎖状高分子を溶解した潤滑油の共振ずり測定の結果。

【研究成果】これらの研究成果については、第 71 回高分子学会年次大会にて発表予定である。

Trace metal elemental and isotopic composition in the North Pacific Ocean: sources and internal cycling (2)

Tung-Yuan Ho　Academia Sinica

Objectives:

The major objective of this joint study is to investigate the sources and internal cycling of dissolved and particulate trace metals in the water column of the Northwestern and subarctic Pacific Ocean and to evaluate the impacts of lithogenic and anthropogenic aerosols originating from East Asia on the processes. My host at ICR, Kyoto University, is Prof. Yoshiki Sohrin.

Methods:

My laboratory has joined two Japanese GEOTRACES cruises, KH11-7 and KH15-3, with Prof. Yoshiki Sohrin's and other Japanese research groups in the subarctic North Pacific Ocean. Seawater and particulate samples in the oceanic regions were taken on the cruises. Both dissolved and suspended particulate samples were collected for trace metal elemental and isotopic composition analysis. Elemental and isotopic composition of trace metals were determined by HR-ICPMS and MC-ICPMS, respectively. The detailed information of the sampling and pretreatment are described in the following two published papers.

Result and Discussions:

The details of the results and discussions are described in the following two papers. Chih-Chiang Hsieh, my Ph.D. student, has already finished the measurement of Fe isotopic composition in the samples and is preparing a manuscript. In brief, although we have observed lighter Fe isotopic composition in the suspended particles, the quantitative c ontribution of anthropogenic aerosol Fe is smaller than what we expected in the oceanic region (Hsieh et al. in prep).

Publications:

Again, due to the impact of Covid-19, it was pity that I could not visit ICR, Kyoto University in 2021. However, Prof. Sohrin's and my laboratory members have still kept close interaction in the research topics. During the past year, we have published the following two papers. One paper is under review (Takano et al. *Marine Chemistry*, minor revision); two more papers are under preparation.

Liao, W.-H., S. Takano, H.-A. Tian, H.-Y. Chen, **Y. Sohrin**, and **T.-Y. Ho*** (2021) Zn elemental and isotopic features in sinking particles of the South China Sea: Implications for its sources and sinks. *Geochimica et Cosmochimica Acta* doi: 10.1016/j.gca.2021.09.013

Zheng*, L., T. Minami, S. Takano, **T.-Y. Ho**, and **Y. Sohrin** (2021) Sectional distribution patterns of Cd, Ni, Zn, and Cu in the North Pacific Ocean: relationships to Nutrients and importance of scavenging.*Global Biogeochemical Cycles*doi: 10.1029/2020GB006558.

Resolving the structure-dynamics-property relationship in polymer nanocomposites under uniaxial stretching

Tadanori Koga　Stony Brook University

Objective. The addition of nanoparticles (NPs) to polymer matrices is a simple route to improving mechanical properties and designing next generation polymer nanocomposites (PNCs). The key role in this phenomenon is ascribed to polymer chains (physically) adsorbed on the NP surface ("bound polymer") that act as *tight* polymer-mediated bridges between neighboring NPs at high NP loadings above the percolation threshold, leading to a network-like microstructure that reinforces the PNCs as a large-scale skeleton. However, little is known about the effects of external stimuli on the structure-dynamics-property relationship, which is crucial in developing next generation engineered PNCs. To tackle this, we aim to understand the structures and dynamics of NP network in the polymer melts using X-ray photon correlation spectroscopy (XPCS) under uniaxial stretching as a function of temperature, filler loading, and molecular weights of the matrix polymer. Here we report the feasibility test of the proposed "rheo-XPCS" measurements with calcium carbonate (the size of 30 nm, the filler loading (x) =20%, which is above the gel point ($x_c \approx$ 16 vol%)) filled cross-linked silicone elastomer.

Experimental. In recent years, XPCS has emerged as a powerful probe for gaining direct insight into the microstructural dynamics (on length scales up to a few hundreds of nm) that are relevant to soft material's rheology. XPCS probes the dynamics over a wide range of timescales ($10^{-3} < t < 10^{3}$ seconds that is commensurate with the time window for rheology), allowing the characterization of internal relaxation processes associated with viscous flow, mechanical stress, and cross-linking. When the structure and corresponding dynamics of NPs change ("out-of-equilibrium") on the time scale of experiments, a one-time correlation function, which describes the equilibrium dynamics of NPs[1], does not correctly describe such a phenomenon. Therefore, a two-time correlation function $C(q, t_1, t_2)$[2] is necessary, which defines the intensity-intensity autocorrelation for any respective times t_1 and t_2 in the time series. The details have been described elsewhere.[3] The corresponding g_2 function was then fit with a KWW function (i.e., $g_2(q,t^*) = c + \beta\left(exp(-2(\Gamma t^*)^{\alpha})\right)$, where β is the Siegert factor (0.14 - 0.18, dependig on X-ray optics) and c is the baseline (=1)). The relaxation rate Γ was determined as a function of q. The PNCs were subjected to uniaxial elongation at room temperature.

Results. Fig. 1 shows preliminary stress relaxation (at constant strain, γ) results for the cross-linked calcium carbonate filled silicone elastomer. The strain was fixed to γ=1% (in the linear response range confirmed by independent stress-strain curve experiments) and the data represents in the direction perpendicular to the stretching direction. We collected the XPCS speckle patterns over the q range of 0.01 $nm^{-1} < q < 0.2$ nm^{-1} that covered the primary peak position q^* corresponding to the interparticle spacing of the fillers. We found that the g_2 functions can be expressed by a KWW function with $\alpha \approx$ 1.5 (i.e., a compressed exponential form) and the relaxation rate Γ scales with q (i.e., $\Gamma \propto q$) (data not shown), both of which are fingerprints of slow relaxation in jammed systems. The local speed of percolated network ($V_p = \Gamma/q$) was then determined accordingly. Hence the preliminary data demonstrates the feasibility of rheo-XPCS to quantify the local filler dynamics during stress relaxation. The azimuthal angle (φ)-dependence of XPCS data is being checked since the filler dynamics induced by tensile strain are expected to be anisotropic. In addition to the dynamics, the microstructure of fillers is being resolved through the analysis of SAXS intensity as a function of φ, since filler network may not follow affine deformation. The structural and dynamical information will be directly linked to the macroscopic stress relaxation data where logarithmic-scale stress relaxation over time is expected.

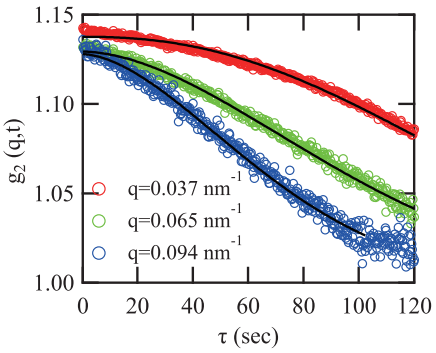


Fig. 1. g_2 functions for the cross-linked calcium carbonate filled silicone elastomer at room temperature at γ =5% in the vorticity direction. The solid lines are the best fits of a KWW function with $\alpha \approx$ 1.5.

References

1. Yavitt, B. M.; Salatto, D.; Zhou, Y.; Huang, Z.; Endoh, M. K.; Wiegart, L.; Bocharova, V.; Ribbe, A. E.; Sokolov, A. P.; Schweizer, K. S.; Koga, T., Collective Nanoparticle Dynamics Associated with Bridging Network Formation in Model Polymer Nanocomposites, *ACS Nano*, 15, 11501-11513, 2021.
2. Madsen, A.; Leheny, R. L.; Guo, H.; Sprung, M.; Czakkel, O., Beyond Simple Exponential Correlation Functions and Equilibrium Dynamics in X-Ray Photon Correlation Spectroscopy., *New J. Phys.*, 12, 055001, 2010.
3. Yavitt, B. M.; Wiegart, L.; Salatto, D.; Huang, Z.; Endoh, M. K.; Poeller, S.; Petrash, S.; Koga, T., Structural dynamics in UV curable resins resolved by in situ 3D printing X-ray photon correlation spectroscopy, *ACS Appl. Polym. Mater.*, 2, 4096-4108, 2020.

Development of simulation scheme for wall-slip of polymers

Giovanni Ianniruberto　Università degli Studi di Napoli “Federico II”

Wall-slip of polymers is a long-standing and challenging problem in polymer science and industry. In industrial polymer processing, there are a lot of practical problems induced by the wall-slip, such as the shark-skin. While extensive studies have been made, the capability of conventional theoretical/computational methods is rather limited at present. Due to the huge computational cost, it is difficult to use molecular dynamics simulations for practical wall-slip problems. On the other hand, while the mean-field theories (e.g., the tube model) have attained success in polymer rheology, these theories have fundamental difficulties to address interfacial phenomena. In summary, there is no practical method to predict/reproduce the wall-slip for industrial polymers.

In this project, we will attempt to develop a mesoscopic multi-chain model to reproduce polymer dynamics at the interface between polymeric liquids and the solid wall under fast shear flow. Furthermore, to construct a practical simulation method for wall-slip of polymers, we will incorporate the mesoscopic model into the macroscopic fluid simulation method, i.e., the smoothed particle hydrodynamics (SPH). The team members have been separately developing mesoscopic models for bulk polymers and attained success to reproduce the rheological properties. We have been working on modeling entangled polymer dynamics [1]. The Masubuchi group at Nagoya University has been working on several multi-chain simulation methods for entangled polymers. On the other hand, Takeshi Sato in the molecular rheology group at ICR has been working on the development of the SPH technique.

In this year, due to the difficulty related to the COVID19, our group and the molecular rheology group have independently conducted the research activity while sharing information. We have developed the multi-chain slip-link model to address the wall-slip of entangled polymers in collaboration with the Masubuchi group [2]. In this model, the effect of the wall-slip is artificially incorporated into the multi-chain slip-link model originally developed to reproduce entangled polymer dynamics (without the wall-slip). The results obtained by this model are in qualitative agreement with experimental results. Our ICR partner Takeshi Sato has improved the simulation code of SPH for efficient flow simulations. In the future, we hope to unify these models for the further understanding of the wall-slip of polymers.

References:

[1] Y. Masubuchi, J. Takimoto, K. Koyama, G. Ianniruberto, G. Marrucci, and F. Greco, *J Chem. Phys.*, **115**, 4387 (2001).

[2] Y. Masubuchi, D. Vlassopoulos, G. Ianniruberto, and G. Marrucci, *J. Rheol.*, **65**, 213 (2021).

High Frequency Response of Polymeric Liquids: Rheology and Dielectric Relaxation

Sathish K. Sukumaran　Yamagata University

The response of polymeric liquids to imposed fields is investigated using experiments typically performed under isothermal conditions. It is assumed that the imposed field does not affect the system temperature, which continues to remain uniform throughout the system. The theoretical analyses correspondingly employs isothermal response functions. If thermal equilibration is hindered due to the imposed field, the assumptions of constant and uniform temperature might become invalid. This might be the case for the response at high frequencies/short times. In this case, the adiabatic response functions might be more appropriate. To investigate this problem, the experimental and theoretical expertise of ICR (Sato, Watanabe, Matsumiya), and the computational, theoretical and experimental expertise of international (Ramirez, Madrid; Tassieri, Glasgow) and domestic (Masubuchi, Nagoya) researchers have been combined to form a collaboration between ICR and several international and domestic research partners.

The effect of imposing isothermal and adiabatic conditions on the linear rheology of an unentangled (short chain) polymer melt was investigated. For simplicity, the polymer chains were modelled as beads connected by springs and their motion simulated using molecular dynamics (Kremer-Grest model). The isothermal simulations were performed by controlling the temperature using a Langevin thermostat (NVT). In the adiabatic simulations, the system was decoupled from the thermostat thereby preventing energy exchange and thermal equilibration. Oscillatory shear deformation, with an amplitude sufficiently small for the response to remain in the linear regime, was imposed at several frequencies. We found that the obtained storage modulus, G’, and the loss modulus, G’’, under both the isothermal and the adiabatic conditions were rather close to each other. This implied that the imposed conditions had negligible effect on the relaxation times or equivalently, the dynamics of the polymer chains, at least in the linear regime investigated here. Under adiabatic conditions however, the system temperature progressively increased with time and the temperature increase under high frequency oscillatory shear deformation was significantly larger than under low frequencies. Needless to add, the increase in temperature under adiabatic conditions cannot be sustained indefinitely without affecting both the state of the system and its response to the external field. For instance, the system might undergo a change in state due to the heat generated by the imposed oscillatory shear deformation. We are currently investigating the response when the shear (oscillatory and step) is applied for longer times. Based on these results, we plan to investigate the more interesting but more difficult nonlinear response regime in the future.

Molecular understanding on the structures and dynamics of end-modified polymers.

Visit Vao-soongnern　Suranaree University of Technology

For high-*cis* linear polyisoprene (PI) head-modified with an associative metal-carboxylate (salt) group, PI30-COOM with M = Li, Na, and K, we have conducted linear viscoelastic and dielectric measurements to examine an effect(s) of the head-to-head association on the chain dynamics.[1] The molecular weight of the PI30-COOM chains was high enough ($M = 30.5\times10^3$) compared to the entanglement molecular weight for PI ($M_e = 5.0\times10^3$), and their slow dynamics was governed by the entanglement relaxation. Those chains had type-A dipoles so that their large-scale dynamics was reflected in both viscoelastic and dielectric data at low angular frequencies ω. The salt groups associate and dissociate (without ionization) with a rate that changes with the temperature T, as known for ionomers having non-polar backbones.[2] Correspondingly, PI30-COOM exhibited failure of the time-temperature superposition for both viscoelastic and dielectric data.

This failure was characterized through comparison with non-associative reference homo-PI, the PI30 unimer (a precursor of PI30-COOM), $(PI30)_2$ dimer, and $(PI30)_6$ star-type hexamer. The viscoelastic data of PI30-COOLi at low and intermediate T (−20˚ and 20˚C), respectively, were found to be close to those of the star-hexamer and dimer data in the iso-frictional state (defined for monomeric segments), and a further increase of T resulted in deviation from the dimer data toward the unimer data, as noted for the ω dependence of the storage modulus $G'(\omega)$ data shown in Figure 1. This "crossover" was observed also for PI30-COONa and PI30-COOK but at lower T,[1] which possibly reflected a barrier for the dissociation of the COOM groups lowering in the order of COOLi > COONa > COOK. The decrease of the real part of dielectric permittivity from the static state, $\Delta\varepsilon'(\omega) = \varepsilon'(0)-\varepsilon'(\omega)$, and the imaginary part (dielectric loss), $\varepsilon''(\omega)$, measured for PI-COOLi are shown in Figure 2. These dielectric data exhibit a crossover similar to that seen for $G'(\omega)$ but at higher T compared to the latter. This difference between the viscoelastic and dielectric behavior can be related to the dynamic tube dilation mechanism that affects the viscoelastic data more significantly than the dielectric data[3] and also to the conformation exchange[4] (motional coupling) among the PI30-COOLi chains dynamically coexisting in different association forms, the unimer, dimer, and star-like multimers.[1]

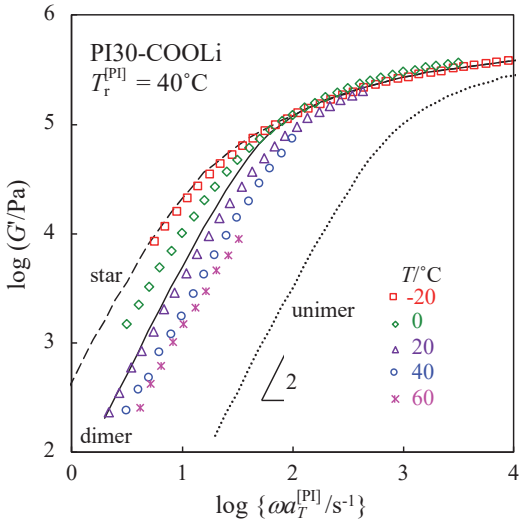


Fig.1 Viscoelastic behavior of PI30-COOLi.

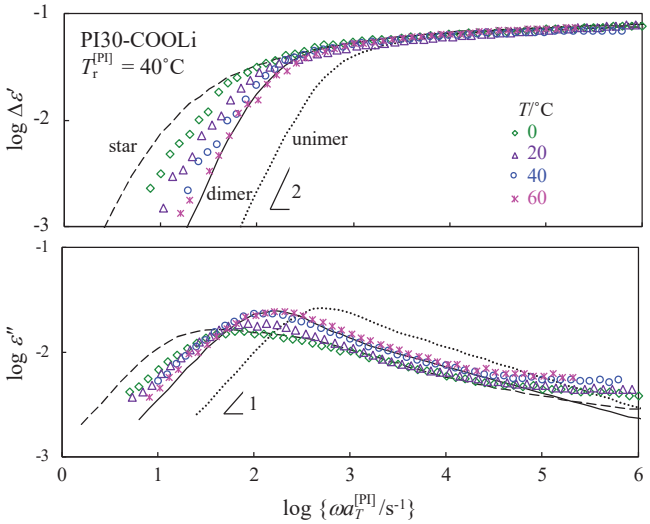


Fig.2 Dielectric behavior of PI30-COOLi.

References

1) Y. Matsumiya, H. Watanabe, N. Sukhonthamethirat, and V. Vao-soongnern, *J. Soc. Rheol. Japan*, *49*, 181 (2021).
2) Z. Zhang, Q. Chen, and R. H. Colby, *Soft Matter*, *14*, 2961 (2018).
3) Y. Matsumiya and H. Watanabe, *Rubber Chem. Technol.*, *93*, 22 (2020).
4) H. Watanabe, Y. Matsumiya, and Y. Kwon, *J. Rheol.*, *61*, 1151 (2017).

光エネルギー変換に対する振電効果：固体 NMR と時間分解 EPR の連携による解明

小堀康博　神戸大学

序：本研究では、磁気共鳴分光法を主たる手法とし、有機系分子を中心とした次世代の光エネルギー変換材料の創成に向け、分子機構の解明が重要な有機薄膜系や連結系において、動的エキシトンによるスピン系相互作用をオングストローム領域の三次元映像で可視化し、三重項励起子や電荷分離立体構造による動的機構･電子状態を明らかにした。梶らと連携して過渡種の運動性を特徴づけ、電子スピン分極の三次元画像から、時々刻々変化する励起子対、光電荷分離状態の立体配置、運動性による磁気的相互作用の変化を映像化すると共に、電子的カップリングを定量化している。[1] 結晶性と非晶性を併せ持つ有機エレクトロニクス薄膜や有機光触媒のエントロピー効果と運動による電子的効果を用いるデバイス効率飛躍的向上化の知的基盤を獲得し、有機薄膜太陽電池や有機発光素子(OLED)開発で課題となっている超高効率化への指針を提示[1]することができるようになってきた。

実験方法・結果と考察：共同研究者の梶 弘典先生との研究では、高効率な OLED 特性を示す、アクリダン-トリアジン系の熱活性化遅延蛍光材料 MA-TA を対象とし、時間分解電子スピン共鳴（TREPR）法を用いて光照射直後に生成する励起状態の観測と解析を行った。三重項励起子による電子スピン分極の効果を解析することによって中間体励起子の立体構造を図 1 のように決定した。さらにスピン格子緩和時間に対する分子異方性の情報も得ることができた。これにより、アダマンチル基の結合軸回りに対する分子回転運動(図 1)による動的ゆらぎ効果を特徴づけることができた。

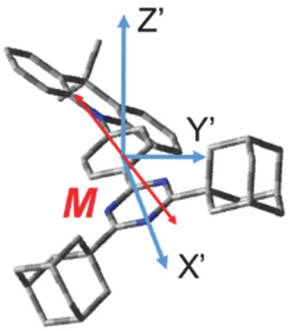


図 1. MA-TA の TREPR 計測で明らかになった三重項励起子の立体構造

成果（論文、学会発表等）学会発表

1. Imahori, H.; Kobori, Y.; Kaji, H., Manipulation of Charge-Transfer States by Molecular Design: Perspective from “Dynamic Exciton”. *Acc. Mat. Res.* **2021,** *2* (7), 501-514. （査読あり）

2. 勝平譲治・日下部 悠・和田啓幹・菅野奈都子・Ren Yongxia・梶 弘典・小堀康博 “時間分解 EPR 法による熱活性化遅延蛍光分子の励起状態の解析” 2021 年光化学討論会 2021.9.14-16.
3. 勝平譲治・日下部 悠・和田啓幹・菅野奈都子・Ren Yongxia・梶 弘典・小堀康博 “時間分解 EPR 法による熱活性化遅延蛍光分子の励起状態の解析” 日本化学会第 102 春季年会(2022) 2022.3.23-3.25.

Effect of microplastics on distribution of trace heavy metals in seawater

Yuzuru Nakaguchi Kindai University

Purpose) Trace metals were play an important role in marine biogeochemistry. These elements exist as the dissolved state (dMs) and labile particulate (lpMs) in seawater. The particulate matter in seawater includes metal oxides, hydroxides, sulfates, carbonate compounds, mineral particles, and biological particles. In recent years, microplastics produced by UV degradation and weathering have been added to particulate matter in seawater. However, the detail relationship between trace metals and microplastics remain unknown. In this research, In this study, we targeted Osaka Bay, which is greatly affected by human activities. In order to clarify the relationship between the trace metal speciation and microplastics, we determined trace metals and microplastics in seawater.

Experimental) Sea water samples were collected by Niskin sampler in September. 8, 9 and October 26 in 2021. Water temperature, salinity and pH were measured on-site. All sea water samples were transferred to precleaned LDPE Nalgene bottles. Unfiltered samples were directly collected from Niskin bottles to determine the concentrations of total dissolvable trace metals (tdMs). Some portions of samples were filtered through PTFE membrane filters with pore size 0.2 μm to determine the concentrations of dissolved trace metals (dMs). All the filtered and unfiltered samples for trace metals were acidified with 20% HCl (Tamapure AA-10) to achieve a final HCl concentration of 0.010 mol/kg (pH ~2.2). Nitrate, nitrite, phosphate, and silicic acid were determined by autoanalyzer. Chlorophyll a was determined by high performance liquid chromatography. Fluorescent organic matter (FDOM) was analyzed by three-dimensional fluorescence method.

The trace metals were preconcentrated using a chelating resin which ethylenediaminetriacetic and iminodiacetic acids were immobilized (NOBIAS CHELATE-PA-1, Hitachi High-Technology). A high-resolution ICP-MS (HR-ICP-MS) equipped with a magnetic sector mass spectrometer (ELEMENT 2, Thermo Fisher Scientific). The sample solutions for microplastics were filtered by PTFE membrane filters with pore size 5.0 μm. After filtration, the samples with filters transferred to separatory funnel. A saturated NaI solution was added to the separating funnel, and the microplastics were separated by the difference of density. After separation, the organic matters remaining in the sample were decomposed by mixed acid (HNO_3+$HClO_4$+HF). Microplastics were identified by Microscopic Raman photoluminescence system (LabRam HR type, HORIBA, Ltd.,)

Results and discussions) The concentrations of microplastics in the Osaka Bay are 8.5 (0 m), 8.0 (10 m), and 7.3μg/L (15 m), respectively. The types of microplastics at the surface (0 m) were polypropylene (19%), polystyrene (42%), and others (39%), respectively. The types of microplastics at 10 m were polypropylene (25%), polystyrene (16%), polyethylene (6%), Nylone66 (3%), polyvinyl chloride (3%), respectively.

Achievement report) Nakaguchi, Y., Ikeda, Y., Sakamoto, A., Zheng, L., Minami, T., Sohrin, Y., 2021, Distribution and stoichiometry of Al, Mn, Fe, Co, Ni, Cu, Zn, Cd, and Pb in the East China Sea, Journal of Oceanography, https://doi.org/10.1007/s10872-020-00577-z

2021-54

イオン液体含有高分子膜を用いた金属イオンの液膜輸送に関する研究

向井浩　京都教育大学

【目的】　将来的な電気自動車の普及に伴い、リチウムイオン電池の材料であるリチウム、コバルト等の希少金属の安定供給のため、これらのリサイクルの必要性が高まることが予想される。リサイクル技術の一つとして、金属を溶解した酸性溶液から目的とする金属イオンを抽出する湿式精錬法があるが、抽出溶媒として有機溶媒の代わりに疎水性の液膜を用いる液膜輸送はその一種に位置付けられる。液膜輸送は、膜の反対側に第 2 の水相を設け、膜を介して一方から他方の水相へ金属イオンを能動輸送させることで、目的イオンの分離濃縮を達成しようとする方法である。液膜中を輸送するキャリアーとしてプロトン解離型の有機配位子であるキレート試薬を用いることで、2 つの水相間の pH 差に基づくプロトンと金属イオンの陽イオン交換反応を利用した金属イオン（M^{n+}）の能動輸送が可能である。本研究では、イオン液体（IL）を液相とした液膜輸送により、リチウムイオンとコバルトイオンを相互分離することを目指し、その基礎的検討を行った。

【方法】　**(1) イオン液体含有高分子膜の作成**　キレート試薬 1-phenyl-3-methyl-4-benzoylpyrazol-5-one (BMPP) を 0.05 mol kg^{-1} 含む疎水性 IL 1-butyl-3-dodecylimidazolium bis(trifluoromethanesulfonyl)-imide ($[C_4C_{12}im][Tf_2N]$) 1.0 g に、tetrahydrofuran 5 g に溶かした polyvinyl chloride (PVC) 0.1 g を加え、内径 49 mm のガラス製シャーレ内に 3 日以上静置して円形の膜を作成した。**(2) 液膜輸送**　**(1)** の膜を PVC 製 U 字形液膜輸送セルの中央に挟み込み、膜の両側の容器に、HCl で pH を調節した供給相水溶液（$[M^{n+}] = 2.0\times10^{-5}$ mol dm^{-3}, $[CH_3COONa] = 0.01$ mol dm^{-3}, [KCl[= 0.1 mol dm^{-3}, pH 5）と受容相水溶液（$[CH_3COONa] = 0.01$ M, [KCl[= 0.1 mol dm^{-3}, pH 1 or 2）を、それぞれ 30 cm^3 入れた。両水相を 24 時間撹拌後、pH、体積、金属濃度を測定し、金属イオンの物質量と存在率を算出した。

【結果と考察】　**(1) イオン液体含有高分子膜の作成**　imidazolium イオンの 1 位と 3 位の alkyl 基の炭素数が 1 と 6 の$[C_6C_1im][Tf_2N]$、及び、1 と 8 の$[C_8C_1im][Tf_2N]$を用いた膜は、硬く不透明で IL の含有率も低かった。一方、炭素数が 4 と 12 の$[C_4C_{12}im][Tf_2N]$を用いた膜は、柔らかく透明で IL 含有率が約 90%と高かった。このため、$[C_4C_{12}im][Tf_2N]$膜を液膜輸送に用いた。**(2) 液膜輸送分離**　Li^+と Co^{2+}を等量含む混合水溶液からの相互分離を検討した。Co^{2+}のみを 34%の輸送率で受容相に輸送することが出来、Co^{2+}の分離が達成できた。しかし、Li^+と共に 29%の Co^{2+}が供給相に留まったため、Li^+のみを供給相に分離することは出来なかった。また、Co^{2+}が液膜相中に残存し、これが輸送率と回収率を低下させる原因となった。**(3) 輸送率向上の検討**　Co^{2+}の輸送率を向上させる試みとして、液膜相中に予め Co^{2+}を錯形成により含ませた膜を調製し、液膜輸送に用いた。その結果、錯化容量の 45-68%の Co^{2+}を含んだ膜で、Co^{2+}の 97%以上が供給相から除かれ、かつ、受容相への輸送率が 100%以上となった。輸送率が 100%を超えるのは、膜中に予め含ませた Co^{2+}の一部が受容相に溶離して合算されるためである。この結果は、供給相から受容相へのほぼ完全な輸送が達成されたことを示すものであり、Li^+と Co^{2+}の高い分離能が期待できる結果が得られたと言える。

【成果報告】

1. 向井浩, 安達智哉, 三嶋大侑, 宗林由樹, *日本分析化学会第 70 年会講演要旨集*, P3111 (2021).

硫黄系高分子薄膜材料における硫黄元素が構成するナノ構造の空間不均一性評価

藤原明比古　関西学院大学

1. 緒言: SAXS-CT 法では、各投影角度において試料を y 方向に走査して SAXS 測定を実施する必要がある。測定により、各投影角（ϕ）における各試料位置（y）での SAXS 像が得られる。像内の任意の $\boldsymbol{q}$ 位置における散乱強度を選択することで、CT 像を再構成するためのシノグラムが ϕ に対する y のイメージとして得られる。しかしながら、試料と空気界面部分では、時として余計な散乱像が生じる要因ともなり得る。入射 X 線が試料の表面や、角部分に照射されることで、表面・界面での反射や散乱がストリークの起源になる。シグナル上にストリークの強度がオーバーラップしてしまうと、再構成した CT 像では強いアーティファクトの発現要因となる。そこで我々は、シノグラム上において、試料表面で発現した位置のストリーク強度をノイズと見なし、Tikhonov 正則化によりその除去を試みた。

2. 実験：代表的な結晶性高分子である高密度ポリエチレン（HDPE, Toshoh Coporation）を角柱状に成形した試料を測定に用いた。切削により試料サイズを制御することが容易であるため、本デモンストレーションを示す最適な試料として HDPE を選定し、測定用試料を成形した。

3. 結果：図 1 に、試料から得られた二次元 SAXS 像を示す。図 1 (a)では、リング上の q = 0.21 nm^{-1} 近傍においてブロードなピーク（位置 A）が発現しており、この位置はラメラ構造間の周期長に対応している。一方で、入射 X 線が試料の端部分に照射した時に得られる代表的な二次元像の図 1(b)では、中心位置から赤道線方向に非常に強いストリークが発現した。特に $q_y > 0$ nm^{-1} 方向でのストリークが強く、これは試料の片側表面において反射した X 線がこの方向に減衰せずに観察されていることを示している。逆側の試料表面で反射した時には、$q_y < 0$ nm^{-1} 方向でのストリークが強く観察された（図 1(c)）。例えば、図 1 のリングパターン上のピーク位置 q_y = 0.17 nm^{-1}（図 1 内の A 部分）を選択し、各 φ と y に関する散乱強度を二次元上にプロットしたシノグラムイメージから再構成した CT 像は試料の四面部分において非常に強いアーティファクトが発現した（図 2(a)）。一方で、我々の開発した Tikhonov 正則化によるフレームワークを使い、ノイズを除去したシグナル成分のシノグラムから CT 像を再構成すると、輪郭部分のアーティファクトが除去されており、表面領域が明確に観察された（図 2(b)）。

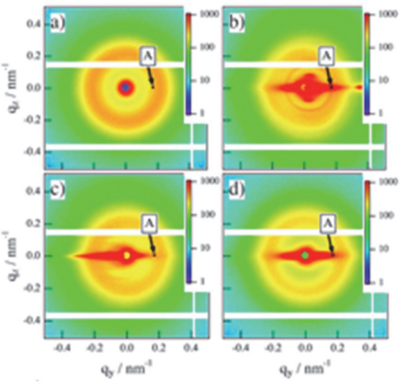


Figure 1. (a) 2D SAXS image without streak patterns. (b)-(d) Representative 2D SAXS images containing streak patterns.

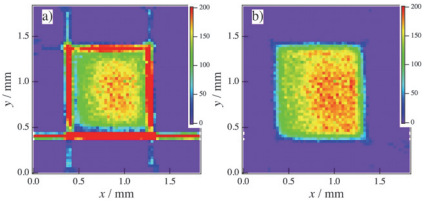


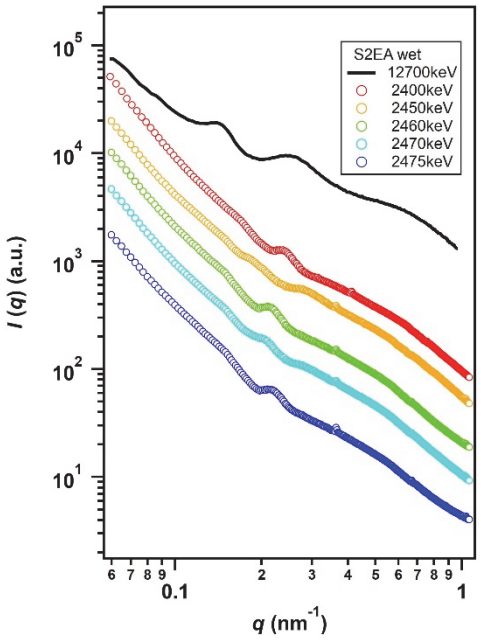
Figure 2. (a) Original CT images reconstructed from the original sinogram. (b) Improved CT images reconstructed from the sinogram of the signal components obtained after noise elimination.

Structure analysis of polymer materials having sulfur atoms in a wet state by resonant small-angle scattering methods

Katsuhiro Yamamoto　Nagoya Institute of Technology

Polymer structure analysis by the small-angle X-ray scattering method has become popular. Utilizing tender X-rays (1-5 keV) enables us to analyze the distribution state in the structure elementally selectively for light elements such as phosphorus, sulfur, and sodium, which are important elements for living organisms and functional polymer materials. In particular, there are almost no examples of analyzing these spatial structures and their distribution by the X-ray scattering method in the tender region. The amount of structural information obtained by the resonance scattering method near the absorption edge of X-rays peculiar to an element increases dramatically, and it becomes possible to analyze the chemical state of a specific element in addition to the local structure of element and component selection. We aim to expand the use of the tender X-ray region and perform scattering experiments in a more natural state, especially in wet environments. This application will work on a detailed structural analysis of polymer materials that are important in today's society, such as fuel cell membranes containing sulfur elements, targeting sulfur elements. Developing a scattering method that utilizes the unused wavelength region will open up a new path for structural analysis of multicomponent polymer materials by a new analysis method that can directly extract buried structural information.

We made a special sample cell suited for an X-ray scattering experiment under a high vacuum utilizing tender X-rays. The figure shows the energy-dependent SAXS profiles (X-ray energy of 2479 eV is the adsorption K-edge of Sulfur) of poly(styrene sulfonic acid)-*b*-poly(2-ethyl hexyl acrylate) (S2EA) thin film (20 μm in thickness) swollen with water. The block copolymer forms a microphase-separated structure. SAXS profiles of the microphase-separated structure in water were slightly different from each other. That means that sulfur atoms do not distribute uniformly in the PSSA domain. If sulfur atoms were uniformly distributed, all the SAXS profiles would be identical (shape) except for SAXS intensity. We will continuously proceed with the detailed structure analysis (distribution of water molecules and sulfonic acid groups). A part of the study was summarized to present an annual conference of the Society of Polymer Science, Japan. Related work (water distribution in polymer thin film) from our groups has been published in Langmuir (K.Yamamoto et al. *Langmuir 37*, 14550-14557, **2021**).



プラズモニック合金ナノ粒子を設計するための理論的指針の構築

飯田健二　北海道大学

[目的] 自然界の限られた資源を有効活用するためには、様々な元素を組み合わせて高性能な物質・材料を創造していくことが求められる。可視域に局在表面プラズモン共鳴(LSPR)吸収を示す材料の場合、周期表 11 族の単金属（Cu、Ag、Au）のみが使われてきた。しかし近年、京大化研の寺西研究室において、B2（塩化セシウム）型 PdIn ナノ粒子が可視域に LSPR 吸収を示すことが発見された。組成比や原子種を改変することで LSPR 吸収波長を制御できると期待される。

我々は、合金ナノ粒子の第一原理計算を行い、LSPR 特性を制御するための理論的指針を構築することを目的として研究を進めてきた。これまで、B2 型合金の比較的疎な構造によって LSPR が発現することを明らかにしてきた。そこで本年度は、PdIn と同様に比較的疎な C1 型構造を持つ $PtIn_2$ に着目して、光学特性を解析した。

[計算手法] 本研究では、直径数 nm のナノ粒子の光電子物性を原子・電子のレベルで明らかにすることが求められる。そのために、高い並列化効率を有する第一原理計算プログラム SALMON を用いた大規模計算によって、光励起電子ダイナミクスのシミュレーションを行った。対象としたのは、図 1 に示した C1 型構造を持つ $PdIn_2$ のナノ粒子である。結晶構造から直径約 3 nm の粒径の $Pt_{249}In_{432}$ を切り出して計算した。比較のために、同程度の大きさの Au_{561} についても計算を行った。

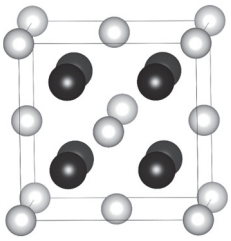


図 1. 対象とした $Pt_{249}In_{432}$ ナノ粒子の結晶構造。黒が In で灰色が Pt。

[結果と考察] 光吸収スペクトルを計算したところ、$Pt_{249}In_{432}$ は 2.8 eV 付近に Au_{561} の LSPR と類似のピークが見いだされた。そこで $Pt_{249}In_{432}$ について、2.8 eV の光によって誘起される電子ダイナミクスを解析した結果、電子の集団振動が励起されることが見いだされた。この結果から、$Pt_{249}In_{432}$ でも可視光で LSPR が励起されることが明らかになった。

[学会発表]

1. 飯田健二,「ナノ界面系の電圧や光に対する応答の理論的研究」京都大学福井謙一記念研究第 311 回化学コロキウム，東京都立大，東京都八王子市，2021 年 12 月 17 日(招待講演)
2. 飯田健二，「不均一触媒の光や電圧に対する応答の理論計算研究」触媒・電池戦略研究拠点第 18 回公開シンポジウム，オンライン開催，2021 年 11 月 15 日(招待講演)
3. 飯田健二，「ナノ界面系の光や電圧に対する応答の理論的研究」第 15 回分子科学討論会，オンライン開催，2021 年 9 月 18-21 日(招待講演)

2021-58

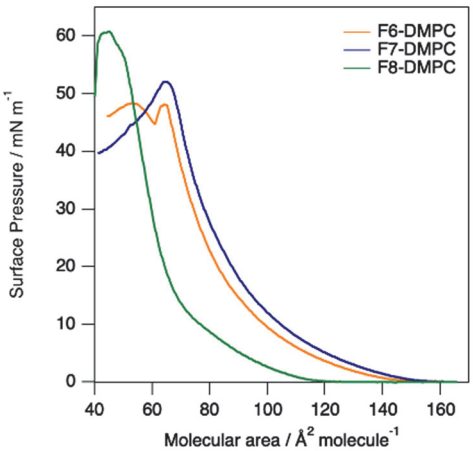
部分フッ素化両親媒性分子の膜物性・構造に対する R_f 鎖長依存性の解析

園山正史　群馬大学

【目的】　私たちは膜タンパク質研究に資する部分フッ素化リン脂質の設計指針を得るための物理化学的な研究により，パーフルオロアルキル基(R_f, C_nF_{2n+1})を疎水鎖末端に部分的に導入した両親媒性分子が，R_f 鎖長依存的な際だった物性を示すことを明らかにして来た。本研究では，n = 5 および 7 の R_f 基を有する，リン脂質 Dimyristoylphosphatidylcholine（DMPC）の部分フッ素化アナログ分子 F5-DMPC および F7-DMPC を新たに合成し，表・界面物性および分子構造を解析することにより，膜物性・構造の R_f 鎖長依存性の起源を明らかにすることを目的とした。

【方法】　これまでの方法に準じて合成した部分フッ素化リン脂質 F7-DMPC を用いて，水面上単分子膜の表面圧−面積（π−A）等温曲線を 15℃および 25℃において測定した。さらに，水面上単分子膜を基板に転写し，赤外反射吸収（RAS）スペクトルを測定した。

【結果と考察】　25 ℃において測定した F7-DMPC 水面上単分子膜のπ−A 曲線を，F6-DMPC および F8-DMPC とともに右図に示す。F7-DMPC では F6-DMPC と同様に気体膜に特徴的なπ−A 曲線となり，分子間の強い相互作用により非圧縮時から分子が凝集し，液体膜の特徴を示す F8-DMPC とは大きく異なることがわかった。長い R_f 鎖を有する化合物の場合，異なる結晶型を示す 15 ℃においても，F7-DMPC は同様の傾向を示した。さらに，RAS スペクトルにおいて CF_3 対称伸縮振動バンドが明瞭に観測されたことから，F7-DMPC の R_f 基は水面に対して垂直方向に配向している可能性が示唆された。この分子配向の特徴は F6-DMPC および F8-DMPC と同様であった。F5-DMPC のグラムスケールの合成は精製条件の最終検討の段階に入っており，間もなく完了する予定である。今後 F5-DMPC のπ−A 曲線および RAS スペクトルの測定を行い，二本鎖分子である部分フッ素化リン脂質 F*n*-DMPC の膜物性・構造において観測されている興味深い R_f 鎖長依存性の物理化学的起源を，長谷川らが提唱している階層双極子アレー（SDA）理論との関連から明らかにする。



図．F*n*-DMPC（*n* =6,7,8）水面上単分子膜の表面圧−面積等温曲線（25 ℃）

【成果報告】

学会発表：中川原亜依ら　「一本の疎水鎖をフッ素化した新規部分フッ素化リン脂質の合成と熱物性」，日本化学会第 102 春季年会　（2022 年 3 月 24 日（予定）），他 1 件。

A spectroscopic analysis on bio-degradation processes of polymer thin film surfaces

Takashi AOKI Kyoto Institute of Technology

1. Objectives

A spectroscopic study of the degradation process on the surface of polymers is very significant as pollution caused by plastics remaining in the oceans is attracting worldwide attention. We focused on the surface of the poly(L-lactic acid) (PLLA) thin film where the biodegradation initiates and measured the degradable process on its surface using multiple-angle incidence resolution spectrometry (pMAIRS). The spectroscopic instrument provides attractive information on the presence or absence of functional groups and their orientation in polymer chains for amorphous samples, making it a very useful tool for understanding the reaction occurring near surfaces. This study was conducted under the precious guidance of Prof. Takeshi Hasegawa of the Institute for Chemical Research, Kyoto University.

2. Experimental methods

PLLA was dissolved in chloroform, and the PLLA thin film was coated on a silicon wafer surface using a spin coater. The film thickness was measured by ellipsometry. The PLLA-coated Si wafers were immersed in Tris-HCl buffer solution of Proteinase K (100 μg/mL) at 25˚C for a predetermined time, washed and dried, and then subjected to the pMAIRS measurement.

3. Results and Discussion

The thickness of the as-prepared PLLA film was 115 nm, and after immersion in Proteinase K solution for 5 and 10 min, it was 104 and 81 nm, respectively. The overall absorbances in the regions between 4000 and 650 cm^{-1} of the spectra of pMAIRS also decreased with the time of the enzymatic reaction. The polyester was degraded by the enzyme, resulting in a corresponding decrease in the film thickness on the silicon wafer. The pMAIRS operation gives us two components of the in-plane (IP) and out-of-plane (OP) spectra of the polymer against the substrate surface. The intensity ratios of IP and OP spectra around 1760, 1185, and 1190 cm^{-1} were found to vary with the time of the enzymatic reaction. At present, additional analytical approaches such as AFM and WAXD are being carefully carried out to ensure that the variations in the spectra can be accurately interpreted. In addition, as the orientation of the polymeric chains in the thin film may be affected by the substrate, we are preparing films with different thicknesses and also investigate the film thickness dependence of the IP and OP spectra. Through several analyses, information such as the degree of orientation of any functional group on the surface of PLLA will elucidate the degradation process.

Identification of an active gibberellin compound in the basal land plant Marchantia polymorpha

Takayuki Kohchi Kyoto University

A plant hormone gibberellin (GA) is a diterpene compound that regulates plant growth and development, including seed germination, cell elongation, and flower bud formation. Genome analyses revealed that the biosynthetic pathway and signal transduction of GA were acquired in the land plant lineage during evolution. However, the function and ancestral form of GA in the basal land plants are still unknown. The liverwort *Marchantia polymorpha L.* is a model of basal land plants to understand the molecular evolution of the mechanisms in plant development. The *M. polymorpha* genome encodes all genes necessary for the biosynthesis of GA12, a precursor for active GAs. Furthermore, the mutants of GA biosynthetic genes showed pleiotropic phenotypes including growth retardation and delayed sexual development. We have developed a bioassay system to elucidate the bioactive form of GA (GAx) in *M. polymorpha*. In collaboration with Dr. Shinjiro Yamaguchi (co-researcher) and Dr. Kiyoshi Mashiguchi (research collaborator), Institute for Chemical Research, Kyoto University, we found that a specific fraction prepared by the combination of the two-phase partitioning method and HPLC gradient program restored the defects of GA biosynthesis mutants. We will determine the chemical structure of GAx by combining mass spectrometry and NMR. Furthermore, it is crucial to identify the receptor for active GAs in *M. polymorpha.* The *M. polymorpha* genome does not encode GID1, a component of the typical receptor of GAs known in vascular plants. The ligand-receptor co-evolution might have occurred during land plant evolution. A genetic approach has been taken to identify the GA receptor in *M. polymorpha*. The mutant of Mp*SABATH2*, which is expected to encode an inactivating enzyme of GAx, showed severe phenotypes such as dwarfism and growth inhibition. We conducted the EMS mutagenesis to screen suppressors of the Mp*sabath2* mutant. The molecular genetic analysis of the obtained mutants is ongoing.

Shimokawa, E., Kawamura, S., Sun, R., Suzuki, K., Yoshitake, Y., Yasui, Y., Nishihama, R., Yamaoka, S., Mashiguchi, K., Yamaguchi, S., and Kohchi, T. Screening of novel mutants affecting a gibberellin-related methyltransferase function in *Marchantia polymorpha.* The 63rd Annual Meeting of the Japanese Society of Plant Physiologists. March 22-24, 2022.

Glass Transition and Molecular Dynamics of Guest Low Mass Molecules in the Clathrate of Polymer Crystals

Osamu Urakawa Osaka University

Syndiotactic polystyrene (sPS) forms co-crystalline structures with several guest molecules, called δ-phase or ε-phase. The δ-phase accommodates each guest molecule in the isolated space, while the ε-phase confines guest molecules in a channel-like one-dimensional space. We found that dielectric measurements could detect the rotational relaxation of polar guest molecules confined in both phases, where the guest dynamics were highly asymmetric [1-3].

The dynamics of spatially confined molecules is influenced by (1) the interaction with the cavity wall and (2) the physical confinement effect [4]. This study used polar guest molecules such as benzonitrile, halobenzene, nitrobenzene, etc., which do not interact strongly with the cavity wall inside the sPS crystal. Therefore, simple confinement effects are considered to determine the guest dynamics. Experimentally, the rotational relaxation times τ of various guest molecules in the δ phase correlate well with only the guest molecular length l (in the long axis direction), suggesting that the confinement effect governs the guest dynamics.

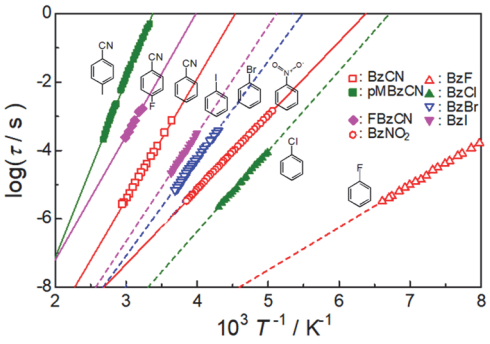


Fig.1. Crystalline structures of δ and ε phases.

Fig.1 shows the temperature (T) dependence of τ for several guest molecules in the δ-phase. In the time and temperature ranges examined, all the $\tau(T)$ obey the Arrhenius equation: $\tau \propto \exp(E_a/RT)$, where E_a is the activation energy. This behavior was the same in the case of the ε phase. However, the τ and E_a of the same guest molecule are shorter and lower in the ε phase than in the δ phase. This means that the confinement of guest molecules is weaker in the channel-like space of the ε phase.

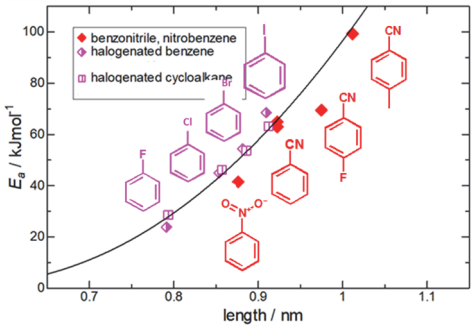


Fig.2. l dependence of E_a. The solid line represents the model prediction.

Fig.2 shows the l dependence of E_a for several guest molecules in the δ-phase, indicating the excellent correlation between l and E_a.

[1] O. Urakawa, F. Kaneko, H. Kobayashi, *J. Phys. Chem. B.* **2012**, *49*, 14461.
[2] H. Kobayashi, O. Urakawa, *Chem. Phys.* **2016**, *479*, 122.
[3] H. Kobayashi, S. Akazawa, O. Urakawa. F. Kaneko, T. Inoue, *Macromolecules*, **2018**, *51*, 8611.
[4] F. Kremer, A. Huwe, M. Arndt, P. Behrens, W. Schwieger, *J Phys Cond Matter*, **1999**, 11, A175.

Nonlinear Rheological Behavior of Telechelic Ionomer with Distribution of Ionic Stickers at the Ends

Zhijie Zhang　Chinese Academy of Sciences

Objectives

In our previous studies, we consider that the neighboring ions should exhibit motional coupling if their distance is shorter than the Kuhn length so that the strand between them becomes non-flexible. This idea is tested in our previous studies. (ACS Macro Letters, 2020, 9, 917-923). Based on the study explained above, we will continue to examine nonlinear rheology behavior of this new type of telechelic ionomers.

Experimental methods

A new type of telechelic ionomers was synthesized through a two-step polymerization utilizing a bifunctional initiator.

Experimental results and Discussion

The damping function $h(\gamma)$ of the TPiBA-m samples of m = 0.54-0.98 and rTPiBA are compared in Figure 1. For comparison, the damping behavior of unentangled linear chains, entangled linear and star-shaped chains reported by Watanabe and coworkers are added (gray squares and spheres). In our opinion, this difference of damping behavior is owing to the different damping mechanisms: Besides, we find that using γ/γ_{peak} as the horizontal axis normalizes $h(\gamma)$ reasonably, and $h(\gamma)$ drops significantly at $\gamma/\gamma_{peak} > 1$, both features suggest the damping of the current samples are mainly due to the strain-induced dissociation.

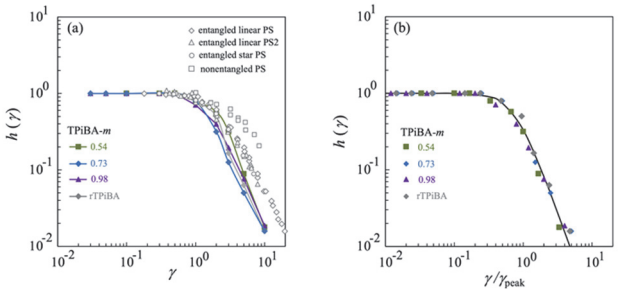


Figure 1: (a) The damping function of TPiBA-*m* and the reference sample rTPiBA obtained from step-strain relaxation experiments. (b) The damping function of TPiBA-*m* and rTPiBA plotted against normalized strain γ/γ_{peak}.

Outcome reports

This study investigated the non-linear rheology properties of a newly designed type of telechelic ionomers. The damping of the current samples is mainly attributed to the strain-induced dissociation.

Role of PX-PH-type Phospholipase Ds in Plant Intracellular Membrane Traffic

Yohei Ohashi　MRC Laboratory of Molecular Biology

Objectives: Phospholipase D (PLD), which hydrolyzes glycerophospholipids to produce phosphatidic acid (PA), is involved in dynamic cellular processes, including membrane traffic, signal transduction, and cytoskeletal reorganization through molecular functions of PA. PLD is requisite for plants in their development according to the genetic program and responses to environmental stimuli. However, particular cell biological processes that PLD promotes for those phenomena largely remain elusive partly because subcellular loci where PLD functions for each phenomenon remain unknown. In this collaboration research, we performed comparative analysis for subcellular localization patterns of PLDζ1 and PLDζ2, eukaryote-general PX-PH-type PLDs of *Arabidopsis thaliana*, for a clue as to their functions in cell biological processes.

Experimental Methods: Transgenic *Arabidopsis* lines, which expressed fluorescence protein fusions of PLDζ1 and PLDζ2, and their N-terminal partial proteins, were constructed, and then crossed with lines expressing various fluorescence markers for intracellular localization. Root cells of those constructed transgenic lines were observed by confocal laser-scanning microscopy.

Results and Discussion: Own promoter-driven fluorescence protein fusions of PLDζ1 and PLDζ2 were detected in various types of cells and only mature lateral root cap cells, respectively. In mature lateral root cap cells, fluorescence protein fusions of PLDζ1 localized to the entire *trans*-Golgi network (TGN) while that of PLDζ2 localized to the tonoplast and punctate structures including a part of the TGN and multi-vesicular bodies. These localization patterns were reproduced using their N-terminal partial proteins containing PX-PH domains. An inducibly overexpressed fluorescence protein fusion of the PLDζ2 partial protein first localized to the punctate structures, and then accumulated predominantly on the tonoplast. Further domain dissection analysis revealed that the N-terminal moiety preceding the PX-PH domain of PLDζ2 was required for the tonoplast-predominant accumulation while either PLDζ1 or PLDζ2 PX-PX domain alone is able to localize to punctate structures. These findings suggest that PLDζ1 and PLDζ2 play partially overlapping but nonetheless distinctive roles in the post-Golgi membrane trafficking from the TGN to the tonoplast.

Publication: Shimamura, R., Ohashi, Y., Yamamoto, Y. Y., Kato, M., Tsuge, T., and Aoyama, T. (2022) *Arabidopsis* PLDζ1 and PLDζ2 localize to post-Golgi membrane compartments in a partially overlapping manner. *Plant Mol. Biol.* 108:31-49.

Role of Phosphoinositide Signaling in Pollen Development

Sheng Zhong　Peking University

Objectives: Phosphatidylinositol 4,5-bisphosphate [PtdIns(4,5)P_2], a minor phospholipid component of eukaryotic membranes, is involved in the regulation of various intracellular events, including actin cytoskeletal organization and membrane trafficking, through the interaction with its effector proteins. The spatiotemporal existence of PtdIns(4,5)P_2 is a critical factor for its signaling function, and established basically via its metabolization. Although the metabolic pathways of phosphoinositides are elaborately linked to one another, phosphatidylinositol 4-phosphate 5-kinase (PIP5K), which produces PtdIns(4,5)P_2 by phosphorylating PtdIns(4)P, is thought to be a key enzyme responsible for the spatiotemporal pattern of PtdIns(4,5)P_2 in higher plants, in which some of the phosphoinositide metabolic pathways found in animals and fungi are missing. The model plant *Arabidopsis thaliana* has 11 PIP5Ks, which are classified into type A (PIP5K10 and 11) and type B (PIP5K1–9) based on the absence and presence of membrane occupation and recognition nexus (MORN) repeats at their N-termini, respectively. In this collaboration work, we investigated functions of PIP5K and PtdIns(4,5)P_2 in pollen development and pollen tube growth. We prepared a series of PIP5K loss-of-function mutants. Starting with these, we identified a set of PIP5K genes required for pollen development and pollen tube growth.

Experimental Methods: T-DNA or transposon tagging mutant lines of PIP5K genes were obtained from public organizations of biological resources. Null alleles for each type-B PIP5K genes were established and crossed with one another to obtain multiple mutant lines. Single and multiple mutant lines of the PIP5K genes were examined for their phenotypes in pollen development and pollen tube growth.

Results and Discussion: Using the multiple mutants *pip5k4pip5k5*, *pip5k4pip5k6*, and *pip5k5pip5k6*, which were constructed previously, we confirmed that the *PIP5K4–6* genes redundantly function in pollen tube growth. Consistent with this, either YFP-fused PIP5K4–6 transgene could rescue the sterility of *pip5k4pip5k5pip5k6* triple mutant pollens. In transgenic plants heterozygously harboring the PIP5K6-YFP transgene under the *pip5k4pip5k5pip5k6* triple mutant background, pollens without and with the YFP fluorescence were apparently the same in their morphology. However, the former could not germinate at all in vitro whereas the latter normally germinated. Phylogenetic analysis of angiosperm type-B PIP5Ks revealed that the clade containing PIP5K4–6 is conserved in angiosperms, and that PIP5K6 orthologs constitute a distinct subclade from that containing PIP5K4/5 orthologs in core eudicots. These facts suggest that the common ancestor of the *PIP5K4–6* genes evolutionally differentiated to function in pollen development and/or pollen tube growth, and then further functional differentiation occurred between PIP5K4/5 and PIP5K6 orthologs.

Self-Assembling Adjuvant-Built-In Vaccines for Cancer Immune Therapy

Yan-Mei Li　Tsinghua University

The Uesugi group of ICR recently discovered cholicamide, a self-assembling small-molecule vaccine adjuvant that potentiates innate immune responses through its interaction with toll-like receptor 7 (TLR7) [***Angew. Chem. Int. Ed.***, 2021]. During the course of the cholicamide study, the Uesugi group observed its induction of IL12p70, a cytokine that plays a major role in cancer immunosurveillance and promotes immune responses of CD8 T-cells and natural killer (NK) cells. This observation encouraged us to explore the utility of cholicamide in cancer immune therapy.

In FY2011, we examined the anti-tumor activity of cholicamide together with an antigen peptide. However, cholicamide exhibited cytotoxicity in bone-marrow-derived dendritic cells (BMDC), which encouraged the Uesugi group to further optimize the structure of cholicamide. Evaluation of 12 new derivatives led to the discovery of C7, which was found to be three times more immunostimulating than cholicamide in BMDC. Importantly, C7 showed almost no cytotoxicity in BMDC up to 80 μM. The toxicity of C7 was also evaluated in mice. No increase in ALT, AST, and ALP (indicators of hepatotoxicity) and UREA and CREA (indicators of nephrotoxicity) was observed even when 500 μg of the compound was administered to the mice.

The potent immunostimulating activity and low toxicity of C7 encouraged us to examine its ability as an adjuvant for cancer vaccines. After constructing the melanoma tumor-bearing mice, we evaluated cancer volumes, survival rate, and mice weight. While the control group and the group receiving only C7 showed an increase in cancer volume and all mice died within 15 days, the group receiving the antigen-peptide and C7 showed a marked suppression of cancer volumes and a 21-day survival rate of 80%. In contrast, the group receiving only antigen peptide showed a slight inhibition of cancer volume growth, but the 21-day survival rate was only 20%.

The reason why C7 exhibits low cytotoxicity but potent immune activation remains unclear. Dynamic light scattering experiments suggest that the assemblies of C7 are thermodynamically more stable than those of cholicamide. The stable C7 assembly may play a role in its excellent property as a cancer vaccine adjuvant.

Site-Selective Protein Acetylation by a Small Molecule

Lu Zhou　Fudan University

Post-translational modifications (PTMs) play essential roles in regulating a myriad of cellular processes in mammalian cells, including signal transduction, metabolism, and gene transcription. Among protein modifications, acetylation and phosphorylation represents the most critical PTM. In FY2021, we continued our collaboration with the Uesugi research group in ICR to design small molecules that specifically acetylate or phosphorylate cellular proteins.

- **Acetylation of cGAS.** The presence of DNA in the cytoplasm is normally a sign of microbial infections and is quickly detected by cyclic GMP-AMP synthase (cGAS) to elicit anti-infection immune responses. Chronic activation of cGAS by self-DNA leads to severe auto-immune diseases. It has been reported that Lys acetylation of cGAS inhibits its activation to impair cGAS-mediated immune responses. Exogenous control over the acetylation status of cGAS may provide a potential therapy for treating DNA-mediated autoimmune diseases. To discover a small molecule that selectively acetylates cGAS, we exploited the structure of RU521, a known cGAS inhibitor, as a starting point. Introduction of an acetyl ester group to the structure at varied positions led to a series of candidate cGAS-acetylation compounds. We found one compound we named F108-1 that potently acetylated cGAS and thereby inhibits its enzyme activity.
- **Development of small-molecule kinases.** Our preliminary investigations found a nitro-benzyl phosphate group as a donor of UV-induced phosphate transfer reactions. In FY2021, we conjugated a nitro-benzyl phosphate group to a number of different molecules. For the proof of the concept, we designed and synthesized a hybrid compound (Q1), in which a nitro-benzyl phosphate group is conjugated with biotin. Co-crystal structure of the avidin-Q1 complex revealed that the phosphonic acid group of Q1 formed a hydrogen bond with Ser112. However, UV irradiation failed to transfer phosphate group to serine residue. The possible explanation is that reactive intermediate “metaphosphate anion” is too active to phosphorylate serine residue.
- **Others.** Our group also collaborated with the Uesugi group for the proteomic discovery of covalent enzyme inhibitors. Our findings exemplify that activity-based proteomic screening with a cysteine-reactive probe can be used for discovering covalent inhibitors that react with non-cysteine residues. The collaboration has now been accepted for publication in *ACS Chem. Biol.*

Orbitronics with new material systems

Sanghoon Kim　University of Ulsan

Atom itself becomes a magnet because electron has properties such like a top. Because of the reason materials like Fe, Ni, Co and etc. can be magnets lies here. Countless atoms' spins in a material interact with each other! These interactions create that all spins attempt to align in the same direction. In nature, common metals have crystal symmetry, where an arrangement of atoms is uniform and periodic. In the case of specific materials, the symmetry is broken, which creates special energy causing spins to twist (see the illustration in Fig. 1(a)). This is called as Dzyaloshinskii-Moriya interaction. Twisted spin structure has received immense attentions recently in modern physics. These small magnetic particles can create skyrmions and can be thermally stabilized and will enable the development of high density, high efficiency memory devices. Therefore, it is important to find materials that have the Dzyaloshinskii-Moriya interaction which is needed to make twisted spin structure.

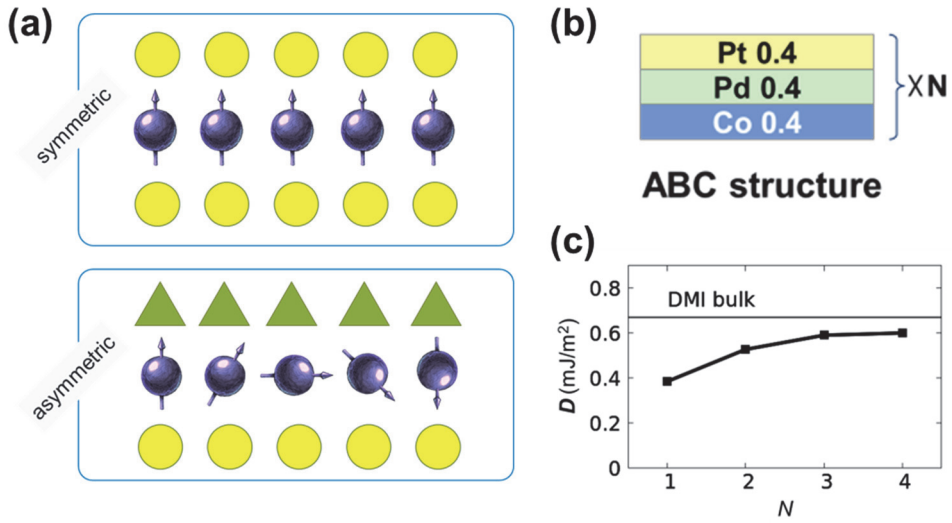


Figure 1. (a) Schematic illustration of spin alignments with symmetric (top) and asymmetric (bottom) systems. (b) The ABC-type structure in this study. (c) Dzyaloshinskii-Moriya interaction energy in terms of the unit-layer-structure numbers.

The research team of Professor Teruo Ono, Kyoto University, Professor Sanghoon Kim, University of Ulsan proposed and experimentally verified the fact; when multiple layers of atomic layer structure artificially prepared is asymmetric as shown in Fig. 1(b), spins have Dzyaloshinskii-Moriya interaction energy (see Fig. 1(c)), which means artificial superlattice with crystal asymmetry can create twisted spin structures. This study leads that material studies to create subsequent twisted spin structures can be extended to a combination of various materials which does not have to be limited to elements present in nature. This study was published in npj Computational Materials [7: 129 (2021)].

Study of characteristics of spin wave in magnetic insulator

Kab-Jin Kim　KAIST

Objective:

The aim of the research is to study the characteristic properties of spin wave in magnetic insulators.

Experimental methods:

For this study, we prepared magnetic insulators, such as YIG, TmIG, and GdIG. The YIG is selected as a control sample, because the spin wave of YIG is already well known in the community. TmIG was selected because it shows spin reorientation from perpendicular magnetic anisotropy to in-plane magnetic anisotropy above room temperature. GdIG was used because it shows compensation point where the total magnetization becomes zero. To measure the spin wave, we developed the antenna measurement setup with vector network analyser. In addition, quantum imaging by means of NV center is also adopted.

Experimental results:

We first investigated the spin wave in YIG as a control experiment. The spin wave profile was successfully imaged using NV center, indicating that our quantum measurement is well operated. We also investigated the magnon (quantum of spin wave) and phonon in TmIG, and found that the magnon and phonon exhibit a non-equilibrium under the thermal gradient. As for GdIG, the experiment is on-going (currently, we are confirming the material properties of GdIG by using XRD and MPMS).

Discussion:

The spin wave experiment in ferrimagnetic insulators is a challenging topic, which requires a long time. Therefore, in this year we focused on the development of the experimental setup as well as the characterization of the magnetic insulators. Although it is in the beginning stage, we obtained several positive results, including the successful quantum imaging, evidence of magnon-phonon in-equilibrium. As this is a long-term project, we would like to continue our spin wave research next year. We lastly note that it was impossible to visit the ICR directly due to the Covid-19. We look forward to collaborating through direct exchange next year.

Application of ferrimagnets for spintronics devices

Alexander Samardak　Far Eastern Federal University

The main purpose of this study is to construct a new field called "ferrimagnetic spintronics" by clarifying the universality and diversity of the behavior of ferrimagnets as "antiferromagnets with magnetization", and to develop them for device application. In this study, we prepare and study thin-film ferrimagnet CoTb alloy, which "behaves as an antiferromagnet with magnetization".

A series of samples of the composition W(4)/$Co_{56}Tb_{44}$(x)/Ru(2 nm), x from 1.5 to 7 nm, was prepared by magnetron sputtering on Si/SiO_2 substrates. To study the magnetic transport properties, the Hall bar structures were prepared by photolithography and ion plasma etching.

Decreasing thickness brings the sample to the Co-rich state: the magnetic moments of Co atoms are oriented along the external field, while Tb is antiparallel. The passage of current pulses through the Hall bar structure in the presence of a constant in-plane field B_x leaded to a reversible switching of the magnetization orientation in the structure from the up to the down due to the spin-orbit torque effect. It was found that the efficiency of current exposure had a complex dependence, determined both by the thickness of the FIM layer and by the value of the saturation magnetization.

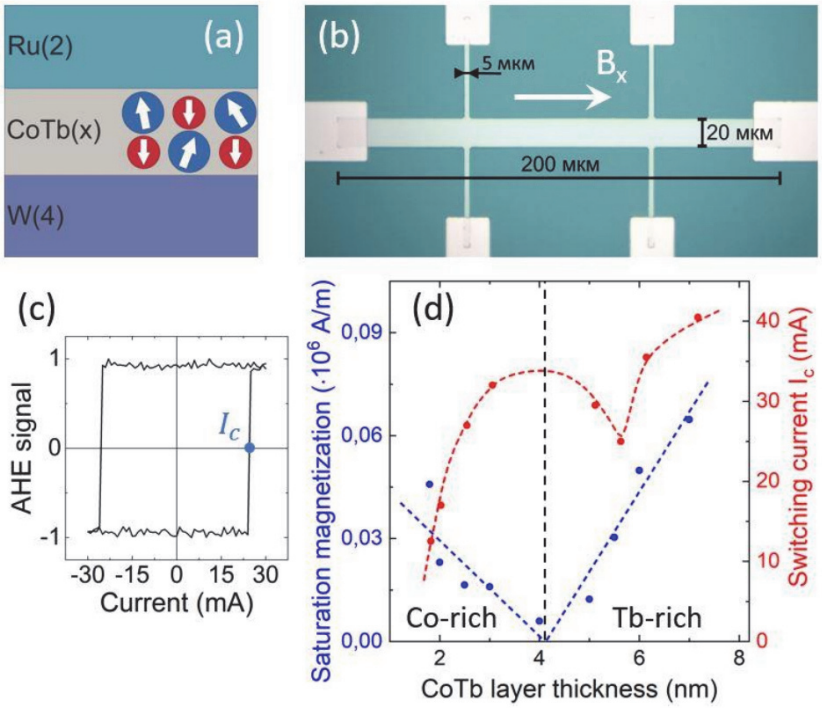


Fig. 1. (a) Composition of the investigated structure, thickness in nm. (b) Image of the Hall bar structure with orientation of the external field in the plane. (c) Hysteresis loop obtained by the current propagation through the Hall bar structure. (d) Saturation magnetization and switching current versus CoTb layer thickness.

We lastly note that it was impossible to visit the ICR directly due to the Covid-19. We look forward to collaborating through direct exchange next year.

Highly efficient red thermally activated delayed fluorescence emitters with sterically hindered donor skeleton

Jang Hyuk Kwon　Kyung Hee University

In the organic light emitting diodes research field, thermally activated delayed fluorescence (TADF) materials have received tremendous attention due to their ability to achieve internal quantum efficiency (IQE) of 100%. A number of blue and green TADF materials with external maximum efficiency (EQE_{MAX}) of over 30% have been proposed, while an advance of highly efficient red TADF materials has been hampered by the energy gap law. To overcome this problem, rigid electron donor and acceptor unit are promising. This is because the rigid molecular structure can reduce molecular vibration and rotation related to non-radiative decay. Recently, we reported a new 10,15-dihydro-5H-diindolo[3,2-a:3′,2′-c]carbazole (i.e., diindolocarbazole) donor for efficient TADF materials (*J. Mater. Chem. C*, **2018**, *6*, 1343-1348; *Nat. Photon*., **2019**, *13*, 540-546). The diindolocarbazole donor has a rigid π-extended molecular structure and resulting shallow HOMO energy level, which is suitable for the donor of red TADF emitters with a small HOMO-LUMO energy gap (E_g). Using this donor, Kaji group designed a new red TADF emitter with a rigid and π-extended acceptor based on quantum chemical calculation. Therefore, the diindolocarbazole synthesized by our group was sent to the Kaji's group.

This past year, Kaji's group has succeeded in the synthesis of the designed red emitter. From photophysical measurements, small E_g of 2.34 eV and red emission with the maximum peak emission wavelength of 646 nm were observed. (Figure 1A). In addition, a delayed fluorescence was observed for the red emitter doped in mCBP film suggesting the TADF characteristics. For electroluminescence properties, the new material-based OLEDs exhibited relatively low external quantum efficiency with orange-red emission. Kaji's group is now working to improve the device performance by using other hosts and optimizing device configurations.

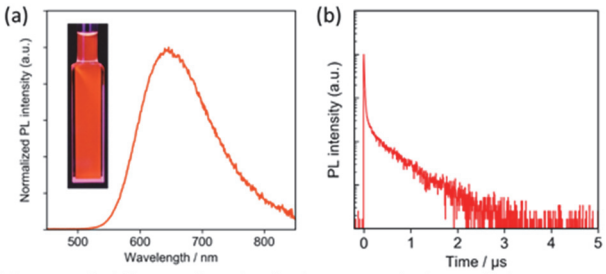


Figure 1. Photophysical characteristics of the new red TADF material. (a) PL spectrum in solution state and (b) transient PL decay curve in a film state.

Developments of highly efficient and high color purity organic electroluminescent devices based on thermally activated delayed fluorescent materials exhibiting ultrafast reverse intersystem crossing process

Lian Duan　Tsinghua University

To develop highly efficient and high color purity organic light-emitting diode (OLED) devices, utilization of emitter molecules with a narrow spectral width is necessary. As an alternative strategy instead of thermally activated delayed fluorescence (TADF)-based OLEDs that generally shows broad spectral widths, hyperfluorescence (HF)-based OLEDs have attracted great attention. In the HF-based OLEDs, electrically generated triplet excitons are up-converted into singlet excitons by the TADF molecule used as an assistant dopant. The singlet excitons are finally transferred to a lowest excited singlet state of a terminal emitter (TE) molecule by Förster-resonance energy transfer (FRET) mechanism. Therefore, the color purity of the HF-based OLEDs strongly depends on spectral features of the TE molecules. Recently, we reported an ultrapure-green fluorophore (tPhBODIPY) based on a boron-dipyrromethene (BODIPY) skeleton, which exhibited the spectral feature with a small full width at half maximum (fwhm) of 28 nm and high photoluminescence quantum yield (PLQY) of 97% (*Adv. Optical Mater.* **2020**, *8*, 2000483). Utilization of tPhBODIPY as the TE molecule can be expected to afford the highly efficient and high color purity OLEDs.

Toward the highly efficient and high color purity OLEDs, Kaji's group has planned fabrications of the HF-based OLEDs using tPhBODIPY as the TE. As the assistant dopant, TpAT-tFFO with a large rate constant (10^7 s^{-1}) for a reverse intersystem crossing process was used. Overlap between absorption spectrum of tPhBODIPY and emission spectrum of TpAT-tFFO was found to be sufficient to generate the energy transfer by the FRET mechanism. Solution-processed HF films composed of tPhBODIPY, TpAT-tFFO and CzSi (host) showed narrow PL spectrum with fwhm of ~28 nm and high PLQY (~93%). From transient PL measurements, obviously shortened decay curves were obtained as shown in Figure 1. By analyzing the transient PL decay curves, we estimated a rate constant for the FRET process (k_{FRET}) to be 4.6×10^7 s^{-1}. These results indicate that efficient energy transfer from TpAT-tFFO to tPhBODIPY occurred in the HF films. The fabrications of the HF-based OLEDs are in progress.

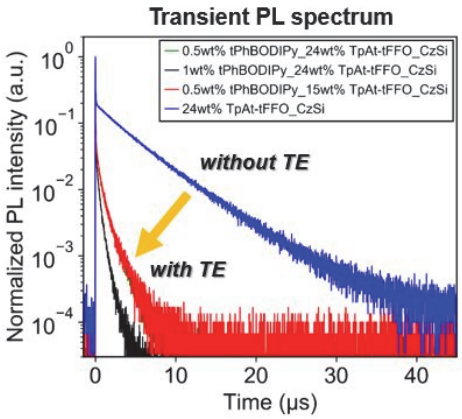


Figure 1. Transient PL decay curves of the doped films w/wo the TE molecule.

Structural and functional analysis of the surface polysaccharides of outer membrane vesicles released by bacteria

Maria Michela Corsaro　University of Naples Federico II

Objectives: The aim of this research has been the characterization of the capsular polysaccharides (CPS) isolated from both the cells and the outer membrane vesicles (OMVs) secreted by the bacterium *Shewanella vesiculosa* HM13. The group of the ICR partner researcher (Prof. Tatsuo Kurihara) has furnished both the samples, and the characterization has been performed by NMR spectroscopy.

Experimental: Dried cells (4.43 g) and OMVs (202 mg) of *S. vesiculosa* HM13 (rifampin-resistant mutant) were extracted with phenol/chloroform/light petroleum method (Galanos et al 1969) and the crude lipooligosaccharide (LOS) was precipitated as already reported (Di Guida et al. 2020). The phenolic phases were dialyzed against water (cut-off 3500 Da) and lyophilized, to obtain 161 mg and 37.4 mg from cells and OMVs, respectively. Each sample was subjected to a mild acid hydrolysis with 1% CH_3COOH (100 °C, 3 h). The resulting mixture was centrifuged (4 °C, 7500 rpm, 45 min), and the supernatants were fractionated on a Bio-Gel P-10 column (Sigma, 110 × 0.75 cm, flow rate 12.7 mL/h, fraction volume 2.5 mL) eluted with water. The CPS fractions (CPS_{cells} 16.4 mg and CPS_{OMV} 9.9 mg) were analysed by chemical analysis and ^1H NMR spectroscopy. Finally, the monosaccharide composition was obtained after derivatization as acetylated methyl glycosides (AMG) and analysis by GC-MS.

Results: The cells and the OMVs of *S. vesiculosa* HM13 were extracted by PCP method. After the precipitation of the LOSs, the residual phenolic phases were dialyzed against water. The isolation of the CPS from both cells and OMVs was achieved by mild acid hydrolysis, followed by purification on a size exclusion gel chromatography column. The obtained pure CPS fractions (CPS_{cells} and CPS_{OMV}) were analysed by ^1H NMR revealing the same polymer from both cells and vesicles. The GC-MS analysis of the monosaccharides derivatized as AMG disclosed the presence in both cases of rhamnose (Rha), glucose (Glc), and 2-amino-2-deoxy-glucose (GlcN).

Galanos, C. et al. Eur. J. Biochem. (1969), 9, 245-249.
Di Guida, R. et al. Marine Drugs (2020), 18, 231.

Construction of heterologous protein secretion system at low temperatures by using cold-adapted microorganisms

Xianzhu Dai　Southwest University

[Objectives] *Shewanella vesiculosa* HM13, a psychrotrophic bacterium isolated by the group of the ICR partner researcher (Prof. Tatsuo Kurihara) from fish intestine, secretes a large number of spherical particles called extracellular membrane vesicles (EMVs) at low temperatures. These vesicles carry an S-layer protein-like protein, P49, as a single major cargo protein. This highly selective cargo transportation mechanism is expected to be useful for vesiculation-mediated heterologous protein production. In this study, to elucidate the P49-selective secretion mechanism via vesiculation, the involvement of genes coding for functionally unknown proteins found in the vicinity of the P49 gene in the cargo transportation was analyzed.

[Experimental methods] Genes coding for subunit homologs of type II secretion system (T2SS) widely conserved in Gram-negative bacteria, GspDEFGK, and functionally unknown proteins (HM3352, HM3353, HM3355, HM3356, and HM3357) were found in the upstream region of the P49-coding gene (*hm3347*). To delete these functionally unknown genes, two-step single crossover homologous recombination using a *pyrF*-based gene-knockout plasmid, pKKPH, and a *pyrF*-deleted strain, Δ*pyrF*^{HM13}, was conducted. The gene-deletion mutants were cultured at 18 °C, and the localization of P49 in the EMVs was analyzed by western blotting with an anti-P49 antibody. Protein structure prediction programs, I-TASSER and AlphaFold2, were used to predict the function of the functionally unknown proteins.

[Experimental results and discussion] Whole-genome sequence of *S. vesiculosa* HM13 showed that the P49-coding gene was found in the downstream region of a gene cluster including the genes coding for subunits of T2SS and functionally proteins, suggesting that these proteins including functionally unknown proteins form a non-canonical T2SS and play a role in the secretion of P49 to EMVs. Deletion of *hm3353*, *hm3355*, *hm3356*, and *hm3357* caused disappearance of the EMV-localized P49, and P49 was enriched in the cell fraction of the mutants. *In silico* structure prediction of these functionally unknown proteins suggested that the structures of HM3355, HM3353, and HM3352 are similar to those of subunits of T2SS, minor pseudopilin (GspJ) and inner membrane components (GspL and GspM), respectively. It was also predicted that HM3356 and HM3357 form pseudopilin-like structures. These results revealed that these functionally unknown proteins contribute to the transportation of P49 to EMVs as subunits of the non-canonical T2SS.

Optimizing sampling devices and procedures to quantify sources of metals and microplastics in Metro Manila, Philippines' water resources

Abigail P. Cid-Andres　Polytechnic University of the Philippines

Objectives. The main aim of this study was to determine the mechanisms of microplastics and metals in the Philippine environment. The challenges that the microplastics research are undergoing is the lack of devices for sampling and extraction. A device for microplastic sample collection was fabricated. Sampling, collection and extraction with minimal chemicals was optimized.

Experimental Methods. Samples were gathered from various rivers and shoreline in the Philippines for simple chemical analysis. Equipment and consumables were from Professor Yoshiki Sohrin of the Institute for Chemical Research through Global Frontier and Interdisciplinary Research Core for Deepening Investigations and Promoting Collaboration in Chemistry-oriented Fields.

Results and Discussion. Site visits and analysis showed that many of the rivers and shoreline in the study sites were lower than the water quality standard for class C. The Metro Manila bodies of water is gradually rehabilitated. Microplastic mechanisms was not directly related to the concentration of metals in the water. Pb which was formerly used on the pigment materials of plastic were not detected.

Outcome report. The results reported and other addition data will be published in a Scientific Journal. Outreach projects for elementary school children may also be conducted via online platforms. The equipment provided will be used for the continuation of the research.

Workshops. Two (2) Master of Engineering Students were trained using the water quality multiparameter: John Helarch Antoni and Kalvin Campang

Acknowledgement. The authors would like to thank Dr. Yoshiki Sohrin of the Institute of Chemical Research, Kyoto University. This work was supported by the International Collaborative Research Program of Institute for Chemical Research, Kyoto University (grant 2021-74).

Fabrication of Nanotopographical Polymer Surfaces for Bactericidal Properties-III

Maya Endoh　Stony Brook University

Introduction. Bacteria that adhere to the surfaces of implanted medical devices can cause catastrophic infections. Surface topology is of great interest to develop bactericidal surfaces in place of traditional chemical-based approaches that are often toxic to human beings and environments. We have demonstrated a new approach to promote perpendicularly oriented microdomains within block copolymers (BCP) thin films (up to 100 nm thickness) [1]. Through the ICR-iJURC program in collaboration with Dr. Takenaka (ICR), we have identified that polystyrene (PS) "nanopillars" (with the height of 20 nm and the spacing of 60 nm), which are created by preferentially removing the matrix of a cylinder-forming polystyrene-*block*-poly(methyl methacrylate) (PS-*block*-PMMA) thin film, exhibit antibiofouling, bactericidal, and self-cleaning properties against Escherichia coli (*E. Coli*). Moreover, we have identified that the multifunctional properties are significantly enhanced by coating the PS nanopillars with a very thin layer of titanium oxide (TiO_2).

Experiment & Result for Bactericidal Properties. The details of sample preparation can be found in the 2020 report, 2020-73. *E. coli* adsorption experiments on the TiO_2-coated PS nanopillars were conducted as follows: *E. coli* cultures were thawed at room temperature and swabbed on nutrient agar medium in a petri dish. The petri dish was incubated at 37 °C overnight and then multiple swabs of the resulting *E. coli* colonies were transferred into 25 mL of Lysogeny Broth (LB) medium in a centrifuge tube. 100 µl of the bacterial solution was pipetted out from the tube onto a clean petri dish. The TiO_2-coated PS nanopillars were placed on the bacterial droplet with the nanopillars side in contact with the solution and the uncoated side facing the air surface. The petri dish was thereafter covered and incubated at 37°C. Post incubation, the incubated nanopillars were rinsed gently in distilled water twice and dried under air-flow with very low pressure. The viability of *E. coli* on the samples was assessed using the BacLight Live/Dead staining kit (Molecular Probes, Life Technologies, Carlsbad, CA). The samples were incubated for 15 min in the staining solution and rinsed with phosphate-buffered saline. The samples were then examined with an EVOS Microscope (ThermoFisher Scientific) using a standard green filter set to image live cells and a standard red filter to image dead cells. Both live and dead cells were counted using ImageJ software.

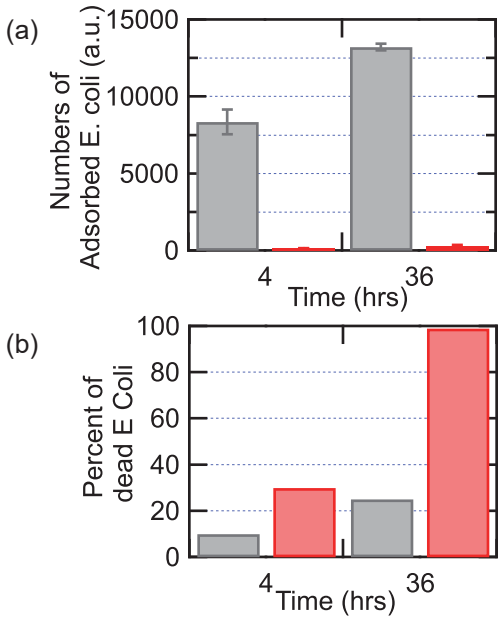


Fig. 1. (a) Numbers of *E. coli* adsorbed on the TiO_2 coated PS nanopillars (red) and a flat TiO_2 control surface (gray) after 4 h and 36 h of immersion in an *E. coli* suspension. (b) Percentage of dead *E. coli* in the LB solution in the presence of the TiO_2-coated PS nanopillars (red) and a flat TiO_2 control surface (gray) after 4 h and 36 h of immersion.

The results demonstrated that the TiO_2-coated nanopillars reduced the amount of adsorbed *E. coli* by about 99% (i.e., *an* anti-fouling property) compared to a 3 nm-thick flat TiO_2 layer after 4 h or 36 h of immersion in a bacterial suspension (Fig. 1a). Notably, the percentage of dead cells adsorbed on the patterned surface was nearly 100 % after 36 h of immersion (i.e., *a* bactericidal property) (Fig. 1b), while more than 60 % of *E. coli* adsorbed on the flat TiO_2 surface were alive under the same conditions. We also analyzed the percentage of dead *E. coli* in the LB solution taken after submersion of the nanopatterned surfaces for up to 36 hours. The results (data not shown) demonstrated that there was no live *E. coli* in the LB solution in the presence of the TiO_2-coated nanopillars after 36 h, whereas the percentage of dead *E. coli* in the presence of the flat TiO_2 sample was just above 20 % under the same conditions. Hence, our results indicate that the TiO_2-coated nanopillars possess *a* self-cleaning property.

Synthesis of Polyether Nanocomposite Solid Polymer Electrolytes for Lithium Ion Batteries

Robert C. Ferrier, Jr.　Michigan State University

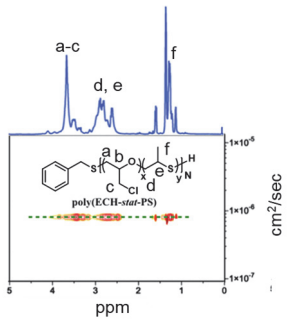


Figure 1. DOSY NMR spectrum of P(ECH-*stat*-PS).

Objective. The objective of this work was to develop novel polyether-based nanocomposite materials by combining the epoxide polymerization techniques of the PI and the surface initiated polymerization techniques developed by the ICR partner researcher, Prof. Ohno from Kyoto University. **Experimental Methods.** Initiators were characterized by ^{1}H NMR spectroscopy. Polymers were characterized by size-exclusion chromatography (SEC), ^{1}H and ^{13}C NMR spectroscopy, diffusion ordered spectroscopy (DOSY), differential scanning calorimetry (DSC), rheometry, and small angle X-ray scattering. Membranes were characterized by FTIR spectroscopy and CO_2 permeability and selectivity were measured in a custom built chamber. **Experimental Results.** Previous results showed interesting ionic conductivity behavior when tuning polymer dielectric constant. To further enhance ionic conductivity, functional copolymers of sulfur containing polymers were synthesized from the statistical copolymerization of propylene sulfide (PS) and epichlorohydrin (ECH). A DOSY spectrum of the copolymer can be seen in **Figure 1**, which suggests both monomers are present along a single backbone and the presence of additional peaks suggests successful statistical copolymerization. Statistical copolymerization of epoxides and PS has not been demonstrated previously. Work is on-going for grafting the initiator to the surface of silica nanoparticles and polymerizing these materials from them. As part of this work, a tetra-functional initiator was produced. We have utilized this newly accessible architecture to create membranes for CO_2 separation, as shown in **Figure 2**. CO_2 selectivity and permeability measurements were undertaken which put our membranes close to the Robeson line. **Publications.** An article co-authored by PI Ferrier and Co-PI Ohno entitled “Facile Synthesis of Epoxide-co-Propylene Sulphide Polymers with Compositional and Architectural Control” was submitted to Polymer Chemistry in December and is currently in revision. Another manuscript based on the membrane work is currently in preparation. My student, Dr. Niloofar Safaie, presented this work at the April meeting of ACS, held virtually, with a talk entitled: “Aluminum-based initiators from thiols for epoxide polymerizations.” Another student, Dr. Geetanjali Shukla presented the membrane work at ACS in August in Atlanta Georgia, with a talk entitled “Star shaped polyether-based cross-linked membranes for separation applications.”

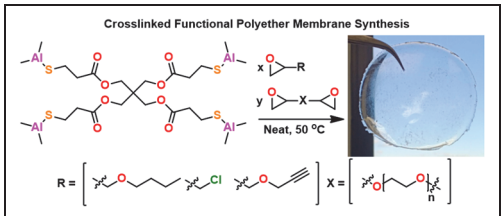


Figure 2. Membrane synthesis.

Verification and development of dynamic stiction theory

Ken Nakano　Yokohama National University

Objectives – Since the time of Charles-Augustin de Coulomb (1736–1806), we have believed that there exist two types of solid friction: static and kinetic friction. However, in 2020, Nakano and Popov published a different friction theory indicating that static friction might be an illusion made by the rotation of kinetic friction [Nakano & Popov, *Phys. Rev. E* **102**, 063001 (2020)]. This friction theory, termed the dynamic stiction (DS) theory, is described within a purely mechanical framework by introducing a geometrical misalignment, the impact of which had been overlooked over two hundred years. In this study, we aimed to verify and develop the DS theory for polymeric materials, including the unique polymeric swollen materials termed the concentrated polymer brushes (CPBs) that have been developed by Professor Yoshinobu Tsujii, ICR, Kyoto University.

Results – A unique friction apparatus that enables direct measurements of the friction force vector has been developed, termed Friction Vector Apparatus (FVA). Sliding tests for 15 polymeric materials were carried out with the FVA. The counter surface was a smooth glass ball with a diameter of 10 mm. The misalignment angle was 0 to 60 degrees, the normal load 6 N, and the drive speed 0.1 mm/s. For PET, the FVA measured the distinct kinetics of friction, showing the friction vector rotation and slow slip in stick phases, which directly supports the validity of the DS theory. However, before sliding under the normal load, it measured an unexpected horizontal force along the principal axis of stiffness of a double cantilever. For the PMMA-CPB swollen by an ionic liquid as a good solvent, the horizontal force at stationary contact disappeared even under the same normal load, although the kinetics of friction was below the measurement range of the FVA because of its ultralow friction.

Discussion – Comparing the results of PET and PMMA-CPB tells us that the horizontal force was caused not by structural errors or measurement errors. It resulted from frictional force even though it was in a stationary state before sliding, indicating that in reality, the stationary contact was subject to an undetectable slow slip. Although generating the horizontal force is still unclear, it is definite that it is similar to the slow slip in the stick phase described by the DS theory.

Outcome report – [1] K. Nakano, “The dynamic stiction mode as a different description of macroscopic static friction”, *Annual Meeting of the Japan Society of Vacuum and Surface Science 2021*, Online, 03 November 2021 (Invited).

Development of semiconductor quantum dot solid films and their charge carrier dynamics

Yasuhiro Tachibana RMIT University

Introduction

Semiconductor quantum dots (QDs) have been recognised as the most promising material for optoelectronic devices such as next generation photovoltaic devices owing to their unique optical and electronic properties. Although their solar cells show relatively high solar energy conversion efficiency, charge carrier dynamics of QD solid films were not well understood. In this project, we develop visible light active semiconductor quantum dots, and assess charge carrier dynamics to compare with their solar cell performance. We have conducted this project with Professor Teranishi at the ICR.

Experimental

A transparent TiO_2 nanocrystalline film (printed area: 0.25 cm^2, film thickness: 6 μm) was prepared by screen-printing the TiO_2 paste (Solaronix SA, Ti-Nanoxide HT/SP) on the FTO substrate. A CdS QD attached nanocrystalline film was prepared by using the ‘‘successive ionic layer adsorption and reaction’’ technique. Transient absorption spectrometers were employed to characterize TiO_2 films [1] and QD/TiO_2 films [2].

Results and Discussion

The charge recombination lifetime at the QD/TiO_2 interface increases, as the QD size increases. An absorbed photon to current conversion efficiency (APCE) of the QDSSC increases, as the QD size increases. Therefore, we conclude that the APCE of the CdS QDSSC is controlled by the interfacial charge recombination dynamics competing with dynamics of the hole transfer from the QD valence band to the reduced electrolyte [2].

Outcomes

[1] H. Liu, M. Liu, R. Nakamura, **Y. Tachibana,** *Appl. Catal. B-Environ.*, **296** (2021) 120226.

[2] S. R. Padmaperuma, M. Liu, R. Nakamura, **Y. Tachibana,** *J. Photopolym. Sci. Technol.*, **34**(3) 271-278 (2021).

Interdisciplinary Approach to Nanostructured Materials for Applications

Jean-Pierre Bucher　Université de Strasbourg

Here we summarize the discussions and first experimental steps that took place around the two main interdisciplinary projects for which Prof. T. Teranishi is our ICR contact.

1) **Structural changes of nanoparticles under pulsed laser irradiation evidenced by means of HR-TEM**. Teranishi's groups (Kyoto) successfully synthesized single crystalline Pd nanocrystals (NCs) capped with phosphine or thiol ligands. These NCs are ready for the investigation by Banhart's group (Strasbourg) of the phase change from crystalline Pd to amorphous PdPx or PdSx under a laser pulse by means of electron diffraction. Further strategies and alternative materials are currently explored.

2) **Self-organization of single molecule magnets (SMM's) by means of macrocycle networks and characterization by LT-STM**. The synthesis of the SMMs takes place in Strasbourg (Ruben's group). This compound is currently sent to Nagoya where it is incorporated in the synthesis of the 2D-crystal made of properly functionalized pi-conjugated macrocycles (Tanaka's group). Next step consists in characterizing the crystallized sample, by means of conventional techniques such as X-ray diffraction and optical techniques. After drop casting on a Au(111) substrate (Nagoya), the 2D network will be examined using low temperature (LT)-STM in Strasbourg (Bucher's group) to study locally the embedded $TbPc_2$ SMM's for their magnetic properties. A first check of the proper growth of the 2D-network on Au(111) will be done in Nagoya by Onoe's group by room temperature STM.

Due to the Covid pandemics, no face-to-face workshops or meetings could be organized in 2021 but a number of Zoom meeting were held during the period. The partners all took part in a kick-off meeting on the 26th of April 2021. A follow-up Zoom-meeting with all participants took place on the 5th of October 2021. Zoom progress-meetings were held on the 22nd of November 2021 and on the 25th January 2022 between Strasbourg and Nagoya (M. Ruben, J.P. Bucher, K. Tanaka, J. Onoe). Other bilateral discussions (phone calls) and meetings took place, between participants.

Novel strategy for intracellular delivery of nanomedicines

Sílvia PUJALS　Institute for Bioengineering of Catalonia

Nanomedicine arose 20 years ago with the promise of selectively delivering drugs to target sites, thus increasing their effectivity while minimizing undesired side effects. However, despite the great promise behind nanomedicine for drug delivery, very few products have been approved for patient use. This poor translation into clinic comes from different factors, some of them being a poor characterization of the nanomaterials or a simplistic model to evaluate them. Poor cellular uptake efficacy of these nanomedicines is also a big obstacle. Our research group has a speciality in preparation of nanoparticles being applied for nanomedicine. We also have strong background of nanomaterials characterization and intracellular behavior using various microscopic techniques (including electron microscopy and super resolution microscopy). On the other hand, Professor Futaki at ICR, Kyoto University is an expert on intracellular delivery of nanomedicines.

The successful cytosolic delivery of nanoparticles is hampered by their endosomal entrapment and degradation. To push forward the smart development of nanoparticles we must reliably detect and quantify their endosomal escape process. However, the current methods employed are not quantitative enough at the nanoscale to achieve this. Nanoscopy is a rapidly evolving field that has developed a diverse set of powerful techniques in the last two decades, opening the door to explore nanomedicine with an unprecedented resolution and specificity. The understanding of key steps in the drug delivery process – such as endosomal escape – would benefit greatly from the implementation of the most recent advances in microscopy. Futaki and coworkers developed delivery peptides potentially applicable to cytosolic delivery of nanoparticles.[1,2] Our group has formulated few batches of Poly(D,L-lactide-co-glycolide) (PLGA) nanoparticles. They are around 200 nm and have DiI (exc 550 nm) or DiO (exc 484 nm) for visualization of their methods of cellular internalization. PLGA-based nanoparticles are biodegradable and widely employed in drug delivery systems in various medical applications. Methods in cellular uptake of these particles are now understudy in Futaki laboratory.

References

1) K. Sakamoto, M. Akishiba, T. Iwata, K. Murata, S. Mizuno, K. Kawano, M. Imanishi, F. Sugiyama, S. Futaki, *Angew. Chem. Int. Ed.* **2020**, *59*, 19990-19998.

2) J. V. V. Arafiles, H. Hirose, Y. Hirai, M. Kuriyama, M. M. Sakyiamah, W. Nomura, K. Sonomura, M. Imanishi, A. Otaka, H. Tamamura, S. Futaki, *Angew. Chem. Int. Ed.* **2021**, *60*, 11928-11936.

Structural and functional analysis of curvature-inducing peptides and application

Anne S. Ulrich　Karlsruhe Institute of Technology

Epsin-1 is a representative protein which induces the positive curvature necessary for the formation of clathrin-coated pits during endocytosis. Modulating the structural dynamics of biomembranes by inducing bilayer curvature and lipid packing defects has been highlighted as a practical tool to modify membrane-dependent cellular processes. Collaborative research of Ulrich research group at KIT with Futaki research group at ICR, Kyoto University has already shown that the N-terminus 18-residue peptide of epsin-1 (EpN18) possess curvature inducing abilities of the parent protein. We also reported that EpN18 also promotes membrane remodeling including lipid packing defects in cell membranes [1]. However, a high concentration is required to exhibit a pronounced effect. We therefore demonstrate a significant increase in the membrane-remodeling effect of EpN18 by constructing a branched EpN18 homotrimer. Both monomer and trimer could enhance cell internalization of octaarginine (R8), a cell-penetrating peptide. The EpN18 trimer, however, promoted the uptake of R8 at an 80-fold lower concentration than the monomer. Analysis of the generalized polarization of a polarity-sensitive dye (di-4-ANEPPDHQ) revealed a higher efficacy of trimeric EpN18 in loosening the lipid packing in the cell membrane. Circular dichroism measurements in the presence of lipid vesicles showed that the EpN18 trimer has a higher α-helix content compared with the monomer. The stronger ability of the EpN18 trimer to impede negative bilayer curvature is also corroborated by solid-state ^{31}P NMR spectroscopy. Hence, trimerizing peptides can be considered a promising approach for an exponential enhancement of their membrane-remodeling performance [2]. In this study, we aimed to study the relationship between the structural factors of EpN18, especially about the helix forming propensity, the component amino acids, and the resulting effects on membrane structures, and to obtain knowledge for the rational design of curvature-inducing peptides. We found the critical contribution of some amino acid residues in EpN18 to enhancing membrane interaction, helical structural formation, curvature induction and lipid packing.

[1] Pujals et al.*ACS Chem. Biol*. **2013**, *8*, 1894
[2] Hsu et al. *Bioorg. Med. Chem. Lett.* **2020**, *30,* 127190.

Research toward stable NV centers at shallow region and spin dynamics in diamond

Gopalakrishnan Balasubramanian　Leibniz institute for surface engineering

Recently, NV centers (Figure 1) in diamond are significantly interested as a candidate of a resource for quantum sensing with nano-scale spatial resolution and ultra-high sensitivity. It is because that single spins can be coherently controlled and the spin coherence time is significantly long even at room temperature (RT) in the NV center. In other solid materials such as quantum dot, molecules, and silicon, those are realized only in extremely low temperature. By utilizing nanoscale shallow NV centers, applications for nanoscale imaging [1] and nanoscale nuclear magnetic resonance were demonstrated. Furthermore, NV centers were successfully integrated into photonic and mechanical structures, and in electronic devices, which expands their versatility.

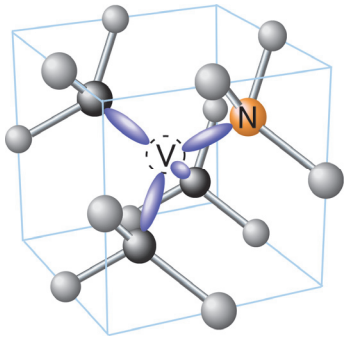


Fig. 1, The NV center in diamond.

Toward these issues, Kyoto University group demonstrates the extension of the spin-coherence time (T_2), the stabilization of the charge state, and an improvement of the creation yield of NV centers formed by the ion-implantation technique at a depth of ~15 nm in phosphorus-doped n-type diamond [2]. We demonstrated the extension of T2, the stabilization of the charge state, and the improvement of the creation yield of the NV centers compared with those generated by the same ion-implantation technique in non-doped diamond. As far as we know, the enhanced T2 is longer than in other reported nanoscale shallow NV centers created by ion-implantation with similar depth. Additional significance stems from the usage of a diamond semiconductor to obtain the enhancements. The present result is important for nano-fabrication of integrated devices, so it paves the way to the development and application of diamond-based quantum-information, sensing, and spintronic devices.

References

[1] Balasubramanian, G., Chan, I., Kolesov, R. et al. Nanoscale imaging magnetometry with diamond spins under ambient conditions. Nature 455, 648–651 (2008).

[2] A. Watanabe, T. Nishikawa, H. Kato, M. Fujie, M. Fujiwara, T. Makino, S. Yamasaki, E. D. Herbschleb, N. Mizuochi, *Carbon*, 178, 294-300 (2021).

Research of quantum controls in multi-qubit diamond quantum processors and quantum sensors

Marcus W. Doherty　Australian National University

Quantum communication and quantum computation are expected to establish a new paradigm and advance our understanding of quantum mechanics. It is considered that they will provide cryptography that can not be decoded and super parallel computation that is much faster than that of ordinary computers. Besides these, technical issues and intriguing questions concerning quantum mechanical phenomena can be addressed. NV centers in diamond (Figure 1) are significantly interested as a candidate as a resource for demonstration and realization. It is because single spins can be coherently controlled [1] at room temperature (RT).

We would like to develop this system further with multi-nuclear spin qubits in this project. We discuss new architectures to enhance the speed and fidelity of quantum processors by using multi-qubits NV centers in diamonds. We discuss the usage and production of isotopically engineered diamonds to improve the speed and fidelity of quantum processors. It is considered that quantum communication and quantum computation will, e.g., provide secure data encryption and super parallel calculation that, in some instances, outperforms classical computers. The realization of them has a strong impact not only on science but also on industry and society.

We recently proposed a full model of multi-qubit diamond quantum processors and developed a semi-analytical method for designing gate pulses [2]. This method optimizes gate speed and fidelity in the presence of random control errors and is readily compatible with feedback optimization routines. We theoretically demonstrate infidelities approaching ~10−5 for single-qubit gates and established evidence that this can also be achieved for a two-qubit CZ gate. Consequently, our method reduces the effects of control errors below the errors introduced by hyperfine field misalignment and the unavoidable decoherence that is intrinsic to the processors. Having developed this optimal control, we simulated the performance of a diamond quantum processor by computing quantum Fourier transforms. We find that the simulated diamond quantum processor can achieve fast operations with low error probability. We continue to discuss the experimental demonstration of this method in this project.

References

[1] P. Neumann, N. Mizuochi, F. Rempp, P. Hemmer, H. Watanabe, S. Yamasaki, V. Jacques, T. Gaebel, F. Jelezko, J. Wrachtrup. *Science*, 320, 1326 (2008).

[2] Y. Chen, S. Stearn, S. Vella, A. Horsley, M. W. Doherty, *New J. Phys.* 22, 093068 (2020).

Molecular mechanisms for the inactivation of a growth hormone in rice

Zuhua He　Chinese Academy of Sciences

Objectives: Gibberellins (GAs) are a class of diterpenoid carboxylic acids. They act as plant hormones that control diverse developmental processes. Bioactive GAs play critical roles in promoting growth, including internode (stem) elongation of rice. The *elongated uppermost internode 2* (*eui2*) mutant of rice shows a tall phenotype due to its elongated uppermost internode. Because of this reason, this mutant has been utilized in hybrid rice breeding in order to eliminate panicle enclosure in male sterile parents. Previously, we have shown by map-based cloning that EUI2 is a functionally-uncharacterized protein that belongs to the α,β-fold hydrolase superfamily. In collaboration with Shinjiro Yamaguchi's group, we have previously characterized the rice *eui* mutant and found that *EUI* encodes a cytochrome P450 enzyme that deactivates GAs via epoxidation. Based on these results, we speculated that EUI2 might act as an epoxy hydrolase and further deactivate epoxidated GAs in the uppermost internode of rice. Last year, in collaboration with Prof. Shinjiro Yamaguchi at ICR in Kyoto University, we found that EUI2 protein could in fact hydrolyze epoxy GAs *in vitro*. In addition, we determined the levels of endogenous epoxy GAs in wild type and the *eui2* mutant by LC-MS/MS analysis.

Experimental methods: Epoxy GAs in rice plants were analyzed by LC-MS/MS after derivatization as ethyl esters. Biological activity of epoxy GAs was determined by a micro-drop method using GA-deficient rice seedlings. The physical interaction between the GA receptor GID1 and epoxy GAs was analyzed by isothermal titration calorimetry (ITC).

Experimental results: To confirm the results obtained last year, we analyzed endogenous epoxy GAs in another genetic background of WT and *eui2* mutant rice plants. Consistent with the previous data, the *eui2* mutant accumulated epoxy GAs at much higher levels than does WT. We chemically synthesized epoxy GA_4 and found that it is weakly, but significantly active in promoting leaf elongation in rice. In addition, our data also showed that the biological activity of the hydrolyzed product (dihydroxy GA_4) was significantly weaker. This finding suggests that EUI2 plays a role in further deactivating epoxy GAs. ITC was used to examine the physical interaction of epoxy GA_4 with the GA receptor GID1. The results demonstrated that epoxy GA_4 is able to weakly interact with GID1 *in vitro*, supporting the notion that epoxy GA_4 was weakly bioactive. ITC analysis also showed that the interaction of dihydroxy GA_4 with GID1 is weaker than that of epoxy GA_4.

Publications: In preparation.

Analysis of novel transporters for strigolactones or their biosynthetic intermediates

Yunde Zhao　University of California San Diego

Objectives: Strigolactones (SLs) are carotenoid-derived plant hormones that regulate many processes of plant growth and development. They are also secreted from plant roots and function as allelochemicals for symbiosis with arbuscular mycorrhizal fungi and stimulating seed germination of parasitic plants. Classical grafting studies have suggested that SL and/or its biosynthetic intermediate(s) can move from roots to shoots, but much has not been fully elucidated about SL transport. Previously, we likely have identified novel transporters for SLs or intermediates for SL biosynthesis in rice. The knockout mutants of the transporters are phenotypically very similar to those well-characterized SL biosynthesis mutants and signaling mutants. The physiological and biochemical roles of the identified transporters need to be experimentally demonstrated.

Experimental methods:

Our group

• Phenotypic and genetic interaction studies of the mutants whose ability to transport SLs or SL biosynthetic intermediates have potentially been compromised.

• Generation of additional mutants using CRISPR/Cas9 gene-editing technology.

ICR partner researchers (Dr. Kiyoshi Mashiguchi, Prof. Shinjiro Yamaguchi)

• Analysis of the endogenous levels of SLs and SL biosynthetic intermediates by LC-MS/MS to find transporters' substrate(s).

• Evaluation of transporters' export/import activity toward the candidate compound(s).

Experimental results: This year, we further conducted genetic studies on the putative SL transporters. Moreover, ICR partner researchers established the method to purify and analyze both the endogenous SLs (4-deoxyorobanchol and orobanchol) and their biosynthetic intermediates (carlactone, carlactonoic acid, methyl carlactonoate) from the same plant sample by using several solid-phase extraction（SPE）cartridges and LC-MS/MS, respectively. We are going to analyze the endogenous amounts of SLs and their biosynthetic intermediates using the knockout mutants of the transporters.

Publications: No publications from the collaboration in FY2021.

1,3-Dipolar Cycloaddition Reactions of Cycloparaphenylenes with Azomethine Ylide

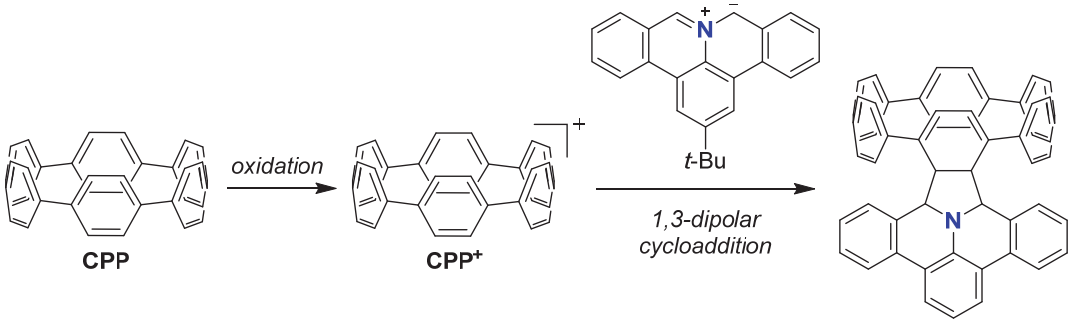
Shingo Ito　Nanyang Technological University

Objective

In this research, we aim to develop the synthesis of novel nitrogen-containing carbon nanotubes and their application to novel organic electronic devices. Since Prof. Yamago is a pioneer of cycloparaphenlyne (CPP) chemistry[1] and Prof. Ito has an effective π-extension method using azomethine ylides (AMY),[2] we offer novel synthetic methods for breakthrough tube-shaped molecules throughout this collaborative research.

Results and Discussion

First, DFT calculations were performed to confirm whether the 1,3-dipolar cycloaddition reaction of CPP and AMY is feasible. The results indicated that the reaction with neutral CPP may not proceed, but the reaction with cationic CPP could proceed. Therefore, a cationic CPP was prepared by oxidation and used for a cycloaddition reaction with azomethine ylide. However, no compound corresponding to the cycloadduct was detected by MALDI and NMR analyses.



Scheme 1

Reference

1) Yamago, S.; Kayahara, E. *J. Synth. Org. Chem. Jpn.* **2019**, *77*, 1147–1158.
2) S. Ito, Tokimaru, K. Nozaki, *Angew Chem. Int. Ed.* **2015**, *54*, 7256–7260.

Dendritic Amphiphilic Block Copolymers as Additive for Polyvinylidenedifluoride Based Membranes

Mona Semsarilar　University of Montpellier

This project is a collaboration between Dr. Mona Semsarilar from University of Montpellier (France), Prof. Shigeru Yamago and A/Prof. Yangtian Lu from University of Kyoto (Japan).

Objectives:

The aim of this project is to prepare porous polyvinylidene difluoride (PVDF) membranes with hydrophilic character for water filtration. PVDF is hydrophobic and incompatible (immiscible) with all other polymers apart from polymethyl methacrylate (PMMA). PVDF is normally blended with hydrophilic polymers in order to confer hydrophilicity to the prepared membranes. However, due to the immiscibility of PVDF with other polymers this method would result in membranes with inhomogeneous and short-lived hydrophilic character. To solve this major problem we propose to synthesize an amphiphilic block copolymer where one block is a linear hydrophobic PMMA and the other block is a dendritic hydrophilic polymer. The linear PMMA block will fully blend with the high molecular weight PVDF and allow the homogeneous dispersion of the hydrophilic polymer segments within the PVDF matrix.

Experimental methods and results: As per the original design of the project, Prof. Yamago's team has synthesied amphiphilic dendritic block copolymers via TERP controlled polymerization. A library of twelve polymers have been prepared. The French team has studied the blending properties of the synthesized block copolymers with the high molecular weight PVDF and the membrane fabrication. Via solvent/ non-solvent phase inversion method (SNIPS). The prepared membranes were fully characterized (SEM, AFM, FTIR and water contact angle). The performance of the resulting membranes were verified via a dead-end filtration set-up. Flux and permeability values at different pressure points were collected and evaluated.

Publications: This collaborative project started in March 2021. As all the countries are still under restrictions imposed by COVID19 pandemic, none of the planned visits could take place. As the proposed tasks in the project could not be carried as planned due to border closures, the two partners have rework the plan and deploy some exiting funds to carry on the work. The Yamago team, prepared some block copolymers (sent to France by air post) and the French team worked on the preparation and characterization of the membranes. An article based on the data acquired is under preparation.　Regardless of the unfortunate circumstances, both partners are enthusiastic to carry on with this collaboration.

Search for four-wave-mixing in the vacuum
- Unveiling dark components in the Universe –

Kensuke Homma　Hiroshima University

Purpose and Method

The purpose of this study is to search for Four-Wave-Mixing (FWM) phenomena in the vacuum in order to understand dark components in the Universe. So far, we have constructed and improved an ultra-high vacuum chamber in ICR toward the search. In this vacuum chamber, two-color laser pulses are collinearly combined and focused into the vacuum along the same optical axis. If photon-photon interactions occur in the vacuum environment, generation of intrinsic FMW photons via the stimulated interaction $\omega+\omega\rightarrow(2\text{-u})\omega+\mathrm{u}\omega$ is enhanced, where ω is the energy of the creation laser pulse and $\mathrm{u}\omega$ is the energy of the inducing laser pulse with $0<u<1$. The signal photon energy in this scattering process corresponds to $(2\text{-u})\omega$.

Progress and Achievements

We have extended the search by increasing laser intensity and also updating the theoretical interface to obtain the exclusion domain on the coupling parameter between a new particle state and photons.

As the present status, we have succeeded to publish a paper on the search result to a journal. On this paper we have called a press conference in Hiroshima University and the article has been published in MyNavi. In addition, we have published a paper on a perspective of our approach including GHz-band photon sources in addition to the laser sources. We summarize the published papers, two relevant invited talks and the press release during FY2021 as follows.

Published papers:

[1] **Search for sub-eV axion-like resonance states via stimulated quasi-parallel laser collisions with the parameterization including fully asymmetric collisional geometry**, Kensuke Homma*, Yuri Kirita, Masaki Hashida, Yusuke Hirahara, Shunsuke Inoue, Fumiya Ishibashi, Yoshihide Nakamiya, Liviu Neagu, Akihide Nobuhiro, Takaya Ozaki, Madalin-Mihai Rosu, Shuji Sakabe and Ovidiu Tesileanu (The SAPPHIRES collaboration), Journal of High Energy Physics volume 2021, Article number: 108 (2021).（acknowledge the support by ICR）

[2] **Perspective of Direct Search for Dark Components in the Universe with Multi-Wavelengths Stimulated Resonant Photon-Photon Colliders high-quality vacuum system",** Kensuke Homma*, Yuri Kirita, Fumiya Ishibashi,　Universe 7 (2021) 12, 479.（acknowledge the support by ICR）

Invited talk:

[1] **Perspective of direct search for dark components in the Universe with multi-wavelengths photons**

Kensuke Homma, Nuclear Photonics 2020 (2021.6.9)

[2] **Search for Sub-eV Axion-Like Resonance States via Stimulated Quasi-Parallel Laser Collisions with the Parameterization Including Fully Asymmetric Collisional Geometry**

Kensuke Homma, 29th ANNUAL INTERNATIONAL LASER PHYSICS WORKSHOP (2021.7.22)

Press release:

[1] https://www.hiroshima-u.ac.jp/research/news/68458

Development of Perovskite and Perovskite-like Emitters and Their Applications

Hao-Wu Lin National Tsing Hua University

Developing high-performance halide perovskite light-emitting materials has also become a popular research topic. The research topics of this study are the syntheses, properties, and applications of 0 ~ 2 dimensional perovskite and perovskite-like halide materials.

We developed an antisolvent reprecipitation method to synthesize lead-free halide double perovskite materials $Cs_2(Na,Ag)(In,Bi)Cl_6$. After the optimization of process parameters and compositions, yellowish-white light-emitting materials with ultra-broad photoluminescence spectrum from visible to near-infrared (see Figure 1) and a decent photoluminescence quantum yield (PLQY) of 50% were obtained.

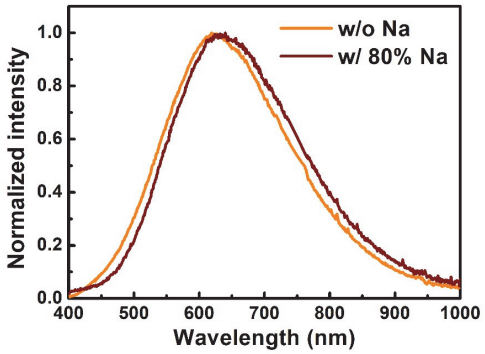


Fig. 1. Emission spectra of $Cs_2(Na,Ag)(In,Bi)Cl_6$.

We also investigated the ball-milling mechanosynthesis procedure, which has attracted much attention recently. A variety of emitting materials were synthesized through ball-milling, including $CsPbBr_3$, lead-free halide double perovskites, and 0-dimensional copper(I)-based halide materials such as $Cs_3Cu_2I_5$, $CsCu_2I_3$, and $(MA)_4Cu_2Br_6$. The convenience and universality of the ball-milling procedure were verified through these attempts.

These materials were utilized as X-ray scintillators for X-ray image applications. Fig. 2 shows the detected photon counts versus X-ray dose rate curve. The scintillator exhibited promising linear response characteristics and very low detection limit of 15 nGy/s, indicating a great potential of using these lead-free $Cs_2(Na,Ag)(In,Bi)Cl_6$ perovskite for X-ray detectors targeting to the medical and industrial inspection applications.

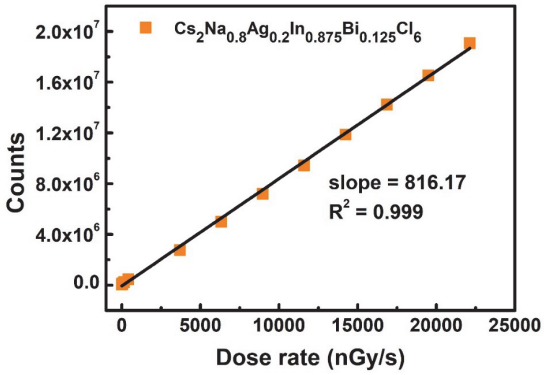


Fig. 2. X-ray response of light emitting $Cs_2(Na,Ag)(In,Bi)Cl_6$.

[1] Po-Ting Lai, Hao-Cheng Lin, Yung-Tang Chuang, Chien-Yu Chen, Wei-Kai Cheng, Guang-Hsun Tan, Bo-Wei Hsu, Lin Yang, Shiu-Cheng Lou, Li-Jen Chien, Hau-Wei Wang, and Hao-Wu Lin, *ACS Appl. Mater. Interfaces* **2022**, *14,* 19795.

[2] Shu-Wen Dai, Ying-Lin Lai, Lin Yang, Yung-Tang Chuang, Guang-Hsun Tan, Shin-Wei Shen, Yu-Sheng Huang, Yuan-Chih Lo, Tzu-Hung Yeh, Chih-I Wu, Lih-Juann Chen, Ming-Yen Lu, Ken-Tsung Wong, Shun-Wei Liu, Hao-Wu Lin, *ACS Appl. Mater. Interfaces* **2021**, 21, 25202.

モデルポリアルキルスチレン類を用いた分子構造と粘弾性パラメータの相関解析

高野敦志　名古屋大学

【緒言】高分子物性の中には高分子を構成するモノマーの分子構造には依存しない性質（例えば、ゼロずり粘度の分子量依存性など）がある一方で、個々の分子構造に依存する性質（例えば、ガラス転移温度（T_g）、絡み合い点間分子量（M_e）、など）もある。後者の研究例として、モノマーユニットに対して炭素数、線状－分岐状、および結合位置などの異なるアルキル側鎖が導入された一連の高分子を利用したものがあり、例えばポリ（n-アルキルメタクリレート）系などで Tg などのアルキル側鎖依存性が調べられている。しかし、分子量分布が狭く、かつ高分子量に及ぶ広い分子量範囲で試料調製を行い、分子構造を系統的に変化させた一連のモデル高分子を用いて粘弾性評価がなされた例は少ない。本研究では一連のポリアルキルスチレン類（Figure 1）を精密合成し、分子構造と粘弾性パラメータの相関関係を調査、検討した。

【実験】側鎖の直鎖アルキル基の炭素数（m）が異なる n-アルキルスチレン（m＝1, 2, 3, 4, 6, および 8）、ならびに分岐アルキル基（イソプロピル、*tert*-ブチル、*sec*-ブチル）を有するアルキルスチレンをモノマーとしてリビングアニオン重合により、狭い分子量分布を持ち、かつ広い分子量範囲でポリマーを合成した。ポリマー試料の分子量および分子量分布は多角度光散乱（MALS）およびサイズ排除クロマトグラフィー（SEC）により評価した。T_g は示差走査熱量（DSC）測定により求めた。動的粘弾性（TA instruments 社製 ARES-G2 使用）は、8mm ϕパラレルプレート、N_2 雰囲気下、 歪み 1～5%（線形領域）の条件下で測定した。

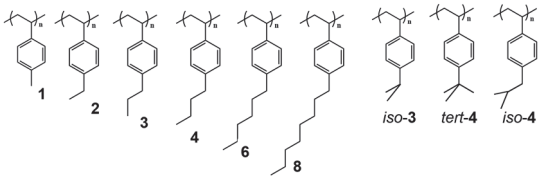


Figure 1. The molecular structure of the polymers used in this study.

【結果と考察】ポリアルキルスチレン試料の T_g の分子量依存性を調べたところ、両者の関係は Fox-Flory の経験式により概ね記述できることが示された。ポリ（n-アルキルスチレン）試料のアルキル炭素数と T_g の関係を調べてみると、ポリスチレンの T_g（＝100℃）を基準とするとき、メチル基の導入により一旦 T_g は増加するが、その後炭素数の増加に伴い、T_g は単調に低下していくことが分かった。一方、分岐アルキル基の導入は T_g の増加をもたらすことが確認された。分子構造と T_g の関係を考察してみると、まずポリ（4-メチルスチレン）では、メチル基は回転に伴う分子鎖まわりの自由体積の変化はほとんどないことから、主鎖に対してはフェニル基より大きな側鎖官能基が連結しているとみなすことができる。大きな官能基は主鎖の運動性を低下させるため、T_g の上昇につながると予想される。一方、ポリ（4-エチルスチレン）になると、エチル基の C-C-C 結合が 109.28 度で連結しているため、側鎖の回転運動に伴い、分子鎖まわりに自由体積の変化が起こる。これが主鎖の運動性を高め、T_g を低下させると予想される。従ってエチル基→オクチル基への炭素数の増加に従い、T_g は低下していくと考えられる。一方、ポリ分岐アルキルスチレン類の場合、側鎖官能基が嵩高く、側鎖官能基の回転に伴う分子鎖まわりの自由体積の変化は少ない。そのため上述のメチル基同様、大きな側鎖官能基が連結されているとみなすことができる。

【成果報告】以上の成果は、レオロジー討論会（オンライン）にて口頭発表した。

Study on the Regulatory Network of Plant Epidermal Cell Differentiation

Rumi Tominaga　Hiroshima University

Objectives: The cell differentiation and its deposition pattern are crucial determinants of plant structures and functions. Among multiple types of plant cells, the root epidermis of *Arabidopsis thaliana* has served as an excellent model system for studying plant cell differentiation and pattern formation. In *Arabidopsis*, the root epidermis is composed of the non-hair (N) and hair (H) cell files, and only cells in the H cell files develop root hairs. For root hair development, numerous transcription factor genes constitute a regulatory network, and *GLABRA2* (*GL2*) is located at the bottleneck between the cell pattern formation and subsequent cell differentiation. We have identified several *Arabidopsis* bHLH transcription factor genes, including *ROOT HAIR DEFECTIVE6* (*RHD6*), *ROOT HAIR DEFECTIVE6-LIKE1* (*RSL1*), *RSL2*, *Lotus japonicus ROOTHAIRLESS1-LIKE1* (*LRL1*), and *LRL2*, as direct targets of GL2. These genes are suppressed by GL2 in N cell files and are expressed in various developmental stages of root hair cells. Among transcription factors encoded by them, only LRL1 and LRL2 conferred root hairs in N cell files when ectopically expressed. To understand the transcriptional network and cell biological events downstream LRL1 and LRL2, we performed genetic analysis in combination with a glucocorticoid (GR) induction system.

Experimental Methods: Transgenic *Arabidopsis* lines with the transgene *LRL1g-GR*, which expressed the fusion protein LRL1-GR by the *LRL1* promoter, were established under the *lrl1* mutant background. Root hair phenotypes of the transgenic lines and the *lrl1* mutant were observed under normal conditions or induction conditions with glucocorticoid treatment. The transgenic lines were crossed with the *lrl2* mutant line to establish the transgenic line with the *lrl1lrl2* background.

Results and Discussion: Seedlings of the *lrl1* mutant exhibited significantly shorter root hairs than the wild type. The phenotype was completely rescued by the *LRL1g-GR* transgene under glucocorticoid treatment conditions, but not under normal conditions, indicating that the fusion protein LRL1-GR is conditionally functional depending on glucocorticoid. After crossing the transgenic rescue lines with the *lrl2* mutant line, we first selected *LRL1g-GR* transgenic plants with the genetic background of *lrl1lrl2*/+ (*lrl1*-homozygous and *lrl2*-heterozygous) among the F2 plants. When the selected plants were grown under normal growth conditions, their progeny didn't include transgenic plants with the *lrl1lrl2* background (*LRL1g-GR*/*lrl1lrl2*). However, *LRL1g-GR*/*lrl1lrl2* plants were obtained by continuously treating their parental plants with glucocorticoid. The *LRL1g-GR*/*lrl1lrl2* plants exhibited a no-root-hair phenotype, which was rescued by glucocorticoid treatment. These indicate that the *LRL1* and *LRL2* genes redundantly function in essential processes for both root hair development and male gametophyte fertility.

免疫賦活化するナノ集合体

山崎晶　大阪大学

ワクチンは感染症を予防するための最も良い医学的介入の一つである。安全なワクチンとして、病原体の抗原となる部分だけをとりだしたサブユニットワクチンが開発され、臨床的に広く用いられている。しかしながら、サブユニットワクチンは十分な免疫原性を有しておらず、十分な免疫応答を誘導するためにはアジュバントと呼ばれる抗原性補強剤との併用が必要である。これまでにアラムや水中油型エマルションなどが開発されているが、数が限られている。新興ウイルスに対応して効果的なワクチンを準備しなければならず、また、今後実用化されるであろう癌ワクチンにもアジュバントが必要とされる。アジュバントのレパートリーを増やすことが急務である。一般に、免疫応答とアジュバント活性には、分子の大きさが関与している。本研究では、自発的に集合して巨大化する「自己集合」という材料化学の概念、ケミカルバイオロジー、免疫学の手法を組み合わせて、アジュバント材料を発見・理解することを試みた。

2021 年度は、コリカマイドと抗原ペプチドとの併用による抗腫瘍活性を検討した。しかし、骨髄由来樹状細胞(BMDC)においてコリカマイドは細胞毒性を示したため、コリカマイドの構造を最適化して低毒性化することにした。アジュバントの安全性は実用化にとって極めて重要である。12 種類の新しい誘導体を評価した結果、C7 が発見され、BMDC においてコリカマイドの 3 倍以上の免疫賦活効果を示すことがわかった。重要なことに、C7 は 80 μ M まで BMDC にほとんど細胞毒性を示さなかった。C7 の毒性をマウスでも評価した。500 μg 投与しても、肝毒性の指標である ALT、AST、ALP および腎毒性の指標である UREA、CREA の上昇は認められなかった。C7 を新たな候補として研究をすすめた。

C7 は免疫賦活作用が強く、毒性も低いことから、癌ワクチンのアジュバントとしての可能性を検討した。マウスにメラノーマを移植し、癌体積、生存率、体重減少を評価した。対照群および C7 のみを投与した群では、癌体積が増加し、15 日以内にすべてのマウスが死亡したが、抗原ペプチドと C7 を投与した群では、癌体積の増加が著しく抑制され、21 日生存率は 80%に達した。一方、抗原ペプチドのみを投与した群では、癌体積の増加はわずかに抑制されたものの、21 日生存率は 20%にとどまった。C7 の細胞毒性が低い理由はまだ不明である。動的光散乱実験から、C7 の集合体は、コリカマイドの集合体よりも熱力学的に安定であることが示唆された。この C7 集合体の安定度が、癌ワクチンアジュバントとしての優れた特性の一端を担っているのかもしれない。

自己集合性分子による心筋細胞移植の効率化

柴祐司　信州大学

現在の内科的、外科的治療法は心不全患者の症状の緩和と、病気の進行抑制に有効であるが、病気を治癒させることは出来ない。重症心不全に対する唯一根本的な治療は心臓移植であるが、ドナー不足は深刻である。近年、多能性幹細胞から心筋細胞を作製するプロトコールが複数報告され、大量の心筋細胞を作製することが可能となっている。

本研究では、京都大学化学研究所の上杉グループと共に、心筋細胞分化を誘導する化合物 KY02111 のメカニズムを解明した。本化合物は上杉グループと中辻グループによって発見された化合物であり、強力な心筋分化能力をもつ。現在、心筋分化の大量調整に利用されている。しかし、そのメカニズムは解明されていなかった。共同研究研究により、KY02111 の標的タンパク質として酵素 SQS を同定した。面白いことに、KY02111 は SQS の酵素活性には影響せず、SQS と TMEM43 とのタンパク―タンパク相互作用を阻害していた。

TMEM43 は核膜の維持に重要とされているがその役割は明確にされていない。TMEM43 の変異は主に心臓疾患に見られる。最も侵攻性の高い不整脈原性心筋症/ARVC サブタイプは ARVC5 型（ARVC5）で、TMEM43 の S358L 変異が原因である。S358L 変異が SQS との相互作用に及ぼす影響を調べたところ、変異した TMEM43 は SQS と会合しなかった。TMEM43 と SQS の相互作用の阻害が ARVC の表現型と関係している可能性が示唆された。

柴グループでは、心筋形成において、KY02111 によって SQS-TMEM43 の相互作用が阻害され続けることが、ARVC の表現型につながるのではないかと推測した。この仮説を検証するために、ヒト iPS 細胞の 18 日間の心筋形成プロトコルの間、KY02111 を培養液に添加した。この確立されたプロトコルは、高い TNNT2 発現レベルを有する 80%の cTNT 陽性細胞を生成する。これら 2 つの心筋細胞マーカーの発現レベルは、KY02111 による連続処理によって有意に減少した。KY02111 処理細胞は、前脂肪細胞マーカー（DLK1 および PPARG）のレベル上昇を示した。これらのデータを総合すると、SQS-TMEM43 相互作用の破壊が ARVC 表現型に寄与し、KY02111 は疾患を模倣するツールとして機能することが示唆された。これらの上杉グループとの共同研究は 2021 年に *Angew. Chem. Int. Ed.*に発表した。

Y. Takemoto, S. Kadota, I. Minami, S. Otsuka, S. Okuda, M. Abo, L. L. Punzalan, Y. Shen, Y. Shiba, M. Uesugi, Chemical Genetics Reveals a Role of Squalene Synthase in TGFβ Signaling and Cardiomyogenesis, ***Angew. Chem. Int. Ed.*** 2021, 60, 21824.

共役系ポリマーの開発と非フラーレン型太陽電池の高効率化

尾坂格　広島大学

【研究背景と目的】

有機薄膜太陽電池（OPV）は、次世代の太陽電池として注目されている。OPV の課題はエネルギー変換効率（PCE）の向上であり、これに向けて高性能な発電材料の開発が求められている。一方、発電材料の結晶状態は OPV 特性に大きな影響を与えるため、これを制御することが高効率化に向けて重要である。我々は以前、ドナー材料に高い結晶性を有するチアゾロチアゾール系ポリマーPTzBT（Figure 1）、アクセプター材料にフラーレン誘導体 PCBM を用いた OPV 素子が、良好な PCE を与えることを報告した。一方、PTzBT は非フラーレン系アクセプター材料を組み合わせると、変換効率が低下することを報告した。これは、非フラーレンと組み合わせることで、PTzBT の結晶性が著しく低下したためである。そこで本研究では、PTzBT におけるアルキル基をエステル基に置換した PTzBTE（Figure 1）を合成した。PTzBTE は、エステル基内の酸素と主鎖内の硫黄との分子内非結合性相互作用により、結晶性の向上が期待できる。

【実験結果と考察】

PTzBTE は PTzBT とほぼ同様の吸収スペクトルを示したが、HOMO および LUMO 準位は PTzBT よりも深いことが分かった。これは、エステル基の電子求引効果に起因する。また、ポリマー単独膜の X 線回折測定を行ったところ、PTzBTE は PTzBT に比べて、結晶性がやや高く、電荷輸送性に有利な Face-on 配向性が強くなっていることが明らかとなった。

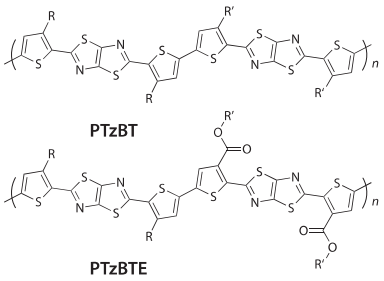


Figure 1. Chemical structure of PTzBT and PTzBTE.

次に、PCBM を用いた OPV 素子を作製したところ、PTzBT は約 7%の PCE を与えたが、PTzBTE は主に V_{OC} が向上し、8%を超える高い PCE を示した [3]。一方、非フラーレンアクセプター材料である IT-4F や Y6 を用いた OPV 素子では、PTzBT の PCE は 6〜8%程度であったが、PTzBTE の PCE は 12〜13%と顕著に高い値を示した。しかし興味深いことに、Y6 と類似の非フラーレンアクセプターである Y12 を用いた素子では、PTzBT は最大 13.8%、PTzBTE は最大 14.8%と高い PCE を示した。これは、ポリマーとアクセプターの組み合わせにより、それぞれの結晶状態が変化したことと相関することが分かった。

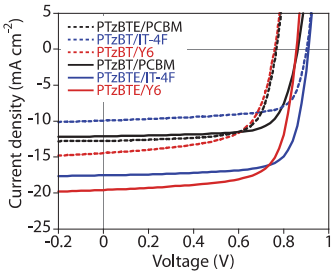


Figure 2. Current-voltage curves of the OPV cells based on PTzBT and PTzBTE.

【成果報告】

＜論文＞ (1) K. Yamanaka, M. Saito, T. Mikie, I. Osaka, *Bull. Chem. Soc. Chem.*, **2021**, *94*, 2019-2027.

＜学会発表＞ (1) 山中 滉大，三木江 翼，斎藤 慎彦，キム ヒョンド，大北 英生，尾坂 格「分子内非結合性相互作用によるチアゾロチアゾール系ポリマーの高結晶化と有機太陽電池の高効率化」，第 70 回 高分子討論会（オンライン）

Demonstration of topological phase control in chalcogenide superlattice

Misako Morota AIST

Purpose: The aim of this research is to create topological properties from materials used in the phase-change memory devices and to demonstrate new functions of these materials. Topological materials have a characteristic surface electronic state caused by strong spin-orbit coupling, and are expected to be the next generation of highly efficient spin current sources to replace transition metals. On the other hand, the superlattice type phase-change memory, which is currently being developed, is composed of germanium telluride (GeTe) and antimony telluride (Sb_2Te_3), which are normal insulator (NI) and topological insulator (TI), respectively. This superlattice is expected theoretically to be possible to produce various topological phases by controlling the degree of hybridization of wave functions on the TI surface. In this study, the goal is to investigate the correlation between the spin generation efficiency of GeTe and Sb_2Te_3 multilayers and the stacking order by Spin Torque Ferromagnetic Resonance (ST-FMR) measurements. So firstly, we confirmed the fabrication process and the measurement system for a single layer of topological insulator Sb_2Te_3.

Experimental: ST-FMR measurement samples were first deposited at AIST using RF sputtering of Sb_2Te_3 5nm/CoFeB 5nm/SiO_2 3nm, and then the device and electrode fabrication and ST-FMR measurement were performed at Institute for Chemical Research, Kyoto University. In order to check the fabrication process and to compare with topological insulators, the sample was also prepared by replacing the Sb_2Te_3 layer with transition metal platinum (Pt).

Results and Discussion: The figure shows the relationship between the external magnetic field and the voltage at different frequencies in the Sb_2Te_3 and Pt layers with 5-nm thickness. Comparing the Sb_2Te_3 and Pt samples, the voltage spectra are asymmetric in the Pt samples, while apparently symmetric in the Sb_2Te_3 samples. This means that the spin torque generated by the spin current from Sb_2Te_3 is larger than the torque induced by the magnetic field caused by the current flowing in the Sb_2Te_3 layer. this result suggests that the highly efficient charge-spin current conversion property of Sb_2Te_3, which is worthy of further investigation in the future.

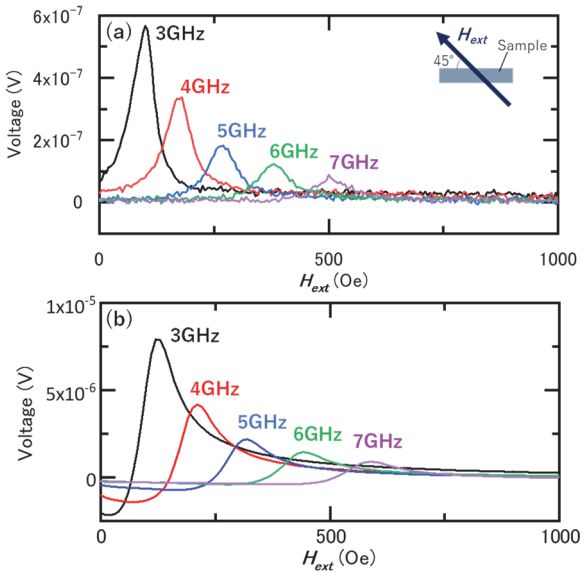


Figure. ST-FMR signals as a function of external field for (a) Sb_2Te_3 and (b) Pt with varied frequencies. The inset shows the direction of the applied external magnetic field for a sample.

Study of spin dynamics in garnet nanocrystal thin films prepared by co-precipitation method

Keisuke Yamada　Gifu University

【**Introduction**】Thermoelectric conversion elements utilizing the spin Seebeck effect (SSE) enabled in such a simple structure have recently attracted much attention owing to their unique properties and demands for future practical use. Synthetic YIG, including bismuth-doped YIG (Bi-YIG), is also attractive as materials gain large SSE voltages. Since Bi is characterized by strong polarizability, the effective spin-orbit coupling (SOC) is induced in Bi-YIG, therefore, the SOC might affect the spin–thermoelectric phenomena for SSE. In this report, we report on the longitudinal SSE (LSSE) voltage in Bi-YIG films prepared on a Si substrate via a sol-gel solution using a spin-coating process to investigate the effect of Bi composition on the LSSE voltage.

【**Experimental Method**】$Bi_xY_{3-x}Fe_5O_{12}$ ($0 \leq x \leq 1.2$) film samples were made on a Si substrate by sol-gel, spin-coating, and annealing at T_a = 973-1073 K for 2 hours in air. Their structure and magnetic properties were characterized by X-ray diffractometry (XRD), scanning electron microscopy (SEM), ferromagnetic resonance (FMR) measurements and LSSE measurements. FMR measurements were performed at ICR of Kyoto Univ.

【**Results and Discussion**】According to the X-ray diffraction spectra of the samples, diffraction peaks associated with the garnet phase are readily observed. Figure 1(a) shows surface and cross-sectional SEM images of the Bi-YIG film at x = 0.8 annealed at 973 K. The thickness of the film formed by the agglomeration of nanoparticles was approximately 50 nm. Figure 1(b) shows that the LSSE constant (S) and thermoelectric performance (TP) of the Bi-YIG/Pt (5 nm) films tends to increase with increasing Bi composition ($0 \leq x \leq 0.8$), and the value of the TP at x = 0.8 is 1.7 times larger than that at x = 0. This result indicates that the increasing tendency of the TP occurs because of the efficient spin current conversion from Bi-YIG to the Pt layer due to Bi substitution.

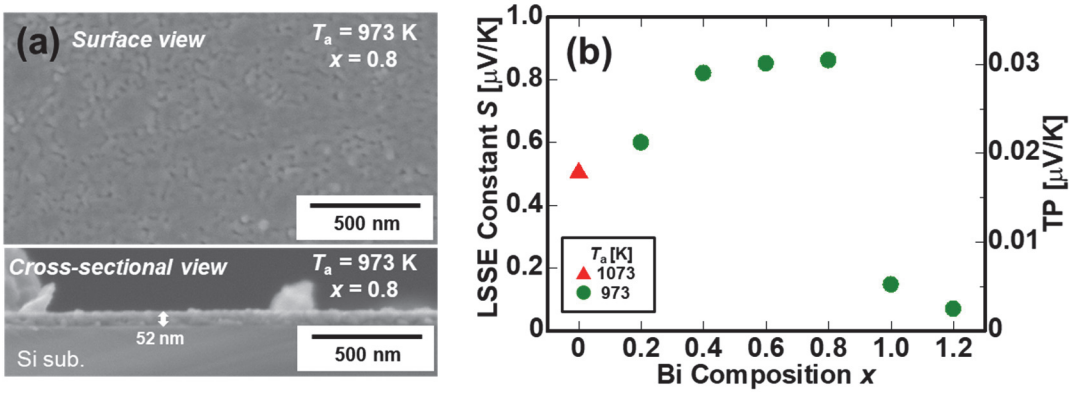


Figure 1: (a) Surface and cross-sectional SEM images of Bi-YIG at x = 0.8 annealed at 973 K. (b) Bi composition x dependence on S (left axis) and TP (right axis) at various T_a.

【**Achievement reports**】(1) M. Yamamoto, et al. *under Review*. (2) K. Yamada, et al. *Journal of Magnetism and Magnetic Materials* **535**, 168093 (2021).

Study on electronic and magnetic behavior of perpendicularly magnetized cobalt ferrite films

Masaaki Tanaka Nagoya Institute of Technology

The tunneling electron through ferromagnetic insulator films is spin-polarized because of the barrier height difference depending on spin. Ferrimagnetic insulator $Co_xFe_{3-x}O_{4+\delta}$ (CFO, $0<x<1$) films with in-plane elongational strain, which have large perpendicular magnetic anisotropy (PMA), can be applied for spin injection source of PMA spintronics devices. In this study, the tunnel magnetoresistance (TMR) effect using perpendicularly magnetized CFO films was investigated.

CFO (x=0.6, t = 0.8 nm, 1.5 nm, and 3.0 nm)/MgO (2.0 nm)/Co (1.5 nm)/$\{Tb/Co\}_n$ (13 nm)/Co(2.0 nm) films were grown on conductive $Co_{0.2}Fe_{2.8}O_{4+\delta'}$ films of 20 nm thickness. The conductive $Co_{0.2}Fe_{2.8}O_{4+\delta'}$ films, which have conductivity due to electron hopping between Fe^{2+} and Fe^{3+} and have PMA, are used for the bottom electrodes of magnetic tunnel junctions (MTJs). The CFO films grown on the $Co_{0.2}Fe_{2.8}O_{4+\delta'}$ films can be expected to decrease antiphase boundary because both CFO and $Co_{0.2}Fe_{2.8}O_{4+\delta'}$ are inverse spinel structures. The out-of-plane hysteresis loops of these films show two magnetization switching steps. The MTJs with a junction diameter of 15 μm were fabricated using photolithography and dry etching by an ion-milling method. This microfabrication was carried out at ICR, Kyoto University. The current-voltage and magnetoresistance measurements of the MTJs were performed using a four-probe method at various temperatures.

The current-voltage measurements indicated that the CFO/MgO layer shows good tunneling properties. The resistance increased dramatically with decreasing temperature, which indicates that the conductivity of the junction is governed by the tunneling current. Figure 1 shows the magnetoresistance of the MTJ (t= 3.0 nm) at 300 K at the bias voltage of 200 mV. The TMR effect caused by the magnetization switching of CFO and CoFe/$\{Tb/Co\}_n$ layers was observed. The TMR ratio at 100 K and 300 K were −18% and −2.7 %, respectively. It was also found that the TMR ratio decreased with the decrease of CFO thickness.

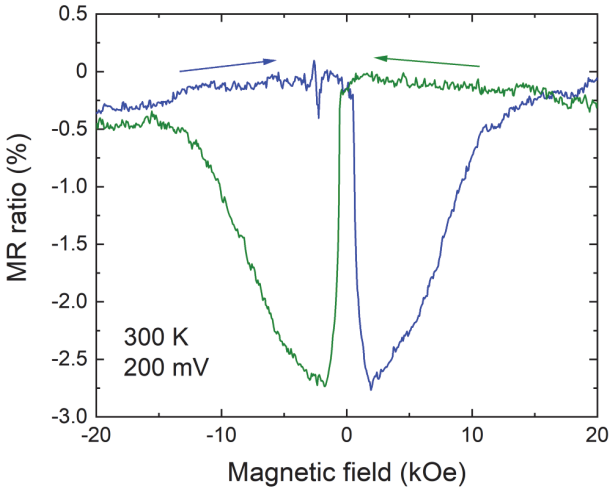


Fig. 1 Magnetoresistance of the MTJ (t= 3.0 nm) at 300 K at the bias voltage of 200 mV.

Electronic and spintronic properties of multilayer system including $NiCo_2O_4$ and Fe_3O_4

Taro Nagahama　Hokkaido University

Introduction: Recently, spinel oxides have attracted considerable attention because of their potential in spintronics research. The inverse spinel oxide $NiCo_2O_4$ (NCO) is a promising magnetic oxide with potential applications in spintronics devices due to its metallic conductivity and ferrimagnetism. In particular, NCO was theoretically predicted to have electronic states corresponding to a half-metal with perfect negative polarization of −100% at the Fermi level, indicating that it provides a highly spin-polarized current. More recently, large TMR ratios in excess of 200% were experimentally observed for NCO/MAO/NCO perpendicular MTJs, demonstrating that NCO has a large spin polarization. However, the sign of spin polarization remains unclear. In this study, direct evidence of negative spin polarization, namely the inverse TMR effect, was observed in NCO/MgO/Fe MTJs.

Experiment: Multilayers were prepared on MgO(100) substrates by reactive molecular beam epitaxy method. The layer structure of the MTJs was MgO(100) substrate/MgO buffer (20 nm)/NiO (5 nm)/NCO (24 nm)/MgO (2.2 nm)/Fe (10 nm)/Au (30 nm). The MTJ structures with a junction area of 10 × 10 μm^2 were patterned by a conventional microfabrication process involving photolithography and Ar ion milling.

Results and discussions: We confirmed the epitaxial growth of films by RHEED. The RHEED patterns of NCO film changed from rock salt-type crystal structure to spinel-type by annealing under an oxygen atmosphere. Figure 1 shows the TMR curve of MTJ with NCO at 14 K at 10mV with the in-plane magnetic field. An inverse TMR effect was observed, which is the direct evidence of negative spin polarization of NCO. As the bias voltage increased, the absolute value of the TMR ratio decreased monotonically. With regarding to the temperature dependence of the TMR ratio, the TMR ratio was -25% at 10 K, and the absolute value of the TMR ratio decreased with increasing temperature and was less than -1.0% at 100 K. The behavior could be attributed to the temperature dependence of magnetization of NCO.

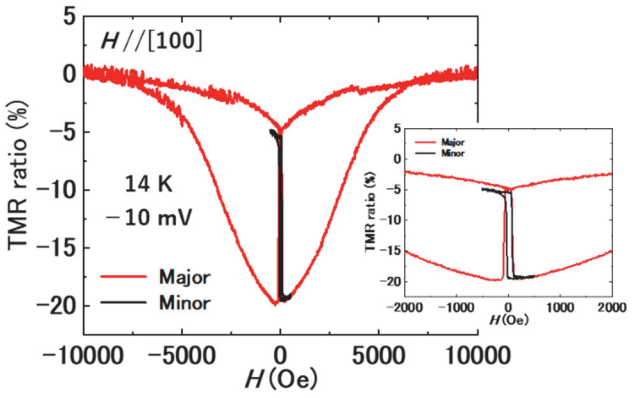


Fig.1 The inverse TMR curve of NCO/MgO/Fe MTJ. Inset is the enlarged plot of low magnetic field region.

Publication and Conference: 1. Hara et al., "Inverse Tunnel Magnetoresistance of Magnetic Tunnel Junctions with a $NiCo_2O_4$ Electrode" submitted to Appl. Phys. Lett. **2.** Nagahama et al., "Tunnel magnetoresistance effect of $NiCo_2O_4$/MgO/Fe magnetic tunnel junctions" 2022 Joint MMM-Intermag Conference, online.

ナノ秒オーダーの逆項間交差を示す熱活性化遅延蛍光材料の開発

相澤直矢　大阪大学

本研究は、化学研究所 環境物質化学研究系 分子材料化学領域の梶 弘典教授と共同で、三重項励起状態から一重項励起状態への遷移である逆項間交差 (RISC) をナノ秒オーダーで引き起こす熱活性化遅延蛍光 (TADF) 材料を創出することを目的とする。本年度は、その候補分子として、大きなスピン-軌道相互作用が期待できる Se を含む MOCz-SXT (Fig 1a) を設計し、その RISC の速度定数 (k_{RISC}) を理論的に予測した。

【実験】時間依存密度汎関数 (TDDFT) 法を用いて、MOCz-SXT の励起一重項および三重項状態とそれらの間の最低エネルギー交差シームの構造最適化計算を行った。汎関数には長距離補正を含む LC-BLYP を用い、その距離補正パラメーターを Janak の定理に基いて非経験的に最適化した。基底関数には 6-31G(d)を用いた。スピン-軌道相互作用の計算には一電子近似 Breit-Pauli ハミルトニアンを用いた。各励起状態のエネルギーとスピン–軌道相互作用を用いて、マーカス型の非断熱遷移モデル（式 1）より、k_{RISC} を算出した。

$$k_{\mathrm{RISC}} = \frac{2\pi}{\hbar}\left|H_{\mathrm{SO}}\right|^2 \left(4\pi\lambda k_{\mathrm{B}}T\right)^{-\frac{1}{2}} \exp\left(\frac{-E_{\mathrm{A}}}{k_{\mathrm{B}}T}\right) \tag{1}$$

ここで、H_{SO} は一重項および三重項励起状態間のスピン–軌道相互作用、λ は再配列エネルギー、E_A は活性化エネルギー（交差シームと三重項励起状態の平衡構造とのエネルギー差）、$\hbar$ はディラック定数、k_B はボルツマン定数、T は温度である。

【結果】MOCz-SXT の最低エネルギー交差シームは、第一励起一重項 (S_1) と第二励起三重項 (T_2) の間で発見された (Fig 1b)。その構造における H_{SO} は 29.7 cm^{-1} と有機分子として大きな値が計算された。この大きな H_{SO} に由来して、k_{RISC} は 3.6×10^9 s^{-1} とナノ秒オーダーに達することが予測された。

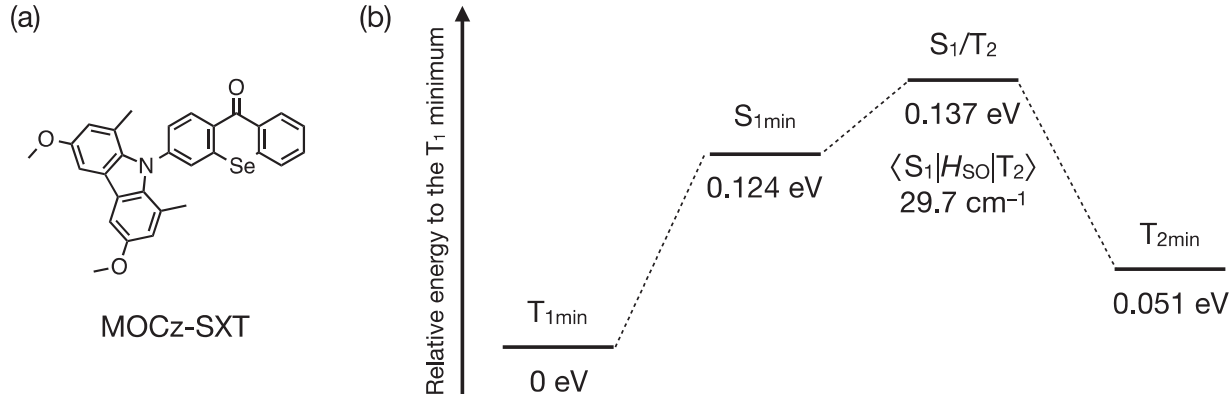


Fig 1 (a) MOCz-SXT の分子構造 (b) 励起状態のポテンシャルエネルギープロファイル

時間分解分光計測による熱活性化遅延蛍光における逆項間交差の機構解明

山方啓　豊田工業大学

目的　熱活性化遅延蛍光(TADF)は有機発光素子の高効率化に有用であることから盛んに研究が行われている．京都大学化学研究所の梶教授らによって近年開発された MA-TA[1-3]は塗布成膜可能な青色 TADF 材料として注目されているが，その励起ダイナミクスはまだに十分明らかにされていない．そこで本研究ではこの理解を深めるため，フェムト秒時間分解分光装置を用いて MA-TA の光励起過程を詳しく調べた．

実験方法　MA-TA は本課題の共同研究者である梶教授より提供を受けた．過渡吸収分光計測におけるポンプ光には波長 355 nm，パルスエネルギー1 μJ，パルス幅 90 fs(ピコ秒領域用)または 800 ps(ナノ秒領域用)のレーザーパルスを使用した．プローブ光には 1250 nm のフェムト秒パルスを BaF_2 板に集光して発生させた白色光パルスを用いた．

実験結果と考察　MA-TA のトルエン溶液を Ar ガスでバブリングした後に過渡吸収を測定すると，ピコ秒領域では図 1a のように，500~1000 nm にかけてブロードな吸収が観測されるが，時間の経過と共に 850 nm 付近の吸収が減少し 600 nm 付近の吸収が増加することが分かった．これは MA-TA のドナー(D)部位で励起された電子がアクセプタ(A)部位に移動する過程に対応し，その時定数は 7.8 ps と求められた．次にナノ秒領域を測定すると，図 1b のように 600 nm 付近の吸収は減少し，逆に 800~1000 nm のブロードな吸収が増加した．この吸収は O_2 バブリングで減衰が加速されることから(図 1c)，三重項励起子に帰属され，項間交差が 17ns の時定数で進行することが確認できた．なお，TADF を誘起する MA-TA の逆項間交差の速度は D-A 連結接合部位のねじれ角によって変化するという興味深い性質が報告されており[2]，今後，赤外パルスによる振動励起や発光測定を組み合わせてこの過程を詳細に調べる予定である．

参考文献

[1] Y. Wada, S. Kubo, and H. Kaji, Adv. Mater. **30**, 170564 (2018).

[2] Y. Wada, Y. Wakisaka, and H. Kaji, ChemPhysChem **22**, 625 (2021).

[3] Y. Wada, K. Shizu, and H. Kaji, J. Phys. Chem. A **125**, 4534 (2021).

成果報告

[1] 学術変革領域 A・動的エキシトン，第 4 回領域会議.

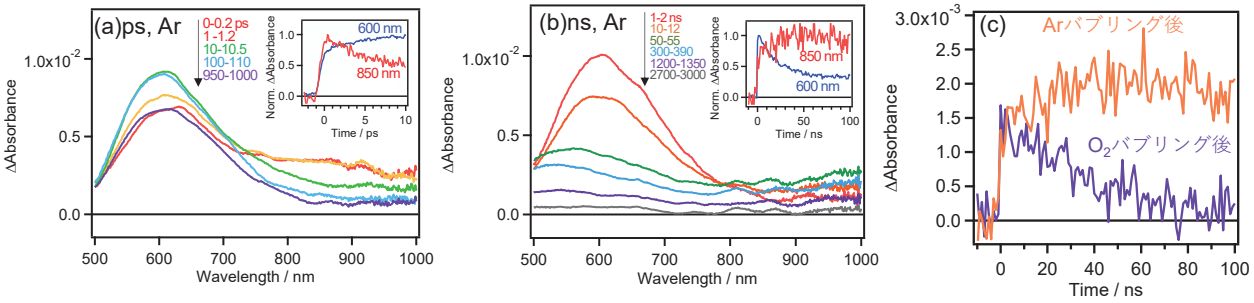


図 1 MA-TA トルエン溶液の過渡吸収スペクトル。内挿図はそれぞれの 600 nm および 850 nm の時間変化.
(a)ピコ秒領域，Ar バブリング後．(b) ナノ秒領域，Ar バブリング後．(c) 850 nm の減衰曲線の比較.

Functional characterization of extracellular vesicles produced by intestinal bacteria and development of their applications

Shino Yamasaki　Kansai University

Introduction:

The human gastrointestinal tract is inhabited by a wide variety of intestinal bacteria whose metabolites affect host physiology. Furthermore, it has been found that the extracellular vesicles (EVs) released by intestinal bacteria play important roles in the interaction between bacteria and the host, such as the regulation of biological functions and colonization of the host. In this study, we analyzed the production and secretion mechanisms of EVs by intestinal bacteria and investigated the biological responses elicited by EVs. Based on the findings, we developed novel systems for the secretion and production of heterologous proteins using EVs.

Results:

1. Immunomodulatory effects of EVs produced by intestinal bacteria

To prevent inflammatory bowel disease, EVs produced by intestinal bacteria with anti-inflammatory effects were screened. EVs derived from *Lactiplantibacillus plantarum* suppressed the inflammation induced by lipopolysaccharide in human colonic epithelial HT29 cells. This anti-inflammatory effect was found to be unique to these EVs, suggesting that the effect was induced by the uptake of nano-sized EVs by HT29 cells.

With regard to the immunostimulatory effect, it was elucidated that EVs produced by *Lactobacillus* sp. induced IL-6 production from macrophage-like RAW264 cells and enhanced IgA secretion by murine Peyer's patch cells. GAPDH was identified as a specific protein in the EVs by MALDI-MS analysis. Recombinant GAPDH also induced IL-6 production from RAW264 and monocyte THP-1 cells, suggesting that GAPDH in the EVs activates immune cells.

2. Improvement of EV production by breaking outer membrane-peptidoglycan linkage

Shewanella vesiculosa HM13, a Gram-negative bacterium isolated from intestinal contents of horse mackerel (*Trachurus japonicus*), abundantly produces EVs and is considered useful as a host for production of heterologous proteins as cargoes of EVs. In this study, we aimed to enhance the EV productivity of this bacterium. For this purpose, the linkage between the outer membrane (OM) and the peptidoglycan (PG) was weakened by deleting the genes coding for Braun’s lipoprotein (Lpp), which connects OM to PG, and L,D-transpeptidase, which catalyzes the formation of a covalent crosslink between Lpp and PG. Both gene deletions resulted in about 2.5-fold increase in EV productivity. Thus, this approach will contribute to the development of the EV-based protein production system by using *S. vesiculosa* HM13 as the host.

2021-102

Analysis of membrane lipid-dependent fermentation stress response in acetic acid bacteria

Yosuke Toyotake Ritsumeikan University

[Introduction] Acetic acid shows potent antimicrobial activity and inhibits the growth of most microorganisms even at low concentrations. However, acetic acid bacteria (AAB) such as *Acetobacter* spp. and *Komagataeibacter* spp. can produce acetic acid from ethanol and possess exceptional resistance to acetic acid, which is not found in other bacteria. It is thought that there is a close relationship between the cell membrane of AAB and their resistance to acetic acid, but the molecular analysis of membrane function has not been progressed.

AAB produce phosphatidylcholine (PC) as a membrane phospholipid (PL) constituting the cell membrane. Although previous studies suggested that PC is involved in acetic acid tolerance, the physiological functions of PC in detail are still unclear. In this study, we constructed the PC-deficient mutant of *Acetobacter pasteurianus* SKU1108, isolated from Thailand, and investigated the phenotypes of the mutant under various growth conditions.

[Results and Discussion] AAB synthesize PC from phosphatidylethanolamine (PE) using PE *N*-methyltransferase (PmtA). Thus, we constructed a markerless *pmtA*-deletion mutant (Δ*pmtA*) from the parental strain of *A. pasteurianus* SKU1108 by homologous recombination. The membrane PL composition of Δ*pmtA* was analyzed by thin-layer chromatography and compared with the parental strain. As a result, it was confirmed that PC was not produced, but PE was accumulated in Δ*pmtA*. In addition, the introduction of the *pmtA*-complementation plasmid, under the control of its native promoter, into Δ*pmtA* restored the synthesis of PC.

The colony-forming ability of Δ*pmtA* on agar medium supplemented with acetic acid was compared with that of the parental strain, and Δ*pmtA* showed higher sensitivity to acetic acid than the parental strain. In addition, Δ*pmtA* did not grow well on agar medium acidified with hydrochloric acid to pH 3.5 compared with the parental strain. These results indicated that PC is important for the growth of this strain both in the presence of acetic acid and in low pH environments. Interestingly, the colony-forming ability of Δ*pmtA* was restored to the parental level when the medium containing acetic acid was neutralized with potassium hydroxide but not when neutralized with sodium hydroxide. These results suggested that PC is also involved in the tolerance of this strain to sodium acetate under neutral pH conditions.

擬秩序ガラスの熱伝導

増野敦信　弘前大学

目的：ガラスとは一般に，SiO_2 等の網目形成酸化物によって形成される，隙間の多い三次元不規則ネットワーク構造を有する非晶質材料であると認識されている．それに対して我々は，原料を空中に浮かせたまま溶融，凝固させる無容器法を用いて，ネットワークを形成していないガラスの合成に成功している．これまでの構造解析の結果から，この特異なガラス中の構成成分は，結晶に準じたある程度の秩序をもって密に詰まっていることがわかってきた．我々がよく知るガラスとは全く異なる，「擬秩序ガラス」とも呼ぶべき新しいカテゴリーの物質である．酸化物ガラスの熱は主にフォノンによって伝播することを考えると，特異な構造を有する擬秩序ガラスの熱伝導特性は，従来型のネットワーク系ガラスとは異なる振る舞いを示す可能性がある．そこで本研究ではまず，$CaO\text{-}Al_2O_3$ 系ガラスについて，熱伝導特性の組成依存性を調べることとした．

実験：$CaO\text{-}Al_2O_3$ 二元系は，通常の溶融急冷法では共晶点近傍組成でのみしかガラス化しないが，無容器法によってガラス化範囲は大幅に広がる．ガス浮遊炉を用いて，xCaO-(100−x)Al_2O_3 (x = 50, 55, 60, 65, 70)を合成した．浮遊には O_2 ガスを用いた．ガラス転移温度（Tg）は，TG-DTA により決定した．物性計測や構造解析には，Tg 近傍でアニール後，徐冷することでガラス内部のひずみを取り除いた試料を用いた．密度はピクノメータによって計測し，充填密度を算出した．室温での熱拡散率は温度波法によって，また室温から低温までの比熱は京都大学化学研究所島川研究室の PPMS によって測定した．ラマン散乱分光，^{27}Al MAS NMR によってガラスの構造解析を行った．

結果：合成したガラスはいずれも透明であった．xCaO-(100−x)Al_2O_3 ガラスの充填密度は，CaO 含有量増加に対して大きな変化はなかったが，x = 70 でやや増加していた．^{27}Al MAS NMR からは，Al のほぼ全ては 4 配位となっていることがわかった．NMR のケミカルシフトにおける組成依存性は小さかったが，Raman 散乱スペクトルでは，x の増加とともに非架橋酸素の割合が増加する傾向が確認された．熱拡散率は，CaO 含有量増加に伴って減少する傾向が見られた（Figure 1）．比熱のデータについては，今年度は x = 70 のガラスで室温近傍のみ取得することができた．得られた密度，熱拡散率，比熱の値から算出した熱伝導率は，1.5 (W/m·K)であった．一般的なネットワーク系ガラスと比較して，1.5〜3 倍程度の値である．今後は，熱伝導率の組成依存性とガラス構造との相関を，構造モデルをもとに明らかにすることが求められる．

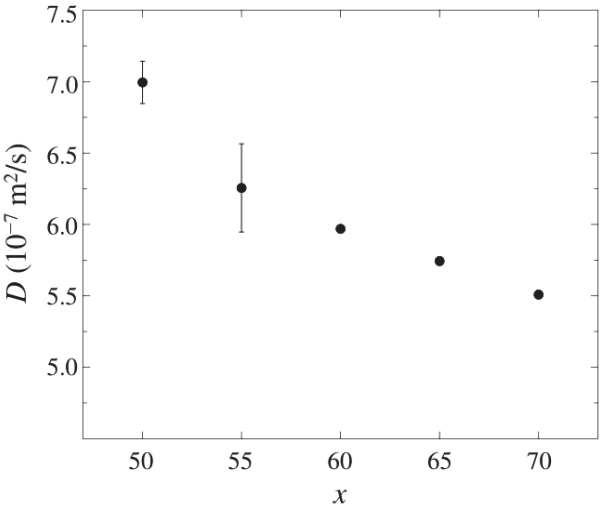


Figure 1. xCaO-(100−x)Al_2O_3 ガラスの熱拡散率.

2021-104

異常高原子価イオンを含む機能性酸化物合成とその構造物性研究

齊藤高志　高エネルギー加速器研究機構

鉄イオンは通常+2 価や+3 価の状態が安定であるが、強い酸化雰囲気を利用して+4 価、+5 価、+6 価といった異常高原子価と呼ばれる価数を持つ場合がある。このような異常高原子価 Fe イオンを含む化合物では Fe-3*d* 軌道と O-2*p* 軌道が強く混成した特徴的な電子状態を持つ。Fe^{4+}イオンは低温で $2Fe^{4+} \rightarrow Fe^{3+} + Fe^{5+}$で表される電価不均化反応を起こし、これに伴って金属絶縁体転移や負の熱膨張等の興味深い性質がしばしば発現する。$CaFeO_3$ や $CaCu_3Fe_4O_{12}$ 等、酸素に八面体配位された *B* サイトに Fe^{4+}のみを含むペロブスカイト型化合物にける電荷不均化では、価数が低くイオン半径が大きな Fe^{3+}と価数が高くイオン半径が小さな Fe^{5+}がランダムに配置するより交互に並んだ方が系全体のエネルギーが低くなるため、電価不均化状態では Fe^{3+}/Fe^{5+}が交互に並んだ構造をとる。このように Fe^{3+}/Fe^{5+}が交互に並んだ構造は、Fe^{4+}を含む高温相におけるフォノンのブリージングモードが凍結した状態と見ることができる。一方、$CaFeO_3$ における *B* サイトの Fe^{4+}の半分を Mn^{4+}で置換して得られる $Ca(Fe_{0.5}Mn_{0.5})O_3$ では、*B* サイトにおいて Fe^{4+}と Mn^{4+}がランダムに配置していることから Fe^{3+}/Fe^{5+}が交互に並ぶことはできないが、低温で Fe^{4+}が電価不均化を起こすことが知られている。したがって $Ca(Fe_{0.5}Mn_{0.5})O_3$ における電価不均化状態では、フォノンのブリージングモード凍結とは異なる形で Fe^{3+}と Fe^{5+}の電荷不均化が起こっている可能性がある。$Ca(Fe_{0.5}Mn_{0.5})O_3$ における電価不均化状態を明らかにするためには Fe^{3+}/Fe^{5+}の配列情報を含む詳細な結晶構造解析を行う必要があるが、一般に電荷不均化による構造変化は酸素の原子座標の微細なズレによるものであることから、これを検出するためには酸素原子座標をきわめて精密に求める必要がある。$Ca(Fe_{0.5}Mn_{0.5})O_3$ において軽元素である酸素の原子座標を高精度で求めるためには統計精度の高い中性子回折データが不可欠であることから、$Ca(Fe_{0.5}Mn_{0.5})O_3$ の中性子回折実験を行った。

試料合成には化学研究所・島川研究室の高圧合成装置を利用した。炭酸塩、酸化物原料から作製した前駆体 $Ca(Fe_{0.5}Mn_{0.5})O_{2.5}$ を $KClO_4$（酸化剤）と共に 3GPa、1000℃で処理することにより、$Ca(Fe_{0.5}Mn_{0.5})O_3$ 多結晶試料を得た。また J-PARC/MLF の BL09 に設置された高強度・高分解能 TOF 中性子回折装置 SPICA を用い、300 K～20 K における粉末中性子回折実験を行った。室温では Fe/Mn の長距離秩序/短距離秩序の痕跡は観測されず、Fe/Mn がランダムに配列した $Ca(Fe_{0.5}Mn_{0.5})O_3$ が得られたことが確認された。低温の電荷不均化相における詳細な結晶構造解析を現在進めている。

界面活性剤を抽出剤として利用した固相抽出による Eu 分離法の開発

倉橋健介　大阪府立大学工業高等専門学校

１．　目的

工業分野における需要の高まりから，希土類元素のリサイクルが期待されている．希土類元素の主要な分離法である溶媒抽出法は，揮発性有機溶媒の使用が問題視されており，揮発性有機溶媒の少ない固相抽出法が注目されている．先行研究では，陰イオン界面活性剤のみを用いて溶媒含浸樹脂（SIR）を調製し，Eu の固相抽出を行った場合でも，界面活性剤の濃度上昇に伴い抽出率が向上するが，疎水基が同じ陽イオン界面活性剤の場合は低下することを見出した．界面活性剤は安価で多様な種類の試薬が市販されており，界面活性剤単独で希土類金属を抽出できれば，高価な抽出剤の使用を削減し，分離コストを大きく下げることができる．そこで本研究では，親水部が同じで疎水基の長さが異なる界面活性剤を使い，疎水基の長さが与える抽出率への影響を観察するとともに，物性の近いその他の希土類元素との選択性について検討した．

２．　実験方法

含浸する界面活性剤は親水基が陰イオン性である Sodium Dodecylsulfate (SDS)と Sodium Hexadecylsulfate (SHS)を使用した．エタノールで洗浄後、乾燥した Amberlite XAD-7HP 1.0 g に対して任意の濃度の界面活性剤を含むエタノール溶液を加え，1 日含浸させた．溶媒を減圧留去し，50℃で 1 日真空乾燥させ，目的の SIR を調製した．

0.1 mM の La, Eu, Lu と，緩衝液として 0.1 M クロロ酢酸ナトリウムを含む水溶液 2.5 mL を HCl と NaOH で任意の pH に調整した．この水相に SIR を 0.1 g 加え，2 時間振とうした．振とう後，水相を分取し pH を測定した．分取した水相は Ni を内標準として，誘導結合プラズマ発光分光分析装置(ICP-OES)を用いて金属濃度を測定した．

３．　結果と考察

界面活性剤 SHS は溶解度が低いことから，先行研究で用いた調製法では，含浸溶媒中に溶けずに粉状で残ることがわかった．そこで，SDS を含浸させる際の溶媒量を増やしたところ，含浸する SDS の物質量が同じなら，溶媒の量を変えた場合でも抽出率はほとんど変化せず，溶媒量を増やすことで SHS の低溶解度を回避し，SHS を含浸した SIR を調整できることがわかった．調製した SIR を用いて，界面活性剤疎水基の影響を比較ところ，疎水基の短い SDS で調製した SIR がより高い抽出を示した．また，希土類金属同士の分離選択性の検討では，La > Eu > Lu の順で抽出率がわずかに下がっているがその差は小さく，元素間の分離は難しいことがわかった．

４．　成果報告

1)　小笠原拓海ら，第 23 回化学工学会学生発表会，オンライン開催，2022.3.

2021-106

Fine synthesis of polymer brush on nano-platelet for functional photonic LC

Yoshiaki Uchida　Osaka University

The rapid spread of automated systems in factories and vehicles has required visible light communication systems using optical fibers made of inexpensive polymers. As the communication accelerates, the number of nodes incorporated in the systems increases. These systems have potential problems: interference between cables, complicated wiring, and bending flexibility limits. Fiber-free visible light communication systems are promising to solve the problems.

We have focused on switchable photonic structures of liquid crystalline (LC) phases. Cholesteric LC (CLC) materials and hyperswollen lamellar (HL) materials with flexible one-dimensional periodic structures [1,2], nematic LC (NLC) materials showing strong light scattering as random laser resonators [3], and whispering gallery mode (WGM) in an LC microsphere [4] are promising. Light is trapped inside the LC materials. Magnetic fields are expected to be useful for the remote control of optical transmission devices. We have already fabricated magnetically switchable photonic systems with LC materials. The random laser action in NLC materials doped with ferromagnetic nano-platelet is magnetically controllable [3].

We focus on the stable dispersion of the ferromagnetic nano-platelet in the photonic LC phases to obtain ferromagnetic photonic materials for the magnetic switching of light emission. We have investigated the dispersion of ferromagnetic particles with polymer brushes into various liquid crystals. To disperse the nano-platelet in photonic LC materials, we have been optimizing the polymer brush structure in this project. This year, we have tried to disperse the nano-platelet in HL phases to prepare magnetically controllable photonic LC materials. We successfully prepared ferromagnetic LC mixtures using previously reported methods to disperse nanosheets and nano-platelet in the HL phases [5]. Now we are preparing the paper on the ferromagnetic LC mixtures.

References

1. Y. Iwai, R. Iijima, K. Yamamoto, T. Akita, Y. Uchida, N. Nishiyama, *Adv. Opt. Mater.,* **8**, 1901363 (2020).

2. Y. Uchida, T. Nishizawa, T. Omiya, Y. Hirota, N. Nishiyama, *J. Am. Chem. Soc.*, **138**, 1103–1105 (2016).

3. T. Naruta, T. Akita, Y. Uchida, D. Lisjak, A. Mertelj, N. Nishiyama, *Opt. Express*, **27**, 24426–24433 (2019).

4. Y. Uchida, Y. Takanishi, J. Yamamoto, *Adv. Mater.*, **25**, 3234–3237 (2013).

5. K. Sasaki, T. Okue, T. Nakai, Y. Uchida, N. Nishiyama, *Langmuir*, **37**, 5872–5877 (2021).

高分子ブラシ層内の水の構造および凍結挙動の解析

源明誠　富山大学

［目的］　固体高分子は高分子鎖が絡み合った状態で，特異な官能基を付与することで生体適合性や電気伝導性などの機能材料として，構造材やフィルムなどに使われている。近年開発された原子移動ラジカル重合法による固体表面に高分子鎖を緻密に生長させた高分子ブラシは，次元規制された高分子鎖によって，防汚性や生体適合性などの機能を付与するとされる。この機能発現には水が関与しているとされるが，これまでにブラシ内部のみの評価はなされていない。本研究では，内部全反射近・中赤外吸収（ATR near/mid-IR）スペクトルから Poly(polyethylene glycol monomethoxy ether methacrylate)（P(PEGMA)，Fig. 1）ブラシ内部の水構造を評価した。

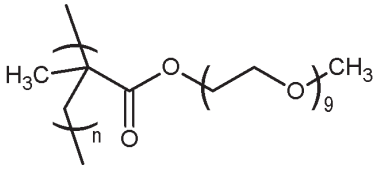


図 1 P(PEGMA) の構造

［実験］　自作の ATR セルを使用し，種々濃度の P(PEGMA) 水溶液および種々膜厚（70, 218, 1130 nm）の P(PEGMA) ブラシ中の水の ATR near/mid-IR スペクトルを得た。水の OH 伸縮振動 $\nu_1+\nu_3$ 領域（7800－5860 cm^{-1}）の解析は，二次微分スペクトルから決定したピーク位置をもとにした成分分離により行った。

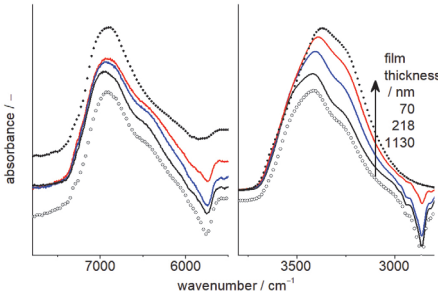


図 2 膨潤 P(PEGMA) ブラシ中の水の ATR near/mid-IR スペクトル

実線：P(PEGMA)ブラシ
白抜き点線：P(PEGMA) 水溶液
点線：純水

［結果および考察］　Fig. 2 に，純水，ブラシ中および遊離高分子水溶液（32.1 wt%）中の水の OH 伸縮振動 $\nu_1+\nu_3$ 領域（左図）および基準振動領域（右図）の ATR near/mid-IR スペクトルを示す。ブラシ膜厚が薄くなるにつれてスペクトル形状は純水（点線）に近くなり，それは基準振動領域で特に顕著であった。これはもぐり込み深さの波数依存性により，膜厚の薄いものではブラシ外の水まで観測していることに由来する。種々濃度の P(PEGMA) 水溶液とブラシ中の水の吸収強度の比較から膨潤ブラシの含水率は～29 wt% と推測した。また，$\nu_1+\nu_3$ 領域の成分分離結果から，P(PEGMA)ブラシでは，水の回転運動に由来する成分（$\nu_1+\nu_3+\nu_R$）の吸収が，ブラシの含水率に最も近い P(PEGMA)水溶液よりも小さくなっていることがわかった（Fig. 3）。このことは高分子鎖の片末端が固定化されたブラシは，遊離高分子鎖と比較し，高分子鎖の運動性が抑制されており，その結果，水の回転運動が制限されていることを示唆する。

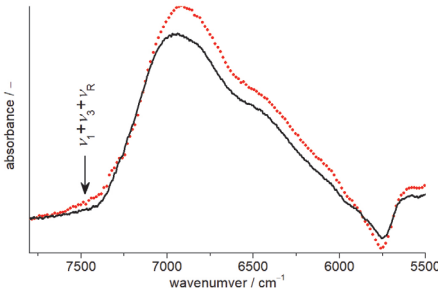


図 3 ブラシおよび遊離高分子水溶液の OH 伸縮振動 $\nu_1+\nu_3$ 領域の ATR near-IR スペクトル

実線：P(PEGMA)ブラシ（1130 nm）
点線：P(PEGMA)水溶液

Study on water freezing with lignocellulose nanofibers and their surface modification toward functional materials

Keita Sakakibara　National Institute of Advanced Industrial Science and Technology

Objective. Cellulose nanofiber (CNF) has attracted much attention in material sciences, since it is thin (3 to sub-microns in diameter), renewable, biocompatible, low cost, and exhibits remarkable mechanical properties such as high Young's modulus. CNF can be obtained from wood pulp fibers through chemical and/or mechanical disintegration methods. When applying wood flour to the mechanical disintegration, lignocellulose nanofiber (LCNF) can be obtained, in which macromolecular lignin and hemicellulose are tightly adhered to CNF as the same composition ratio of the raw materials. LCNF provides a variety of applications to reinforce and strengthen plastics, rubbers, coatings and paintings, and others. Furthermore, surface properties of LCNF can be regulated by polymer grafting, forming polymer brush as a shell around LCNF as a core. Especially, concentrated polymer brush (CPB), which is highly dense assemblies of grafted polymers, have successfully been synthesized through surface-initiated (SI) reversible-deactivation radical polymerization [1]. Recently, with the collaboration of Prof. Yoshinobu Tsujii (ICR, Kyoto University), it has been revealed that CNF (not having lignin and hemicellulose) surface-modified with CPB, so called CNF-CPB, has exhibited synergistic properties including high mechanical strength, ultralow friction, and bioinertness [2]. Hence, LCNF (having lignin and hemicellulose) could also be upgrading by the CPB modification, generating LCNF-CPB. One of the promising properties of CPB is to form anti-icing layer on top surfaces. Thus, we, with the collaboration of Prof. Tsujii, attempted to study the preparation of LCNF-CPB toward novel functional materials

Results. To begin with, LCNF was prepared by ball-milling. Oven-dried wood flour (particle size < 0.2 mm, Japanese cypress) with 7.5% (w/v) of water, *N*,*N*-dimethylacetamide (DMAc), *N*,*N*-dimethylformamide (DMF), dimethyl sulfoxide (DMSO), and *N*-methylpyrrolidone (NMP) was subjected to a ball-milling for 4 h at 450 rpm (repeated milling and pausing of 10 min each). The solvent of LCNF slurry was substituted to *tert*-butanol, and then lyophilized. The specific surface areas (SSA) of the LCNFs were determined by the BET plots from their nitrogen adsorption-desorption isotherms (Fig).The thin LCNFs with SSA of more than 100 m^2 g^{-1} was only obtained using water. The CPB modification was carried out following our previously reported procedure [2]. The characterization for LCNF-CPBs is underway.

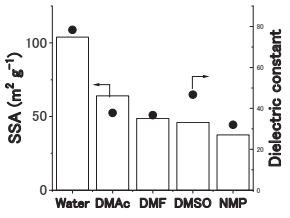


Fig. SSA of LCNFs.

References. 1) Y. Tsujii, et al., *Adv. Polym. Sci.*, **2006**, *197*, 1–45. 2) K. Sakakibara, et al., *ACS Appl. Nano Mater.*, **2021**, *4*, 1503–1511.

Giant Magnetic Resistance on Single-Electron Transistor

Yutaka Majima　Tokyo Institute of Technology

The purpose of this study is to observe the giant magnetic resistance on single-electron transistor. Spin-dependent single-electron tunneling, which is based on interplay between single-electron changing effect and tunnel magnetoresistance (TMR) effect, has attracted much attention owing to its unique phenomena such as the enhancement and the oscillation of TMR. These phenomena have been observed in ferromagnetic tunnel junctions and ferromagnetic granular structures.

Recently, we have reported a chemically-assembled single-electron transistor (SET) using Pt-based nanogap electrodes and an Au nanoparticle, which showed clear and ideal Coulomb diamonds. To realize the chemically-assembled SET, robust Pt-based nanogap electrodes with a 10-nm-scale ultrafine linewidth were fabricated by electron-beam lithography (EBL) and electron-beam (EB) evaporation, and an alkanethiol-protected Au nanoparticle was chemisorbed between the gap using alkanedithiol self-assembled monolayer (SAM).

In this project, we studied external magnetic field dependent current in a chemically-assembled SET based on Pd nanogap electrodes and an Au nanoparticle. Pd was used as a paramagnetic material for nanogap electrodes. Pd nanogap electrodes with a gap separation of 7.5 nm were fabricated on Si substrates by a combination of EBL and EB evaporation. An Au nanoparticle with a core diameter of 5.8 nm was synthesized at Prof. Teranishi laboratory and then introduced between the gap using alkanedithiol SAM. Finally, an SET structure consisting of Pd source/tunnel barrier/Au island/tunnel barrier/Pd drain (Pd/Au/Pd) with gate was realized.

The electrical characteristics of the fabricated SET were measured at 9 K with and without an external magnetic field. In the absence of a magnetic field, clear Coulomb blockade was observed, indicating that single-electron charging effect (Figure 1). When a magnetic field was applied to the SET, an increase and decrease in current compared to the one without magnetic field were observed in accordance with applied drain voltage, which could be attributed to spin-dependent single-electron tunneling in the Pd/Au/Pd SET structure.

The manuscript related to the above results is in preparation.

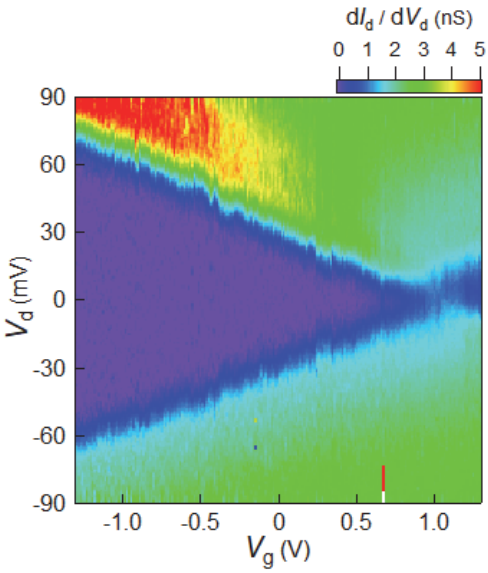


Figure 1: Stability diagram of the SET based on Pd nanogap electrodes and an Au nanoparticle at 9 K.

2021-110

再生可能資源・木質バイオマスの先端化学材料への効率的変換法の開発

秦野修　奈良県立医科大学

目的:

研究代表者は、カルボニル基をもつ化合物（ステロイド等）を誘導体化し、化学研究所の FT-ICR MS 装置を用いることにより、極めて高分解能（質量分解能 100 万）かつ高感度な質量分析検出、及び、イメージング解析を行なう系を構築している。又、スギ木幹部の光学顕微鏡切片の組織切片上で化学反応を行い、反応行程の前後変化を、光学/蛍光顕微鏡、及び、電子顕微鏡（無蒸着 SEM 観察）レベルで追跡する実験系を構築した。又、顕微 FT-IR イメージングを用いて、木材の主要成分である Lignin, Cellulose 等のイメージング検出を行ない、晩材部において早材部よりも Lignin 及び Cellulose 量が多い結果を得た。本年度は、薄い木材切片を用いて、簡便で効率的な木材分解条件を探索する実験系の構築を行ない、化学研究所・中村研究室が行っている再生可能バイオマス資源であるスギ等の人工森林木材から有用化合物生産を行う研究に適用することを目的として行った。

実験方法、実験結果、考察:

本年度は、光学顕微鏡用の薄いスギ切片（9 μm 厚）を用いて、簡便な木材分解実験系を構築した。スギ木幹・心材部の木口面切片（約 4 mm x 5 mm x 0.009 mm）を作成して、40 μl の 30 %、20 %、0 % H_2O_2 液中に浸して、静置化で 60 ℃保温を行ない、切片の形がくずれる時間を調べたところ、30 % H_2O_2 液中では 24 時間後、20 % H_2O_2 液中では 48 時間後に目視で切片の形状が崩れ、ごく薄い切片を用いることにより、触媒の添加なしでも効率的に仮道管細胞壁の分解が起こると考えられた。又、0 % H_2O_2 中では、切片の形状は 1 週間経過後も保たれていた。この実験系は、薄い切片を 60 ℃の液中に静置するだけの簡便さで、ごく微量の木材量（約 4 x 5 x 0.009 mm = 0.18 mm^3）と、反応液（40 μl）を用いて、効率的にスギの化学分解条件を探索できる利点を持つ。今後、化学研究所・中村研究室で行われている鉄錯体触媒、イオン液体触媒、有機酸触媒等の効率的な木材化学分解の濃度、温度、時間等の条件を探索する実験系に応用していきたい。

又、分解過程の組織形態変化を解析する目的で、スギ切片の Lignin, Cellulose の同時検出を行っている。Cellulose を Calcofluor White（UV-A 励起、青色）で、Lignin を Basic Fuchsin（G 励起、赤色）で染色したところ、Cellulose は仮道管の細胞壁に、Lignin は隣り合う仮道管の細胞間層に強く染色が認められた。

今後、中村研究室の共同研究者、研究協力者らが行っている触媒を用いたスギ等の木質バイオマスから有用化学物質を生産するための木質分解過程の解析に、これらの実験系（触媒のスクリーニング法や、Lignin, Cellulose の同時検出法）を適用していくと共に、超解像光学顕微鏡（解像度：数 10nm）、SEM による立体観察、顕微 FT-IR イメージング法、MS Imaging 法等と組み合わせて、木材分解過程の組織形態イメージング解析を行っていきたい。

成果報告:

Hayazaki M, Hatano O, Shimabayashi S, Akiyama T, Takemori H, Hamamoto A.
Zebrafish as a new model for rhododendrol-induced leukoderma.
Pigment Cell Melanoma Res. 2021 Nov;34(6):1029-1038. doi: 10.1111/pcmr.13005.

新規細胞内取込誘導タンパク質の同定

桑田啓子　名古屋大学

細胞膜透過ペプチド (CPP)は、細胞内移行性を示す数残基から 20 残基程度のペプチドで、タンパク質や核酸等の生理活性物質の細胞内導入キャリアーとして利用されている[1]。オリゴアルギニンは代表的な CPP の一つであるが、このうち D 体のオクタアルギニン (r8)、ドデカアルギニン (r12)が腫瘍組織集積性を示すことが化学研究所の二木教授らによって報告され[2]、医薬品等の送達への応用も期待される。CPP と血清タンパク質との相互作用が知られており[3]、CPP−血清タンパク質複合体が、Enhanced Permeation and Retention (EPR)効果によって腫瘍組織に集積する機構が考えられる。しかし、CPP がいずれの血清タンパク質と相互作用するかに関しては詳細には調べられていない。本研究では、オリゴアルギニン、特に r8 と相互作用する血清タンパク質の同定を目指した。

オリゴアルギニンとして、高い腫瘍集積性を示した r8、r12 とともに、顕著な集積性を示さない D 体のテトラアルギニン (r4)をコントロールに用いた。これらのペプチドの蛍光標識体を Fmoc 固相合成法により調製し、質量比で血清タンパク質の大部分を占めるアルブミンとの相互作用に関して検討した。r4、r8、r12 それぞれについて、アルブミンと混合した後に限外濾過を行い、フィルター上に残った CPP と透過した CPP の割合を算出した。その結果、いずれの CPP も、アルブミンと混合することでフィルター上に残存する割合が高まったことから、アルブミンの相互作用が示唆された。さらに、等温滴定型カロリメトリー (ITC)を用いてこれらの相互作用を確認したところ、算出された解離定数はいずれも数十 μM オーダーであった。以上より、r4、r8、r12 はいずれもアルブミンと相互作用するがその相互作用は比較的弱いものであると示唆された。

これらの結果から、血清中にはアルブミンの他に、オリゴアルギニンと相互作用する血清タンパク質が存在しているのではないかと考え、その探索を行った。上記 3 種のオリゴアルギニンの中で最も高い腫瘍集積性を示す r8 と血清との混合液を Native PAGE で展開し、蛍光の検出されたバンドを切り出してトリプシン消化した。得られたペプチド断片を質量分析により解析しデータベースと照合することで、バンド中に含まれていたタンパク質の候補が得られた。これら候補タンパク質と r8 との相互作用を、蛍光相関分光法 (FCS)を用いて個別に評価した。その結果、r8 と特に強く相互作用するタンパク質が明らかになった。また、r12、D-Rev、D-FHV などの CPP においても同様の傾向が見られた。現在、上記で見出されたタンパク質の CPP の細胞内移行における寄与に関して精査しているところである。

【参考文献】

[1] Futaki, S., Biopolymers, (2006) 84, 241-249

[2] Nakase, I. et al. J. Control. Release, (2012) 159, 181-188

[3] Kosuge, M. et al. Bioconjugate Chem., (2008) 19, 656-664

2021-112

マクロピノサイトーシスによる細胞内取込様式

前川大志　慶應義塾大学

目的：マクロピノサイトーシスは、細胞骨格(アクチン)の再構築と細胞膜の隆起・融合を伴い、広い範囲の細胞外液および細胞膜を細胞内に取込む。外的刺激により誘導される普遍的な液相エンドサイトーシス(細胞の生理的養分取込機構)であると共に、近年では、がん細胞への養分取りこみにおける外的誘導を特に伴わない定常レベルのマクロピノサイトーシスの重要性が指摘されている。最近、マクロピノサイトーシスに注目が集まっている一方で、その分子基盤や細胞膜形態変化の詳細については不明な点が多く残されている。そこで本研究では、ペプチドによるマクロピノサイトーシスの誘導様式ならびに、細胞外微粒子の取り込みにおけるマクロピノサイトーシスの寄与とその分子機序解明に焦点を当て、理解を深めることを目的とする

実験方法：共同研究者である京都大学化学研究所の二木、広瀬らが開発したマクロピノサイトーシス誘導活性が報告されているペプチドをHeLa cellsに処理し、細胞膜形態変化を走査型電子顕微鏡で観察した。また、マクロピノサイトーシス様の経路で取り込まれる事が示唆されている蛍光ビーズについても、二木、広瀬から提供してもらい、HeLa cellsに添加し、細胞膜形態変化を走査型電子顕微鏡で観察した。更に、アクチン重合やカルシウムシグナリング等の既知の各種エンドサイトーシス阻害剤をHeLa cellsに処理し、細胞膜形態変化を走査型電子顕微鏡で観察した。

実験結果：HeLa cellsにマクロピノサイトーシス誘導ペプチドを処理しても、顕著な細胞膜の形態変化は認められなかった。一方で、蛍光ビーズがHeLa cellsに取り込まれる際に、特殊な細胞膜の形態変化が観察された。更に、この蛍光ビーズが取り込まれる際に生じていると考えられる細胞膜形態変化を阻害する阻害剤を複数同定するに至った。

考察：本研究を通して、HeLa cellsは一般的なマクロピノサイトーシスとは異なる経路でマクロピノサイトーシス様の細胞外微粒子取り込み活性を有する事が示唆された。今後は、本研究で同定した阻害剤を足掛かりにその分子機構の解明を継続する。

成果報告：該当なし。今後、データを更に集めて論文発表を計画している。

原子レベル平坦表面ダイヤモンドを用いた量子情報科学研究

徳田規夫　金沢大学

【緒言】

ダイヤモンド中の単一窒素 - 空孔複合体（NV）中心は優れたスピン特性及び光学特性を有する。他材料と比べ特筆すべき点は、NV 中心では単一スピンを室温において光検出・操作できる点である。その単一スピンをプローブとし、単一 NV 中心を用いた磁気センサ、電場センサ、温度センサに関して、近年、優れた実証研究がなされてきた。NV 中心のセンサ応用において、NV 中心は感度向上のため数ナノレベルの浅い領域に存在していることが望ましい。しかし、ナノレベルでの表面付近では、センサとして使える電荷状態が－1 価に荷電した NV^-の電荷状態が不安定になることや、スピンコヒーレンス時間の短時間化によりセンサ感度が著しく低下するなど、重要な克服すべき課題がある。

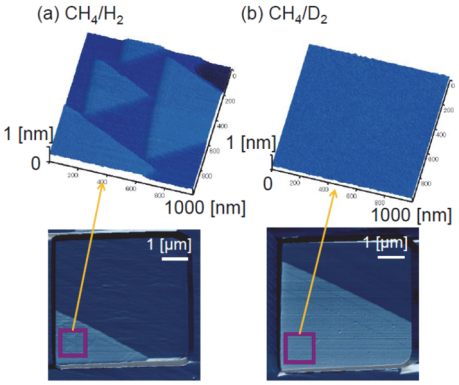


図　重水素合成を用いた原子レベルで平坦化された表面における AFM 像[発表文献 1]

【実験と結果】

ダイヤモンドにおいて、ある CVD 合成条件を満たすと、図に示したように数十 μm 四方の面積において、原子レベルでフラットな表面を持つ試料を作成することができる。成膜プロセスの提案や合成条件における窒素濃度の制御の条件出しを、共焦点レーザ顕微鏡によって行った。課題として、新たな表面処理等を施して更なる安定化を行い、それらの測定を目指している。

また、共同研究成果として、京大化学研究所の我々の研究室で立ち上げた化学気相堆積（CVD）法によるダイヤモンド合成装置により、ダイヤモンドを合成し、n 型半導体ダイヤモンドの合成に成功した。単一 NV 中心の T_2 をスピンエコー法により確かめ、ミリ秒以上に十分に長くなることも実証した[2]。

また、共同研究成果として、我々はドレスト状態生成によるスピンコヒーレンス時間の桁違いの長時間化を実現し、それを用いて温度感度向上の実証研究を行った[3]。ダイヤモンド中の NV 中心は、細胞内部の温度分布の不均一性や局所的な温度変化によって引き起こされる細胞の生理機能の研究における高感度量子温度センサとしての応用が期待されている。

【参考文献】

[1] N. Mizuochi, N. Tokuda, M. Ogura, S. Yamasaki, Jpn. J. Appl. Phys., 51, 090106 (2012).

【成果報告】

[2] R. Kawase, H. Kawashima, H. Kato, N. Tokuda, S. Yamasaki, M. Ogura, T. Makino, N. Mizuochi, "n-Type diamond synthesized with tert-butylphosphine for long spin coherence times of perfectly aligned NV centers", 審査中.

[3] H. Tabuchi, Y. Matsuzaki, N. Furuya, Y. Nakano, H. Watanabe, N. Tokuda, N. Mizuochi, J. Ishi-Hayase, "Temperature Sensing with RF-Dressed States of Nitrogen-Vacancy Centers in Diamond", 審査中.

量子センサの高感度化に向けたダイヤモンド合成と量子技術開発研究

牧野俊晴　産業技術総合研究所

【緒言】ダイヤモンド中の複合欠陥である窒素 - 空孔複合体（NV）中心は、量子科学技術分野において研究が精力的に行われ、優れた特性が明らかにされてきた。特に、NV 中心は固体中のスピンとしては群を抜く長いスピンコヒーレンス時間（T_2）を持つことにより高い感度が実現し、磁場、電場、温度、圧力、pH などの高感度センサとして幅広い分野での応用が期待される。

【実験と結果】

これまで産総研グループが合成した n 型ダイヤモンド中の NV 中心を用いて、単一 NV ダイヤモンド量子センサで世界最長の T_2 と室温での最高磁場感度を実現していたが [1]、今回、図 1 に示した京大化学研究所の我々の研究室で立ち上げた化学気相堆積（CVD）法によるダイヤモンド合成装置により、ダイヤモンドを合成し、特性を評価した。

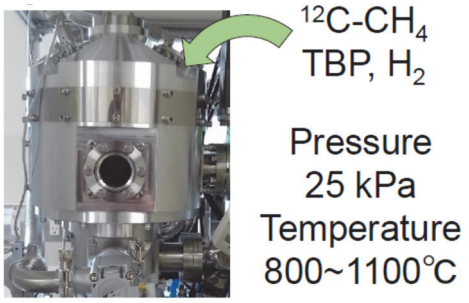


図 1　京大化学研究所で立ち上げた CVD 法によるダイヤモンド合成装置

以前の合成条件とは異なり、今回、より毒性の低いターシャルブチルフォスフィンガス（TBP）を用いてリンドープを行った。ホール測定の結果、n 型半導体ダイヤモンドが合成できたことが確かめられた。ダイヤモンドにおいて、n 型半導体は天然に存在せず、不純物制御等の難しさから、合成できたグループは世界でも 4 つのみであったが、今回、不純物制御の最適条件を丹念に調べ、n 型半導体ダイヤモンドが合成できた。

単一 NV 中心の T_2 をスピンエコー法により確かめ、ミリ秒以上に十分に長くなることも実証した[2]。今回の成功は、将来の量子センサ高感度化や、半導体特性を生かしたデバイス作製、及び集積化にとって重要な一歩である。

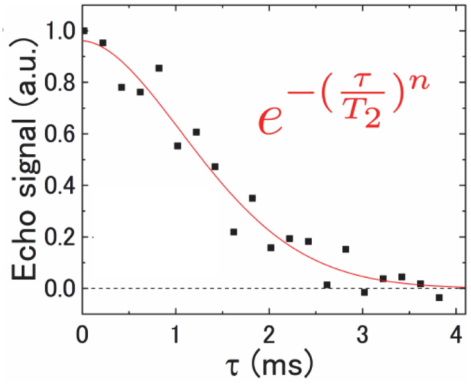


図 2　合成したダイヤモンド試料中の単一 NV 中心におけるスピンエコー測定結果．十分に長いスピンコヒーレンス時間が得られた。

【参考文献】

[1] E. D. Herbschleb, H. Kato, Y. Maruyama, T. Danjo, T. Makino, S. Yamasaki, I. Ohki, K. Hayashi, H. Morishita, M. Fujiwara, N. Mizuochi, Nature Communications, 10, 3766 (2019).

【成果報告】

[2] R. Kawase, H. Kawashima, H. Kato, N. Tokuda, S. Yamasaki, M. Ogura, T. Makino, N. Mizuochi, "n-Type diamond synthesized with tert-butylphosphine for long spin coherence times of perfectly aligned NV centers", 審査中.

Functional analysis of non-canonical strigolactones as plant hormones and root-derived signals

Yoshiya Seto　Meiji University

【The aim of this study】Strigolactones (SLs) are plant hormones that regulate shoot branching, and also function as root-derived chemical signals. SLs are biosynthesized from carotenoids via a key intermediate molecule called carlactone (CL). In a model plant, Arabidopsis, CL is further converted into carlactonoic acid (CLA) by a cytochrome P450 monooxygenase, MORE AXILLARY GROWTH1 (CYP711A). We previously identified methyl esterified derivative of CLA, methylcarlactonoate (MeCLA) in Arabidopsis, and found that MeCLA can interact with the Arabidopsis SL receptor protein, AtD14. On the other hand, CL and CLA were not able to interact with AtD14, suggesting that the methyl esterification step is critical to convert a biologically inactive precursor to a bioactive hormone molecule. Conventional SL molecules have the tricyclic lactone ring part (ABC-ring) that is connected to another butanolide lactone part (D-ring) via an enol ether bridge. However, CL derivatives lack BC ring system, and possesses only A and D rings. After the discovery of CL derivatives, structurally similar molecules have been isolated from various plant species. Currently, these new types of SL molecules are classified to be 'non-canonical' SLs, whereas the conventional SLs are called 'canonical' SL (Fig. 1). Although, these new types of SL molecules have been identified, the functional difference between canonical and non-canonical SLs are not fully understood. In this collaborating project with Prof. Shinjiro Yamaguchi in ICR, Kyoto University, we planned to clarify the biological role of non-canonical SL by chemical and genetic approach.

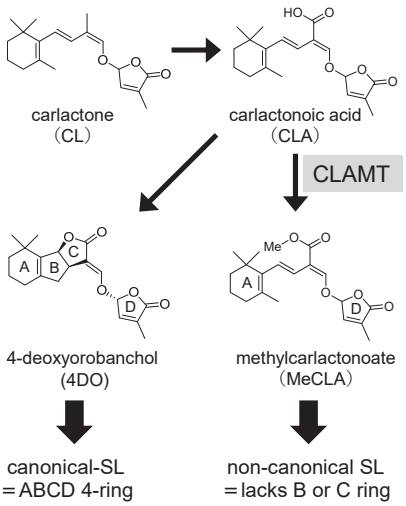


Fig. 1, The outline of the biosynthetic pathway for canonical and non-canonical SLs.

【Results】Using an important crop, tomato, we have successfully identified a CLAMT candidate by a biochemical analysis. Now we are preparing the tomato *clamt* knockout mutants using CRISPR-CAS9 technology. In parallel with the genetic analysis, we decided to explore chemical inhibitors for CLAMT. We aimed to prepare some structural analogs of the CLAMT substrate, CLA, and we have synthesized two analogs (Fig. 2). One of these two analogs (CLA analog2) lacks the methyl group in the butanolide D-ring, which was demonstrated to be an important part for the SL activity. We found that CLAMT could accept this analog as a substrate. We expect that the methylation product of this analog does not have the SL activity. Thus, although this analog is not a simple inhibitor for CLAMT, this analog may function as a functional inhibitor when applied to plant.

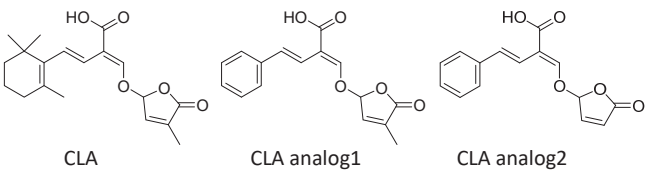


Fig. 2, Chemical structures of CLA and its synthetic analogs.

光励起に伴うシクロパラフェニレン酸化体の芳香族性・反芳香族性のスイッチング

藤塚守　大阪大学

ベンゼン環オリゴマーであるパラフェニレンが環状構造になっているシクロパラフェニレン(CPP)は、高い歪みと環状に整列した p 軌道に由来する物性が関心を集めており、その機能評価が近年進められている。われわれは、化学研究所の山子教授のグループと CPP 類の励起状態およびラジカルイオン状態などに関する共同研究を展開し、種々の知見を報告してきた。近年、山子グループは CPP 内にエチニル基を導入した化合物(Fig.)の合成に成功し、諸物性ならびに酸化挙動を報告している。[1] 本研究では種々の時間分解分光法を適用し、当該化合物の励起状態物性の検討を行った。

本化合物の蛍光物性を Table に示す。エチニル基が 1 個 2 個のいずれの場合においても蛍光量子収率(Φ_f)がベンゼン環とともに増加する傾向はエチニル基を含まない CPP と同様であるが、エチニル基を 2 個含む場合には 1 個のものよりΦ_fが小さくなることが示されている。蛍光寿命も短寿命化が確認されたが、輻射速度(k_r)にはエチニル基の数により顕著な差がみられなかったことより、項間交差および内部転換速度がエチニル基の数により依存することが示唆された。これらに関し過渡吸収測定により検討を進める予定である。

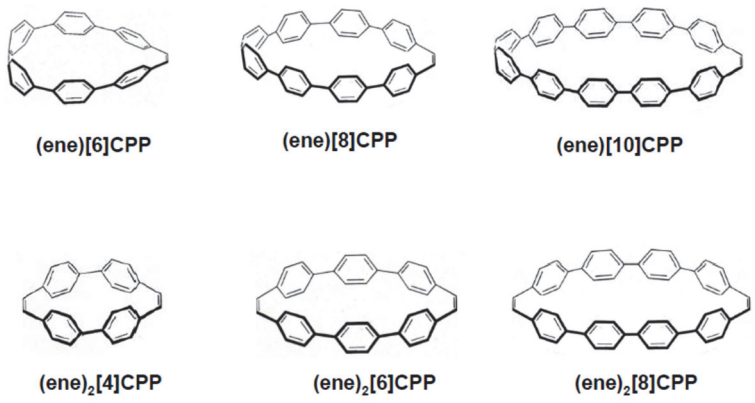


Fig. Molecular structures of CPPs in this study.

Table. Fluorescence quantum yield (Φ_f), lifetime (τ_f) and radiative rate (k_r) of CPPs.

	λ_{em} / nm [a,b]	Φ_f [a,b]	τ_f / 10^{-9} s		k_r / 10^8 s^{-1} [b]
			in THF	in CH_2Cl_2	
(ene)[6]CPP	520		1.44	2.14	
(ene)[8]CPP	483	0.59	2.01	2.72	2.17
(ene)[10]CPP	462	0.84	2.46	2.35	3.57
(ene)$_2$[4]CPP			1.10	0.93	
(ene)$_2$[6]CPP	409, 424	0.25	0.89	0.79	3.16
(ene)$_2$[8]CPP	419, 434	0.36	1.11	0.90	4.00

[a] From ref. 1. [b] in CH_2Cl_2

【文献】(1) T. Terabayashi, E. Kayahara, Y. Mizuhata, N. Tokitoh, T. Nishinaga, T. Kato, S. Yamago ChemRxiv DOI: 10.26434/chemrxiv.14547384.v1

高強度レーザーと構造性媒質の相互作用による高エネルギー密度プラズマの生成・保持に関する実験研究

岸本泰明　京都大学

【計画全体の目的】集光強度が $I\sim10^{18\text{-}20}$ W/cm^2 の高強度レーザーをサブ μm オーダの微細構造を有する物質（構造性ターゲット）に照射することにより高エネルギー密度状態のプラズマを生成するとともに、その過程において現出するプラズマの自己組織化機能や構造形成機能を制御することにより、kT オーダの準定常強磁場の生成やそれによる生成プラズマの慣性時間を超えた保持（閉込め）を実現できる可能性が提案者等のシミュレーション研究により示されている。これが実現すれば、中性子を出さない究極の核融合である陽子・ホウ素（P-B）反応など、これまでにない新たな応用が期待される。本研究では、上述の仮説を検証することを目的に、ナノ工学と材料工学を用いて構造性ターゲットを作製するとともに、これに京大化研 T6 レーザーを照射する実験を行うことにより上述の仮説を検証することを目的とする。

【得られた成果】(1)高アスペクト比のロッドターゲットの作製：電子線リソグラフィーとプラズマエッチングを含む半導体技術を用いて、京大ナノハブ拠点において、厚さ 500 μm のシリコンウエハ（基板）上に、直径がサブμm で間隔がμm オーダの円柱状ケイ素が多数配列したターゲット（ロッドターゲット）を作製した。京大化研 T6 レーザーを用いた照射実験(2019 年 11 月実施)では、ロッドの高さが 5 μm 程度と T6 レーザーのレイリー長 20 μm と比較して小さく、レーザーと基板との相互作用が支配的である可能性があった。そこで本年度は、エッチングパラメータを調整することで、高アスペクト比(高さ/半径~50-100)のロッドの作製に成功した(図 1)。2021 年 9 月には作製したロッドを用いた照射実験を実施し、電子エネルギーに関するデータを取得した。

(2)アライメントのための新奇ターゲットの開発：ロッドに対する正確な照射実験を実施するため、図 1 に示すようなターゲットを開発した。具体的には、T6 レーザー集光時のスポット径(3-4 μm 程度)を正確に同定するため、ロッド周辺に数μm オーダの様々なサイズの円柱と角柱を設置した。また、照射位置を厳密に決定するため、ロッド集合体から正確な距離に鋭利なくさび型の構造物を設計・配置した。加えて、高性能のデジタルカメラと、従来のレンズと比較して収差の少ない顕微鏡用高倍率対物レンズを導入し、無限遠光学系によるロッド集合体の観察手法を確立した。

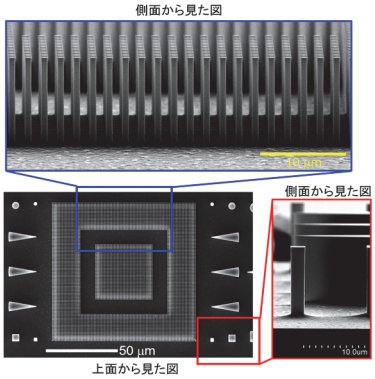


図 1 レーザー照射実験におけるアライメントへの利用を想定したターゲット（SEM 画像）。

(3)実験システムの構築：ロッドターゲットは、質量を保った場合に半径を変化させることで表面積が自在に調節可能であり、レーザーとの相互作用において元の形状を保持したまま「バルク」としてのプラズマが生成することを粒子シミュレーションにより見いだしている。我々は、プラズマの2方向（ロッド軸方向／ロッド側面方向）からの電子温度の同時測定を目的として、拠点予算の援助を得て、京大化研の電子スペクトルメータ(ESM)と同一の性能を有する ESM を製作した。また、プラズマの干渉計測と磁場計測を目的として、チャンバー内において光学機器、観察用モニターの配置の検討を行っている。2021 年度で構築した実験体制を踏まえ、2022 年度ではレーザー照射実験を実施し、プラズマの2方向電子温度および電子密度を測定し、3次元粒子シミュレーション結果との比較・検証を行う予定である。

参考文献：松井隆太郎，上田永樹，太田雅人，福田祐仁，坂和洋一，岸本泰明、「高強度レーザーと波長オーダの構造性ターゲットとの非線形相互作用特性」、日本物理学会　2021 年秋季大会、2021.9.20、online

Coupling of concentration fluctuation and orientation fluctuation in mixture of nematic liquid crystal and solvent

Ryoko Shimada　Japan Women's University

In a mixture of a liquid-crystalline (LC)-forming material and an ordinary (non-LC) material, the volume fraction ϕ and the orientational order parameter Q of the LC molecules serve as the order parameters that may *couple* with each other to affect the static (thermodynamic) and dynamic (rheological) properties of the mixture. Utilizing 4-cyano-4'-pentylbiphenyl (5CB) and dimethyl phthalate (DMP) as the LC and ordinary materials, this study examined the dielectric relaxation and viscosity of a DMP/5CB mixture in an isotropic one-phase state. The phase diagram reflecting the thermodynamics in the mixtures of various DMP content w_{DMP} was well described by a simple model of free energy contributed from the Flory-Huggins type mixing entropy (no enthalpic contribution) and the Landau-de Gennes type nematic interaction.

For the mixture with w_{DMP} = 3.1 wt% in a high-T asymptote ($T > T_{IN}$+10˚C with $T_{IN} \cong$ 27.0˚C being the isotropic-to-nematic transition temperature of the mixture), the dielectric relaxation time τ_ε was close to that of pure 5CB, as noted in Fig.1(a); compare red and green symbols at high T. This result suggests no significant effect of the above coupling on the 5CB dynamics in the mixture at such high T. Nevertheless, in a significantly wide *pre-transition zone* of T between T_{IN} and T_{IN}+10˚C, τ_ε of the isotropic one-phase mixture increased on cooling much more significantly compared to τ_ε in that high-T asymptote. The kinematic viscosity ν of the mixture exhibited a qualitatively similar but quantitatively weaker increase in that pre-transition zone, as noted in Fig.1(b).

This difference between the dielectric τ_ε and the rheological ν can be attributed to coupling of the orientation and the composition fluctuations mentioned above. Namely, the composition fluctuation governs ν, and also enhances the orientation fluctuation in the mixture thereby providing τ_ε (reflecting the orientation fluctuation) with an extra increase. Pure 5CB exhibited similar increases of τ_ε and ν, being stronger for the former, but only in a close vicinity of its T_{IN}˚ (within 2-3˚C), because pure 5CB exhibits no composition fluctuation and the orientation fluctuation is coupled only with the density fluctuation. This behavior of pure 5CB in turn suggests an importance of the coupling of the orientation and composition fluctuations in the DMP/5CB mixture.

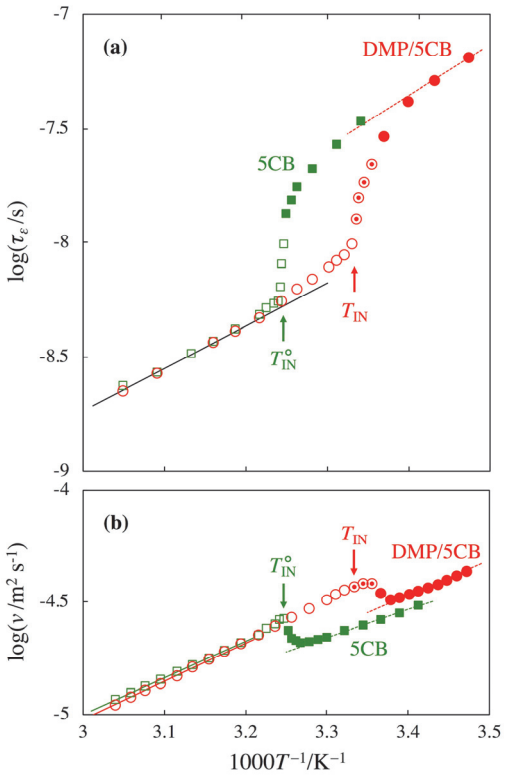


Fig. 1 Temperature dependence of (a) dielectric relaxation time and (b) kinematic viscosity of 5CB and DMP/5CB mixture (w_{DMP} = 3.1 wt%).

Publication: R. Shimada, O. Urakawa, T. Inoue and H. Watanabe, *Soft Matter,* **17**, 6259-6272 (2021).

Determine the three-dimensional structure of ^{13}C labeled α-synuclein(61-95) in the Langmuir-Blodgett film and supported phospholipids bilayers by p-MAIRS FT-IR

Chengshan Wang Middle Tennessee State University

A. Objectives:

1. ^{13}C labeled α-syn(61-95) containing residues 61-95 of α-synuclein will be synthesized and purified.
2. Screen the conformation and orientation of specific amino acid residue of α-syn(61-95) in Langmuir-Blodgett film.
3. Screen the conformation and orientation of specific amino acid residue of α-syn(61-95) in supported phospholipids bilayers.

B. Experimental methods:

Peptide of ^{13}C labeled α-syn(61－95) at position 93G was synthesized via solid phase (Fmoc) chemistry and purified by semipreparative reversed-phase high-performance liquid chromatography (RP-HPLC) on Waters Breeze 2 separation system equipped with 1525 EF binary pump. The success of the synthesis and the purity of the peptide were confirmed by a Waters SYNAPT q-TOF tandem mass spectrometer. The surface pressure-area (π−A) isotherm of α-syn(61－95) were conducted in a A Kibron μtrough. The Langmuir-Blodgett (LB) films of α-syn(61－95) were made by transferring the α-syn(61－95) Langmuir monolayers to quartz slides and silicon (Si) slides under the surface pressure 10 mN/m. The circular dichroism (CD) spectra of the LB films of the ^{13}C labeled α-syn(61－95) were measured by a JASCO J-810 spectropolarimeter. p-Polarized Multiple-Angle Incidence Resolution Spectroscopy (pMAIRS) measurements were performed on the Nicolet IS50 FT-IR spectrometer (Thermo Scientific, Waltham, MA) equipped with a pMAIRS accessory. The LB film monolayer of the ^{13}C labeled α-syn(61－95) at position 93G on Si substrate was put in the pMAIRS accessory and the IR beam transmitted trough the sample.

C. Experimental results:

The ^{13}C labeled α-syn(61－95) was synthesized and purified. Figure 1A shows the π−A isotherm of the ^{13}C labeled α-syn(61－95) and the isotherm is very similar to that of the unlabeled α-syn(61－95). This is not a surprise because replacement of a ^{12}C by ^{13}C in the backbone carbonyl (i.e., C=O) should not change the overall biophysical behavior of the peptide, which contains hundreds of carbon atoms in it. Thus, the CD spectrum of the ^{13}C labeled α-syn(61－95) is also similar to that of unlabeled peptide as shown in Figure 1B. For the LB films of the ^{13}C labeled α-syn(61－95), two negative peaks at 222 and 208 nm in addition to one positive peak at 192 nm are detected. Therefore, the ^{13}C labeled α-syn(61－95) also transforms to α-helix at the

interface. On the other hand, pMAIRS was used to determine the tilted angle of the axis of α-syn(61－95) at 93G and is very different to that of the unlabeled peptide. As shown in Figure 1C, The In-plane Spectrum (S_{IP}) result of the ^{13}C labeled α-syn(61–95) was shown as the top curve in Figure 1C. Both regular amide I and II bands were detected at 1655 and 1535 cm^{-1}, respectively. A very strong ^{13}C amide I band was also detected at 1625 cm^{-1} in the S_{IP}. The position at 1625 cm^{-1} shows that the 93G is in α-helical conformation in the LB film. In addition, the ^{13}C amide I band in the S_{IP} result is even more intensive than the regular amide I band which is the absorption sum of all the other thirty-four residues in the sequence of α-syn(61–95). Such an intensive ^{13}C amide I band suggests a very small tilt angle (i.e., parallel orientation) of the ^{13}C amide I transition moment. The out-of-plan Spectrum (S_{OP}) shown in the bottom curve of Figure 1C also detects the amide I band at 1659 and 1645 cm^{-1}. More importantly, the ^{13}C amide I band at 1625 cm^{-1} was not detected in the S_{OP} result, even though the ^{13}C label does exist at position 93G. According to the selection rule of pMAIRS, the tilt angle of the ^{13}C amide I transition moment at 93G is ~0º. Because the tilt angle of the axis of α-helix is equal to that of the ^{13}C amide I transition moment, the tilt angle of the axis of α-helix at 93G is also ~0º.

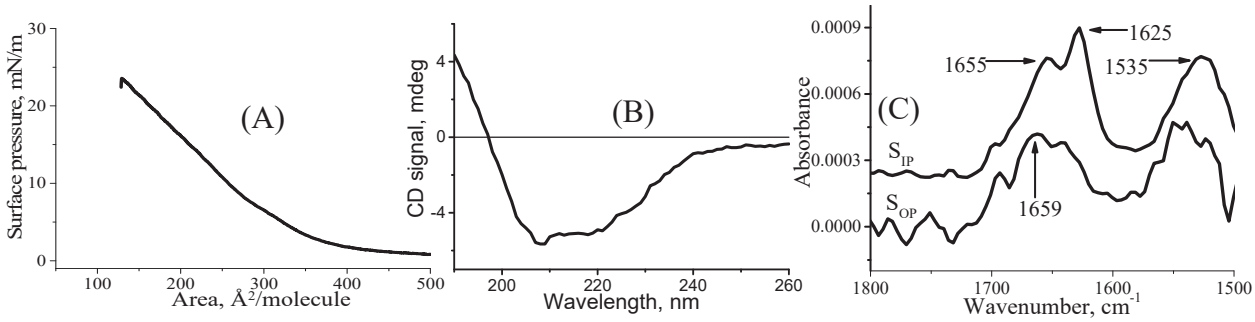


Figure 1. (A) Surface pressure-area isotherm of the ^{13}C labeled α-syn(61－95) on pure water, (B) CD spectra of the LB films of the ^{13}C labeled α-syn(61－95) on quartz slides. (C) p-MAIRS results of the LB monolayer of the ^{13}C labeled α-syn(61－95) transferred under 10 mN/m.

D. Discussion

X-ray crystallography and NMR are two major methods to determine protein's structure. However, neither of them can elucidate the high resolution structure of membrane proteins, which weighs ~ 30-35% of the total proteins, in monolayer structure. Dr. Wang and Dr. Hasegawa are developing a method for membrane proteins in monolayer structure with residue resolution by pMAIRS, which will be a supplement to X-ray crystallography and NMR.

E. Publication.

All the results in Figure 1 have been presented in conference SciX 2021. In addition, one paper about Figure 1 is in preparation for the submission to *Chemistry A European Journal*.

Modulation of in-cell protein-protein interactions using mid-sized peptides

Yoshio Hayashi　Tokyo University of Pharmacy and Life Sciences

Protein-protein interactions (PPIs) are difficult targets for typical small molecule ligands. Mimicking folded domains of proteins, we can modulate the function of a particular protein with metabolically stable synthetic molecules. Therefore, strategies for developing structured mid-sized peptides that display protein-like functionality are highly demanded in drug discovery. This project aims to invite three world-wildly prominent professors in chemical biology and medicinal chemistry to discuss the scope and limitation of current strategies in development of structured mid-sized peptides targeting PPIs. The applicant was the organizer of The 58th Japanese Peptide Symposium (JPS), which was originally scheduled to be held in Hachioji on Oct 20-22, 2021 (Figure 1). Although it is a domestic meeting, all the presentations are made in English every year to facilitate the participation from abroad. The world-wide prominent professors in this research field, including professors Paramjit S. Arora (New York University), Ronald T. Raines (Massachusetts Institute of Technology), Michael D. Burkart (University of California, San Diego) were nominated as the Invited speakers at the 58th JPS (Figure 2). Supported by the international Joint Usage/Research Center (iJURC), Institute for Chemical Research (ICR), Kyoto University, these professors were also supposed to make lectures at Institute for Chemical Research, Kyoto University. However, due to the prevalence of COVID-19, we had to give up on inviting these



Figure 1. The poster of The 58th Japanese Peptide Symposium

speakers to the symposium and to Kyoto as well and to hold the meeting via internet (Figure 3). We were happy to know that Professors Arora and Burkart agreed to make invited talk at the 58th JPS (unfortunately, schedule of Professor Rains did not permit his participation), under the titles of "A Sos proteomimetic as a Pan-Ras inhibitor" and "Directing biosynthesis in type II NRPS pathways", respectively. The three-day symposium was held as scheduled. Even though held as a web-based meeting, we had 51 oral presentations including 7 invited talks from abroad and 4 award talks together with 125 poster presentations. Total numbers of participants were 395 which included 23 participants from abroad and 152 students. The applicant finally thanks to iJURC-ICR to give an opportunity to invite these professors to TUPLS, and ICR Kyoto University although we were not able to make it due to the COVID-19 affairs. The applicant wish to have another chance to invite the above professors to TUPLS and ICR Kyoto University, Japan to have face-to-face discussion.

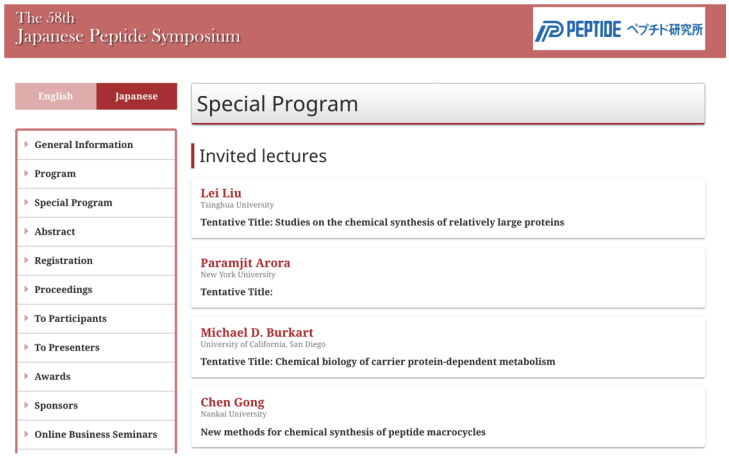


Figure 2. Invited lectures from abroad.



Figure 3. The website of The 58th JPS.

Rheology symposium at ICR
Instead of the 16th International Workshop for East Asian Young Rheologists

Tadashi Inoue　Osaka University

【Purpose of project】The ICR budget was initially proposed to organize the 16 International Workshop on Young Rheologists in East Asia (IWEAYR-16, Thailand). Unfortunately, COVID-19 prevents having the workshop on site. This workshop aims to promote international exchange among young faculty and graduate students in cooperation with researchers from various countries in East Asia in several research fields such as polymer science and materials science. The workshop has contributed to deepen our research activity and formed the basis for future cooperation. Prof. Watanabe (ICR, Kyoto University) launched this workshop as a core member. Considering his retirement in 2022, we decided to have an alternative symposium at ICR to share the new research results and discuss the future plane of IWEAYR with COVID-19. The symposium was organized by Japanese members of IWEAYR.

【Place and schedule of workshop】We had a special rheology symposium with seven invited speakers. The symposium was held from Dec 17, 2021, including the business meeting after the symposium.

【Purpose of the symposium】The purpose of IWEAYR is to promote international exchange and collaboration among young faculties and graduate students who will be the main researchers in the field of rheology and material science in the near future, and therefore, to provide a place for research presentation and discussion, and to revitalize related fields.

The alternative symposium was designed to provide an opportunity for participants to share the new research results and exchange research ideas in an amiable atmosphere.

【Background of workshop】This workshop has been held annually since the first IWEAYR in Seoul (February 2006). After that, it was organized in Kyoto (January 2007), Shanghai (January 2008), Nakhon Ratchasima (January 2009), Busan (January 2010), Yamagata (January 2011), Beijing (February 2012), Phuket (January-February 2013), Seoul (February 2014), Fukuoka (February 2015), Shenzhen (January 2016), Pattaya (February 2017), Jeju Island (January 2018), Nagoya (January 2019) (in a circulating order of Korea, Japan, China, and Thailand).

【Participants】The number of participants in this rheology symposium was over 40. The main participants were:

Hiroshi Watanabe, Professor,	Kyoto University	Japan
Yumi Matsumiya, Asso. Professor,	Kyoto University	Japan
Takeshi Sato, Assi. Professor,	Kyoto University	Japan
Mikihito Takenaka, Professor,	Kyoto University	Japan
Yoshinobu Tsujii, Professor,	Kyoto University	Japan
Takashi Taniguchi, Asso. Professor,	Kyoto University	Japan
Kenji Urayama, Professor,	Kyoto Institute of Technology	Japan

Shinichi Sakurai, Professor,	Kyoto Institute of Technology	Japan
Yuichi Masubuchi, Professor,	Nagoya University	Japan
Takashi Uneyama Asso. Professor,	Nagoya University	Japan
Junichi Takimoto, Professor,	Yamagata University	Japan
Satish K. Sukumaran, Asso. Professor,	Yamagata University	Japan
Takamasa Sakai, Professor,	University of Tokyo	Japan
Naoyuki Sakumichi, Project Lecturer,	University of Tokyo	Japan
Takuya Katashima, Project Lecturer,	University of Tokyo	Japan
Osamu Urakawa, Asso. Professor,	Osaka University	Japan
Tadashi Inoue, Professor,	Osaka University	Japan



Snap shots of the symposium.

【Overview of the symposium】After welcome address by Professor Watanabe, the author provided a topic concerning on “Relationship between molecular structure and entanglement.” Professor Urakawa presented his recent results on “Dynamics of polymer systems with specific interactions.” After a short break, Professor Uneyama introduced his study on “Static and Dynamic Shielding Effects of Interaction in Interacting Dumbbell Systems.” Professor Takimoto presented his results on “Simulation study of the high-speed flow of entanglement-free polymers.”

Young Professors Katashima and Sakumichi respectively talked about “Dynamic of transient networks” and “Negative energetic elasticity of hydrogels.” Professor Masubuchi showed “Relationship between Strength of Tetra-PEG Gel and Molecular Weight Distribution of Prepolymer Studied by Simulation.” Finally, Professor Urayama presented his study on “Crack characterization of elastomers in biaxial elongation field.”

【Summary】 Throughout the symposium, the discussion was very active. The professors gave all presentations, and the scientific level of each presentation was quite high and exciting. This symposium gave us a new trend in rheology and polymer science. The high-density collaboration among researchers is essential for the policy and direction of IWEAYR in the coming years. We appreciate the financial support from ICR. I would like to finish this report hoping to have IWEAYR-16 on-site in Udon Thani, Thailand in next year.

12/17 (Fir) Rheology symposium

@Uji Obaku Plaza, Seminar rooms 1&2　(Uji Campus, Kyoto University)

Chair: Hiroshi Watanabe (Kyoto Univ.)

12:50-13:30　Relationship between molecular structure and entanglement.
Tadashi Inoue (Osaka Univ.)

13:30-14:00　Dynamics of polymer systems with specific interactions.
Osamu Urakawa (Osaka Univ.)

Break

Chair:　Takuya Katashima (Tokyo Univ.)

14:20-14:50　Static and Dynamic Shielding Effects of Interaction in Interacting Dumbbell Systems.
Takashi Uneyama (Nagoya Univ.)

14:50-15:20　Simulation study of the high-speed flow of entanglement-free polymers.
Junich Takimoto(Yamagata Univ.)

Break

Chair:　Sathish Sukumaran (Yamagata Univ.)

15:40-16:10　Understanding the science of dilute polymer networks
Takamasa Sakai (Univ. Tokyo)

16:10-16:40　Relationship between Strength of Tetra-PEG Gel and Molecular Weight Distribution of Prepolymer Studied by Simulation.
Yuichi Masubuchi (Nagoya Univ.)

16:40-17:10　Crack characterization of elastomers in biaxial elongation field.
Kenji Urayama (Kyoto Institute of Technology)

Micro- and Nano-structural Characterization by Advanced Transmission Electron Microscopy of Novel Functional Materials for Battery Development

Torranin Chairuangsri Chiang Mai University

Our research group in Thailand has been collaborating with researchers at the ICR including Hiroki KURATA and Mitsutaka HARUTA in micro- and nano-structural characterization by advanced transmission electron microscopy of novel functional materials for battery development. The results can be summarized as follows:

I. Novel Composites as Anode in LIBs

Online experiment has been conducted on examining the novel composites as anode in LIBs. Ge/NrGO and SiO_2-rGO were examined using the JEM-200FC microscope for determining distribution and characteristics of the nanocomposites. EDS mapping of Ge/NrGO and SiO_2-rGO was performed using the JEM-ARM200F microscope including Ge, N, C, O, and Si. Individual Ge particle sizes were in the range 5–20 nm. It was noticed that the good dispersion of Ge particles was observed on the NrGO sheet because NrGO obstructed the agglomerated matrix of nanoparticles, resulting in an increased dispersion ability of nanoparticles. Both the separated nanostructure and cluster morphology of GeNPs were presented in the pre-pared composites. The existence of Ge has been confirmed, which was unable to reveal by XRD. Polyaniline-SiO_2/rGO nanocomposites has been also examined. Polyaniline deposition on the surface of SiO_2/rGO composites has been confirmed. It is anticipated that its distinct structure will improve the electrochemical performance of Polyaniline-SiO_2/rGO composites as LIBs anodes.

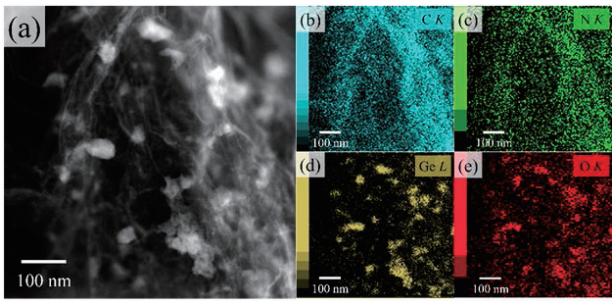


Fig. 1 (a) HAADF-STEM image and EDS mapping images of element distribution corresponded to (b) C, (c) N, (d) Ge, and (e) O signals.

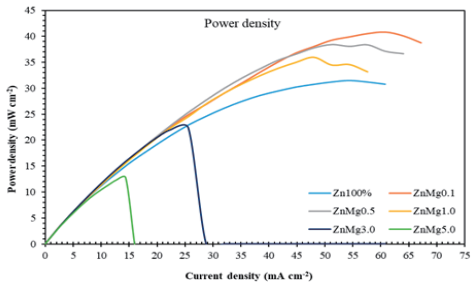


Fig. 2 Power density versus loaded current density of Zn-Mg anodes from the single-cell test.

II. Novel Zn-Mg Alloys as Anode in Metal-Air Batteries

Experiment in Thailand has been conducted and TEM/STEM experiment at ICR is on arranging. Zn-Mg alloys containing Mg up to 5.0 wt.% have been prepared. SEM revealed that the microstructure of hypoeutectic compositions (0.1, 0.5 and 1.0 wt.%Mg) contained Zn-rich primary phase. The composition close to the eutectic point (3.0 wt.% Mg) has almost fully eutectic structure consisting of Mg_2Zn_{11} and Zn-rich phase. The hypereutectic composition (5.0 wt.%Mg) had a primary phase of Mg_2Zn_{11}/$MgZn_2$. Potentiodynamic polarization testing in 6 M KOH has been conduced and the single-cell test using MnO_2 as the air catalyst has been performed. The assembly had an open circuit voltage of 1.4 V and the alloys with small Mg content up to 1.0 wt.% showed better electrochemical performance as anode as compared to pure Zn.

III. Novel Manganese-containing Phosphate Glasses as Cathode in LIBs

Experiment in Thailand has been conducted and TEM/STEM experiment at ICR is on arranging. Structural and local chemical analyses of manganese-lithium-phosphate glasses containing MnO 10-30 mol.% were studied. XRD pattern of the samples showed the containing of some crystalline phase(s). The highest amount of crystalline phase(s) was found in sample with highest MnO containing. It seems likely that Mn ions play an important role on the structural changing, oxidation states of Mn itself and electrochemical property. FTIR, shows the changes in bonding between P-O in the samples as MnO containing increases. Moreover, EXAFS also shows the different in Mn environment as MnO containing changes as two environments was detected. Sample with highest MnO (30 mol%) possess highest specific capacitance.

One paper has been published [Autthawong, T.; Promanan, T.; Chayasombat, B.; Yu, A.-S.; Uosaki, K.; Yamaguchi, A.; Kurata, H.; Chairuangsri, T.; Sarakonsri, T. Facile Synthesis Sandwich-Structured Ge/NrGO Nanocomposite as Anodes for High-Performance Lithium-Ion Batteries. Crystals. 2021. https://doi.org/10.3390/cryst11121582] and other two manuscripts are being prepared.

Tackling the Electronic Instability of Charge-Density Waves by Electron Energy-Loss Spectroscopy

Ming-Wen Chu　National Taiwan University

This project (2021-123) aims at resolving the electronic excitations in charge-density-wave (CDW) CuTe by means of electron energy-loss spectroscopy (EELS), in collaboration with Prof. Hiroki Kurata at ICR. The CDW instability is conventionally correlated with a Fermi-surface nesting and associated Peierls transition, and manifested by concomitant sinusoidal-charge and -structure modulations. Intriguingly, the collective excitation of CDW plasmons has been reported to display an unusual negative dispersion (as a function of momentum transfer q) in some studies, whereas the others suggest an ordinary parabolic dispersion characteristic of conventional electron gas. The existence of a negative dispersion refers to the condensation of the electronic state and is of tremendous physical significance. Its thorough scrutiny is, therefore, timely and calls for elaborate q-dependent EELS investigations with both high q and energy resolutions.

The EELS facility of Prof. Kurata is ideal for achieving the experimental requirement of high q and energy resolutions and, meanwhile, CuTe stands for an unambiguous CDW system, satisfying both the essential ingredients of Fermi-surface nesting and Peierls instability. CuTe forms the model material system to tackle the emergent issue of CDW plasmons. Due, however, to the COVID-19 pandemic, it has been unlikely for my group to conduct q-EELS studies together with Prof. Kurata in ICR. Nonetheless, efforts on the preliminarily investigation of structural characteristics of the CDW order in my group has been fruitful and firm knowledge on the aspect has been established, paving the avenue to extensive q-EELS scrutiny in 2022. Here below is a scanning transmission electron microscopy (STEM) image of the CDW state in CuTe taken by high-angle annular dark field (HAADF) imaging at room temperature.

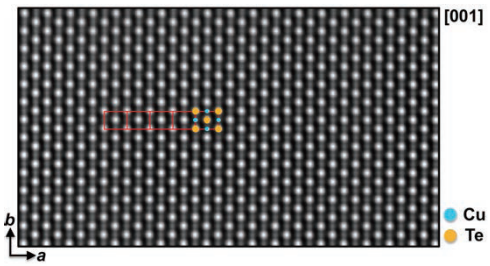


Figure. The STEM-HAADF imaging of a CuTe single crystal, projected along c-axis.

High-pressure synthesis of potential multiferroic oxides

Kunlang Ji　University of Edinburgh

Objectives: High pressure-high temperature (HPHT) synthesis is used to stabilise unusual oxidation states and coordination environments in transition metal oxides, resulting in interesting physical properties. In collaboration with Professor Shimakawa in ICR at Kyoto University, a unique high-pressure multianvil apparatus which reaches up to 20 GPa and 2273 K is available to use. This equipment provides a good opportunity for synthesize the double corundum/perovskite with small tolerance factor and develop their potential multiferroics.

Experimental methods: Due to the Covid-19 special circumstance, we developed our collaboration by communicating e-mails. We focus on writing paper of the new double corundum Co_2InSbO_6 synthesized at Kyoto University during early 2020, while Professor Shimakawa providing very useful scientific guidance for the paper through emails.

Experimental results: Co_2InSbO_6 recovered from high pressure has a new, ordered-*R*32 A_2BCO_6 variant of the corundum structure. Co_2InSbO_6 is also remarkable for showing an unprecedented sequence of two cation redistributions, to $(Co_{0.5}In_{0.5})_2CoSbO_6$ and then Co_2InSbO_6 variants of the ordered-$LiNbO_3$ A_2BCO_6 structure on heating. The cation distributions change magnetic properties as the final ordered-$LiNbO_3$ product has a sharp ferrimagnetic transition at 65 K whereas the initial ordered-*R*32 material has a broader feature indicative of short range spin ordering.

Discussion: The selective site exchange only between Co^{2+} and In^{3+} at different temperatures results from the small size and charge mismatch between Co^{2+} (r^{VI} = 0.745 Å) and In3+ (r^{VI} = 0.8 Å), compare to that between Co^{2+} and Sb^{5+} (r^{VI} = 0.6 Å).

Publication: K. Ji, E. Solana-Madruga, M. Amano Patino, Y. Shimakawa and J. Paul Attfield, A new cation-ordered structure type with multiple thermal redistributions in Co_2InSbO_6, in preparation.

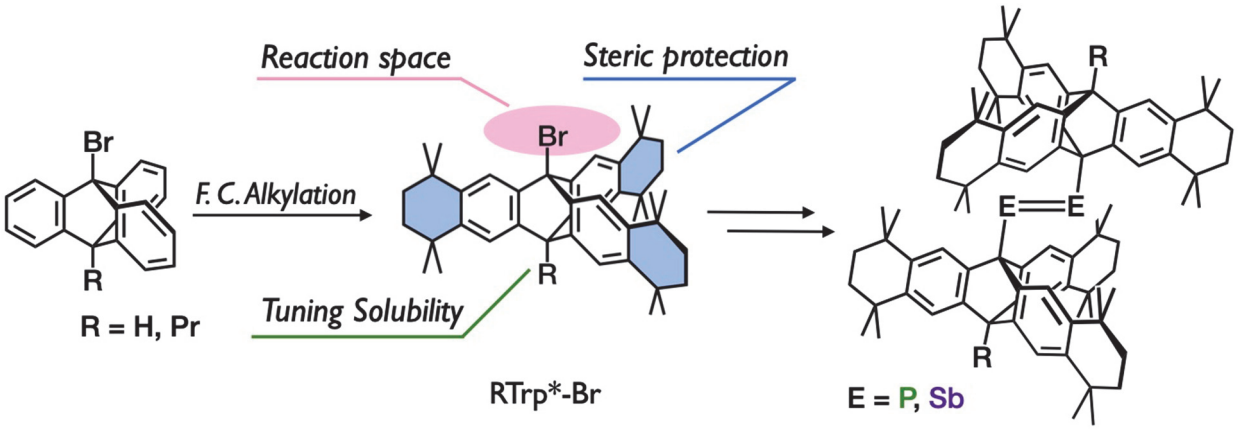
Synthesis and Characterization of Novel Group 16 Element Compouds

Mao Minoura　Rikkyo University

In the field of organoselenium and organotellurium compounds, their synthesis, structural analysis, and reactivity have recently attracted a great deal of research interest not only in chemistry but also in biological applications.[1] It is generally known that P=P and Sb=Sb double bond compounds are highly reactive species and such double bond compounds can easily dimerize. The use of bulky protecting groups enables the synthesis and isolation of such double bond compounds, Tokitoh *et al*. reported the synthesis of those P=P and Sb=Sb double bond compounds with a large aromatic Tbt group. However, in the case of alkyl-substituted species, stable Sb=Sb double bond compounds have not been reported due to the difficulty of ligand design. In recent years, our group has designed and synthesized novel triptycene (Trp)-based aliphatic bulky groups, *i.e.*, Trp* with bulky fused-ring-type substituents around the periphery of the Trp skeleton. In this study, we have synthesized thermally stable Trp*$_2$P$_2$ and Trp*$_2$Sb$_2$ and investigated the reactivity of these double bonded compounds with selenium and tellurium.

The Trp*$_2$P$_2$ and Trp*$_2$Sb$_2$ were synthesized by the reductive coupling reaction of the corresponding dichlorides, Trp*PCl$_2$ and Trp*SbCl$_2$, with alkali metal, respectively. The isolated Trp*$_2$P$_2$ and Trp*$_2$Sb$_2$ are thermally very stable and moisture sensitive, the molecular structures were determined by X-ray crystallographic analysis.[2]

We thank Professors Norihiro Tokitoh, Yoshiyuki Mizuhata, Mariko Yukimoto (ICR, Kyoto University) and Professor David G. Churchill (KAIST, Korea) for their helpful discussions.



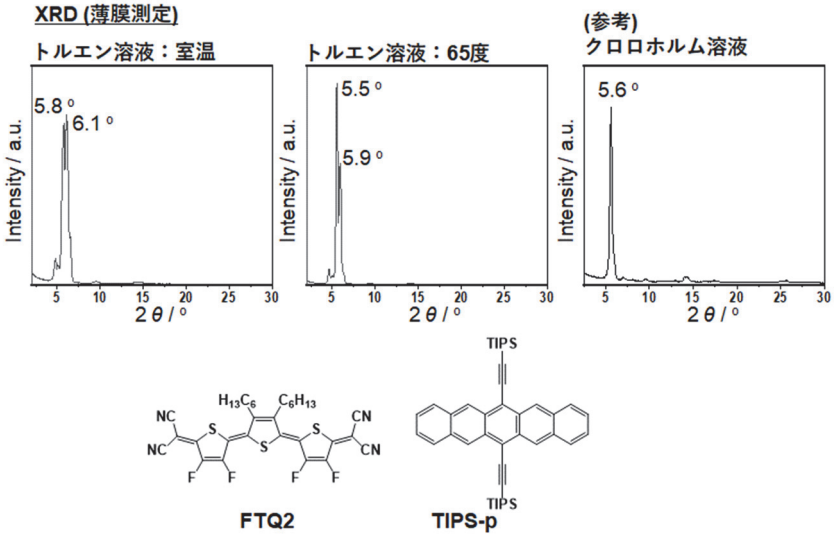
1) David G. Churchill *et al*. *Molecules*, **2021**, 26, 692. doi:10.3390/molecules26030692
2) Mao Minoura *et al*. *Bull. Chem. Soc. Jpn.*, **2021**, 94, 2919. doi:10.1246/bcsj.20210350

固体 NMR を駆使した有機結晶および有機薄膜の分析

家裕隆　大阪大学

π共役系有機分子を有機半導体材料に用いた、有機 EL,有機太陽電池等の有機エレクトロニクス研究が盛んに行われている。これらのデバイスでは、有機半導体材料の薄膜を活性層がその特性に大きな影響を与えることから、原子間力顕微鏡による表面モルフォロジー、粉末 X 線構造解析による分子配列評価を中心とする薄膜解析が行われている。しかし、有機薄膜では、分子の固体状態で様々な集合状態、すなわち、結晶、非晶、結晶―非晶混合状態をとるため、これらの解析手法では、分子レベルの情報を得ることが困難である。一方、固体 NMR を用いた薄膜分析は、有機非晶性膜の局所構造、ダイナミクス解析が可能であることから、有機エレクトロニクス素子開発において、極めて重要な測定技術である。しかし、現状では研究例は極めて少ない状況である。NMR 測定において ^{19}F 核は天然存在比が高く、高感度な核種であることから、含フッ素材料を用いることで ^{19}F 核をプローブとした高感度分析の実現が期待できる。そこで、本研究では我々が見出した含フッ素キノイド構造のアクセプター分子（FTQ2）とドナー性分子（TIPS-p）を混合して得られる結晶あるいは非晶性膜を作製し、固体 ^{19}F NMR 測定を行うことで、分子レベルの相分離構造、分子コンフォメーション、分子運動性を解明し、有機太陽電池の高効率化に繋がる学術的知見を得ることを目的とした研究を行った。

これまでに FTQ2 と TIPS-p の 2:1 混合比のクロロホルム溶液からドロップキャスト法で薄膜作製すると結晶性薄膜が得られることを見出している。そこで、薄膜作製条件の違いによる結晶構造の調節を目的として、より TIPS-p と親和性の高いトルエン溶媒で薄膜作製を行った。XRD 測定の結果、クロロホルム溶媒の時とは異なる結晶系となることが明らかとなった。さらに、ドロップキャストの温度を 65 度まで上昇させることで、結晶性が変化することも明らかとなった。京都大学化学研究所の梶・鈴木グループでこれら薄膜の固体 ^{19}F NMR 測定の測定・解析を進めている。



2021-127

核融合プラズマ対向材料中の水素・ヘリウム挙動の高精度測定

宮本光貴　島根大学

核融合炉発電の実現には，高性能プラズマの安定維持に加え，それを取り囲む材料との相互作用を正確に把握する必要がある．特に，プラズマ対向材料中の水素同位体およびヘリウムの挙動の理解は，プラズマ制御および材料の健全性に関わる極めて重要な課題である．本研究では，昨年度に引き続き，国際熱核融合実験炉(ITER)のプラズマ対向材料に利用が予定されているベリリウムを対象として，バブル内のヘリウムの定量化を試み，さらにその形状や温度依存性について評価した．

図には，室温で 3keV-He^+を $1x10^{21}$ /m^2 照射後，673 K で焼鈍したベリリウム試料内部に観察された(a)ヘリウムバブルの高角度散乱円環暗視野(HAADF)像，(b)ベリリウムの母相と形状の異なる 2 つのバブルの中心部から得られた EELS スペクトルを示した．図(b)に見られるように，バブル中心から得られた EELS スペクトルには，22 eV 付近にヘリウム原子の K-edge に起因する電子線エネルギー損失ピークが観察され，バブル内にヘリウムが存在していることが確認できる．さらに，サイズが同程度(d~40 nm)で，形状の異なるバブルから得られたエネルギー損失ピークの強度は，真円度が高いほど大きい傾向が見られた．図(c)には, EELS 面分析から得られたピーク強度分布からヘリウム密度分布を算出した結果を示しているが，真円度(R)が高いバブル(R~0.93)では, 晶癖面を有するバブル(R~0.63)と比較して 2 倍程度の圧力差があることが明らかになった．さらに，同様の試料を 1073 K 程度まで TEM 内で加熱し，その場観察したところ，バブルの移動度に大きな違いがみられ，球状に近い高圧なバブルほど高い移動度を有することが定量的に示された．バブルの移動度は，照射材料において問題となるボイドスウェリング(体積膨張)に影響を与える一因となることから，本研究で得られた成果は，プラズマ対向材料の寿命評価や使用条件の提案においても有意義な知見となる．

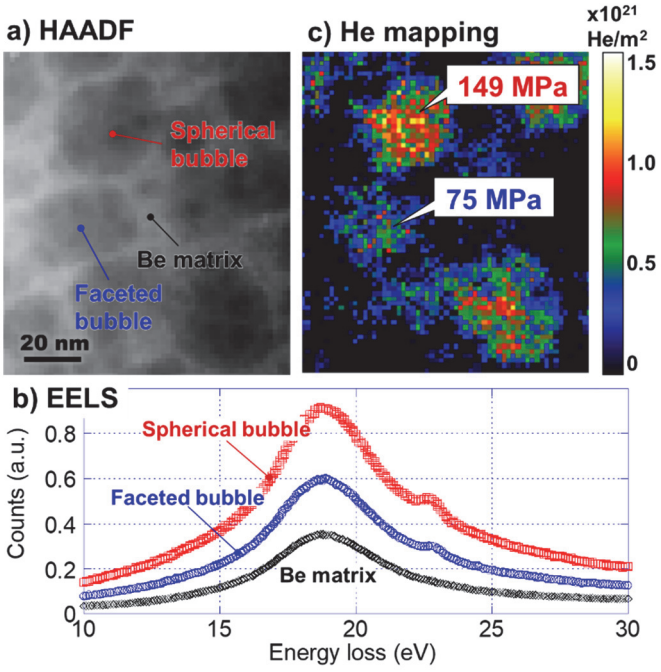


図　ヘリウムイオン照射したベリリウム試料の(a)HAADF 像，(b)ベリリウムの母相と形状の異なる 2 つのバブルの中心部から得られた EELS スペクトル，および(c)ヘリウム密度分布像．

なお，本研究は倉田博基教授，治田充貴准教授（京都大学化研），杉本有隆，原一智（島根大学）らとの共同研究として実施されたものである．また，本成果については，2021 年 10 月に開催された核融合炉材料国際会議 ICFRM-20 にて 2 件の報告を行った．

希土類共ドープナノ粒子の寿命制御

斉藤光　九州大学

希土類イオンを発光中心とした酸化物蛍光体は熱的・化学的安定性が高いことから照明器具や蛍光センサ、検出器など多くの分野で応用されている。このタイプの蛍光体の高輝度化には、固溶限内で希土類イオンの添加量を増やしつつも、母体中に均一に分散させることが重要であることが報告されている[G. Dosoviskiy et al., *J. Lumin.*, **236**, (2021), 118140.]。本研究では、優れた特性を示す酸化物蛍光体の一つである、セリウムを発光中心としたイットリウム・アルミニウム・ガーネット（Ce:YAG）の発光効率向上を目的とし、Ce を高濃度かつ均一に分散させる合成条件について検討した。

純水とエタノールの混合液中に $AlCl_3 \cdot 6H_2O$、$YCl_3 \cdot 6H_2O$、$CeCl_3 \cdot 7H_2O$、およびポリビニルピロリドンを添加して攪拌した。次いで、酸化プロピレンを加えて 2 分攪拌した後、30 分静置した。このゾル溶液をアルミナボートに移し、ホットプレート上で 80 ℃、200 ℃、300 ℃の各温度で 30 分ずつ段階的に加熱し、電気炉内において 1150 ℃で 2 時間焼成することで成生物を得た。また、ゾル溶液調製の際、Ce 添加量を Y に対して① 2.0 mol%、② 4.0 mol%、③ 8.0 mol%と変調した。成生物の Ce 含有量・分布を走査透過電子顕微鏡-エネルギー分散型 X 線分光（STEM-EDS）により評価するとともにフォトルミネセンス（PL）測定により、それぞれの試料の蛍光特性を評価した。

STEM 観察により、得られた生成物はどれも数 10 nm の大きさの YAG の結晶であることがわかった。また、Fig. 1 に示すように、どの試料からも Ce:YAG 由来の 575 nm を中心とした幅広い PL ピークが確認された。YAG 中の Ce 量と分布を STEM-EDS で評価したところ、①、②では YAG 中に Ce が均一に分布しており、③では Ce の偏析が確認された（Fig.2）。Fig.2 の視野全体における、Y に対する Ce 含有量はそれぞれ① 2.3 mol%、② 4.2 mol%、③ 9.4 mol%であり、③において Ce 偏析が確認されない Area 1 の領域では 3.9%であった。したがって、YAG 中に固溶できる Y に対する Ce の最大濃度は、4 mol%程度であることが示唆され、Ce を高濃度かつ均質に分散させるという観点から当該条件が Ce:YAG の発光効率を最大化すると考えられる。

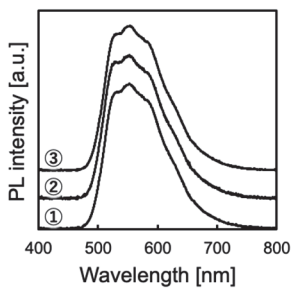


Fig. 1 Normalized PL spectra of Ce:YAG nanoparticles.

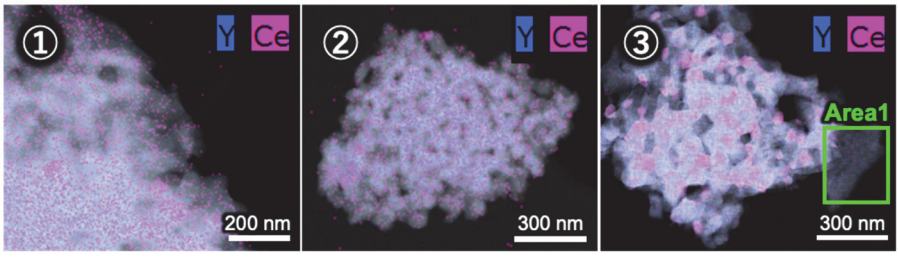


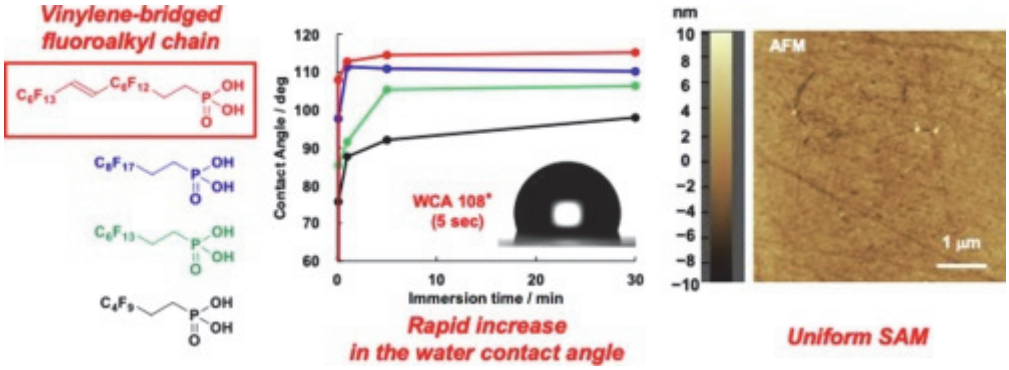
Fig. 2 EDS maps of Ce:YAG nanoparticles superimposed to their HAADF-STEM images.

単結晶 X 線構造解析を用いた、含フッ素共役分子の結晶構造における フルオラス相互作用の解明

吾郷友宏　茨城大学

フッ素置換基は化合物の電子受容能の向上や凝集状態での分子配列制御に寄与するが、フッ素置換基の構造と分子間相互作用の関係に未解明の点が多く、有機材料の凝集構造制御にフルオラス相互作用を積極的に活用するまでに至っていない。例えば、平面π共役分子は有機半導体の重要な構造モチーフであるが、単結晶 X 線構造解析が困難であることが多く、含フッ素共役分子におけるフルオラス相互作用の実験的知見はほとんど無い。本研究では、化学研究所の極微小結晶用 X 線単結晶 X 線構造解析装置である VariMax を用いて、フッ素置換基を導入したπ共役分子の凝集構造制御に有効なフッ素置換基の構造を明確化する。また、昨年度から環境適合の含フッ素有機材料の開発に着手しており、VariMax を用いたミクロ構造解析も実施している。

本年度の研究では、COP9 で廃絶対象物質に追加された長鎖フッ素置換基に代わる、環境負荷が低い新規フッ素置換基の開発を検討した。具体的には、ペルフルオロアルキレンユニットがビニレンユニットで架橋された構造のフッ素置換基であり、COP9 で指定された長鎖ペルフルオロアルキル基と異なりペルフルオロオクタン酸（PFOA）等の生物濃縮性物質は生じない一方、長鎖フッ素置換基に期待される撥水・撥油性や耐熱性などの物性は維持できると考えられる。昨年度の検討では、本フッ素置換基を側鎖としたポリ(メタ)アクリレート樹脂を合成し、既存の長鎖フッ素置換基を持つ類縁樹脂と同等の耐熱性、撥水・撥油性を持つことを明らかにしている。今年度は本フッ素置換基のさらなる応用として、本フッ素置換基を導入したホスホン酸型表面処理剤を合成し、ガラス及び SUS 基盤の表面処理機能を検討した。開発した表面処理剤は、PFOA 発生源となる長鎖ペルフルオロアルキル基を持つ既存のホスホン酸型表面処理剤と同等の撥水・撥油性、耐熱性を持つだけでなく、SUS 基盤の表面処理速度が飛躍的に向上していることも見出した。今後は、本フッ素置換基を導入した含フッ素共役分子を合成し、単結晶 X 線構造解析によるフルオラス相互作用評価を実施する。



【成果報告】Shirai, T.; Yamauchi, S.; Kikuchi, H.; Fukumoto, H.; Tsukada, H.; Agou, T. *Applied Surface Science* **2022**, *577*, 151959.

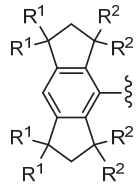
Synthesis and Structural Characterization of Halostannylenes

Tsukasa Matsuo Kindai University

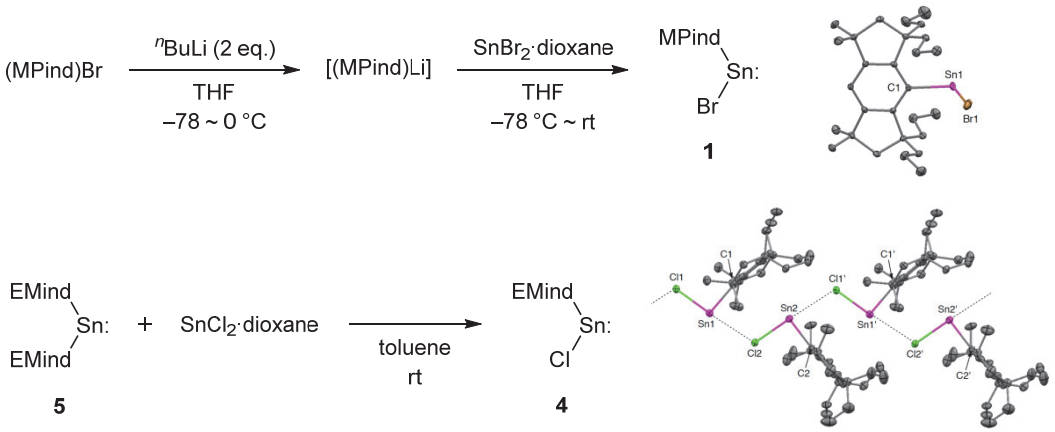
In this collaborative research, we examined the synthesis and structures of a series of halogen-substituted divalent tin compounds, halostannylenes, (Rind)XSn:, by virtue of the steric effects of the fused-ring bulky Rind group (Rind = 1,1,3,3,5,5,7,7-octa-R-substituted *s*-hydrindacen-4-yl).

As shown in Scheme 1, the bulkier MPind-based bromostannylene, (MPind)BrSn: (**1**), was obtained by the reaction of $SnBr_2$·dioxane with an equimolar amount of (MPind)Li in THF, similar to the synthesis of the bulky Eind-based bromostannylene, (Eind)BrSn: (**2**). In contrast, the less bulky EMind-based halostannylenes, (EMind)BrSn: (**3**), and (EMind)ClSn: (**4**), were obtained by the ligand redistribution between the diarylstannylene, $(EMind)_2Sn$: (**5**), and SnX_2·dioxane (X = Br and Cl) in toluene.

A series of arylhalostannylenes **1**–**4** were isolated as thermally stable orange crystals. and their structures were confirmed by X-ray crystallography. While the monomeric structure was found for the bulkier MPind-based **1**, the less bulky EMind-based **4** exhibits a unique one-dimensional polymer with alternating Sn and Cl atoms.



MPind: R^1 = Me, R^2 = ^{n}Pr
Eind: R^1 = R^2 = Et
EMind: R^1 = Et, R^2 = Me



Scheme 1. Synthesis of **1** and **4**.

Theoretical design of planar silicene nanoribbons and search for new operating principles

Masae Takahashi　Tohoku University

【Objectives】The emergence of flat one- and two-dimensional materials, such as graphene and its nanoribbons, has promoted the rapid advance of the current nanotechnology. Silicene, a silicon analogue of graphene, has the great advantage of its compatibility with the present industrial processes based on silicon nanotechnology. The most significant issue for silicene is instability in the air due to the nonplanar puckered (buckled) structure. Another critical problem is that silicene is usually synthesized by epitaxial growth on a substrate, which strongly affects the π conjugated system of silicene. The fabrication of free-standing silicene with a planar configuration has long been pursued. Here, we report the strategy and design to realize the flat zigzag silicene nanoribbon.

【Structure of Theory】We theoretically investigated the stability of various silicene nanoribbons with substituents at the zigzag edges.

【Results and Discussion】We found that zigzag silicene nanoribbons with beryllium (Be) bridges (Be-bridged 2-chain ZSiNR) are very stable in a planar configuration. The obtained zigzag silicene nanoribbon has an indirect negative band gap (Fig. 1) and is nonmagnetic unlike the magnetic buckled silicene nanoribbons with zigzag edges. The linearly dispersive behavior of the π and π* bands associated with the out-of-plane $3p_{Si}$ and $2p_{Be}$ orbitals is clearly observed, showing the existence of a Dirac point slightly above the Fermi level. We also observed that spin−orbit coupling induces a gap opening at the Dirac point.

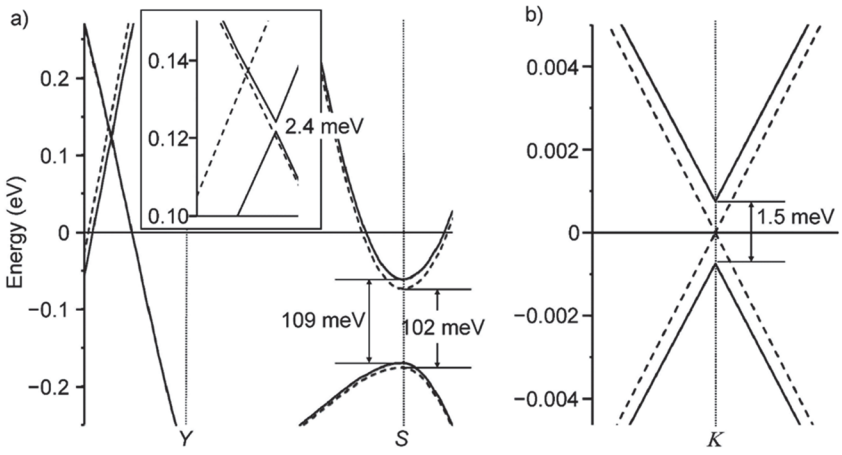


Fig. 1 Electronic band structures of the band gap region of (a) Be-bridged 2-chain ZSiNR and (b) buckled silicene. The solid and dashed lines are the results with and without spin−orbit coupling, respectively. The inset in (a) is magnification around the Dirac point.

【Publications】

[1] M. Takahashi, *ACS Omega*, **2021**, *6*, 12099.

[2] M. Takahashi, M. Kowada, H. Matsui, *et al*., *Appl. Phys. Lett.* **2022**, *120*, 051104.

Synthesis and structures of cationic aromatics bearing thiopyrylium units

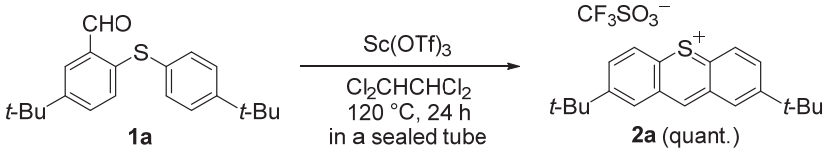
Noriyoshi Nagahora Fukuoka University

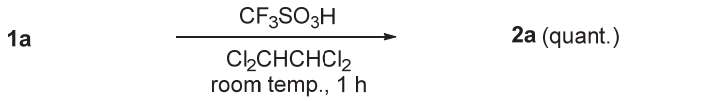
Introduction

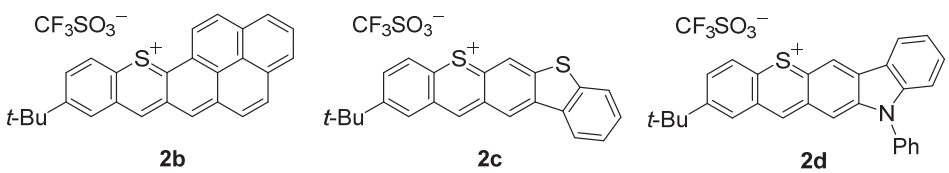
Thiopyrylium salts exhibit a unique electronic structure, which renders these compounds interesting potential building blocks for sulfur-containing aromatic molecules. Recently, thiopyrylium-containing molecules have received substantial attention due to their fascinating structures, optoelectronic and physicochemical properties. In this work, we present studies on the synthesis of linearly fused thiopyrylium compounds via Lewis- or Brønsted-acid-promoted intramolecular cyclization of thioethers.

Results and Discussion

In order to optimize the reaction conditions, we initially investigated the Lewis/Brønsted-acid-induced cyclization of diarylthioether **1a**. When the Lewis acid $Sc(OTf)_3$ was used, the cyclization of **1a** proceeded at high temperature to quantitatively afford thiopyrylium trifluoromethanesulfonate **2a**. We also discovered that TfOH is the most effective Brønsted acid for the promotion of the cyclization, which affords **2a** in quantitative yield at room temperature within 1 h. The reaction still proceeded when the pi-expanded 1-pyrenyl thioether **1b** was treated with TfOH at room temperature for 2 h. This reaction afforded pyrene-fused thiopyrylium salt **2b** as the sole product. These reactions demonstrate that this transformation could be used to form molecules with extensive pi-systems as well as molecules that contain sulfur or nitrogen heterocycles, such as **2c**/**2d**. Consequently, we have established the Lewis/Brønsted-acid-induced cyclization of thioethers that contain a formyl group at the 2′-position as an extremely versatile reaction that allows constructing a variety of thiopyrylium frameworks.







Publications

1. (a) Nagahora, N.; Tanaka, R.; Tada, T.; Yasuda, A.; Yamada, Y.; Shioji, K.; Okuma, K. *Org. Lett.* **2020**, *22*, 6192–6196. (b) Nagahora, N.; Kitahara, K.; Mizuhata, Y.; Tokitoh, N.; Shioji, K.; Okuma, K. *J. Org. Chem.* **2020**, *85*, 7748–7756.

FT-ICR-MS を用いた湖沼及び土壌環境中溶存有機物の化学特性および起源解析

布施泰朗　京都工芸繊維大学

【目的】　FT-ICR-MS は，その高い質量分解能と質量確度により，溶存有機物（Dissolved Organic Matter : DOM）の分子組成解析においてもっとも優れた機器のひとつである．我々は，化学研究所保有の FT-ICR-MS を用いて，琵琶湖をはじめとする自然環境下での水域や土壌における溶存有機物の分子構造の推定を行うとともに，鉄イオンなどの金属イオンと錯体形成したときの化学形態を評価する手法について検討を行い，物質循環における金属元素移送への腐植物質の役割を明らかにすることを目指している．本年度は，FT-ICR-MS による DOM の測定条件の最適化をまずおこない，将来的な高頻度分析の土台固めをすることを目的とした．

【実験】　国際腐植学会頒布の標準フルボ酸（Pony Lake Fulvic Acid：PLFA）を超純水とメタノールを等量混合した溶媒に溶解させた溶液を用いて条件検討をおこなった．検討事項は以下の通り．

1 回目検討事項

TOF：0.575～0.45 秒，accumulation: 0.25～1.25 秒，濃度：3～100mgC/L.（積算回数 100）

2 回目検討事項.

Q1 mass：150，545，TD：1～4M（試料濃度 3mgC/L，TOF0.5 秒，accumu. 0.75 秒，積算回数 200）

Accumulation：0.2～0.75（試料 3 mgC/L），0.2～0.8（試料 10 mgC/L），0.2～0.8（試料 20 mgC/L：一部 SRNOM を使用）全て TOF 0.5 秒，TD 2M，Q1 mass 150 により検討した．

【結果と考察】

・第 1 回目の検討では，TOF：0.5 秒，accumulation：0.75 秒で良好なスペクトルが得られた．濃度については，6 mgC/L の時に最大ピーク強度を示し，12.5 mgC/L 以上では高 m/z 側にピークのスプリッティングが確認され，accumulation 0.75 秒では試料濃度が高すぎると考えられた．

・第 2 回目の検討より，Q1 mass は適正値の 150（観測幅の最小値）に変更した．TD 1 M では分解能が足りず，4M では測定時間がかかりすぎるため，2M とした．accumulation：TD 2M 条件では，試料濃度 10 mgC/L までは十分な強度が得られず．試料濃度 20 mgC/L 時には accumulation 0.5 秒以上時に m/z 300 以上でピークのスプリッティングが観測された．以上より，試料濃度 20 mgC/L，accumulation 0.2 もしくは 0.3 秒が最適であると考えられた．

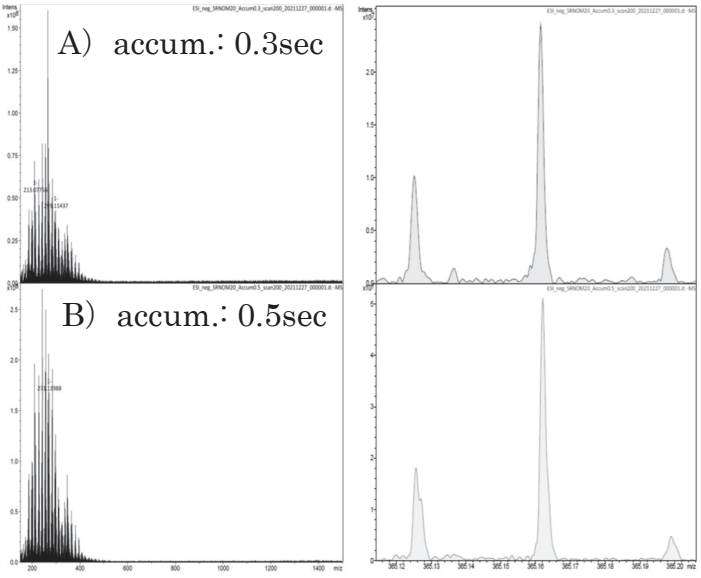


Fig. FT-ICR-MS spectrum of SRNOM
（left: range150-1500m/z, right: range 365.12-365.20m/z）

2. 国際会議、シンポジウム・研究会報告

6th International TADF Workshop 実施報告書

主　催：九州大学最先端有機光エレクトロニクス研究センター
共　催：京都大学化学研究所　国際共同利用・共同研究拠点、公益財団法人九州先端科学技術研究所（福岡市）、公益財団法人福岡県産業・科学技術振興財団、沖縄県科学技術大学院大学、大阪府立大学（現・大阪市立大学）、仏・ソルボンヌ大学、英・セント・アンドリュース大学、豪・クイーンズランド大学、独立行政法人日本学術振興会
日　時：2021 年 12 月 9 日（木）～12 月 10 日（金）
場　所：オンライン開催（実施本部、九州大学最先端有機光エレクトロニクス研究センター）

2021 年 12 月 9 日（木）～12 月 10 日（金）の 2 日間にわたり、6th International TADF Workshop（学会ホームページ https://www.tadf.jp/）をオンライン開催した。TADF Workshop は熱活性化遅延蛍光（TADF）及びそれに関連する有機エレクトロニクスの最新の研究成果を議論する場として、第 1 回（2013 年）が開催されて以来、2017 年より継続的に開催してきた。第 6 回目となる今回は、九州大学最先端有機光エレクトロニクス研究センター・安達千波矢センター長がチェアを務め、京都大学化学研究所国際共同利用・共同研究拠点、公益財団法人九州先端科学技術研究所（福岡市）、公益財団法人福岡県産業・科学技術振興財団、沖縄県科学技術大学院大学、大阪府立大学（現・大阪市立大学）、仏・ソルボンヌ大学、英・セント・アンドリュース大学、豪・クイーンズランド大学の協力、並びに独立行政法人日本学術振興会・研究拠点形成事業（Core to Core Program））の支援を受けている。

未曾有のコロナ渦に始まったオンライン開催は昨年度に引き続き 2 回目であったが、、昨年度開催を上回る 21 カ国から総勢 250 名の参加者があった。参加国は従来の日本、アジア周辺国に加え、ポーランドやリトアニアなど東欧からの参加が目立った。

今回は、「The cutting-edge science and technologies of TADF」、「related topics based on charge-transfer complexes」、「new application based on organic electronics」を小テーマとして設け、幅広い研究分野をカバーした。また、「Future Organic Electronics」という題目にて有機エレクトロニクス分野をリードする 11 名の研究者による特別パネルディスカッションを行ったほか、若手研究者・大学院生交流と育成を目的としたショートプレゼンテーションの場を設けた。世界の各国からのライブ参加を促進するために、日本時間の午後 15 時開始としたことにより、海外参加者のライブ参加が促進されたと考えられる。秘密保持上の問題から、各講演の録画は行わずリアルタイムの講演とし、視聴者との質疑応答に専念した。

今回の TADF Workshop では、今回の TADF Workshop では、 最先端 TADF の材料技術、また、それを用いた OLED の高性能化に関する議論が進んだ。さらに、有機 CT 状態の学理と次世代研究の方向性に関する端緒を掴むことができた。

最後に、本ワークショップを開催するにあたりご支援をいただいた京都大学化学研究所国際共同利用・共同研究拠点に厚く御礼を申し上げる。

文責：安達　千波矢

10th Aquatic Virus Workshop (AVW10) 実施報告書

主　催：日本微生物生態学会
共　催：京都大学化学研究所　国際共同利用・共同研究拠点
協　賛：ゴードン・アンド・ベティ・ムーア財団
　　サイモンズ財団
　　京都大学教育研究振興財団
日　時：2021年6月27日（日）～7月1日（木）
場　所：オンライン開催（実施本部、京都大学化学研究所）

2021年6月27日（日）～7月1日（木）の4日間にわたり、10th Aquatic Virus Workshop (AVW10, ホームページ https://www.avw10.jp/)をオンライン開催した。AVWは水圏ウイルスに関する最新の研究成果を議論する場として、ノルウェーで第1回（1998年）が開催されて以来、2～3年毎に継続的に世界各国で開催されてきた。記念すべき第10回にあたるAVW10は、日本微生物生態学会主催、京都大学化学研究所国際共同利用・共同研究拠点共催のもと、京都大学化学研究所 緒方博之教授 を実行委員長として、京都大学、高知大学、海洋研究開発機構、筑波大学、東京工業大学、水産研究・教育機構所属の実行委員と海外の国際委員（表１）の協力を得て開催された。また、ゴードン・アンド・ベティ・ムーア財団、サイモンズ財団、京都大学教育研究振興財団からの支援を受けた。

AVW10では、招待講演（Featured Talk）13題、一般公演（Live Talk）37題、オンデマンドプレゼンテーション46題の研究発表があった（要旨集を添付する）。演題は「Virus-host interaction」、「Isolation, genome, structure」、「Infection cycle, molecular basis」、「Ecogenomics」、「Microbial food web & biogeochemical cycle」、「Modelling」、「Evolution」の7つのテーマにわたり、幅広い水圏ウイルス研究分野をカバーした。また、21カ国から総勢200名の参加者を得た（表２）。従来の対面開催では100名程度以下の参加人数であったところ、オンライン開催により広く参加者を募ることができ、参加者からも好評であった。

今回のオンライン開催では下記の三点を含む工夫を行った。第一に、時差対応である。世界の各国からのライブ参加を促進するために、午前（9時～12時)、午後（3時～6時)、夜間（10時～11時）の3つのセッションを設けた。これにより、海外参加者のライブ参加が促進された。第二に、全てのセッションを録画配信し、時差により参加できなかったセッションの発表を後日視聴できる仕組みを設け、参加者の利便性を図った。第三に、従来のポスターセッションに代わり「オンデマンドプレゼンテーション」を設けた。録画済のプレゼンテーションを会議前から視聴できるようにし、当日の発表の場では、繰り返しの説明を行わずに、質疑応答に専念できる形式である。その他、参加ルールの説明等の文書配布を丁寧に行った。参加者からは「今までに見たことのない最高のオンライン会議であった」など、好

評をいただいた。

今回の AVW10 では、世界各地で得られた水圏ウイルスを巡る最新の研究成果を踏まえた議論ができた。そして、環境中でのウイルスの挙動や微生物との関係性を理解することが、生態系を根底から理解する上で必要不可欠であるとの認識が高まった。また、総会にて次回 AVW11 はカナダ主催で実施することに決定された。

最後に、本ワークショップを開催するにあたりご支援をいただいた京都大学化学研究所国際共同利用・共同研究拠点に厚く御礼を申し上げたい。

文責：緒方博之

表１　AVW10 実行委員会構成員

国内

京都大学・化学研究所	緒方　博之
京都大学・化学研究所	遠藤　寿
京都大学・化学研究所	岡崎　友輔
産業技術総合研究所	鎌形　洋一
北海道大学	岡部　聡
京都大学・農学研究科	吉田　天士
高知大学	長崎　慶三
高知大学	高橋　廸子
海洋研究開発機構	布浦　拓郎
東京工業大学	望月　智弘
筑波大学	浦山　俊一
国立研究開発法人水産研究・教育機構	外丸　裕司

海外

University of Bergen, Norway	Gunnar Bratbak
Royal Netherlands Institute for Sea Research/University of Amsterdam, The Netherlands	Corina Brussaard
University of Nebraska-Lincoln, US	David Dunigan
Max Planck Institute, Germany	Matthias Fischer
Technion-Israel Institute of Technology, Israel	Debbie Lindell
University of Toronto, Canada	Steven Short
University of British Columbia, Canada	Curtis Suttle
Georgia Institute of Technology, US	Joshua S. Weitz

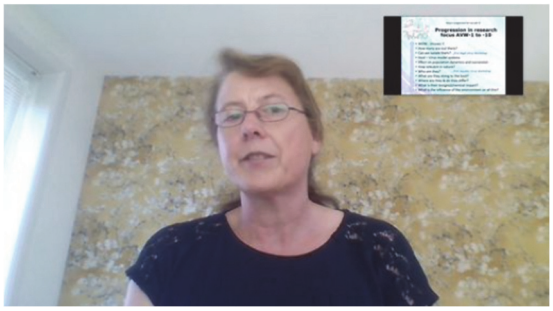
表２　AVW10 参加国

国	参加者数
日本	56
米国	54
イスラエル	15
カナダ	13
ドイツ	10
ノルウェー	9
フランス	9
オランダ	6
中国	6
メキシコ	5
スウェーデン	4
英国	2
スペイン	2
ブラジル	2
シンガポール	1
パナマ	1
インド	1
フィンランド	1
エジプト	1
デンマーク	1
オーストラリア	1

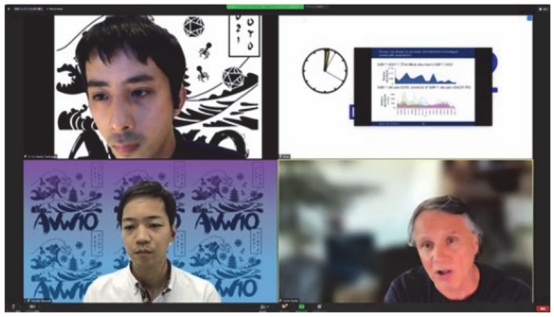
付録１　国際共同利用・共同研究拠点からの支出

項目	金額（円）
ミーティングポータル作成費	396,900
Zoom オンライン開催サポート	482,218
合計	878,218

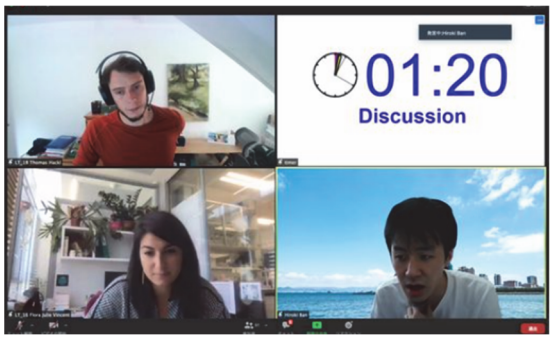
付録２　オンライン会議風景













第 5 回 MAIRS ワークショップ

主　催：（公社）日本分光学会・赤外ラマン研究部会
共　催：京都大学化学研究所共同利用・共同研究拠点
協　賛：日本化学会，応用物理学会，日本分析化学会，分子科学会
日　時：2021 年 11 月 19 日（金）　13:00〜17:00
場　所：京都大学化学研究所・共同研究棟 大セミナー室，および Zoom 配信によるハイブリッド形式

2016 年からシリーズ化して開催している，日本分光学会・赤外分科会企画の部会イベントである“MAIRS ワークショップ”の第 5 回を，京大化研の国際共共拠点を支援により，対面とオンラインのハイブリッド方式で実施した．昨年は，コロナ禍の行く末がまったく見えず，あえなく中止としたが，今回は状況の改善が見込めたため，講師の方々の交流にとって重要な対面式を含む方式とした．一方，コロナ終息後もオンライン参加のメリットは残ることを考え，今後ハイブリッド方式がスタンダードになる可能性を視野に入れて，試しに運用してみることにした．その結果，対面に 24 名，オンラインで 47 名で合計 71 名の参加者を得た．学生の参加者が 22 名と，若手の参加者も多かった．

今年は日本化学会，日本分析化学会，分子科学会，応用物理学会の 4 学協会の協賛を得て実施し，これら協賛学会からの参加者は分光学会員と同額の参加費とした．また，コロナ禍での出費の厳しさも勘案して例年より低価格に設定し，学生は例年通り無料とした．

ハイブリッド開催をスムーズに実現するため，専門業者にマイクなどの設定を任せたことが功を奏し，非常に順調なハイブリッド開催が実現した．

5 回目の今回は“第 5 回 MAIRS ワークショップ｜MAIRS で進める薄膜工学”として開催した。対面式の会場は京大化研で，プログラムは次のとおりである。

1. 有機薄膜における高次構造形成機構－分子配向制御の先駆者に敬意を表して－（久保野 敦史・静岡大）
2. 有機半導体の塗布変換成膜における分子配向制御（鈴木 充朗・阪大）
3. キラルな低分子量ゲル化剤の分子配向の研究：フィブリール形成におけるパーフルオロ基の特異性（佐藤 久子・愛媛大）
4. 有機薄膜の分子配向形成に関わるエネルギー障壁（永井さえ・ソニーグループ(株)　R&D センター）
5. テトラピリジルポルフィリンの超分子構造を利用した分子配向制御（冨田 和孝・京都大 D3）
6. Ph-BTBT-Cn の製膜温度を利用した分子配向制御（吉田 茉莉子・京都大 M2）
7. MAIRS2 による極低温の真空蒸着薄膜のその場構造解析（羽馬 哲也・東大）



はじめに，基調講演枠で久保野先生による分子配向制御の重要性について，その歴史を含む専門家ならではの視点でお話しいただいた．Langmuir-Blodgett（LB）法のような湿式法が全盛の 1980 年頃に，蒸着法による分子配向の制御を始められた上田裕清先生

（神戸大）らの研究を紹介され，そこから熱力学的考察を経て配向制御に向かった道のりを示されて圧巻だった．本ワークショップは，配向マニアが集まる場であることを意識した，素晴らしい導入講義であった．

阪大の鈴木充朗先生は，塗布熱変換法と呼ばれる，湿式で前駆体化合物を製膜した後に，加熱により目的の薄膜を得る手法について，詳しく説明された．合成化学の立場からのお話しながら，MAIRS2 および pMAIRS を使った配向解析の取り組みについて紹介され，定量解析でなければ見逃してしまうような配向変化をたよりに，研究を進めている実際を熱く語っておられた．

愛媛大の佐藤久子先生は，信州大の英先生らが始められたゲル化剤に，パーフルオロアルキル（R_f）基を導入すると，炭化水素のときとは大きく異なるゲル化の特性が現れることについてお話しされた．炭化水素では鎖長とともにゲル化能が増すのに対し，R_f 基を導入すると，その鎖長の偶奇がゲル化能に反映される興味深いものである．こうした R_f 鎖の特性を，水面上の単分子膜を用いて解析する試みも紹介され，そこで LB 膜の pMAIRS スペクトルが登場し，階層双極子アレー（SDA）理論との一致について述べられた．

ソニーグループ（旧 SONY）の永井さえ氏は，有機薄膜の成長過程を基板上分子の運動性により解明する，開拓的な取り組みを示された．ここでは，分子 1 個の動くに注目するのではなく，クラスターが水平および垂直配向のパターンに大別できると仮定し，その間のエネルギー障壁を MAIRS スペクトルから定量的に決められるというもので，物理化学的にも極めて面白い内容であった．実際，この話題は優れた質疑が続き，大変に会場を盛り上げた．

続く 2 題は化研・長谷川グループの学生によるもので，pMAIRS を用いた実際の分子配向制御の話題が提供された．

最後の東大の羽馬哲也先生による講演は，宇宙の原子が分子になる過程を，宇宙に浮かぶ塵に吸着した原子の反応として理解する話題である．実験室で超高真空中で疑似宇宙空間を作り，ここに MAIRS2 を組み込んで氷表面のダングリング OH 結合を定量的に解析することで，赤外線の吸光係数（吸収断面積）決定という長年の課題を初めて解決したという革新的な内容であった．

このように，今年の講演会は，MAIRS がユーザーの手によって自由に羽ばたき，想像以上の広がりを示し始めていることを実感できる内容となった．

会のスムーズな運営を可能にしてくれた，国際共共拠点にこの場をお借りして，厚く御礼を申し上げる．

長谷川健（分子環境解析化学研究領域）

第 42 回生体膜と薬物の相互作用シンポジウム

二木史朗　京都大学化学研究所

第 42 回生体膜と薬物の相互作用シンポジウムを、本年（2021 年）10 月 28 日（木）、29 日（金）、オンラインで開催しました（主催：日本薬学会物理系薬学部会；実行委員長：二木 史朗）。

生体膜と薬物の相互作用シンポジウムは、1976 年に第 1 回が開催された日本薬学会が主催する多くのシンポジウムの中で最も長い歴史を持つシンポジウムです。細胞生物学・分子生物学に加え、薬剤学・薬物動態学の観点も交えつつ、本シンポジウムは、生体膜に関わる生命現象の解明・創薬の基礎から臨床までをカバーする学際的でユニークな成果発表・情報交換の場として発展しています。

今回のシンポジウムでは、特別講演に、アミノ酸トランスポーターとアミノ酸シグナルの生理機能や病態との関連において世界を先導する研究を展開しておられる大阪大学大学院医学系研究科の金井好克先生をお招きしました。また、シンポジウム初日には「生体膜研究の新視点」を、二日目には「膜タンパク質研究の分子的視点」の二つのミニシンポジウムを企画しました。前者では、オートファジー、エクソソームの形態制御機構や、膜タンパク質の光操作など、生体膜に関連する最先端の研究対象や手法に関して、また、後者では、構造生物学から明らかになってきた膜タンパク質・トランスポーターの姿や機能に関して、計 10 名の第一線の研究者の方から研究内容をご紹介頂きました。また、口頭発表 33 題、ポスター発表 8 題の計 41 題の一般講演も行われました。

当初は、京都大学化学研究所での実地開催を計画しておりましたが、新型コロナウイルスの蔓延状況からオンライン開催となりました。しかし、オンラインにかかわらず、124 名（うち、学生 58 名）もの方に参加いただき、活発な討論が繰り広げられました。

本シンポジウム開催にあたり、生体膜に関わる分子相互作用を学際的な視点から密に討論するシンポジウムの趣旨は、京都大学化学研究所の「化学関連分野の深化・連携を基軸とする先端・学際グローバル研究拠点」における共同研究の輪を一層拡げるものとして、後援を頂きました。お陰様で、本シンポジウムを、盛会の裡に終了することが出来ました。この場を借りて厚く御礼申し上げます。



3. 成果発表論文

紙数の都合により、目次に記載した論文の一部についてのみ、別刷りを次頁以降に掲載する。

Reprinted from *Nat. Commun.*, 12, 306 (2021)

nature COMMUNICATIONS

ARTICLE

https://doi.org/10.1038/s41467-020-20561-x OPEN

Ultra-high dynamic range quantum measurement retaining its sensitivity

E. D. Herbschleb [1✉], H. Kato [2], T. Makino[2], S. Yamasaki[2,3] & N. Mizuochi [1✉]

Quantum sensors are highly sensitive since they capitalise on fragile quantum properties such as coherence, while enabling ultra-high spatial resolution. For sensing, the crux is to minimise the measurement uncertainty in a chosen range within a given time. However, basic quantum sensing protocols cannot simultaneously achieve both a high sensitivity and a large range. Here, we demonstrate a non-adaptive algorithm for increasing this range, in principle without limit, for alternating-current field sensing, while being able to get arbitrarily close to the best possible sensitivity. Therefore, it outperforms the standard measurement concept in both sensitivity and range. Also, we explore this algorithm thoroughly by simulation, and discuss the T^{-2} scaling that this algorithm approaches in the coherent regime, as opposed to the $T^{-1/2}$ of the standard measurement. The same algorithm can be applied to any modulo-limited sensor.

[1] Institute for Chemical Research, Kyoto University, Gokasho, Uji-city, Kyoto 611-0011, Japan. [2] National Institute of Advanced Industrial Science and Technology (AIST), Tsukuba, Ibaraki 305-8568, Japan. [3] Present address: Kanazawa University, Kanazawa, Ishikawa 920-1192, Japan.
✉email: herbschleb@dia.kuicr.kyoto-u.ac.jp; mizuochi@scl.kyoto-u.ac.jp

Supreme sensitivities are realisable by exploiting the coherence of quantum sensors[1]. For quantum-sensing applications, nitrogen-vacancy (NV) centres in diamond have attracted considerable attention due to their exceptional quantum-mechanical properties[1,2], including long spin-coherence times[3,4], and due to their great potential for far-field optical nanoscopy[5–8]. Furthermore, an increase in sensitivity can be gained for alternating current (AC) field sensing by prolonging the NV spin coherence with dynamical decoupling of the centre's spin from its environment[2,3,9–12]. Therefore, AC field sensing is applied in various areas of physics, chemistry and biology: to detect single spins[13–15], for nuclear magnetic-resonance of tiny sample-volumes[16–20], for nanoscale magnetic-resonance imaging[13,21–23] and to search for new particles beyond the standard model[24,25]. In these applications, both a wide range of the AC field amplitude and a high sensitivity are very important, because the magnitude of the AC field strongly depends on the distance r from the NV spin (r^{-3} in case of a magnetic dipole field). This outlines the most relevant variable for this field of research: the dynamic range, which is the ratio of the range to the sensitivity, the latter being a measure for the smallest measurable field amplitude.

In previous research, NV centres were utilised for sensitive high-dynamic range direct current (DC) magnetic field measurements. A theory paper[26] discussed the application of a more general phase-estimation method[27] to a single NV nuclear spin in diamond, read out with single-shot measurements. They combined Ramsey interferometry on the nuclear spin with different delays to improve the sensitivity via Bayes' theorem applied to binary data, which precision, given full visibility, scaled as T_{meas}^{-1} (with T_{meas} the measurement time), dubbed Heisenberg-like scaling[28]. Adaptive[27] and non-adaptive[28,29] approaches were discussed, but they found to their surprise that under more realistic circumstances, only the non-adaptive method could still show sub-$T_{\mathrm{meas}}^{-0.5}$ scaling, by applying different amounts of iterations in a linear way[29]. The range itself remained the same as with the standard measurement, but they improved the sensitivity for this range, hence improving the dynamic range. This theory was applied to the electron spin[30] and the nuclear spin[31] of the NV centres via the non-adaptive method. Indeed, they found that the uncertainty scaled sub-$T_{\mathrm{meas}}^{-0.5}$ ($T_{\mathrm{meas}}^{-0.77}$ [30] and $T_{\mathrm{meas}}^{-0.85}$ [31]), while they improved the dynamic range by 8.5[30] and 7.4[31]. More recently, in an experiment at low temperature the adaptive method showed improved results, with scaling close to T_{meas}^{-1} and a claimed improvement (compared to refs. [30,31]) of the dynamic range by two orders of magnitude[32].

A similar method for AC magnetic field sensing applied different order dynamic-decoupling sequences[33]. Their improvement of the dynamic range compared to a sequence with 16 π-pulses was about 26, and they explored the effect of the phase of the measured field in depth. Besides, one of the advantages of the previously reported dynamical sensitivity control[11] was the increase in the range by 4000 times, up to a theoretical maximum of 5000 times. Their uncertainty for a single measurement was about double that of a similar standard measurement, while the required multi-measurement for the large range worsened the sensitivity further (which is the uncertainty times $\sqrt{T_{\mathrm{meas}}}$) by $\sqrt{N_\phi}$ with N_ϕ the number of phases applied in their method (the more phases, the larger the range, but each phase requires an additional measurement).

As to see why dynamic-range increasing algorithms are required, we look at the standard measurement. In the standard method to measure the AC magnetic field with NV centres with a synchronised Hahn-echo measurement[2,3,9,10] (Fig. 1b), after initialisation into a superposition state with a laser pulse and the first microwave (MW) π/2-pulse, the AC magnetic field is applied. Hence, the spin rotates along the z-axis, thus its phase changes. Halfway the period of the magnetic field, a MW π-pulse flips the spin, such that the phase accumulated during the negative half of the period doubles the acquired phase. The final phase is essentially converted into a population with a final MW π/2-pulse before read-out with a laser pulse. The larger the amplitude of the field, the further the spin rotates, thus the final phase of the spin relates directly to this amplitude.

However, the phase of the spin can be determined only within 2π at best, thus the range of amplitudes is limited. If the sensor is more sensitive, the spin accumulates more phase, thus it revolves for 2π for a smaller AC field amplitude already. Therefore, the more sensitive the system, the smaller the range is. Thus, to benefit from extremely sensitive sensors which utilise entanglement[34–36] without the limitation of their minuscule range, it is important to increase this range, while retaining their high sensitivity (thus low uncertainty) as much as possible. Moreover, since the measurements of the electron spin of a single NV centre consist of iterating a sequence many times to accumulate sufficient signal (photons for NV centres), the uncertainty scales as $T_{\mathrm{meas}}^{-0.5}$ [37].

In this work, we demonstrate and explore a non-adaptive algorithm for quantum sensors to measure AC fields with a large range for which the loss in sensitivity is negligible (thus maximising the dynamic range), both by measurement and extensive simulation. This shows that our algorithm scales nearly Heisenberg-like (here T_{meas}^{-2}) under realistic circumstances, thus even with the reduced contrast in the spin read-out (normally about 30% for NV centres); we explain why this happens, and its importance. Finally, we establish with our algorithm how to increase the range beyond the limit given by the best possible standard measurement, which in principle allows to extend it without bound. Throughout this paper, we use the electron spin of a single NV centre to measure magnetic fields with the phase of the spin coherence. However, the insights of this paper remain the same for similar quantum systems.

Results

Base algorithm. We start with explaining the base of our algorithm (illustrated in Fig. 1), and we clarify the terms referred to throughout the paper and supplementary information. The standard measurement for AC magnetic fields, applying the Hahn-echo sequence, has a limited range $B_{\mathrm{range}} = B_{\mathrm{period}}/2$ due to the sinusoidal shape (with period B_{period}) of the signal response to magnetic field amplitudes (Fig. 1a). The sensitivity is defined as $\sigma_B\sqrt{T_{\mathrm{meas}}}$ with σ_B the uncertainty of the sensed quantity (here magnetic field amplitude) and T_{meas} the measurement time. For this standard measurement, $\sigma_B = \sigma_S/\mathrm{grad}_{\mathrm{max}}$ where σ_S is the uncertainty in the measured signal of a single measurement (in our case shot-noise limited), and $\mathrm{grad}_{\mathrm{max}}$ the maximum gradient in the response[3] (for example at the inflection point of the sinusoid in Fig. 1a). Therefore for these measurements, the shorter B_{period} (thus the smaller the range), the steeper the slope, thus the more sensitive, as mentioned earlier.

For the maximum sensitivity, a standard Hahn-echo sequence is performed over the full period of the magnetic field (Fig. 1b, for single NV centres this period should be shorter than about half the coherence time[3]). Since the acquired phase of the spin is proportional to the area under the magnetic field curve (see Supplementary Information of ref. [3]), and hence B_{period} is proportional to this area as well, by reducing the measured area M times (Fig. 1b), the effective period increases by M (Fig. 1a, d). The time delay between the π/2-pulses in the sequence follows from integration to compute the probed area (Fig. 1c). Hereafter, measuring an area A means applying a sequence with this calculated time delay, and A_0 is the maximum area. Thus,

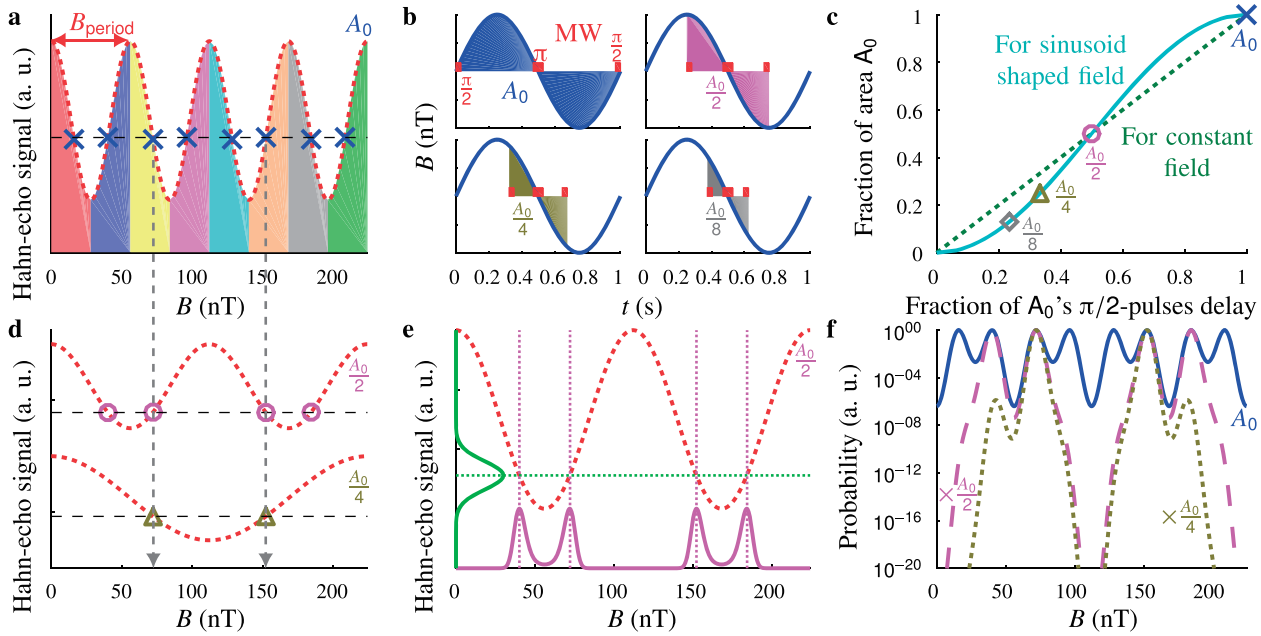


Fig. 1 Algorithm base principle. a Since the measured signal (red dotted line) oscillates due to the rotating spin, the magnetic field B can be determined up to a certain range only. Example ranges are indicated by different colours, and the resulting magnetic field for each range given the measured signal (horizontal black dashed line) with blue crosses. **b** The conventional and most sensitive way to measure an AC field is given at the top left, with π/2-pulses of a Hahn-echo sequence at the beginning and end of the period, and the π-pulse halfway at the inflection point. The measured area A_0 can be reduced by moving the π/2-pulses closer to the centre (top right $A_0/2$, bottom left $A_0/4$, bottom right $A_0/8$). **c** The fraction of the maximum area A_0 vs the fraction of the longest time delay between the π/2-pulses for DC (green dotted line) and AC (cyan line) fields. For DC, this is linear, while for AC, this depends on the area of a sinusoid, which resembles a line near the inflection point, thus the relation becomes quadratic for short time delays. The area and thus uncertainty/range can be changed continuously by changing this delay. **d** For smaller measured areas, the probed field decreases proportionally, as does the effective frequency. In **a**, the signal for area A_0 was shown, while here, the signals for areas $A_0/2$ and $A_0/4$ are drawn in similar fashion, which are offset for clarity. Combining several measured areas reduces the potential fields (vertical grey dashed arrows), thus increasing the overall range. **e** After measuring the signal (horizontal green dotted line), with the known uncertainty of the signal (green line along the vertical axis), the probability distribution of the field (magenta line along the horizontal axis) follows via the sinusoidal relationship (red dotted sine-shaped line for area $A_0/2$). **f** The measurement with the largest area A_0 gives several similar peaks in the probability distribution (blue line). However, when combining measurements with different areas (magenta dashed line added $A_0/2$, olive dotted line added $A_0/4$ as well), the number of remaining peaks reduces, while the sharpness (thus uncertainty) remains similar to that of the first measurement.

performing a measurement with a sufficiently small area would be the simplest approach for a large-range measurement. However, roughly comparing with the measurement over the maximum area, using the same number of iterations of the sequence (thus σ_S is similar) and the same measurement time (no optimisations), the gradient for the reduced area $\mathrm{grad}_{\mathrm{max},M} = \mathrm{grad}_{\mathrm{max},1}/M$, hence its sensitivity is M times worse.

To improve the sensitivity for a large range, initially, a number of measurements with different areas are combined to uniquely define the magnetic field amplitude in a range limited by the measurement with the smallest area (Fig. 1d). Consequently, only part of the measurement time is spent on the largest area, which has the best sensitivity (but a small range), while the remainder of the time is spent on areas with a worse sensitivity. Therefore, the sensitivity of the combined measurement is strictly worse than this best sensitivity. Using halved areas (hence requiring at least $\log_2(M)$ additional areas) and the same number of iterations for each area and using no optimisations, for roughly the same σ_B, the measurement time for the combined sequence $T_{\mathrm{meas},M} = \lceil 1 + \log_2(M) \rceil T_{\mathrm{meas},1}$. Thus, the sensitivity would become $\sqrt{\lceil 1 + \log_2(M) \rceil}$ times worse, which is already a significant improvement compared to the straightforward case in the last paragraph.

The measurements resulting from different areas are combined via Bayes' theorem. For area A_n, the measurement gives signal S_n (for example the crosses/circles/triangles on the sinusoids in Fig. 1a, d for three areas). The posterior probability distribution for the magnetic field B given measured signal S_n is

$$P(B|S_n) = \frac{P(S_n|B)P(B)}{P(S_n)}, \quad (1)$$

with $P(B)$ the prior distribution, $P(S_n)$ independent of B, and

$$P(S_n|B) = P(S_n|S(B)), \quad (2)$$

with $S(B)$ the relation between the signal S and the applied field B (the sinusoids in Fig. 1a, d, e). Fig. 1e visualises these equations. $P(S_n|S)$ is a Poisson distribution (counting photons), but it can be approximated by a normal distribution (green line along y-axis in Fig. 1e) when more than ~10 photons arrive (with continuity correction). This is generally the case when the uncertainty is below the maximum uncertainty, as described later. For the first measurement, the prior distribution is flat since there is no initial knowledge about the field, and for the remainder of the measurements, the previous posterior is the new prior distribution. This results in a combined distribution as demonstrated in Fig. 1f.

Uncertainty. Before performing measurements and simulating the algorithm, a definition of merit is required that facilitates both the sensitivity and the range. Therefore, we choose the uncertainty in magnetic field σ_B, defined as the standard deviation of

the magnetic field distribution centred around its maximum value. For sufficiently long measurement times, this gives the same result compared to applying the normal formula. However, the difference is visible for short measurement times, since it takes the range into account: we know the magnetic field is in the given range, which means that if the probability distribution is flat, the uncertainty is at its maximum $\sigma_{B,\max} = B_{\text{range}}/\sqrt{12}$ (see Supplementary Note 1). σ_B multiplied by $\sqrt{T_{\text{meas}}}$ gives the sensitivity, but this is unsuitable as figure of merit at short measurement times, since its limit is 0 nT $\text{Hz}^{-1/2}$ for $T_{\text{meas}} = 0$ s while approaching the asymptotic maximum uncertainty.

At first, since the uncertainty in a range is limited by the worst uncertainty in this range, we simulated the homogeneity of the uncertainty in the complete range. For a standard measurement, the usually reported uncertainty ($\sigma_B = \sigma_S/\text{grad}_{\max}$) is only true for a single magnetic field amplitude at infinite measurement time, but otherwise it is worse and inhomogeneous. By combining two measurements with the same area but their response shifted by a phase of π/2, the uncertainty becomes more homogeneous, and guarantees a lower uncertainty than the standard measurement across its range. Thus, such a measurement consists of two phases (see for example Supplementary Fig. 7a). The homogeneity is improved further by increasing the number of phases; four phases are used throughout this paper. Supplementary Note 2 describes the details of homogeneity for our algorithm, and for previous ones it is explored in ref. [38]. Since the uncertainty is nearly homogeneous, which field is applied is irrelevant while determining this uncertainty. Without prior knowledge or feedback, the uncertainty is ultimately limited by this combination of four phases for the largest area possible[3].

Measurement compared with simulation. For our measurements, we use an n-type diamond sample. This was epitaxially grown onto a Ib-type (111)-oriented diamond substrate by microwave plasma-assisted chemical-vapour deposition with enriched ^{12}C (99.998%) and with a phosphorus concentration of $\sim 6 \times 10^{16}$ atoms cm^{-3} [3,39]. We address individual electron spins residing in NV centres with a standard in-house built confocal microscope. MW pulses are applied via a thin copper wire, while magnetic fields are induced with a coil around the sample. All experiments are conducted at room temperature. We use single NV centres with T_2s of about 2 ms.

We measure and simulate σ_B for five sequences to show the consistency between the measurements and simulations, and to get an idea of the working of the base of our algorithm. Please note that the only difference between our measurements and simulations is that the simulations calculate the signal otherwise measured using the known sequence, the set magnetic field amplitude, and the parameters of the measured NV centre. The analysis applied otherwise is exactly the same, thus realistic circumstances are simulated (small contrast, shot-noise as described in Supplementary Note 2, decay due to coherence time T_2). The first sequence measures the largest area (here a single period of the field); the second, third and fourth use half, a quarter and an eighth of the largest area; and the fifth sequence includes these four sequences equally in a separate measurement/simulation. All include four phases as mentioned in the last subsection. Initially, the objective is to investigate the details of the algorithm itself, hence to nullify artefacts stemming from overhead times (which are implementation-dependent, and could include laser pulses, MW pulses and waiting times), these are ignored at first and explored in the discussion.

The results are shown in Fig. 2a, which reveals a number of important points. Firstly, the measurements closely match simulations. Secondly, below a certain measurement time, no knowledge about the field is gained, and hence σ_B is at its maximum. Thirdly, for longer measurement times, σ_B scales as $T_{\text{meas}}^{-0.5}$. Fourthly, for the combined sequence there is a region in T_{meas} where σ_B scales more steeply (here referred to as the steep region). Finally, as explained in the base-algorithm subsection, the uncertainty of the combined sequence is always higher than the uncertainty of the largest-area sequence, since the former spends measurement time on sequences other than this largest-area sequence which has the lowest uncertainty. Of course, the advantage of the combined sequence over the largest-area sequence is its larger range (please remember that $B_{\text{range}} \propto \sigma_{B,\max}$, see Supplementary Note 1).

Algorithm design. To design our eventual algorithm, its principle is explored in more detail with additional simulations. Fig. 3a shows the result for changing the relative number of iterations for each area, which reveals that there is a trade-off between the lowest uncertainty reached for measurement times at the steep region and at long measurement times. In other words, depending on T_{meas}, a different relative number of iterations gives the lowest uncertainty. When fixing these (Figs. 2a and 3a), the uncertainty is not optimised, and thus it can display very steep curves that can be tuned to even sub-Heisenberg-like scaling (for example $T_{\text{meas}}^{-4.0}$ in Fig. 3a).

For our algorithm, we optimise the relative number of iterations at each measurement time to minimise the uncertainty. The result for this measurement-time-wise optimisation is plotted in Fig. 3b. This shows that the longer T_{meas}, the closer the sensitivity gets to its ultimate limit, where the scaling approaches $T_{\text{meas}}^{-0.5}$. At the steep region of this optimum, the scaling is $T_{\text{meas}}^{-0.98}$.

When we look at Fig. 3c, which depicts the relative number of iterations, we can understand how our algorithm works. For very short T_{meas}, all measurement time is allotted to the smallest area, since the larger areas are at their maximum uncertainty and hence cannot contribute. But for longer T_{meas}, at some time the next area becomes relevant and thus turns on, since it can receive sufficient measurement time to lower σ_B below its maximum uncertainty. This continues until the largest area turns on, which then keeps increasing in relative importance, at which point the scaling of the uncertainty is about $T_{\text{meas}}^{-0.5}$. Thus for longer T_{meas}, the largest area receives increasingly more relative measurement time, meaning the uncertainty continuously approaches this ultimate uncertainty, as plotted by the green dashed line in Fig. 3c.

If we would increase the number of areas in the sequence, the uncertainty becomes steeper during the turning-on region (which is the steep region). Figure 3d plots the result for a large amount of areas, indicating that the uncertainty scales as T_{meas}^{-2} up to nearby the largest area. The scaling follows from the quadratic dependence of the area on the subsequence length (see Fig. 1c). Since closer to the largest area, this is not quadratic yet, it becomes less steep (lowest yellow crosses in Fig. 3d). The decay in coherence due to the finite T_2 negatively effects the uncertainty as well in this region, further decreasing the steepness. Analogue for DC measurements, the uncertainty scales as T_{meas}^{-1} in the steep region. Supplementary Note 3 discusses scaling in more detail beyond the indication given here. When taking any overhead time into account, the effective measurement time decreases, thus the curves would become even steeper.

So far in the examples with our algorithm, we used halved areas ($A_n = A_0/2^n$ for integer $n \geq 0$). Even though the uncertainty is mostly defined by the largest area, and the range by the smallest, the middle areas are important for reaching the lowest uncertainty (see Fig. 3c: they partake in the optimal combination). Adding more areas at integer multiples of the smallest area decreases the uncertainty, though slightly (see Supplementary Note 4).

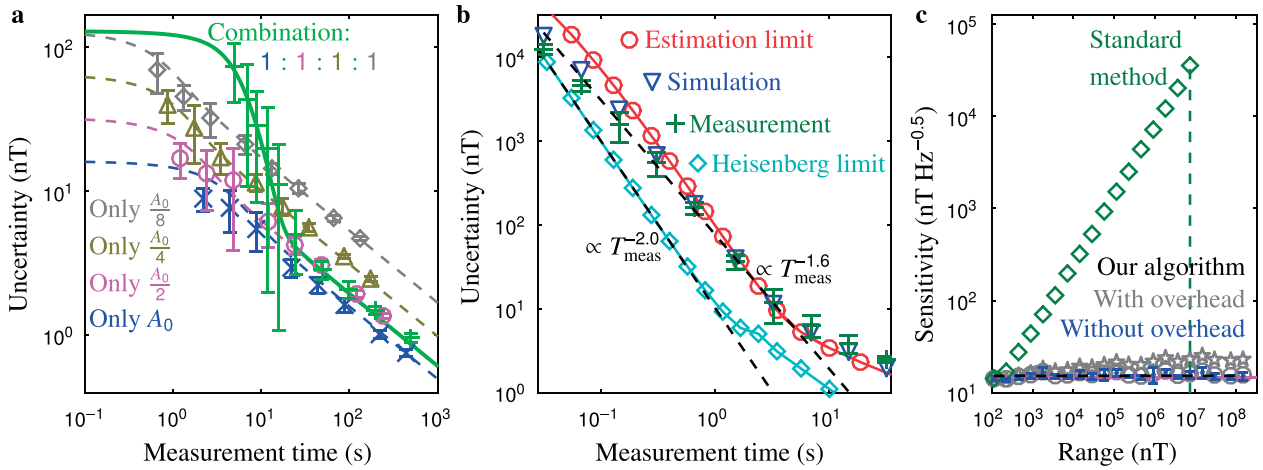


Fig. 2 Measurement and simulation. a Example uncertainty σ_B vs measurement time T_{meas} for AC sensing (1 kHz) comparing simulations (blue dashed line for largest area A_0; magenta, olive and grey dashed lines for $A_0/2$, $A_0/4$ and $A_0/8$; green line for the equally combined sequence with these areas) with measurements (blue crosses, magenta circles, olive triangles, grey diamonds and green pluses, respectively; error bars indicate single standard deviations). The simulations use the same parameters and analysis as the measurements, they are not fits. **b** Optimised uncertainty vs measurement time for AC sensing (2 kHz) around the steep region. Green pluses give the measurement results, the error bars are single standard deviations. Blue triangles are the simulation results. Red circles display the estimation of the large-range limit. Cyan diamonds plot the Heisenberg limit for infinite T_2 (see Supplementary Note 3 for details). The diagonal black dashed lines are guides to the eye for scaling T_{meas}^{-2} and $T_{meas}^{-1.6}$. The overhead time is ignored in order to show the effect of the algorithm only. **c** Sensitivity vs magnetic field range (at 2 kHz). Blue dots with error bars (single standard deviations) give the sensitivity of our algorithm measured at each range excluding all overhead time. Grey circles plot the sensitivity including all overhead time assuming basic compact sequence design (see Supplementary Note 8), while grey pentagons plot the sensitivity assuming each area requires a separate period. The green diamonds plot the sensitivity for the standard measurement (excluding overhead time) extracted from the smallest area of our algorithm. Please note that our algorithm goes beyond the range possible with the standard measurement (vertical green dashed line) by combining non-integer-multiple areas (see Supplementary Note 6 for details). The horizontal magenta line indicates the sensitivity of the most sensitive standard measurement extracted from the largest area of our algorithm, which thus has a single small range only (the leftmost: ~10^2 nT). The horizontal black dashed line (on top of the magenta line) gives the fitted sensitivity of our algorithm.

Algorithm measurement. In Fig. 2b, measurement results of our algorithm in the steep region are plotted (for details of the measurement see Supplementary Note 5), together with the Heisenberg limit (which is only true for a small range and infinite T_2) and the approximate large-range limit explained in Supplementary Note 3. As mentioned before, and just like in Fig. 3d, the focus is on the scaling that originates from the algorithm, hence all overhead time is ignored. Our algorithm is very close to the limit, as could be expected since at long measurement times most time is spent on the sequence with the largest area. Moreover, our results scale approximately as $T_{meas}^{-1.6}$, which is less steep than the Heisenberg-like scaling of T_{meas}^{-2}, since our algorithm keeps approaching this limit.

When merely halving areas in a measurement sequence, its range is defined by the smallest area. Therefore, it would only improve the uncertainty with respect to the standard single-area measurement, but not the range. In this way, given a limit on the time delay between the π/2-pulses, for example owing to a maximum time resolution or waiting time requirements, the maximum range is restricted. However, the range of our algorithm is the inverse of the greatest common divisor of the frequencies in measured signal of all included areas (see Supplementary Note 6). For halved areas, since all larger areas are integer multiples of the smaller ones, this means that the greatest common divisor is the lowest frequency, thus the one related to the smallest area. To increase the range beyond this limit, we combine areas that are not integer multiples of each other. When purely looking at the range, combining two sequences for slightly different areas increases the range far beyond the standard measurement's range. Thus in principle, the range can be extended unlimitedly. Adding the large areas as well, it is still possible to get arbitrarily close to the ultimate uncertainty (for details see Supplementary Note 6).

The dynamic range of our algorithm is explored with measurements in Fig. 2c, which plots the sensitivity with respect to the range of the measurement sequence. Initially, for each increase in the range, an additional subsequence of half the smallest area is added. However, for the final four ranges, a single area is added at 1.5, 1.25, 1.1 or 1.05 times the smallest area. To compare with shorter sequences and with other results fairly, the sensitivity is chosen instead of the uncertainty (to calculate the dynamic range) and the overhead time is still ignored. It is computed by combining measurements from both the left side and right side of the designed range (as explained before, given the homogeneity of the uncertainty in our algorithm, the applied magnetic field does not matter). The sensitivity for the standard measurement with the same range is plotted as well (derived from the smallest area of our algorithm), and the sensitivity of the most sensitive sequence (derived from the largest area of our algorithm), the latter having a small range only (~10^2 nT). Our algorithm is nearly as sensitive as the most sensitive sequence, and its range can go beyond that of a standard measurement. In these measurements, the maximum range was limited by our equipment only, and could be improved further.

Discussion

Given a fixed sequence, a subsequence contributes only to the result when the measurement time it receives is sufficiently long to lower the measured uncertainty below its maximum (see Fig. 3c). Therefore in our algorithm, the optimum sequence for a given measurement time includes contributing subsequences only. On the contrary, when combining subsequences in a fixed way with the least sensitive subsequence measured most often, for short measurement times, the more sensitive subsequences do not contribute, and hence their measurement time is wasted. This

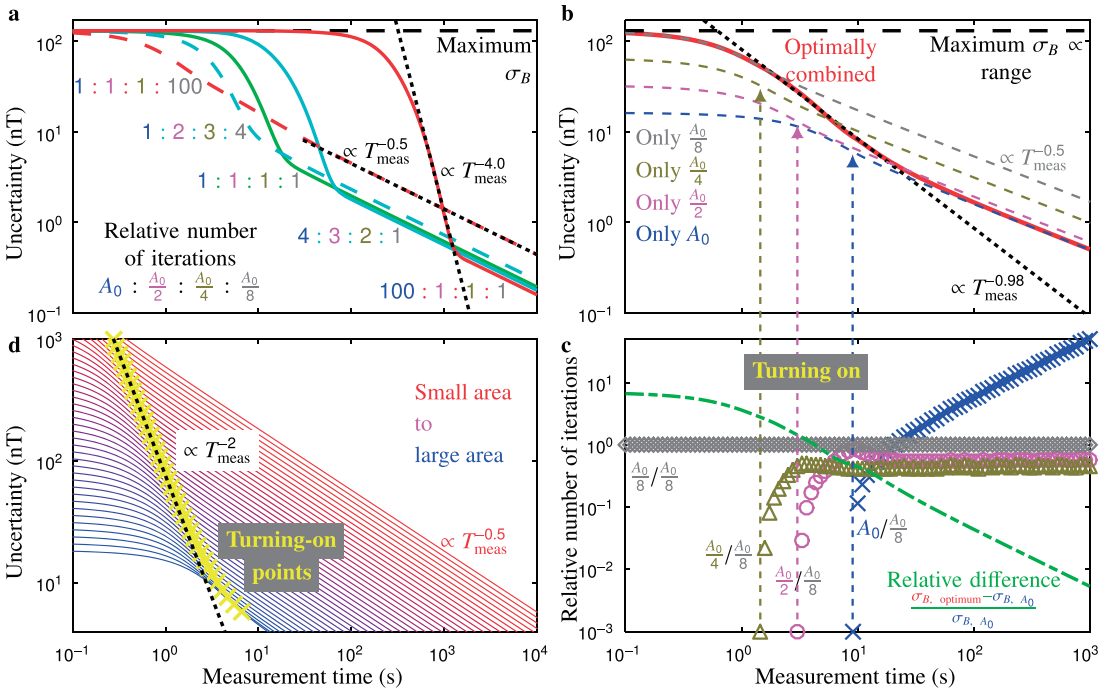


Fig. 3 Simulation analyses. a For different relative numbers of iterations of the subsequences (written directly left of each curve) of areas A, the uncertainty σ_B with respect to measurement time T_{meas} changes. Depending on the measurement time, a different combination gives the lowest uncertainty. **b** Minimised uncertainty for a large-range sequence by optimally combining the subsequences (red line). The dashed lines give the uncertainty for single-area sequences (A_0 blue, $A_0/2$ magenta, $A_0/4$ olive, $A_0/8$ grey). See Supplementary Note 1 for maximum uncertainty ∝ range. **c** The relative number of iterations for each area (A_0 blue crosses, $A_0/2$ magenta circles, $A_0/4$ olive triangles, $A_0/8$ grey diamonds kept at 10^0) for each measurement time to minimise the uncertainty, which results in the red line in **b**. The vertical arrows indicate when a subsequence for its area turns on, since its relative number of iterations becomes significant. The green dashed line gives the relative difference between the most-sensitive small-range sequence (blue dashed line in **b**) compared to the optimally combined large-range sequence. This difference scales inversely with the measurement time. **d** When looking at the turning-on points (yellow crosses, fit with black dotted line) for many sequences with different areas (largest area blue line, smallest area red line), it scales as T_{meas}^{-2} for short measurement times. Please note that the optimally combined result in **b** scales as $T_{meas}^{-0.98}$, since it includes relatively large areas only, equivalent to the lowest lines in this plot.

results in a steeper measurement time dependence in the same way as overhead time does. This illustrates one conclusion of Supplementary Note 3: a steeper dependence leads to a worse algorithm, since when decreasing the measurement time, the uncertainty increases more quickly for a steeper curve.

For our algorithm, if it is possible to choose for which subsequence to increase the number of iterations while measuring, the uncertainty can be minimised for all measurement times (red line in Fig. 3b), since the absolute number of iterations for each subsequence is monotonically increasing over measurement time (see Supplementary Note 7). Please note that it is known beforehand for which subsequence to increase the number of iterations, it does not depend on the measurement results, thus it is a non-adaptive method. Moreover, since our algorithm spends most time on the largest area, any overhead time (which is generally independent of the subsequence) is relatively as short as possible. This is visualised in Fig. 2c, which plots the sensitivities both with and without all potential overhead times, illustrating the overhead is negligible indeed.

For measurement times in the steep region, since quantum sensing is generally chosen for its high sensitivity, a sensor would rather unlikely be used given the high uncertainty. Therefore, this region and its scaling are fairly irrelevant: if a short measurement time is desired, less subsequences are required, which effectively puts the sensor just at the inflection point (when scaling starts to be $T_{meas}^{-0.5}$).

For measurement times beyond the steep region, σ_B and thus sensitivity are very close to the limit for a homogeneous range. This is still about $\sqrt{2}$ worse than the standard sensitivity for a single field at infinite measurement time (Supplementary Fig. 2). It is possible to improve towards this by applying feedback of intermediate results during the measurement, and dropping all but two phases in the process to focus on the two phases with the field to measure located at their maximum gradient, which gives the smallest uncertainty. There is a trade-off between added complexity of such an adaptive measurement[32] (real-time processing of data, changing the sequence during the measurement and/or set any phase in the measurement instead of just four with in-phase-quadrature modulation) and gained sensitivity ($\sqrt{2}$ at best for infinite measurement time), even when ignoring the processing overhead. Moreover, even under these ideal circumstances, the dynamic range, rather relevant for large-range measurements, is actually $\sqrt{2}$ worse for standard adaptive measurements compared to non-adaptive measurements (see Supplementary Note 2).

An important point ignored so far is how to implement this algorithm at all for AC fields, since its shape needs to be taken into account. As opposed to DC measurements, where the area can be reduced simply by shortening the time delay between the π/2 pulses proportionally, for AC it is more complicated, as illustrated in Fig. 1b, c. Moreover, it might seem that for each iteration another period of the magnetic field is required (resulting in the practical but non-optimal sensitivity plotted with pentagons in Fig. 2c), while for DC all measurements can be strung together, the latter limiting the measurement time. However, something similar is possible for AC fields, since the DC

part cancels, as explained in Supplementary Note 8. In our results, we neglected the effect this stringing has on the total measurement time to focus on the working of the algorithm. However, since AC stringing is only slightly less effective than DC stringing, and since often most measurement time is dedicated to the largest area (which has no stringing disadvantage), it justifies the choice to ignore the overhead time of these stringing effects. This is explored in detail in Supplementary Note 8, which describes how to design compact measurement sequences (resulting in the practical closer-to-optimal sensitivity plotted with circles in Fig. 2c). Measurements with these compact sequences illustrate that the practical sensitivity, compared to the overhead-ignored sensitivity, would worsen with about 5% when all overhead time is included using a basic sequence design (see Supplementary Fig. 10).

Additionally, please note that the description of the algorithm focussed on areas to easily translate it to any field, such as DC fields or square waves. Moreover, the frequency of the AC field is not relevant, since for lower frequencies the largest area will not span a whole period, while for high frequencies additional π-pulses are required to optimise the largest area. This defines the lowest uncertainty, which our algorithm approaches for every situation. This uncertainty increases for lower frequencies, since a smaller area is measured within the coherence-limited time delay, while for higher frequencies it decreases, due to the increase in coherence time by a dynamic-decoupling sequence (just for the larger areas, the largest defining the lowest uncertainty). Of course, the shape of the area vs time-delay graph (Fig. 1c) depends on the shape of the field and the chosen pulse sequences.

For practical implementations of the algorithm, as in the example with a single NV centre, the reader is advised that the larger the range becomes, the more prominent the effects of off-resonance MW pulses become. For DC, this is even more important (see for example ref. [31]), while for AC, the pulses are often near low fields (for example for the sensitivity-defining large area they are at the inflection points). Thus, care should be taken during the design depending on the chosen quantum system and the available technology.

As a final remark, applying the optimal number of iterations for a long measurement time gives a small chance to conclude the wrong field, since relatively little time is spent in the smaller range-defining areas (see Supplementary Note 9). However, the analysis does not return a single measured field amplitude, but a probability distribution of the field. As demonstrated in Supplementary Note 9, when the field is within a few σ_B of the actual field, there is a single pronounced peak in this distribution. Oppositely, there are multiple strong peaks if the expected field of the measurement is significantly different. Thus, such a result could easily be discarded (of course effectively slightly reducing the sensitivity to redo the measurement for these cases).

To conclude, we have introduced an ultra-high dynamic-range algorithm for measuring magnetic fields with a quantum sensor, such as a single NV centre, for which the uncertainty, and hence sensitivity, can be arbitrarily close to the ultimate uncertainty/sensitivity by increasing the measurement time. The maximum range depends on the smallest difference in areas attainable, which results in a larger range than possible with a standard measurement. As example, we demonstrated a dynamic range of $\sim 10^7$, an improvement of two orders of magnitude compared to previous algorithms[32] (please note that a fair comparison between algorithms corrects the results for the coherence time, the minimum/maximum time delays, the applied spin-measurement method and the experimental equipment, as these change the results independent of the applied algorithm). Moreover, we explained the origin of Heisenberg-like scaling in algorithms and why steeper scaling indicates a worse algorithm. Our algorithm and its implications are the same for other modulo-limited sensors, thus it paves the way to optimally benefit from extremely sensitive entanglement-based sensors for large-range applications.

Data availability

The data that support the findings of this study are available from the corresponding author upon reasonable request.

Received: 6 December 2019; Accepted: 8 December 2020;
Published online: 12 January 2021

References

1. Degen, C. L., Reinhard, F. & Cappellaro, P. Quantum sensing. *Rev. Mod. Phys.* **89**, 035002 (2017).
2. Rondin, L. et al. Magnetometry with nitrogen-vacancy defects in diamond. *Rep. Prog. Phys.* **77**, 056503 (2014).
3. Herbschleb, E. D. et al. Ultra-long coherence times amongst room-temperature solid-state spins. *Nat. Commun.* **10**, 3766 (2019).
4. Bar-Gill, N., Pham, L. M., Jarmola, A., Budker, D. & Walsworth, R. L. Solid-state electronic spin coherence time approaching one second. *Nat. Commun.* **4**, 1743 (2013).
5. Rittweger, E., Han, K. Y., Irvine, S. E., Eggeling, C. & Hell, S. W. STED microscopy reveals crystal colour centres with nanometric resolution. *Nat. Photonics* **3**, 144–147 (2009).
6. Maurer, P. C. et al. Far-field optical imaging and manipulation of individual spins with nanoscale resolution. *Nat. Phys.* **6**, 912–918 (2010).
7. Jaskula, J.-C. et al. Superresolution optical magnetic imaging and spectroscopy using individual electronic spins in diamond. *Opt. Express* **25**, 11048–11064 (2017).
8. Jin, D. et al. Nanoparticles for super-resolution microscopy and single-molecule tracking. *Nat. Methods* **15**, 415–423 (2018).
9. Taylor, J. M. et al. High-sensitivity diamond magnetometer with nanoscale resolution. *Nat. Phys.* **4**, 810–816 (2008).
10. Wolf, T. et al. Subpicotesla diamond magnetometry. *Phys. Rev. X* **5**, 041001 (2015).
11. Lazariev, A., Arroyo-Camejo, S., Rahane, G., Kavatamane, V. K. & Balasubramanian, G. Dynamical sensitivity control of a single-spin quantum sensor. *Sci. Rep.* **7**, 6586 (2017).
12. Knowles, H. S., Kara, D. M. & Atatüre, M. Observing bulk diamond spin coherence in high-purity nanodiamonds. *Nat. Mater.* **13**, 21–25 (2013).
13. Grinolds, M. S. et al. Nanoscale magnetic imaging of a single electron spin under ambient conditions. *Nat. Phys.* **9**, 215–219 (2013).
14. Shi, F. et al. Single-protein spin resonance spectroscopy under ambient conditions. *Science* **347**, 1135–1138 (2015).
15. Shi, F. et al. Single-DNA electron spin resonance spectroscopy in aqueous solutions. *Nat. Methods* **15**, 697–699 (2018).
16. Aslam, N. et al. Nanoscale nuclear magnetic resonance with chemical resolution. *Science* **357**, 67–71 (2017).
17. Mamin, H. J. et al. Nanoscale nuclear magnetic resonance with a nitrogen-vacancy spin sensor. *Science* **339**, 557–560 (2013).
18. Glenn, D. R. et al. High-resolution magnetic resonance spectroscopy using a solid-state spin sensor. *Nature* **555**, 351–354 (2018).
19. Boss, J. M., Cujia, K. S., Zopes, J. & Degen, C. L. Quantum sensing with arbitrary frequency resolution. *Science* **356**, 837–840 (2017).
20. Schmitt, S. et al. Submillihertz magnetic spectroscopy performed with a nanoscale quantum sensor. *Science* **356**, 832–837 (2017).
21. Rugar, D. et al. Proton magnetic resonance imaging using a nitrogen-vacancy spin sensor. *Nat. Nanotechnol.* **10**, 120–124 (2014).
22. DeVience, S. J. et al. Nanoscale NMR spectroscopy and imaging of multiple nuclear species. *Nat. Nanotechnol.* **10**, 129–134 (2015).
23. Perunicic, V. S., Hill, C. D., Hall, L. T. & Hollenberg, L. C. L. A quantum spin-probe molecular microscope. *Nat. Commun.* **7**, 12667 (2016).
24. Rong, X. et al. Searching for an exotic spin-dependent interaction with a single electron-spin quantum sensor. *Nat. Commun.* **9**, 739 (2018).
25. Budker, D., Graham, P. W., Ledbetter, M., Rajendran, S. & Sushkov, A. O. Proposal for a cosmic axion spin precession experiment (CASPEr). *Phys. Rev. X* **4**, 021030 (2014).
26. Said, R. S., Berry, D. W. & Twamley, J. Nanoscale magnetometry using a single-spin system in diamond. *Phys. Rev. B* **83**, 125410 (2011).
27. Higgins, B. L., Berry, D. W., Bartlett, S. D., Wiseman, H. M. & Pryde, G. J. Entanglement-free Heisenberg-limited phase estimation. *Nature* **450**, 393–396 (2007).
28. Berry, D. W. et al. How to perform the most accurate possible phase measurements. *Phys. Rev. A* **80**, 052114 (2009).

29. Higgins, B. L. et al. Demonstrating Heisenberg-limited unambiguous phase estimation without adaptive measurements. *N. J. Phys.* **11**, 073023 (2009).
30. Nusran, N. M., Momeen, M. U. & Dutt, M. V. G. High-dynamic-range magnetometry with a single electronic spin in diamond. *Nat. Nanotechnol.* **7**, 109–113 (2011).
31. Waldherr, G. et al. High-dynamic-range magnetometry with a single nuclear spin in diamond. *Nat. Nanotechnol.* **7**, 105–108 (2011).
32. Bonato, C. et al. Optimized quantum sensing with a single electron spin using real-time adaptive measurements. *Nat. Nanotechnol.* **11**, 247–252 (2015).
33. Nusran, N. M. & Dutt, M. V. G. Dual-channel lock-in magnetometer with a single spin in diamond. *Phys. Rev. B* **88**, 220410 (2013).
34. Leibfried, D. et al. Toward Heisenberg-limited spectroscopy with multiparticle entangled states. *Science* **304**, 1476–1478 (2004).
35. Nagata, T., Okamoto, R., O'Brien, J. L., Sasaki, K. & Takeuchi, S. Beating the standard quantum limit with four-entangled photons. *Science* **316**, 726–729 (2007).
36. Jones, J. A. et al. Magnetic field sensing beyond the standard quantum limit using 10-spin NOON states. *Science* **324**, 1166–1168 (2009).
37. Giovannetti, V., Lloyd, S. & Maccone, L. Advances in quantum metrology. *Nat. Photonics* **5**, 222–229 (2011).
38. Nusran, N. M. & Dutt, M. V. G. Optimizing phase-estimation algorithms for diamond spin magnetometry. *Phys. Rev. B* **90**, 024422 (2014).
39. Kato, H., Ogura, M., Makino, T., Takeuchi, D. & Yamasaki, S. N-type control of single-crystal diamond films by ultra-lightly phosphorus doping. *Appl. Phys. Lett.* **109**, 142102 (2016).

Acknowledgements

The authors acknowledge the financial support from MEXT Q-LEAP (No. JPMXS0118067395), KAKENHI (No. 15H05868, 16H06326) and the Collaborative Research Program of ICR, Kyoto University (2019-103). They also thank Prof H. Kosaka for helpful discussions.

Author contributions

E.D.H. designed the algorithm, performed the experiments/simulations/analyses and conceived the supplementary; H.K. grew the phosphorus-doped diamond, assisted by T.M. and S.Y.; N.M. supervised the work; E.D.H. and N.M. wrote the manuscript, and all authors discussed it.

Competing interests

The authors declare no competing interests.

Additional information

Supplementary information is available for this paper at https://doi.org/10.1038/s41467-020-20561-x.

Correspondence and requests for materials should be addressed to E.D.H. or N.M.

Peer review information *Nature Communications* thanks the anonymous reviewer(s) for their contribution to the peer review of this work. Peer reviewer reports are available.

Reprints and permission information is available at http://www.nature.com/reprints

Publisher's note Springer Nature remains neutral with regard to jurisdictional claims in published maps and institutional affiliations.

Open Access This article is licensed under a Creative Commons Attribution 4.0 International License, which permits use, sharing, adaptation, distribution and reproduction in any medium or format, as long as you give appropriate credit to the original author(s) and the source, provide a link to the Creative Commons license, and indicate if changes were made. The images or other third party material in this article are included in the article's Creative Commons license, unless indicated otherwise in a credit line to the material. If material is not included in the article's Creative Commons license and your intended use is not permitted by statutory regulation or exceeds the permitted use, you will need to obtain permission directly from the copyright holder. To view a copy of this license, visit http://creativecommons.org/licenses/by/4.0/.

© The Author(s) 2021

Reprinted from *Chem. Sci.*, 12, 13513–13519 (2021)

Chemical Science

ROYAL SOCIETY OF CHEMISTRY

EDGE ARTICLE

View Article Online
View Journal | View Issue

Check for updates

Cite this: *Chem. Sci.*, 2021, **12**, 13513

All publication charges for this article have been paid for by the Royal Society of Chemistry

Received 1st August 2021
Accepted 21st September 2021

DOI: 10.1039/d1sc04221a

rsc.li/chemical-science

Mixed lead–tin perovskite films with >7 μs charge carrier lifetimes realized by maltol post-treatment†

Shuaifeng Hu, [a] Minh Anh Truong, [a] Kento Otsuka, [a] Taketo Handa, [a] Takumi Yamada, [a] Ryosuke Nishikubo, [b] Yasuko Iwasaki, [a] Akinori Saeki, [b] Richard Murdey, [a] Yoshihiko Kanemitsu [a] and Atsushi Wakamiya [a]*

Mixed lead–tin (Pb–Sn) halide perovskites with optimum band gaps near 1.3 eV are promising candidates for next-generation solar cells. However, the performance of solar cells fabricated with Pb–Sn perovskites is restricted by the facile oxidation of Sn(II) to Sn(IV), which induces self-doping. Maltol, a naturally occurring flavor enhancer and strong metal binding agent, was found to effectively suppress Sn(IV) formation and passivate defects in mixed Pb–Sn perovskite films. When used in combination with Sn(IV) scavenging, the maltol surface treatment led to high-quality perovskite films which showed enhanced photoluminescence intensities and charge carrier lifetimes in excess of 7 μs. The scavenging and surface treatments resulted in highly reproducible solar cell devices, with photoconversion efficiencies of up to 21.4% under AM1.5G illumination.

1. Introduction

Lead (Pb)-based perovskite solar cells (PSCs) have reached a power conversion efficiency (PCE) of 25.6%.[1,2] While such devices are highly optimized, the band gap of Pb-based perovskite materials (E_g > 1.45 eV)[3] actually lies slightly outside the range of maximum performance for single-junction solar cells, 1.1–1.4 eV, as determined by Shockley and Queisser.[4] The band gaps of mixed lead–tin (Pb–Sn) perovskite absorbers, meanwhile, fall within the optimal range, being typically 1.2–1.4 eV.[5,6] In the last few years, there has been remarkable progress in the development of Pb–Sn PSCs,[7–11] with cell efficiencies now reaching 21.7%.[12,13] Despite the optimal band gap, however, the reported device efficiencies[5,7,12–21] remain lower than those of their Pb-based counterparts.[1,2,22–24] One of the main impediments for any tin-containing perovskite is the facile oxidation of Sn(II) to Sn(IV). Saidaminov *et al.*[25] and Pascual *et al.*[26] found that the starting material, SnI_2, can be easily oxidized, even by the solvent used for the film fabrication (dimethyl sulfoxide, DMSO). Oxygen levels as low as a few ppm can cause Sn(II) in the perovskite films to oxidize, creating Sn(II) vacancies which lead to an increase in hole density.[27–30] This p-doping effect has a very strong negative impact on device performance.[31]

Various strategies for mitigating this issue have been proposed.[32] One effective way to reduce the Sn(IV) content in the perovskite films is to remove it from the precursor solution, by modifying the perovskite precursor solution *via* various methods. It was reported that the addition of Sn(0) powder into the Sn-containing precursor solution not only improved the purity of the precursor solution but also reduced Sn(II) vacancies in the resulting perovskite films due to extra Sn(II) generated by the reaction of Sn(IV) with metallic Sn(0).[8,9,33] Antioxidants or reducing reagents, like formamidinesulfinic acid,[12] pyrazine,[34] hydroquinone sulfonic acid,[35] and 8-hydroxyquinoline,[36] have also been found to reduce the Sn(IV) content in perovskite precursor solution.

It is also important to reduce the Sn(IV) in the starting materials used to prepare the precursor solution. To this end, we have previously developed highly purified starting materials for the fabrication of Sn-based PSCs.[37–39] We have also recently reported a Sn(IV) scavenging method based on the high chemical selectivity of an 8π electron system 1,4-bis(trimethylsilyl)-2,3,5,6-tetramethyl-1,4-dihydropyrazine (TM-DHP) for SnF_2 over SnI_2.[40] We found that when TM-DHP is added into a $FA_{0.75}MA_{0.25}SnI_3$ precursor solution in the presence of SnF_2, the Sn(II) from SnF_2 is reduced to generate Sn(0) nanoparticles. These Sn(0) nanoparticles effectively scavenge Sn(IV) impurities at the precursor preparation stage, giving Sn(IV)-free perovskites in the bulk of the obtained films.

Despite these notable improvements to the quality of the as-fabricated materials, the perovskite films remain vulnerable to oxidation after fabrication, especially at the exposed surfaces.[41] To address this, post-treatments for the perovskite films have been developed to protect and passivate the perovskite

[a]*Institute for Chemical Research, Kyoto University, Gokasho, Uji, Kyoto 611-0011, Japan. E-mail: wakamiya@scl.kyoto-u.ac.jp*

[b]*Department of Applied Chemistry, Graduate School of Engineering, Osaka University, 2-1 Yamadaoka, Suita, Osaka 565-0871, Japan*

† Electronic supplementary information (ESI) available. CCDC 2080061, 2080062 and 2080063. For ESI and crystallographic data in CIF or other electronic format see DOI: 10.1039/d1sc04221a

© 2021 The Author(s). Published by the Royal Society of Chemistry

surfaces.[42] From a chemical point of view, a strong chelating agent would be a good choice to stabilize the Sn(II) species. Kamarudin *et al.* reported that amine groups in ethylenediamine bind to the undercoordinated Sn(II) species on the Sn perovskite surface, resulting in improved stability towards oxidation.[43] Unfortunately, however, the high basicity of the ethylenediamine resulted in damage to the Sn perovskite films.[44,45] Milder, but effective reagents are therefore desirable for the post-treatment of the Sn-containing perovskite films. Among the candidates, the environmental-friendly molecule; 3-hydroxy-2-methyl-4-pyrone (maltol), known as a 'flavor enhancer', is a promising candidate due to its noteworthy metal chelating ability.[46]

In this work, we extend the use of the Sn(IV) scavenging method to mixed Pb–Sn perovskite system, and introduce an additional post-treatment of the perovskite surface with maltol. The maltol treatment was found to suppress Sn(II) oxidation and reduce the density of defects at the perovskite film surface. The photoluminescence (PL) lifetime increasing from 1.3 to 7.4 μs accompanied with a fivefold increase in PL intensity. The PCE of the champion device fabricated with the combination of Sn(IV) scavenging and maltol post-treatment was 21.4%.

2. Results and discussion

Maltol, $C_6H_6O_3$, is a small α-hydroxy ketone known for having an intense chemical activity towards hard metal ions. We found that the electron-rich oxygen atoms in the carbonyl and the hydroxyl groups of maltol simultaneously coordinate to the Sn(II) in SnI_2 to form SnI(maltol) complex (Fig. 1a and b). Similar complexes were observed to form with SnF_2 and $SnBr_2$ (Scheme S1 and Fig. S1–S7†). We therefore surmise that if maltol binds to the undercoordinated Sn(II) sites (Fig. 1c) at the surface of Pb–Sn perovskite films, it should effectively suppress the formation of the defects, like Sn(II) vacancies, at the perovskite film surface.

To verify this hypothesis, three kinds of perovskite samples were prepared; control films without scavenging or maltol post treatment, films prepared with TM-DHP reductant only, and films prepared with both TM-DHP reductant and maltol post-treatment. The perovskite composition used was $Cs_{0.1}FA_{0.6}MA_{0.3}Sn_{0.5}Pb_{0.5}I_3$ (FA = formamidinium, MA = methylammonium). This composition was selected by evaluating the PL properties and valence band energy levels of a series of 25 candidate materials (Fig. S8 and S9, Table S1†). The perovskite layers were prepared by the one step method with chlorobenzene antisolvent. SnF_2 (10 mol% with respect to SnI_2) and $Pb(SCN)_2$ (2 mol% with respect to PbI_2) were added to the perovskite precursor solution. SnF_2 additive is known to suppress the oxidation of Sn(II) at the precursor preparation stage,[5] while $Pb(SCN)_2$ is commonly added to mediate the perovskite crystal growth.[18] The precursor concentration is 1.8 M, chosen based on previous reports on efficient mixed Pb–Sn PSCs.[9,18] For the samples with Sn(IV) scavenging, 1 mol% TM-DHP was added to the precursor solution as described previously.[40] For the samples with maltol post treatment, 1 mg mL^{-1} maltol dissolved in toluene was applied to the surface of the films by spin-coating, followed by annealing at 65 °C. Accordingly, the control, TM-DHP-treated, and both TM-DHP and maltol treated perovskite films were respectively prepared.

The oxidation state of Sn at the perovskite film surface was examined using X-ray photoelectron spectroscopy (XPS). Fig. 2a–c show the Sn 3d signal for the three perovskite films, which can be deconvoluted into two components; a large main peak, and a single shoulder on the high binding energy side. After peak fitting, the main peaks, centered at about 494.8 and 486.3 eV, are assigned to Sn(II), while the secondary features, at about 496.3 and 487.6 eV, are attributed to Sn(IV). The amount of Sn(IV) content at the surface of the perovskite films was 9% for the control, 6% for TM-DHP-treated films, as estimated from the ratio of the Sn(IV) peak to the total signal area. TM-DHP effectively scavenges Sn(IV) from the precursor materials, resulting in less Sn(IV) in the perovskite films. The Sn(IV) content is reduced further, to 3%, for the TM-DHP and maltol treated films. The maltol helps to decrease the Sn(IV) content by protecting and passivating the surface of the perovskite films, making it more resistant to oxidation by the environment.

The effect of the treatments on the film morphology and crystallinity were examined by the scanning electron microscopy (SEM) and X-ray diffraction (XRD), respectively. No obvious

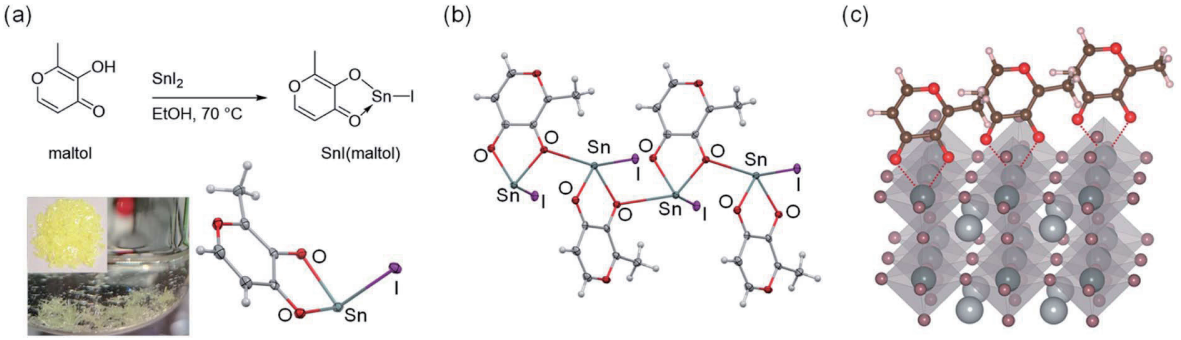


Fig. 1 (a) Synthetic route, picture of single crystals, and ORTEP drawing of SnI(maltol) crystal structure with 50% thermal ellipsoids. (b) The crystal packing structure of SnI(maltol). (c) Schematic illustration of the chelation between maltol molecules and undercoordinated Sn(II) species on the perovskite film surface.

© 2021 The Author(s). Published by the Royal Society of Chemistry

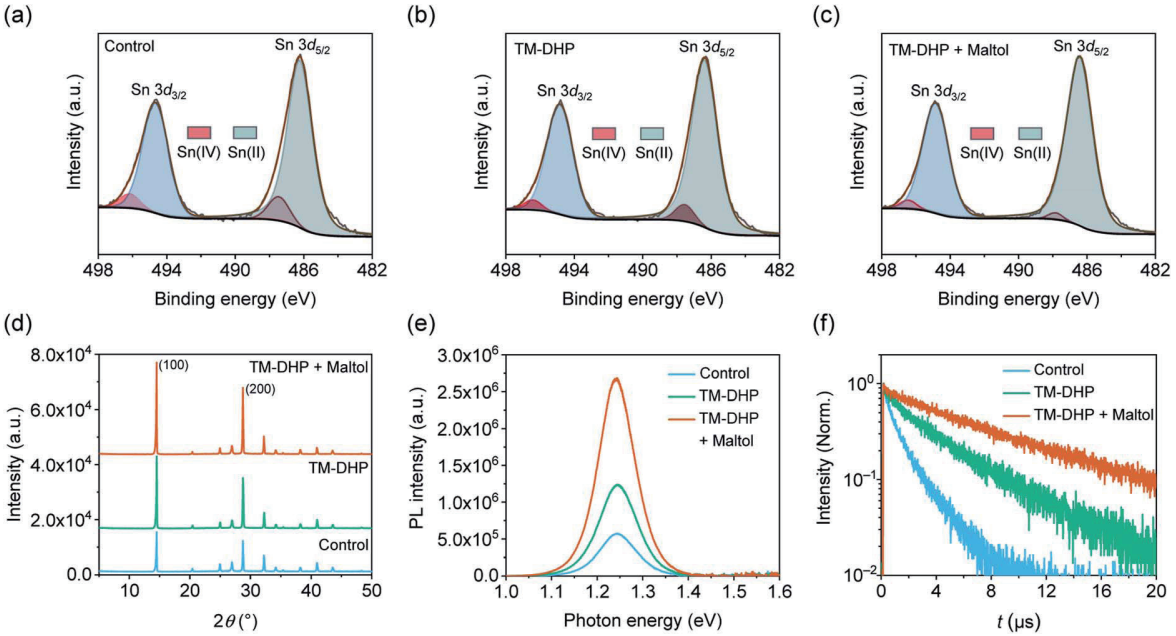


Fig. 2 XPS spectra of Sn $3d_{3/2}$ and $3d_{5/2}$ core levels for the (a) control, (b) TM-DHP-treated, and (c) TM-DHP combined with maltol treated perovskite films. The amount of Sn(IV) content on the surface of the control, TM-DHP, and both TM-DHP and maltol treated perovskite films is 9, 6, and 3%, respectively. (d) XRD patterns of perovskite films fabricated on PEDOT:PSS-coated FTO substrates. (e) Steady-state photoluminescence (PL) spectra, and (f) time-resolved photoluminescence (TRPL) decay curves of the perovskite films fabricated on quartz substrates. The carrier lifetime of the control, TM-DHP, and both TM-DHP and maltol treated perovskite films is 1.3, 3.7, and 7.4 μs, respectively.

differences in grain size or roughness can be discerned from the SEM images (Fig. S10†), and the full-width at half-maximum (FWHM) of the XRD characteristic peaks are largely unaffected by the treatments (Fig. S11†). The films treated with TM-DHP, have improved crystallinity, as indicated by the stronger intensities of the peaks at 14.5° and 28.8°, indexed to (100) and (200) planes of the perovskite, respectively (Fig. 2d). This may be the result of the mediating influence of TMP (tetramethylpyrazine), formed by the reaction of TM-DHP and SnF_2,[40] on the perovskite crystallization process.[34] The intensity of the (100) and (200) peaks increased even more after the maltol treatment, suggesting some additional improvement in film crystallinity. As the surface treatment involves washing the perovskite film with a solution of maltol dissolved in toluene, followed by a second annealing step, we speculate that the improvement in crystallinity in the treated films could be caused by structural reorganization during the annealing process.[47–49]

The treatments were found to have a considerable impact on the charge carrier recombination dynamics, which are critical for achieving efficient conversion of photons to electrical charge. As shown in Fig. 2e, the PL intensity of the perovskite film prepared with TM-DHP is 2.2 times larger than that of control film. After maltol post-treatment, the PL intensity increases to become 4.7 times stronger than the control. The increase in PL intensity indicates that non-radiative recombination is supressed, and, therefore, the trap states in the perovskite films have been reduced by both the TM-DHP treatment and the maltol post-treatment.

The reduction in charge carrier recombination is confirmed by the charge carrier lifetimes, which are estimated from the time resolved photoluminescence (TRPL) decay curves shown in Fig. 2f. These measurements were made under a photon flux of 3.5×10^{11} photons per cm^2, comparable to the incident flux under AM1.5G. The lifetimes were found to depend on the incident light intensity,[50] as shown in ESI Fig. S12 and S13.† With Sn(IV) scavenging, the lifetime increased from 1.3 to 3.7 μs. After maltol post-treatment, the lifetime reached a maximum of 7.4 μs. This is over six times longer than the value of 1.1 μs previously reported for mixed Pb–Sn perovskite films.[7] This value, obtained for thin polycrystalline Pb–Sn perovskite layers, is even comparable to those reported for state-of-the-art perovskite single crystals.[51]

Diffusion lengths could not be readily determined as we were unable to estimate the charge carrier mobility from the space-charge-limited current data.[52] Instead, an approximate evaluation of the diffusion length was realized using reported values for the diffusion coefficients (D) of Pb–Sn perovskite.[7] Using the PL lifetime, $t = 7.4$ μs, determined for our film, and their reported values of 0.02–0.05 $cm^2\ s^{-1}$ for the diffusion coefficients, the carrier diffusion length calculated from $\sqrt{Dt}$, is estimated to fall in the range of 3.8–6.1 μm. The local mobility of the holes and electrons within individual perovskite grains can be estimated using flash-photolysis time-resolved microwave conductivity (TRMC) (Fig. S14 and S15†).[53,54] The values are estimated to be 70 $cm^2\ V^{-1}\ s^{-1}$ and 110 $cm^2\ V^{-1}\ s^{-1}$, respectively. These high values point to the overall high quality of the perovskite

© 2021 The Author(s). Published by the Royal Society of Chemistry

materials, which is also supported by the XRD and PL experiments.

To confirm the impact of the improved charge carrier recombination dynamics on the device performance, the corresponding PSCs were fabricated. The solar cells had an positive–intrinsic–negative structure: fluorine-doped tin oxide (FTO)/poly(3,4-ethylenedioxythiophene):poly(styrene sulfonate) (PEDOT:PSS)/perovskite/fullerene (C_{60})/bathocuproine (BCP)/silver (Ag) (Fig. 3a). The perovskite film thickness was 800–1000 nm. The current density–voltage (J–V) curves of the best devices are shown in Fig. 3b, and the corresponding photovoltaic parameters are listed in Table 1. Measurements were made in inert atmosphere, under AM1.5G simulated solar radiation.

For control devices prepared without the TM-DHP or maltol treatment, the highest PCE was 18.2% (forward scan, J_{SC} = 31.1 mA cm^{-2}, V_{OC} = 0.78 V, and FF = 0.75). With the TM-DHP but without maltol treatment, the forward scan J_{SC}, V_{OC}, and FF was slightly increased to 31.6 mA cm^{-2}, 0.79 V, and 0.76, respectively, and the PCE reached 19.0%. Significantly improved performance was achieved when, in addition to TM-DHP treatment, the perovskite layers were post-treated with maltol. The champion PCE was 21.4% (reverse scan, J_{SC} = 33.1 mA cm^{-2}, V_{OC} = 0.82 V, and FF = 0.79) and devices had considerably improved reproducibility (Fig. S16†). This PCE is very close to the reported best performance for mixed Pb–Sn PSCs, 21.7%.[12,13] In Fig. 3c, we can observe that the PSCs reached the highest external quantum efficiency (EQE) of 91.2% at 680 nm, and the corresponding internal quantum efficiency (IQE) was 98.8%. The integrated J_{SC} was 32.3 mA cm^{-2}, somewhat lower than the maximum value (33.2 mA cm^{-2}) obtained from the J–V curves. The difference is attributed to the spectral mismatch of the solar simulator especially in near-infrared region. Considering the mismatch factor, which was calculated to be 1.027 (Fig. S17†), the J_{SC} values from the J–V curves correspond closely with the integrated value.

Table 1 Photovoltaic parameters of the perovskite solar cells

Device	Scan[a]	J_{SC} (mA cm^{-2})	V_{OC} (V)	FF	PCE (%)
Control	Forward	31.1	0.78	0.75	18.2
	Reverse	30.9	0.78	0.74	18.1
TM-DHP	Forward	31.6	0.79	0.76	19.0
	Reverse	31.3	0.80	0.75	18.7
TM-DHP + maltol	Forward	33.2	0.82	0.77	21.0
	Reverse	33.1	0.82	0.79	21.4

[a] Scan direction: forward and reverse denotes the scan direction from J_{SC} to V_{OC} and from V_{OC} to J_{SC}, respectively.

To investigate the improved device performance in the view of its electronic properties, additional characterizations of the devices were performed. Impedance scans (Fig. 3d and S18†) reveal a single semicircle for each device, the diameter of which

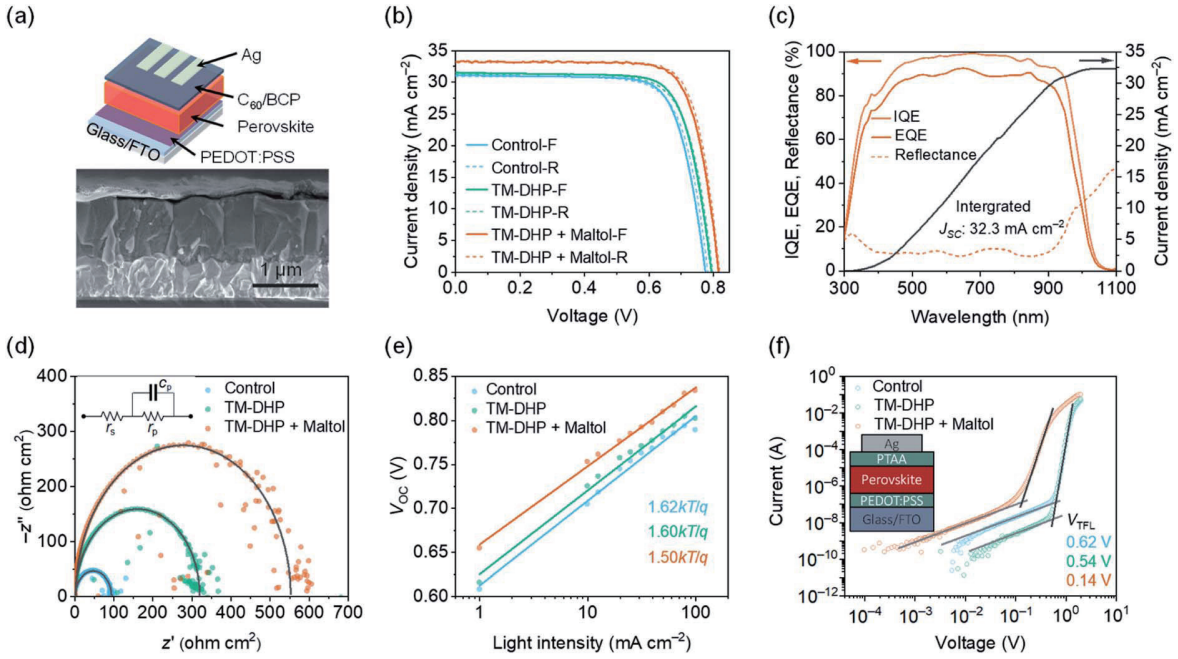


Fig. 3 (a) Schematic illustration and cross-sectional SEM image of a completed device with the architecture of FTO/PEDOT:PSS/perovskite/C_{60}/BCP/Ag. (b) J–V curves of the PSCs. (c) IQE, EQE, reflectance spectra and integrated J_{SC} of the encapsulated champion device under AM1.5G illumination in ambient air, no antireflection technique was applied for the device fabrication. (d) Complex impedance plots of PSCs measured in inert atmosphere under AM1.5G illumination. The shunt resistance across the perovskite layer was estimated at 93, 318, and 550 Ω cm^2 for the control, TM-DHP, and both TM-DHP and maltol treated PSCs, respectively. Insert shows the equivalent circuit model for fitting the electrochemical impedance spectroscopy data. (e) The open-circuit voltage V_{OC} as a function of illumination intensity with an ideality factor of 1.62, 1.60, and 1.50 for the control, TM-DHP, and both TM-DHP and maltol treated PSCs, respectively. (f) Dark current–voltage curves of the hole-only devices with the architecture of FTO/PEDOT:PSS/perovskite/PTAA/Ag. PTAA is poly(triaryl amine).

© 2021 The Author(s). Published by the Royal Society of Chemistry

is equal to the parallel resistance of the equivalent circuit, r_p. At low applied voltage, r_p equates to the shunt resistance across the perovskite layer, estimated at 93, 318, and 550 Ω cm^2 for the control, TM-DHP, and both TM-DHP and maltol treated PSCs, respectively. The increase in shunt resistance correlates with the increase in output current of the PSCs, and confirms the successively improved quality of the treated perovskite films.

Charge carrier recombination mechanisms are reflected by the Shockley diode ideality factor, as determined by the slope of the plot of V_{OC} *versus* incident light-intensity (Fig. 3e).[55,56] The ideality factor is 1.62, 1.60 for the control and TM-DHP treated devices, respectively, falling to 1.50 for the device treated with both TM-DHP and maltol, indicating lower non-radiative (trap-mediated) recombination rates in the maltol-treated PSCs.

To estimate the density of trap states in the films, we measured the dark current–voltage (*I*–*V*) curves of the hole-only and electron-only devices (Fig. 3f). The voltage where the current begins to sharply increase can be assigned to the trap-filled limit voltage (V_{TFL}). V_{TFL} is related to the trap density, N_{trap}, as $V_{TFL} = N_{trap}(eL^2)/(2\varepsilon_r\varepsilon_0)$, where e is the elementary charge of the electron, ε_0 is the vacuum permittivity, ε_r is the relative dielectric constant of the perovskite (around 32),[57] and L is the thickness of the perovskite film. V_{TFL} for the perovskite films in the hole-only devices is 0.62, 0.54, and 0.14 V, respectively, corresponding to trap densities of 2.9×10^{15}, 2.4×10^{15}, and 6.3×10^{14} cm^{-3}. The electron trap densities for the perovskite films modified with TM-DHP and maltol were estimated to be around 3.6×10^{14} cm^{-3} (Table S2, Fig. S19†). These electrical measurements confirm the lower trap-state densities in the treated perovskite films, which leads to longer carrier lifetimes of the treated perovskite films, as well as improved performance of the PSCs.

3. Conclusions

In this study, we found that maltol, a cheap and common flavor enhancer, can coordinate to Sn(II) in SnI_2 to form a stable complex (SnI(maltol)). Based on this strong affinity of maltol for Sn(II), we demonstrated that, when used in combination with a Sn(IV) scavenging method acting on the precursor solution, post-treatment with maltol leads to suppressed Sn(IV) content, decreased defect densities, and remarkably prolonged charge carrier lifetimes in the perovskite films, over 7 μs. A PCE of 21.4% was achieved for the champion solar cell. These high quality Pb–Sn materials achieved by the simple post-treatment should be useful for wide variety of optoelectronic devices.

Author contributions

S. H. and A. W. conceived the idea. S. H. and K. O. performed the synthesis and characterization of Sn complexes. S. H. and M. A. T. conducted the XPS measurements. K. O. conducted the XRD measurements. K. O. carried out the PL measurements with help of T. H., T. Y. and Y. K. R. N. and A. S. conducted the TRMC measurements. S. H., M. A. T., and K. O. fabricated and measured the devices, and conducted SEM characterizations with the help of Y. I. S. H. and K. O. carried out the PYS measurements. R. M. conducted the impedance measurements. S. H. conducted the SCLC measurements with the help of R. M. M. A. T. and K. O. carried out the NMR measurements. S. H., M. A. T., R. M., and A. W. prepared the manuscript. All authors commented on the manuscript. A. W. supervised the project.

Conflicts of interest

There are no conflicts to declare.

Acknowledgements

This work was partially supported by JST-ALCA (JPMJAL1603), JST-COI (JPMJCE1307), JST-CREST (JPMJCR16N3), and NEDO. JSPS KAKENHI (JP19K05666, JP20K22531, JP20H00398, JP20H05836, and JP21H04699), International Collaborative Research Program of ICR, Kyoto University. Additional support was received from MEXT Elements Strategy Initiative to Form Core Research Center (JPMXP0112101001), JSPS for a Research Fellowship for Young Scientists (JP21J14762) and the China Scholarship Council. We thank Prof. Toshiyuki Nohira and Dr Takayuki Yamamoto (Kyoto University) for XPS measurement, Prof. Yuichi Shimakawa and Dr Masato Goto (Kyoto University) for XRD measurement. We thank Dr Tomoya Nakamura (Kyoto University) for fruitful discussions. We thank Ajinomoto Fine-Techno Co., Inc. for providing the materials for device encapsulation.

Notes and references

1 J. J. Yoo, G. Seo, M. R. Chua, T. G. Park, Y. Lu, F. Rotermund, Y.-K. Kim, C. S. Moon, N. J. Jeon, J.-P. Correa-Baena, V. Bulović, S. S. Shin, M. G. Bawendi and J. Seo, *Nature*, 2021, **590**, 587–593.
2 J. Jeong, M. Kim, J. Seo, H. Lu, P. Ahlawat, A. Mishra, Y. Yang, M. A. Hope, F. T. Eickemeyer, M. Kim, Y. J. Yoon, I. W. Choi, B. P. Darwich, S. J. Choi, Y. Jo, J. H. Lee, B. Walker, S. M. Zakeeruddin, L. Emsley, U. Rothlisberger, A. Hagfeldt, D. S. Kim, M. Grätzel and J. Y. Kim, *Nature*, 2021, **592**, 381–385.
3 M. Hu, M. Chen, P. Guo, H. Zhou, J. Deng, Y. Yao, Y. Jiang, J. Gong, Z. Dai, Y. Zhou, F. Qian, X. Chong, J. Feng, R. D. Schaller, K. Zhu, N. P. Padture and Y. Zhou, *Nat. Commun.*, 2020, **11**, 151.
4 W. Shockley and H. J. Queisser, *J. Appl. Phys.*, 1961, **32**, 510–519.
5 M. T. Klug, R. L. Milot, J. B. Patel, T. Green, H. C. Sansom, M. D. Farrar, A. J. Ramadan, S. Martani, Z. Wang, B. Wenger, J. M. Ball, L. Langshaw, A. Petrozza, M. B. Johnston, L. M. Herz and H. J. Snaith, *Energy Environ. Sci.*, 2020, **13**, 1776–1787.
6 A. Goyal, S. McKechnie, D. Pashov, W. Tumas, M. van Schilfgaarde and V. Stevanović, *Chem. Mater.*, 2018, **30**, 3920–3928.
7 J. Tong, Z. Song, D. H. Kim, X. Chen, C. Chen, A. F. Palmstrom, P. F. Ndione, M. O. Reese, S. P. Dunfield,

© 2021 The Author(s). Published by the Royal Society of Chemistry

O. G. Reid, J. Liu, F. Zhang, S. P. Harvey, Z. Li, S. T. Christensen, G. Teeter, D. Zhao, M. M. Al-Jassim, M. F. A. M. van Hest, M. C. Beard, S. E. Shaheen, J. J. Berry, Y. Yan and K. Zhu, *Science*, 2019, **364**, 475.
8 T. Jiang, Z. Chen, X. Chen, T. Liu, X. Chen, W. E. I. Sha, H. Zhu and Y. Yang, *Sol. RRL*, 2020, **4**, 1900467.
9 R. Lin, K. Xiao, Z. Qin, Q. Han, C. Zhang, M. Wei, M. I. Saidaminov, Y. Gao, J. Xu, M. Xiao, A. Li, J. Zhu, E. H. Sargent and H. Tan, *Nat. Energy*, 2019, **4**, 864–873.
10 C. Li, Z. Song, D. Zhao, C. Xiao, B. Subedi, N. Shrestha, M. M. Junda, C. Wang, C.-S. Jiang, M. Al-Jassim, R. J. Ellingson, N. J. Podraza, K. Zhu and Y. Yan, *Adv. Energy Mater.*, 2019, **9**, 1803135.
11 J. Xi and M. A. Loi, *ACS Energy Lett.*, 2021, **6**, 1803–1810.
12 K. Xiao, R. Lin, Q. Han, Y. Hou, Z. Qin, H. T. Nguyen, J. Wen, M. Wei, V. Yeddu, M. I. Saidaminov, Y. Gao, X. Luo, Y. Wang, H. Gao, C. Zhang, J. Xu, J. Zhu, E. H. Sargent and H. Tan, *Nat. Energy*, 2020, **5**, 870–880.
13 G. Kapil, T. Bessho, T. Maekawa, A. K. Baranwal, Y. Zhang, M. A. Kamarudin, D. Hirotani, Q. Shen, H. Segawa and S. Hayase, *Adv. Energy Mater.*, 2021, **11**, 2101069.
14 G. Kapil, T. Bessho, C. H. Ng, K. Hamada, M. Pandey, M. A. Kamarudin, D. Hirotani, T. Kinoshita, T. Minemoto, Q. Shen, T. Toyoda, T. N. Murakami, H. Segawa and S. Hayase, *ACS Energy Lett.*, 2019, **4**, 1991–1998.
15 Z. Yang, Z. Yu, H. Wei, X. Xiao, Z. Ni, B. Chen, Y. Deng, S. N. Habisreutinger, X. Chen, K. Wang, J. Zhao, P. N. Rudd, J. J. Berry, M. C. Beard and J. Huang, *Nat. Commun.*, 2019, **10**, 4498.
16 M. Wei, K. Xiao, G. Walters, R. Lin, Y. Zhao, M. I. Saidaminov, P. Todorović, A. Johnston, Z. Huang, H. Chen, A. Li, J. Zhu, Z. Yang, Y.-K. Wang, A. H. Proppe, S. O. Kelley, Y. Hou, O. Voznyy, H. Tan and E. H. Sargent, *Adv. Mater.*, 2020, **32**, 1907058.
17 W. Ke, C. Chen, I. Spanopoulos, L. Mao, I. Hadar, X. Li, J. M. Hoffman, Z. Song, Y. Yan and M. G. Kanatzidis, *J. Am. Chem. Soc.*, 2020, **142**, 15049–15057.
18 C. Li, Z. Song, C. Chen, C. Xiao, B. Subedi, S. P. Harvey, N. Shrestha, K. K. Subedi, L. Chen, D. Liu, Y. Li, Y.-W. Kim, C.-s. Jiang, M. J. Heben, D. Zhao, R. J. Ellingson, N. J. Podraza, M. Al-Jassim and Y. Yan, *Nat. Energy*, 2020, **5**, 768–776.
19 R. Prasanna, T. Leijtens, S. P. Dunfield, J. A. Raiford, E. J. Wolf, S. A. Swifter, J. Werner, G. E. Eperon, C. de Paula, A. F. Palmstrom, C. C. Boyd, M. F. A. M. van Hest, S. F. Bent, G. Teeter, J. J. Berry and M. D. McGehee, *Nat. Energy*, 2019, **4**, 939–947.
20 J. Tong, J. Gong, M. Hu, S. K. Yadavalli, Z. Dai, F. Zhang, C. Xiao, J. Hao, M. Yang, M. A. Anderson, E. L. Ratcliff, J. J. Berry, N. P. Padture, Y. Zhou and K. Zhu, *Matter*, 2021, **4**, 1365–1376.
21 E. Ruggeri, M. Anaya, K. Gałkowski, G. Delport, F. U. Kosasih, A. Abfalterer, S. Mackowski, C. Ducati and S. D. Stranks, *Adv. Mater.*, 2019, **31**, 1905247.
22 F. Li, X. Deng, F. Qi, Z. Li, D. Liu, D. Shen, M. Qin, S. Wu, F. Lin, S.-H. Jang, J. Zhang, X. Lu, D. Lei, C.-S. Lee, Z. Zhu and A. K. Y. Jen, *J. Am. Chem. Soc.*, 2020, **142**, 20134–20142.
23 A. Y. Alsalloum, B. Turedi, K. Almasabi, X. Zheng, R. Naphade, S. D. Stranks, O. F. Mohammed and O. M. Bakr, *Energy Environ. Sci.*, 2021, **14**, 2263–2268.
24 S. Wu, Z. Li, M.-Q. Li, Y. Diao, F. Lin, T. Liu, J. Zhang, P. Tieu, W. Gao, F. Qi, X. Pan, Z. Xu, Z. Zhu and A. K. Y. Jen, *Nat. Nanotechnol.*, 2020, **15**, 934–940.
25 M. I. Saidaminov, I. Spanopoulos, J. Abed, W. Ke, J. Wicks, M. G. Kanatzidis and E. H. Sargent, *ACS Energy Lett.*, 2020, **5**, 1153–1155.
26 J. Pascual, G. Nasti, M. H. Aldamasy, J. A. Smith, M. Flatken, N. Phung, D. Di Girolamo, S.-H. Turren-Cruz, M. Li, A. Dallmann, R. Avolio and A. Abate, *Mater. Adv.*, 2020, **1**, 1066–1070.
27 T.-B. Song, T. Yokoyama, C. C. Stoumpos, J. Logsdon, D. H. Cao, M. R. Wasielewski, S. Aramaki and M. G. Kanatzidis, *J. Am. Chem. Soc.*, 2017, **139**, 836–842.
28 T.-B. Song, T. Yokoyama, S. Aramaki and M. G. Kanatzidis, *ACS Energy Lett.*, 2017, **2**, 897–903.
29 F. Wang, J. Ma, F. Xie, L. Li, J. Chen, J. Fan and N. Zhao, *Adv. Funct. Mater.*, 2016, **26**, 3417–3423.
30 Q. Chen, J. Luo, R. He, H. Lai, S. Ren, Y. Jiang, Z. Wan, W. Wang, X. Hao, Y. Wang, J. Zhang, I. Constantinou, C. Wang, L. Wu, F. Fu and D. Zhao, *Adv. Energy Mater.*, 2021, **11**, 2101045.
31 K. J. Savill, A. M. Ulatowski and L. M. Herz, *ACS Energy Lett.*, 2021, **6**, 2413–2426.
32 L. Xu, X. Feng, W. Jia, W. Lv, A. Mei, Y. Zhou, Q. Zhang, R. Chen and W. Huang, *Energy Environ. Sci.*, 2021, **14**, 4292–4317.
33 F. Gu, S. Ye, Z. Zhao, H. Rao, Z. Liu, Z. Bian and C. Huang, *Sol. RRL*, 2018, **2**, 1800136.
34 S. J. Lee, S. S. Shin, Y. C. Kim, D. Kim, T. K. Ahn, J. H. Noh, J. Seo and S. I. Seok, *J. Am. Chem. Soc.*, 2016, **138**, 3974–3977.
35 Q. Tai, X. Guo, G. Tang, P. You, T.-W. Ng, D. Shen, J. Cao, C.-K. Liu, N. Wang, Y. Zhu, C.-S. Lee and F. Yan, *Angew. Chem., Int. Ed.*, 2019, **58**, 806–810.
36 Z. Lin, C. Liu, G. Liu, J. Yang, X. Duan, L. Tan and Y. Chen, *Chem. Commun.*, 2020, **56**, 4007–4010.
37 M. Ozaki, Y. Katsuki, J. Liu, T. Handa, R. Nishikubo, S. Yakumaru, Y. Hashikawa, Y. Murata, T. Saito, Y. Shimakawa, Y. Kanemitsu, A. Saeki and A. Wakamiya, *ACS Omega*, 2017, **2**, 7016–7021.
38 J. Liu, M. Ozaki, S. Yakumaru, T. Handa, R. Nishikubo, Y. Kanemitsu, A. Saeki, Y. Murata, R. Murdey and A. Wakamiya, *Angew. Chem., Int. Ed.*, 2018, **57**, 13221–13225.
39 T. Nakamura, T. Handa, R. Murdey, Y. Kanemitsu and A. Wakamiya, *ACS Appl. Electron. Mater.*, 2020, **2**, 3794–3804.
40 T. Nakamura, S. Yakumaru, M. A. Truong, K. Kim, J. Liu, S. Hu, K. Otsuka, R. Hashimoto, R. Murdey, T. Sasamori, H. D. Kim, H. Ohkita, T. Handa, Y. Kanemitsu and A. Wakamiya, *Nat. Commun.*, 2020, **11**, 3008.
41 D. Luo, X. Li, A. Dumont, H. Yu and Z. H. Lu, *Adv. Mater.*, 2021, **33**, e2006004.
42 J. Xue, R. Wang and Y. Yang, *Nat. Rev. Mater.*, 2020, **5**, 809–827.
43 M. A. Kamarudin, D. Hirotani, Z. Wang, K. Hamada, K. Nishimura, Q. Shen, T. Toyoda, S. Iikubo, T. Minemoto,

© 2021 The Author(s). Published by the Royal Society of Chemistry

K. Yoshino and S. Hayase, *J. Phys. Chem. Lett.*, 2019, **10**, 5277–5283.
44 W. Ke, C. C. Stoumpos and M. G. Kanatzidis, *Adv. Mater.*, 2019, **31**, 1803230.
45 S. Shahbazi, M.-Y. Li, A. Fathi and E. W.-G. Diau, *ACS Energy Lett.*, 2020, **5**, 2508–2511.
46 M. C. Barret, M. F. Mahon, K. C. Molloy, J. W. Steed and P. Wright, *Inorg. Chem.*, 2001, **40**, 4384–4388.
47 J. Xue, R. Wang, K.-L. Wang, Z.-K. Wang, I. Yavuz, Y. Wang, Y. Yang, X. Gao, T. Huang, S. Nuryyeva, J.-W. Lee, Y. Duan, L.-S. Liao, R. Kaner and Y. Yang, *J. Am. Chem. Soc.*, 2019, **141**, 13948–13953.
48 T. Wu, Y. Wang, X. Li, Y. Wu, X. Meng, D. Cui, X. Yang and L. Han, *Adv. Energy Mater.*, 2019, **9**, 1803766.
49 H. Zhang, Y. Wu, C. Shen, E. Li, C. Yan, W. Zhang, H. Tian, L. Han and W.-H. Zhu, *Adv. Energy Mater.*, 2019, **9**, 1803573.
50 Y. Yamada, T. Nakamura, M. Endo, A. Wakamiya and Y. Kanemitsu, *J. Am. Chem. Soc.*, 2014, **136**, 11610–11613.
51 Y. Liu, Y. Zhang, X. Zhu, Z. Yang, W. Ke, J. Feng, X. Ren, K. Zhao, M. Liu, M. G. Kanatzidis and S. Liu, *Sci. Adv.*, 2021, **7**, eabc8844.
52 L. Gao, K. Zeng, J. Guo, C. Ge, J. Du, Y. Zhao, C. Chen, H. Deng, Y. He, H. Song, G. Niu and J. Tang, *Nano Lett.*, 2016, **16**, 7446–7454.
53 N. Ishida, A. Wakamiya and A. Saeki, *ACS Photonics*, 2016, **3**, 1678–1688.
54 E. M. Hutter, J.-J. Hofman, M. L. Petrus, M. Moes, R. D. Abellón, P. Docampo and T. J. Savenije, *Adv. Energy Mater.*, 2017, **7**, 1602349.
55 P. Caprioglio, C. M. Wolff, O. J. Sandberg, A. Armin, B. Rech, S. Albrecht, D. Neher and M. Stolterfoht, *Adv. Energy Mater.*, 2020, **10**, 2000502.
56 T. S. Sherkar, C. Momblona, L. Gil-Escrig, J. Ávila, M. Sessolo, H. J. Bolink and L. J. A. Koster, *ACS Energy Lett.*, 2017, **2**, 1214–1222.
57 Q. Dong, Y. Fang, Y. Shao, P. Mulligan, J. Qiu, L. Cao and J. Huang, *Science*, 2015, **347**, 967.

© 2021 The Author(s). Published by the Royal Society of Chemistry

4. 参考資料

京都大学化学研究所
化学関連分野の深化・連携を基軸とする先端・学際グローバル研究拠点
令和３年度国際共同利用・共同研究公募要領

京都大学化学研究所は、「化学に関する特殊事項の学理及び応用の研究を掌る」ために、化学を中心とする分野で基礎研究に重点を置いた先端研究に邁進してまいりました。平成２２～３０年度の期間には、文部科学大臣から国立大学共同利用・共同研究拠点としての認定を受け、化学研究所の活性を基盤とする「化学関連分野の深化・連携を基軸とする先端・学際研究拠点」として国内外の化学関連分野の研究者との共同利用・共同研究を推し進めてまいりました。この拠点活動におけるグローバル共同利用・共同研究が評価され、平成３０年化学研究所は文部科学省から国際共同利用・共同研究拠点に認定されました。これを受けて、平成３１年度からの国際共同利用・共同研究拠点活動においては、多様でグローバルな化学分野の共同研究を一層強力に推進すべく、さらなる事業展開を図っております。

つきましては、化学が関わる分野でご活躍の皆様のご意見・ご要望を尊重しつつ、世界の化学の基礎・応用研究を皆様とともに一層推進することを念頭に置き、下記の要領で令和 3 年度の拠点共同利用・共同研究の課題公募をさせて頂きたく存じます。

この公募に当たりましては、分野選択型（計画研究型）、課題提案型、連携・融合促進型および施設・機器利用型の四つに分けて研究課題を募集いたします。これらの課題の実施に際しては当研究所の専任教員または客員教員との共同研究を基調といたしますが、いずれの課題でも後述の共通設備・機器・資料等のご利用が可能です。なお、各課題とも、海外研究者を研究代表者あるいは研究協力者とする国際共同研究（この場合、英語フォームで申請下さい）と、国内研究者を研究代表者とする国内共同研究を実施致します。これらの点も勘案いただき、本公募要領の詳細について十分ご確認の上、期日までにご申請下さいますようお願いいたします。

京都大学化学研究所長　　辻井敬亘
共同研究ステーション長　寺西利治

1. 研究期間

１年間（令和３年４月１日から令和４年３月３１日まで）。

2. 研究課題分類

下記のような分類（型）ごとに研究課題を募集いたします。いずれの課題についても、分類ないし分野の担当者もしくは当研究所で対応する共同研究者にご一報の上、ご申請下さい。また、研究経費に関しては、p.3 の表をご覧下さい。

2-1. 分野選択型（計画研究型）研究課題

分野選択型（計画研究型）研究課題は、あらかじめ設定された分野に関して化学研究所内の研究者と共同で遂行する課題です。令和２年度は下記の５分野について課題を公募いたします。５分野を合わせて、萌芽的な課題と発展的な課題をそれぞれ２０件程度、採択の予定です。

ビーム科学分野（担当者：若杉 昌徳；wakasugi.masanori.8z@kyouto-u.ac.jp）
基本テーマ：先進量子ビームの開発と新奇診断分析手法の創出
趣旨：レーザー、X 線、電子線、イオンビームなどの量子ビームの高度化とその先端的診断分析法への応用を進めます。また、これらの量子ビームを複合的に用いて、極微細領域での超高速化学・物理現象の解明を目指します。

元素科学分野（担当者：中村 正治; masaharu@scl.kyoto-u.ac.jp）
基本テーマ：元素科学に基づく物質創製・機能創出
趣旨：元素の新たな特性を引き出し、この特性をもとに優れた機能を有する新物質を創製します。元素と社会との関わりを俯瞰した元素戦略研究も推進します。物質の機能は、構成元素の特性を相乗的に反映して発現します。この発現機構を明らかとし、望みの機能を意のままに創出することを目指します。

バイオ情報学分野（担当者：緒方 博之; ogata@kuicr.kyoto-u.ac.jp）
基本テーマ：バイオ情報を含む複合情報の融合解析
趣旨：ゲノムやメタゲノムに代表される最新バイオ情報に立脚して、バイオ情報がいかに生体内や自然環境における化学現象と関わっているかを明らかにし、生命システムについての化学的理解の深化を図ります。さらに、その成果を応用して、ゲノム創薬やパーソナライズド医療などへの展開も目指します。

物質合成分野（担当者：村田 靖次郎; yasujiro@scl.kyoto-u.ac.jp）
基本テーマ：複合機能材料の戦略的創製
趣旨：異種材料のハイブリッド化・複合化ならびにナノサイズ化に重点を置き、新規な機能をもつ新世代材料の創製を目指すとともに、生体の認識、応答、反応などの諸機能を担う例えば生体膜等も複合機能材料と捉え、機能物質と生命現象の化学的相関の解明も目指します。

現象解析分野（担当者：寺西 利治; teranisi@scl.kyoto-u.ac.jp）
基本テーマ：複合測定に基づく物質解析
趣旨：化学を基盤とする多種の分光学的手法・解析的手法を複合的に駆使して、天然および人工物質の構造・性質を分子レベルから巨視的レベルまで階層的に理解・記述することを目指し、一方、その結果を還元することによって新たな物質科学の枠組みを構築する取組みも目指します。

2-2. 課題提案型研究課題（担当者：梶　弘典; kaji@scl.kyoto-u.ac.jp）
課題提案型研究課題は、前項１で設定した一つの分野に留まらない分野、あるいはそれ以外の分野について、化学関連分野の研究者から自由にご提案いただく課題です。萌芽的な課題と発展的な課題を、それぞれ２０件程度、採択の予定です。新分野の開拓につながるような課題を特に歓迎いたします。なお、緊急性・重要性が極めて高いと判断した課題については、前記の応募期日にかかわらず、直ちに採択することもあります。

2-3. 連携・融合促進型研究課題（担当者：渡辺 宏; hiroshi@scl.kyoto-u.ac.jp）
連携・融合促進型研究課題は、化学関連分野における国内外の研究連携の強化を主目的とする共同研究課題です。国外も念頭に置く場合は、化学研究所の部局間国際学術交流締結先 (http://www.kuicr.kyoto-u.ac.jp/sites/international_exchange/agreement/ 参照)との共同研究を開始する場を求めていただくことも可能です。また、この目的に沿った研究集会の開催も本課題として応募いただけます。５件程度を採択する予定です。

2-4. 施設・機器利用型研究課題（担当者：倉田 博基; kurata@eels.kuicr.kyoto-u.ac.jp）
施設・機器利用型研究課題は、http://www.kuicr.kyoto-u.ac.jp/sites/research_activities/joint_research/kaken_kyodo_instr/(拠点ホームページ)に記載の共通設備・機器・資料等の利用を主とする共同研究課題です。１５件程度を採択する予定です。

令和３年度国際共同利用・共同研究経費概算値

	経費上限／件*（千円）	
	国際共同研究	国内共同研究
分野選択型萌芽的研究	1,000	800
分野選択型発展的研究	2,000	1,500
課題提案型萌芽的研究	1,000	800
課題提案型発展的研究	2,000	1,500
連携・融合促進型研究	1,000	800
施設・機器利用型研究	1,000	800

*表中の金額は目安です。予算の状況に応じた減額もありえますことをご了解下さい。
経費内での備品費、消耗品費、旅費の配分は、申請者と化学研究所の共同研究者が協議して決定下さい。特に、旅費については、地域性を勘案してご決定下さい。

3. 共同研究応募方法

3-1. 申請資格

国公私立大学、国公私立研究機関、独立行政法人等の専任研究者、または、これに準ずる者。

3-2. 申請書記入要領

申請に当たっては、該当する募集分類・分野の担当者もしくは当研究所で対応する共同研究者と、事前に研究課題、研究内容、研究経費に関して、必ずご協議下さい。対応する共同研究者は、当研究所の専任教員または令和２年度客員教員からお選び下さい。なお、教員のリストは下記の化学研究所ホームページをご参照下さい。

教員リスト　http://www.kuicr.kyoto-u.ac.jp/sites/research_activities/chemist/

また、対応する共同研究者をお決めになれない場合は、各分類・分野の担当者に、まず、ご相談ください。上記の表の経費上限は目安です。特に、経費内での備品費、消耗品費、旅費の配分については、当研究所で対応する共同研究者と十分にご協議の上で申請下さい。特に、旅費については、地域性を勘案してご申請下さい。

課題申請は、本要領に添付の分野選択型共同利用・共同研究申請書（様式１）、課題提案型共同利用・共同研究申請書（様式２）、連携・融合促進型共同利用・共同研究申請書（様式３）、施設・機器利用型共同利用・共同研究申請書（様式４）に必要事項を記入し、下記の要領で、化学研究所共同研究推進室にご提出下さい。

なお、各課題とも、海外研究者を研究代表者あるいは研究協力者とする国際共同研究も実施可能です。この場合、英語フォーム（Forms 1~4）の左肩の欄にチェックを入れて、当研究所の共同研究者に提出をご依頼下さい。

<記入上の注意事項>

1. ※を付した事項は当研究所で記入します。
2. 当研究所で対応する共同研究者は必ずご記入下さい。
3. 申請者（研究代表者）と共同研究者の役割分担を明記して下さい。事前に共同研究者の承諾を得ていただくことが必要です。
4. 申請書は３頁以内にまとめて下さい。

3-3. 提出期限および提出先

応募に当たっては、前記の申請書にご記入の上、令和３年１月１８（月）までに、下記宛に電子メール添付書類（Word 書類）としてお送り下さい。

問い合わせ先
京都大学化学研究所 共同研究推進室
E-mail: icr-hub@scl.kyoto-u.ac.jp，電話: (0774)38-3121

4. 課題選考と採択通知

応募課題の採否は、当研究所の共同研究委員会で審査し、運営評議会の承認を経て決定されます。審査に際しては、共同研究の申請内容だけでなく、予算枠や、共通設備・機器・資料の使用時間等も考慮いたします。採否の結果（内定）については、令和３年３月に当研究所の所長から研究代表者に通知いたします。

5. 研究の実施および研究成果報告

5-1. 研究経費等

研究代表者と当研究所で対応する共同研究者には、予算の範囲内で、研究経費（備品費および消耗品費）と旅費が支給されます。また、研究協力者（学生も含めることが可能です*）にも予算の範囲内で旅費が支給されます。共同研究の実施に当たっては、まず対応する共同研究者にご連絡下さい。なお、当研究所には、共同研究者のための宿泊施設はありません。

＊研究協力者について、学生の場合は原則として大学院生といたします。なお、傷害保険等に加入していることが必要です。

5-2. 研究成果報告

採択された研究課題については、研究成果報告書を次に記す作成要領に従って記載・提出していただきます。その報告書は、まとめて当研究所の国際共同利用・共同研究報告書集として公開させていただく予定です。また、その内容を研究成果報告会でご報告いただくことがあります。なお、報告会についての詳細は、採択課題の研究代表者に後日お知らせいたします。

5-3. 研究成果報告書の作成要領

分野選択型研究、課題提案型研究、施設・機器利用型研究については１頁、連携・融合促進型研究については２頁の報告書を（様式５）を用いて作成下さい。Ａ４版の用紙には１頁あたり１，２００字程度が記載できます。図表などカラーを用いても構いませんが、報告書集刊行の際はモノクロ印刷になることもありますので、その点をお含み置き下さい。

１頁の１行目の中央に研究課題名、３行目に右詰めで研究代表者の氏名と所属、５行目から本文を記載して下さい。なお、当研究所で対応した共同研究者は報告書の共著者とはせず、必要に応じて本文中に明記して下さい。また、国際共同研究の場合、報告書は英文でご作成ください。

5-4. 報告書の内容

形式は自由ですが、例えば、実験的研究では、目的、実験方法、実験結果、考察、成果報告（論文、学会発表等）をお書き下さい。なお、連携・融合促進型研究で研究集会を開催した場合には、研究集会のプログラム、参加者名簿（所属機関・部局・職名を明記）、および、作成された場合は要旨集またはプロシーディングスを添付して下さい。

5-5. 報告書の提出

提出締切日は、令和４年２月末日とします。電子ファイル（Word ファイルと PDF ファイル）を、WEB から提出してください。なお、ファイル名は「課題番号＋代表者名（姓）」として下さい（例：2021-1 田中.doc、2021-1 田中.pdf）。

問い合わせ先
京都大学化学研究所 共同研究推進室
E-mail: icr-hub@scl.kyoto-u.ac.jp，電話: (0774)38-3121

5-6. 研究成果の公開

学術論文などによる研究成果の公開に際しては、京都大学化学研究所の国際共同利用・共同研究として行われたことを明記して下さい。英文での謝辞例を次に示します。

謝辞例: This work was supported by the International Collaborative Research Program of Institute for Chemical Research, Kyoto University (grant # XXXX).
日本語での謝辞は、この英文表記に準ずるものとして下さい。

化学研究所 国際共共拠点 R3年度採択課題（応募199件，採択 133件，採択率 66.8 %，国際共同研究割合44.4%）

課題番号	研究代表者	研究代表者所属	化研内 研究協力者	型	選択 分野	実施 状況	国際	課題名（和文・英文）
2021-1	中川　充	地方独立行政法人大阪産業技術研究所	倉田 博基	分野選択型	1	萌芽的		アスペクト比の制御された金ナノらせんの合成および光学特性評価 Synthesis and optical characterization of gold nanohelices with controllable aspect ratio
2021-2	山口 由高	理研仁科センター・実験装置開発室	若杉 昌徳	分野選択型	1	萌芽的		蓄積リングのための位置感度型アクティブ標的の開発
2021-3	老川 典夫	関西大学・化学生命工学部	藤井 知実	分野選択型	1	発展的		根粒菌由来GraE タンパク質の結晶構造解析 Crystal Structure Analysis of GraE from Root-Nodule-Forming Bacterium
2021-4	砂原 淳	大阪大学・レーザー科学研究所	井上 峻介	分野選択型	1	発展的		プリパルス付与による高変換TNSA イオン加速機構実証 Enhanced production of fast ions by TNSA with Pre-pulse Laser
2021-5	小平 聡	国立研究開発法人量子科学技術研究開発機構	小川原 亮	分野選択型	1	萌芽的		電子線を用いた超高線量率放射線がん治療（FLASH）の作用機序の解明の試み Verification of radiochemical reaction mechanism for FLASH radiotherapy with electron beams
2021-6	大西 哲哉	理化学研究所・仁科加速器科学研究センター	若杉 昌徳	分野選択型	1	萌芽的		ナノ構造を持つ ISOL 用標的の開発 Development of new nano-structure target for ISOL
2021-7	W. M. C. Sameera	Hokkaido University, Institute of Low Temperature Science	大木 靖弘	分野選択型	2	萌芽的	国際	理論計算による酵素模倣型[Mo_3S_4Fe]クラスターの電子構造解析およびN2 還元反応解析 Electronic Structure of Biomimetic [Mo_3S_4Fe] Clusters and its Relation to the catalytic N2-Reduction: A Computational Study
2021-8	Todd B. Marder	Julius-Maximilians-Universität Würzburg, Institut für Anorganische Chemie	梶 弘典	分野選択型	2	発展的	国際	フッ素化三配位ホウ素をアクセプターとする新規発光材料の開発とデバイス評価 Development and device evaluation of new D-π-A emitters based on fluorinated triarylborone acceptors
2021-9	Haichuan Guo	Ningbo Institute of Industrial Technology (CNITECH) of the Chinese Academy of Sciences	島川 祐一	分野選択型	2	萌芽的	国際	金属酸化物におけるガスセンサー性能研究 Gas sensing properties research of metal oxides
2021-10	Wei-Tin Chen	National Taiwan University, Center for Condensed Matter Sciences	島川　祐一	分野選択型	2	発展的	国際	 Design and Tailoring Advanced Functional Materials: Symmetry Operation and High Pressure Synthesis
2021-11	Simon D. Kloß	Centre for Science at Extreme Conditions and School of Chemistry, University of Edinburgh	島川　祐一	分野選択型	2	萌芽的	国際	 Investigating iron nitrides prepared by new high-pressure synthesis with Mössbauer spectroscopy
2021-12	Rainer Streubel	Institute for Inorganic Chemistry, University of Bonn	時任 宣博	分野選択型	2	発展的	国際	新規なアニオン性FLP を用いた小分子活性化 Small molecule activation using anionic crypto-FLPs
2021-13	Takeaki Iwamoto	Tohoku University, Department of Chemistry	時任 宣博	分野選択型	2	発展的	国際	非対称型高周期典型元素π電子系の開拓と物性解明 Development of Unsymmetrical π-Electron Systems of Heavier Main Group Elements and Elucidation of Their Property
2021-14	Alakananda Hajra	DEPARTMENT OF CHEMISTRY, VISVA-BHARATI UNIVERSITY, SANTINIKETAN-731235, INDIA	中村 正治	分野選択型	2	萌芽的	国際	 C-H Borylation and Silylation under visible-light enabled Fe-catalysis
2021-15	Apurba K. Das	Department of Chemistry, Indian Institute of Technology Indore	中村 正治	分野選択型	2	萌芽的	国際	 Development of Iron-based Electrocatalysts for Electrocatalytic Conversion of Biomass into Value Added Chemicals
2021-16	Laksmikanta Adak	Department of Chemistry, Indian Institute of Engineering Science and Technology	中村 正治	分野選択型	2	萌芽的	国際	 Iron-Catalyzed Asymmetric Carbozincation and Ring-Opening Reactions of Oxabicyclic Alkenes

2021-17	小笠原 正道	徳島大学・大学院社会産業理工学研究部	大木 靖弘	分野選択型	2	萌芽的		フェロセニル基を持つホスフィン配位子の合成とFe クラスター化反応への応用 Synthesis of ferrocenyl-phosphines and their application in the preparation of Fe clusters
2021-18	立崎 武弘	東海大学・工学部 光・画像工学科	金光 義彦	分野選択型	2	萌芽的		極低温強磁場対応THz-STM の開発 Development of THz-STM for low-temperature and high magnetic field
2021-19	桐谷 乃輔	大阪府立大学・大学院工学研究科	金光 義彦	分野選択型	2	萌芽的		微弱な分子振動モードと結合させた極薄膜半導体における励起子発光の変調 Strong carrier modulation in 2D semiconducting materials by coupled molecular vibrations
2021-20	佐藤 琢哉	東京工業大学・理学院	廣理 英基	分野選択型	2	発展的		高強度テラヘルツパルスを駆使したマルチフェロイック物質におけるマグノン・フォノン励起 Magnon-phonon excitation in multiferroic materials by intense pulses
2021-21	藪内 直明	横浜国立大学・工学研究院	菅 大介	分野選択型	2	萌芽的		高圧合成法を利用したエネルギー材料の開発 Exploration of energy materials by high pressure synthesis technique
2021-22	立津 慶幸	名桜大学・リベラルアーツ機構	寺西 利治	分野選択型	2	発展的		新奇三元系ナノ粒子形成の物理的起源に関する研究 Study on the physical mechanism on novel-ternary nanoparticle formation
2021-23	山口 佳隆	横浜国立大学・大学院工学研究院	中村 正治	分野選択型	2	発展的		単核錯体の複核化による協働的反応場の開発 Development of collaborative reaction fields based on dinuclearization of mononuclear complexes
2021-24	橘 洋一	京都市産業技術研究所・高分子系チーム	中村 正治	分野選択型	2	萌芽的		磁性微粒子を用いたウルシオール塗膜の機能発現 Functionalization of urushiol coating film using magnetic particles
2021-25	笹森 貴裕	筑波大学・数理物質系化学域	若宮 淳志	分野選択型	2	発展的		高性能ペロブスカイト太陽電池作成に有効な高活性酸化スカベンジャーの開発 Creation of Effective Oxidation Scavenger for Efficient Perovskite-based Solar Cells
2021-26	光藤 耕一	岡山大学・大学院自然科学研究科	若宮 淳志	分野選択型	2	萌芽的		優れた光物性・電気化学的特性を併せ持つ新奇ヘテロアセン分子の開発 Development of heteroacenes with excellent photophysical and electrochemical properties
2021-27	Jinn-Moon Yang	National Chiao Tung University, Department of Biological Science and Technology/Institute of Bioinformatics & Systems Biology	阿久津 達也	分野選択型	3	発展的	国際	深層学習を用いたオミクスデータとモジュールに基づくネットワークデータの統合解析による腫瘍細胞分類 Integrating omics data and module-based network with deep learning to develop cancer type predictive models
2021-28	Jiangning Song	Monash University・Biomedicine Discovery Institute	阿久津 達也	分野選択型	3	発展的	国際	タンパク質分解酵素の標的タンパク質と切断部位の正確な予測のためのデータ駆動型深層学習方式の開発 Developing data-driven deep learning approaches for accurate identification of protease-specific substrate targets and cleavage sites
2021-29	Tom Delmont	CNRS/Genoscope/UMR8030	緒方 博之	分野選択型	3	発展的	国際	生態学的に重要な海洋巨大ウイルスのゲノムの解明 Unveiling the genomic contents of ecologically important marine giant viruses
2021-30	Samuel Chaffron	LS2N, CNRS UMR6004	遠藤 寿	分野選択型	3	発展的	国際	群集ネットワーク推定とマイニングを用いた全球海洋における巨大ウイルスの宿主生物予測 Revealing associations between giant viruses and eukaryotes in the global ocean through community networks inference and mining
2021-31	Masayuki Karasuyama	Nagoya Institute of Technology, Depertment of Computer Science	馬見塚 拓	分野選択型	3	萌芽的	国際	統計的機械学習による効率的なグラフ構造データ解析法の開発 A Study on Statistical Mashine Learning for Efficient Graph Structurred Data Analysis
2021-32	ホセ ナチェル	東邦大学・理学部情報科学科	阿久津 達也	分野選択型	3	萌芽的		確率的最小支配集合による複雑ネットワークの制御と解析 Control and Analysis of Complex Networks via Probabilistic Minimum Dominating Sets
2021-33	長崎 慶三	高知大学・理工学部門	緒方 博之	分野選択型	3	発展的		複数種の赤潮の消長過程におけるウイルス叢遷移様態の網羅的解析 Comprehensive analysis of viral succession during the transition of multiple types of algal blooms
2021-34	渡辺 登喜子	大阪大学・微生物病研究所	緒方 博之	分野選択型	3	萌芽的		コロナウイルス多様性検出法の開発 Development of the method for the detection of coronavirus diversity

2021-35	茅野 光範	帯広畜産大学・グローバルアグロメディシン研究センター	馬見塚 拓	分野選択型	3	発展的		効果的な分子ネットワーク解析方法の開発と医学・農学への応用 Effective molecular network analysis and application to medical and agricultural research
2021-36	Markus W. Ribbe	University of California, Irvine, Department of Molecular Biology and Biochemistr	大木 靖弘	分野選択型	4	萌芽的	国際	鉄硫黄クラスターの生合成過程解明に資する無機分子の合成 Synthesis of inorganic molecules for elucidation of biosynthetic pathways of iron-sulfur clusters
2021-37	Eli Zysman-Colman	University of St Andrews, Organic Semiconductor Centre, EaStCHEM School of Chemistry	梶 弘典	分野選択型	4	発展的	国際	分子配向を制御した新規青色TADF 発光材料の開発 Development of new blue TADF emitters with horizontal molecular orientations
2021-38	MARGETIC, Davor	Rudjer Boskovic Institute, Division of organic chemistry and biochemistry, Laboratory for physical organic chemistry	村田 靖次郎	分野選択型	4	発展的	国際	グアジニン修飾イソベンゾフランの付加環化反応の開発 Exploration of Cycloaddition Properties of Guanidine Functionalized Isobenzofurans
2021-39	Akinori Saeki	Department of Applied Chemistry, Graduate School of Engineering, Osaka University	若宮 淳志	分野選択型	4	発展的	国際	スズペロブスカイトに特化したホール輸送材の開発と素子評価 Development of hole transport materials for tin-perovskite and device characterization
2021-40	若林 成知	鈴鹿医療科学大学・保健衛生学部医療栄養学科	大木 靖弘	分野選択型	4	萌芽的		自己集合性含ホウ素化合物の合成、集合過程解明ならびに機能開拓 Synthesis of Self-Assembled Organoboran Compounds, Elucidation of Self-Assembly Process, and Creation of New Functions
2021-41	武田 洋平	大阪大学・大学院工学研究科	梶 弘典	分野選択型	4	発展的		ジベンゾフェナジンを電子アクセプターとするスルースペース電荷移動型熱活性化遅延蛍光材料の創製 Development of thermally activated delayed fluorescent materials based on through-space charge transfer using dibenzophenazine as an electron-acceptor
2021-42	平井 智康	大阪工業大学・応用化学科	竹中 幹人	分野選択型	4	萌芽的		キラル転写に基づく新規キラルシリカの調製 Chiral Silica with preferred-handed helical structure via chiral transfer
2021-43	鈴木 充朗	大阪大学・大学院工学研究科	村田 靖次郎	分野選択型	4	発展的		高効率光電変換を志向した非対称型有機半導体分子の開発 Development of nonsymmetrical organic semiconducting molecules toward efficient photovoltaics
2021-44	清水 章弘	大阪大学・大学院基礎工学研究科物質創成専攻	廣瀬 崇至	分野選択型	4	発展的		ソルバトクロミズムを示さないπ共役双性イオンの合成と物性 Synthesis and Properties of π -Conjugated Zwitterions with Negligible Solvatochromism
2021-45	小林 健二	静岡大学・グリーン科学技術研究所（および理学部）	山子 茂	分野選択型	4	発展的		環状ヘキサ-2,7-アントリレンエチニレン誘導体と環状パラフェニレンとのホスト-ゲスト化学に基づく複合化 Host-Guest Complexation of Cyclohexa-2,7-anthrylene Ethynylene Derivatives with [n]CPP
2021-46	髙橋 裕	東北大学・未来科学技術共同研究センター	登阪 雅聡	分野選択型	4	萌芽的		超分岐構造高分子の滑剤作用の解明と最適化 Elucidation of the lubrication properties of hyperbranched polymers and their optimization
2021-47	Ho, Tung-Yuan	Academia Sinica, Research Center for Environmental Changes	宗林 由樹	分野選択型	5	発展的	国際	北太平洋における微量金属の元素・同位体組成：起源と内部循環(2) Trace metal elemental and isotopic composition in the North Pacific Ocean: sources and internal cycling (2)
2021-48	Tadanori Koga	Stony Brook University, Department of Material Science and Chemical Engineering	竹中 幹人	分野選択型	5	発展的	国際	高分子ナノコンポジットの補強メカニズムの解明 Resolving the structure-dynamics-property relationship in polymer nanocomposites under uniaxial stretching
2021-49	Giovanni Ianniruberto	Dipartimento di Ingegneria Chimica, dei Materiali e della Produzione Industriale, Università degli Studi di Napoli “Federico II”	佐藤 健	分野選択型	5	萌芽的	国際	高分子の壁面滑りを計算するシミュレーション手法の開発 Development of simulation scheme for wall-slip of polymers
2021-50	Sathish K. Sukumaran	Graduate School of Organic Materials Science, Yamagata University	佐藤 健	分野選択型	5	発展的	国際	高分子液体の高周波応答: レオロジーおよび誘電緩和 High Frequency Response of Polymeric Liquids: Rheology and Dielectric Relaxation
2021-51	Visit Vao-soongnern	Graduate School of Organic Materials Science, Yamagata University	渡辺 宏	分野選択型	5	萌芽的	国際	末端修飾高分子の構造とダイナミクスに関する研究 Molecular understanding on the structures and dynamics of end-modified polymers
2021-52	小堀 康博	神戸大学・分子フォトサイエンス研究センター	梶 弘典	分野選択型	5	発展的		光エネルギー変換に対する振電効果：固体NMR と時間分解EPR の連携による解明 Vibronic Effect between Photon and Energy Conversions Studied by Solid State NMR and Time Resolved EPR Spectroscopy

2021-53	中口 譲	近畿大学・理工学部	宗林 由樹	分野選択型	5	萌芽的		海水中の微量重金属の分布及ぼすマイクロプラスチックの影響 Effect of microplastics on distribution of trace heavy metals in seawater
2021-54	向井 浩	京都教育大学・教育学部理学科	宗林 由樹	分野選択型	5	萌芽的		イオン液体含有高分子膜を用いた金属イオンの液膜輸送に関する研究 Study on transportation of metal ions through a polymer membrane containing ionic liquid
2021-55	藤原 明比古	関西学院大学・工学部	竹中 幹人	分野選択型	5	発展的		硫黄系高分子薄膜材料における硫黄元素が構成するナノ構造の空間不均一性評価 Spatial distribution of nanostructures composed of sulfur element in polymer thin films
2021-56	山本 勝宏	名古屋工業大学・大学院工学研究科	竹中 幹人	分野選択型	5	発展的		テンダーX 線領域での小角共鳴散乱法による含硫黄ウェット高分子材料のナノ構造解析 Structure analysis of polymer materials having sulfur atoms in a wet state by resonant small-angle scattering methods
2021-57	飯田 健二	北海道大学・触媒科学研究所	寺西 利治	分野選択型	5	発展的		プラズモニック合金ナノ粒子を設計するための理論的指針の構築 Construction of Theoretical Guidelines for Designing Plasmonic Nanoalloys
2021-58	園山 正史	群馬大学・大学院理工学府	長谷川 健	分野選択型	5	発展的		部分フッ素化両親媒性分子の膜物性・構造に対するRf 鎖長依存性の解析 Analysis of membrane structure and properties of partially fluorinated amphiphilic molecules
2021-59	青木 隆史	京都工芸繊維大学・繊維学系	長谷川 健	分野選択型	5	萌芽的		ポリマー薄膜表面の生分解過程に関する分光学的解析 A spectroscopic analysis on bio-degradation processes of polymer thin film surfaces
2021-60	河内 孝之	京都大学・生命科学研究科	山口 信次郎	分野選択型	5	萌芽的		基部陸上植物ゼニゴケにおける活性型ジベレリンの単離と同定 Identification of an active gibberellin compound in the basal land plant Marchantia polymorpha
2021-61	浦川 理	大阪大学・大学院理学研究科	松宮 由実	分野選択型	5	発展的		高分子結晶中に包接されたゲスト低分子のガラス転移と分子ダイナミクス Glass Transition and Molecular Dynamics of Guest Low Mass Molecules in the Clathrate of Polymer Crystals
2021-62	Zhijie Zhang	Changchun Institute of Applied Chemistry, Chinese Academy of Sciences (CAS)	松宮 由実	課題提案型		萌芽的	国際	鎖端のイオン性スティッカー数に分布を有するテレケリックイオノマーの非線形レオロジー Nonlinear rheological behavior of telechelic ionomer with a distribution of number of ionic stickers at the ends
2021-63	Yohei Ohashi	MRC Laboratory of Molecular Biology	青山 卓史	課題提案型		萌芽的	国際	植物細胞内の膜交通におけるPX-PH タイプホスホリパーゼD の役割 Role of PX-PH-type Phospholipase Ds in Plant Intracellular Membrane Traffic
2021-64	Zhong, Sheng	Peking University, School of Life Sciences	青山 卓史	課題提案型		発展的	国際	花粉形成におけるホスホイノシチドシグナルの役割 Role of Phosphoinositide Signaling in Pollen Development
2021-65	Yan-Mei Li	Tsinghua University, Department of Chemistry	上杉 志成	課題提案型		萌芽的	国際	がん免疫療法のための自己集合性アジュバント含有ワクチン Self-Assembling Adjuvant-Built-In Vaccines for Cancer Immune Therapy
2021-66	Lu Zhou	Fudan University, School of Pharmacy	上杉 志成	課題提案型		発展的	国際	小分子化合物による選択的タンパク質アセチル化 Site-Selective Protein Acetylation by a Small Molecule
2021-67	Sanghoon Kim	University of Ulsan	小野 輝男	課題提案型		発展的	国際	新規材料を用いたオービトロニクス Orbitronics with new material systems
2021-68	Kab-Jin Kim	Korea Advanced Institute of Science and Technology, Department of Physics	小野 輝男	課題提案型		発展的	国際	磁性絶縁体でのスピン波研究 Study of characteristics of spin wave in magnetic insulator
2021-69	Alexander Samardak	Far Eastern Federal University, School of Natural Science	小野 輝男	課題提案型		萌芽的	国際	フェリ磁性体のスピントロニクス応用 Application of ferrimagnets for spintronics devices
2021-70	Jang Hyuk Kwon	Department of Information Display	梶 弘典	課題提案型		発展的	国際	剛直なドナー骨格を用いた赤色熱活性遅延蛍光材料の開発 Highly efficient red thermally activated delayed fluorescence emitters with sterically hindered donor skeleton

2021-71	Lian Duan	Tsinghua University, Department of Chemistry	梶 弘典	課題提案型		発展的	国際	迅速な逆項間交差を有する熱活性化遅延蛍光材料を用いた高効率・高耐久青色有機EL 素子の開発 Development of highly efficient and stable blue organic light emitting diodes using thermally activated delayed fluorescent materials with ultrafast reverse intersystem crossing
2021-72	Maria Michela Corsaro	University of Naples Federico II, Department of Chemical Sciences	栗原 達夫	課題提案型		発展的	国際	細菌が放出する外膜小胞の表層多糖の構造機能解析 Structural and functional analysis of the surface polysaccharides of outer membrane vesicles released by bacteria
2021-73	Xianzhu Dai	College of Resources and Environment, Southwest University	栗原 達夫	課題提案型		萌芽的	国際	低温適応微生物を用いた低温異種タンパク質分泌生産系の構築 Construction of heterologous protein secretion system at low temperatures by using cold-adapted microorganisms
2021-74	Abigail P. Cid-Andres	Polytechnic University of the Philippines, College of Science, Department of Physical Sciences	宗林 由樹	課題提案型		萌芽的	国際	 Optimizing sampling devices and procedures to quantify sources of metals and microplastics in Metro Manila, Philippines' water resources
2021-75	Maya K. Endoh	Stony Brook University, Department of Material Science and Chemical Engineering	竹中 幹人	課題提案型		発展的	国際	高分子ナノ表面構造による殺菌効果-III Fabrication of nanotopographical polymer surfaces for bactericidal properties-III
2021-76	Robert C. Ferrier, Jr.	Michigan State University, Chemical Engineering and Materials Science	大野 工司	課題提案型		発展的	国際	リチウムイオン電池用ポリエーテル系ナノコンポジット固体電解質の合成 Synthesis of Polyether Nanocomposite Solid Polymer Electrolytes for Lithium Ion Batteries
2021-77	Ken Nakano	Yokohama National University, Faculty of Environment and Information Sciences	辻井 敬亘	課題提案型		萌芽的	国際	動的固着理論の検証と展開 Verification and Development of Dynamic Stiction Theory
2021-78	Yasuhiro Tachibana	RMIT University, School of Engineering	寺西 利治	課題提案型		発展的	国際	半導体量子ドット個体膜の作製とその電荷移動特性 Development of semiconductor quantum dot solid films and their charge carrier dynamics
2021-79	Jean-Pierre Bucher	Université de Strasbourg, Institut de Physique et Chimie des Matériaux (IPCMS)	寺西 利治	課題提案型		発展的	国際	応用に向けたナノ構造材料への学際的アプローチ Interdisciplinary Approach to Nanostructured Materials for Applications
2021-80	Sílvia Pujals	Nanoscopy for Nanomedicine Group, Institute for Bioengineering of Catalonia (IBEC)	二木 史朗	課題提案型		萌芽的	国際	ナノ医薬の新規細胞内効率的送達法 Novel strategy for intracellular delivery of nanomedicines
2021-81	Anne S. Ulrich	Karlsruhe Institute of Technology (KIT), Institute of Organic Chemistry (IOC) and Institute of Biological Interfaces (IBG-2), Chair of Biochemistry at IOC	二木 史朗	課題提案型		発展的	国際	曲率誘導ペプチドの構造活性相関と応用 Structural and functional analysis of curvature-inducing peptides and application
2021-82	Gopalakrishnan Balasubramanian	Leibniz institute for surface engineering, Leipzig, Germany	水落 憲和	課題提案型		発展的	国際	表面近傍NV 中心の安定化とスピンダイナミクスの研究 Research toward stable NV centers at shallow region and spin dynamics in diamond
2021-83	Marcus W. Doherty	Research School of Physics and Engineering, Australian National University	水落 憲和	課題提案型		発展的	国際	ダイヤモンド多量子ビット量子プロセッサーと量子センサにおける量子制御の研究 Research of quantum controls in multi-qubit diamond quantum processors and quantum sensors
2021-84	Zuhua He	Chinese Academy of Sciences, CAS Center for Excellence in Molecular Plant Sciences, Institute of Plant Physiology and Ecology	山口 信次郎	課題提案型		発展的	国際	イネの成長ホルモンの不活性化機構の解析 Molecular mechanisms for the inactivation of a growth hormone in rice
2021-85	Yunde Zhao	University of California San Diego, Division of Biological Sciences, Department of Cell and Developmental Biology	増口 潔	課題提案型		萌芽的	国際	新規ストリゴラクトン輸送体タンパク質の解析 Analysis of novel transporters for strigolactones or their biosynthetic intermediates
2021-86	Shingo Ito	Division of Chemistry and Biological Chemistry, School of Physical and Mathematical Sciences, Nanyang Technological University (NTU)	山子 茂	課題提案型		萌芽的	国際	シクロパラフェニレンとアゾメチンイリドの1,3-双極子環化反応 1,3-Dipolar Cycloaddition Reactions of Cycloparaphenylenes with Azomethine Ylide
2021-87	Mona Semsarilar	CNRS, Institut Europeen des Membranes (IEM)	山子 茂	課題提案型		発展的	国際	ポリビニリデンジフルオリドベースの膜の添加剤としての樹枝状両親媒性ブロック共重合体 Dendritic Amphiphilic Block Copolymers as Additive for Polyvinylidenedifluoride Based Membranes
2021-88	Kensuke Homma	Hiroshima University, Physics	井上 峻介	課題提案型		発展的	国際	宇宙暗黒成分解明へ向けた真空内四光波混合の探索 Search for four-wave-mixing in the vacuum – Unveiling dark components in the Universe –

2021-89	Hao-Wu Lin	Department of Materials Science and Engineering, National Tsing Hua University, Taiwan	若宮 淳志	課題提案型		発展的	国際	ペロブスカイトと擬ペロブスカイト発光材料の開発とその応用 Development of Perovskite and Perovskite-like Emitters and Their Applications
2021-90	高野 敦志	名古屋大学・大学院工学研究科	松宮 由実	課題提案型		萌芽的		モデルポリアルキルスチレン類を用いた分子構造と粘弾性パラメータの相関解析 Investigation of relationship between molecular structure and viscoelasticparameters of model poly(alkylstyrene)s.
2021-91	冨永 るみ	広島大学大学院・統合生命科学研究科	青山 卓史	課題提案型		萌芽的		植物表皮細胞の分化における制御ネットワークの研究 Study on the Regulatory Network of Plant Epidermal Cell Differentiation
2021-92	山崎 晶	大阪大学・微生物病研究所	上杉 志成	課題提案型		発展的		免疫賦活化するナノ集合体 Immune-Stimulatory Nano-Assemblies
2021-93	柴 祐司	信州大学・医学部	上杉 志成	課題提案型		発展的		自己集合性分子による心筋細胞移植の効率化 Self-Assembling Molecules for Improvement of Cardiomyocyte Engraftment
2021-94	尾坂 格	広島大学・大学院先進理工系科学研究科	脇岡 正幸	課題提案型		発展的		共役系ポリマーの開発と非フラーレン型太陽電池の高効率化 Development of π-conjugated polymers for high-efficiency non-fullerene solar cells
2021-95	諸田 美砂子	国立研究開発法人産業技術総合研究所・デバイス技術研究部門	小野 輝男	課題提案型		萌芽的		カルコゲナイド系超格子のトポロジカル相制御の実証 Demonstration of topological phase control in chalcogenide superlattices
2021-96	山田 啓介	岐阜大学・工学部・化学・生命工学科	小野 輝男	課題提案型		発展的		共沈法を用いて作製したガーネットナノ結晶体薄膜のスピンダイナミクスの研究 Study of spin dynamics in garnet nanocrystal thin films prepared by coprecipitation method
2021-97	田中 雅章	名古屋工業大学・大学院工学研究科	小野 輝男	課題提案型		萌芽的		垂直磁化を有するコバルトフェライト薄膜の電気・磁気的挙動の解明 Study on electronic and magnetic behavior of perpendicularly magnetized cobalt ferrite films
2021-98	長浜 太郎	北海道大学・工学研究院応用化学部門	小野 輝男	課題提案型		発展的		Fe_3O_4/$NiCo_2O_4$ 多層膜の電子およびスピン物性の解明 Electronic and spintronic properties of multilayer system including $NiCo_2O_4$ and Fe_3O_4
2021-99	相澤 直矢	大阪大学・大学院工学研究科	梶 弘典	課題提案型		発展的		ナノ秒オーダーの逆項間交差を示す熱活性化遅延蛍光材料の開発 Development of thermally activated delayed fluorescence materials with nanosecondorder reverse intersystem crossing
2021-100	山方 啓	豊田工業大学・大学院工学研究科	梶 弘典	課題提案型		発展的		時間分解分光計測による熱活性化遅延蛍光における逆項間交差の機構解明 Mechanism of the RISC in TADF Studied by Time-resolved Laser Spectroscopy
2021-101	山崎 思乃	関西大学・化学生命工学部	栗原 達夫	課題提案型		発展的		腸内細菌が生産する細胞外膜小胞の機能解析と応用法の開発 Functional characterization of extracellular vesicles produced by intestinal bacteria and development of their applications
2021-102	豊竹 洋佑	立命館大学・生命科学部生物工学科	栗原 達夫	課題提案型		萌芽的		酢酸菌における膜脂質依存的な発酵ストレス応答の解析 Analysis of membrane lipid-dependent fermentation stress response in acetic acid bacteria
2021-103	増野 敦信	弘前大学・大学院理工学研究科	島川 祐一	課題提案型		萌芽的		擬秩序ガラスの熱伝導 Thermal conduction of pseudo-ordered oxide glasses
2021-104	齊藤 高志	高エネルギー加速器研究機構・物質構造科学研究所	島川 祐一	課題提案型		発展的		異常高原子価イオンを含む機能性酸化物合成とその構造物性研究 Synthesis and study of oxides with unusually high-valent cation
2021-105	倉橋 健介	大阪府立大学工業高等専門学校・環境物質化学コース	宗林 由樹	課題提案型		萌芽的		界面活性剤を抽出剤として利用した固相抽出によるEu 分離法の開発 Development of Eu separation method by solid phase extraction using surfactant
2021-106	内田 幸明	大阪大学・大学院基礎工学研究科	大野 工司	課題提案型		発展的		ポリマーブラシ付与ナノプレートの精密合成による機能性フォトニック液晶の実現 Fine synthesis of polymer brush on nano-platelet for functional photonic LC

2021-107	源明 誠	富山大学・学術研究部工学系	大野 工司	課題提案型		発展的		高分子ブラシ層内の水の構造および凍結挙動の解析 Water in the Polymer Brush Layer: Structure and Freezing Behavior
2021-108	榊原 圭太	産業技術総合研究所・機能化学研究部門	辻井 敬亘	課題提案型		萌芽的		リグノセルロースナノファイバーの氷形成挙動の解明と表面修飾による機能拡張 Study on water freezing with lignocellulose nanofibers and their surface modification toward functional materials
2021-109	真島 豊	東京工業大学・フロンティア材料研究所	寺西 利治	課題提案型		発展的		単電子トランジスタにおける巨大磁気抵抗効果の検討 Giant magnetic resistance on Single-Electron Transistor
2021-110	秦野 修	奈良県立医科大学・医学部	中村 正治	課題提案型		萌芽的		再生可能資源・木質バイオマスの先端化学材料への効率的変換法の開発 Development of efficient conversion method of woody biomass, renewable biological resources, to advanced chemical materials
2021-111	桑田 啓子	名古屋大学・トランスフォーマティブ生命分子研究所	二木 史朗	課題提案型		発展的		新規細胞内取込誘導タンパク質の同定 Identification of novel cellular uptake stimulation proteins
2021-112	前川 大志	慶應義塾大学・薬学部	二木 史朗	課題提案型		発展的		マクロピノサイトーシスによる細胞内取込様式 Cellular uptake using macropinocytosis
2021-113	徳田 規夫	金沢大学・理工研究域 電子情報学系	水落 憲和	課題提案型		発展的		原子レベル平坦表面ダイヤモンドを用いた量子情報科学研究 Research by atomically flat surface diamond for quantum information science and technology
2021-114	牧野 俊晴	産業技術総合研究所・先進パワーエレクトロニクス研究センター	水落 憲和	課題提案型		発展的		量子センサの高感度化に向けたダイヤモンド合成と量子技術開発研究 Development of quantum technology and diamond synthesis for higher sensitivity of NV quantum sensor
2021-115	瀬戸 義哉	明治大学・農学部	山口 信次郎	課題提案型		発展的		「非典型的」ストリゴラクトン類の植物ホルモンおよび根圏シグナルとしての機能解析 Functional analysis of non-canonical strigolactones as plant hormones and root-derived signals
2021-116	藤塚 守	大阪大学・産業科学研究所	山子 茂	課題提案型		萌芽的		光励起に伴うシクロパラフェニレン酸化体の芳香族性・反芳香族性のスイッチング Switching of aromaticity/anti-aromaticity of oxidized cycloparaphenylenes
2021-117	岸本 泰明	京都大学大学院・エネルギー科学研究科	井上 峻介	課題提案型		萌芽的		高強度レーザーと構造性媒質の相互作用による高エネルギー密度プラズマの生成・保持に関する実験研究 Study of the generation and sustainment of high energy density plasmas due to the interaction between high power laser and structured medium
2021-118	島田 良子	日本女子大学・理学部数物科学科	渡辺 宏	課題提案型		発展的		ネマチック液晶-溶媒混合系における濃度揺らぎと配向揺らぎのカップリング Coupling of concentration fluctuation and orientation fluctuation in mixture of nematic liquid crystal and solvent
2021-119	Chengshan Wang	Middle Tennessee State University, Chemistry	長谷川 健	連携・融合促進型			国際	 Determine the three-dimensional structure of 13C labeled α-synuclein(61-95) in the Langmuir-Blodgett film and supported phospholipids bilayers by p-MAIRS FT-IR
2021-120	Yoshio Hayashi	Centre for Science at Extreme Conditions and School of Chemistry, University of Edinburgh	二木 史朗	連携・融合促進型			国際	中分子ペプチドによる細胞内タンパク質-タンパク質相互作用の調節 Modulation of in-cell protein-protein interactions using mid-sized peptides
2021-121	Tadashi Inoue	Osaka University, Department of Macromolecular Science	松宮 由実	連携・融合促進型			国際	東アジア圏の若手レオロジストのための第16 回ワークショップ The 16th International Workshop for East Asian Young Rheologists
2021-122	Torranin Chairuangsri	Chiang Mai University, Industrial Chemistry	倉田 博基	施設・機器利用型			国際	透過電子顕微鏡による電池開発のための新規機能性材料のミクロ・ナノ構造解析 Micro- and Nano-structural Characterization by Advanced Transmission Electron Microscopy of Novel Functional Materials for Battery Development
2021-123	Ming-Wen Chu	Center for Condensed Matter Sciences, National Taiwan University	倉田 博基	施設・機器利用型			国際	電子エネルギー損失分光法による電荷密度波の電子的不安定性の研究 Tackling the Electronic Instability of Charge-Density Waves by Electron Energy-Loss Spectroscopy

2021-124	Kunlang Ji	Centre for Science at Extreme Conditions and School of Chemistry, University of Edinburgh	島川 祐一	施設・機器利用型		国際	
							High-pressure synthesis of potential multiferroic oxides
2021-125	Mao Minoura	Rikkyo University, College of Science, Department of Chemistry	時任 宣博	施設・機器利用型		国際	新規有機16 族元素化合物の合成と性質解明
							Synthesis and Characterization of Novel Group 16 Element Compouds
2021-126	家 裕隆	大阪大学・産業科学研究所	梶 弘典	施設・機器利用型			固体NMR を駆使した有機結晶および有機薄膜の分析
							Analyses of organic crystals and thin films using solid-state NMR spectroscopy
2021-127	宮本 光貴	島根大学・総合理工学部	倉田 博基	施設・機器利用型			核融合プラズマ対向材料中の水素・ヘリウム挙動の高精度測定
							High accuracy measurement of hydrogen and helium behavior in plasma facing materials for nuclear fusion devices
2021-128	斉藤 光	九州大学・先導物質化学研究所	倉田 博基	施設・機器利用型			希土類共ドープナノ粒子の寿命制御
							Radiative lifetime control of rare-earth codoped nanoparticles
2021-129	吾郷 友宏	茨城大学・工学部物質科学工学科	水畑 吉行 時任 宣博	施設・機器利用型			単結晶X 線構造解析を用いた、含フッ素共役分子の結晶構造におけるフルオラス相互作用の解明
							Elucidation of the fluorous interactions in the crystal structures of fluorinecontaining conjugated molecules by the single-crystal X-ray structural analysis
2021-130	松尾 司	近畿大学・理工学部	時任 宣博	施設・機器利用型			ハロスタンニレンの合成と分子構造の解明
							Synthesis and Structural Characterization of Halostannylenes
2021-131	高橋 まさえ	東北大学・大学院農学研究科	時任 宣博	施設・機器利用型			平面シリセンナノリボンの理論設計と新しい動作原理の探究
							Theoretical design of planar silicene nanoribbons and search for new operating principles
2021-132	長洞 記嘉	福岡大学・理学部化学科	時任 宣博	施設・機器利用型			チオピリリウム骨格を組み込んだカチオン型芳香族化合物の合成と構造解析
							Synthesis and structures of cationic aromatics bearing thiopyrylium units
2021-133	布施 泰朗	京都工芸繊維大学・分子化学系	中村 正治	施設・機器利用型			FT-ICR-MS を用いた湖沼及び土壌環境中溶存有機物の化学特性および起源解析
							Analysis of chemical properties and origins of organic matter in lakes and soils using FT-ICR-MS